THÈSE

Pour obtenir le grade de

DOCTEUR DE L'UNIVERSITÉ GRENOBLE ALPES
et BRNO UNIVERSITY OF TECHNOLOGY

École doctorale : PHYS - Physique
Spécialité : Physique des matériaux
Unité de recherche : Institut Néel

Glace de spin artificielle : **interactions à longue portée, processus stochastique et thermodynamique effective dans des réseaux désaimantés de nano-aimants frustrés géométriquement**

Field demagnetised artificial square ice magnets: long-range interactions, origin of stochasticity and effective thermodynamics

Présentée par :

Ondřej BRUNN

Direction de thèse :

Nicolas ROUGEMAILLE DIRECTEUR DE RECHERCHE, CNRS – Institut Néel	Directeur de thèse
Vladimír KOLAŘÍK PROFESSEUR ASSOCIE, ISI CAS	Co-Directeur de thèse

Rapporteurs :

Daniel LACOUR
DIRECTEUR DE RECHERCHE, CNRS – Institut Jean Lamour
Yves LASSAILLY
DIRECTEUR DE RECHERCHE, École Polytechnique

Thèse soutenue publiquement le 19 juin 2024 devant le jury composé de :

Daniel LACOUR DIRECTEUR DE RECHERCHE, CNRS – Institut Jean Lamour	Rapporteur
Yves LASSAILLY DIRECTEUR DE RECHERCHE, École Polytechnique	Rapporteur
Michel HEHN PROFESSEUR, Université de Lorraine	Examinateur
Laurent RANNO MAITRE DE CONFERENCES, Université Grenoble Alpes	Examinateur
Elsa LHOTEL DIRECTRICE DE RECHERCHE, CNRS – Institut Néel	Examinatrice
Alexandr KNÁPEK PROFESSEUR ASSOCIE, ISI CAS	Examinateur

Invités :

Vojtěch UHLÍŘ
DOCTEUR EN SCIENCES, CEITEC – Brno University of Technology

BRNO UNIVERSITY OF TECHNOLOGY

VYSOKÉ UČENÍ TECHNICKÉ V BRNĚ

FACULTY OF MECHANICAL ENGINEERING

FAKULTA STROJNÍHO INŽENÝRSTVÍ

INSTITUTE OF PHYSICAL ENGINEERING

ÚSTAV FYZIKÁLNÍHO INŽENÝRSTVÍ

FIELD DEMAGNETISED ARTIFICIAL SQUARE ICE MAGNETS: LONG-RANGE INTERACTIONS, ORIGIN OF STOCHASTICITY AND EFFECTIVE THERMODYNAMICS

POLEM DEMAGNETIZOVANÉ UMĚLÉ SYSTÉMY SPINOVÉHO LEDU NA ČTVERCOVÉ MŘÍŽCE: DALEKODOSAHOVÉ INTERAKCE, PŮVOD STOCHASTICITY A EFEKTIVNÍ TERMODYNAMIKA

DOCTORAL THESIS

DIZERTAČNÍ PRÁCE

AUTHOR
AUTOR PRÁCE

Ing. Ondřej Brunn

SUPERVISOR
ŠKOLITEL

doc. Ing. Vladimír Kolařík, Ph.D.

SUPERVISOR
ŠKOLITEL

Dr. Nicolas Rougemaille

BRNO 2024

Abstract

In the past two decades, artificial spin ice systems have become a powerful experimental platform to investigate cooperative magnetic phenomena often associated with highly frustrated magnets. Compared to their natural counterparts, artificial spin ice systems made of interacting magnetic nanostructures offer several key advantages. Being engineered through nanofabrication processes, an extensive palette of geometries can be designed. In addition, their magnetic configuration can be visualised directly, at the scale of the spin degree of freedom, using magnetic imaging techniques. Local and global quantities can then be measured conveniently, in real space and time, at almost any desired temperature.

This PhD work focuses on such artificial spin systems, and more specifically on the square geometry, which was initially proposed as a two-dimensional (2D) counterpart of the three-dimensional (3D) pyrochlore crystal structure. However, this 2D approach removes the magnetic frustration present in 3D, and the system orders in a conventional antiferromagnetic fashion rather than exhibiting a highly degenerate, liquid-like ground state.

Following a strategy proposed in the literature, arrays of nanostructures consisting of two vertically offset sub-lattices were fabricated to restore frustration, enabling to reach a spin liquid regime experimentally. Imaging the magnetic configurations obtained after a field demagnetisation protocol, the analysis of the spin-spin correlations reveals deviations from what is predicted by the (short-range) square ice model. Comparing the experimental findings to Monte Carlo simulations, our results indicate that long-range magnetostatic interactions are not washed out in our arrays, contrary to what was initially thought.

Then, these artificial square ice structures were used to understand to what extent the field demagnetisation protocol we apply is a stochastic process. To do so, we studied the magnetic configurations obtained after successive field protocols. Our results show that each captured magnetic micro-state differs substantially from the previous one, but not entirely. Analysing the corresponding spin and vertex configurations, we demonstrate that our field protocol is a stochastic process, although we also observe unambiguous signatures of magnetic determinism that we attribute to the presence of quenched disorder. The possible sources of randomness in our experiment are discussed.

Finally, we explore the behaviour of a series of field-demagnetised conventional (non-offset) square arrays, in which the lattice parameter is gradually varied to tune the interaction strengths. Comparing the experimental vertex populations and spin-spin correlations to Monte Carlo predictions, we show that the lattice series is well approximated by a unique short-range spin Hamiltonian probed at different effective

temperatures. In other words, the lattice parameter can serve as a knob to probe the thermodynamics of a given spin model.

Key words

Artificial spin ice, geometrical frustration, magnetic imaging, field demagnetisation

Résumé

Au cours des deux dernières décennies, les systèmes frustrés de spins artificiels se sont imposés comme une plate-forme expérimentale incontournable pour sonder des phénomènes magnétiques coopératifs souvent associés au magnétisme frustré. Par rapport à leurs équivalents naturels, ces systèmes artificiels constitués de nanostructures magnétiques en interaction offrent plusieurs avantages clés. Fabriqués par des procédés de nanofabrication, ils permettent de concevoir une palette très large de géométries. En outre, leur configuration magnétique peut être visualisée directement, à l'échelle du degré de liberté du spin, à l'aide de techniques d'imagerie magnétique. Les quantités locales et globales peuvent alors être mesurées de manière pratique, dans l'espace réel et en temps réel, à n'importe quelle température.

Ce travail de doctorat se concentre sur de tels systèmes de spins artificiels, et plus particulièrement sur la géométrie carrée qui a été initialement proposée comme un équivalent bidimensionnel (2D) de la structure cristalline tridimensionnelle (3D) des systèmes pyrochlores. Toutefois, cette approche 2D supprime la frustration magnétique présente à 3D, et le système s'ordonne de manière antiferromagnétique au lieu de présenter un état fondamental massivement dégénéré, semblable à celui d'un liquide de spin.

Suivant une stratégie proposée dans la littérature, des réseaux carrés de nanostructures constitués de deux sous-réseaux décalés verticalement ont été fabriqués pour restaurer la frustration magnétique, ce qui a permis d'atteindre expérimentalement un régime liquide de spin. En visualisant les configurations magnétiques obtenues après un protocole de désaimantation, l'analyse des corrélations de spin révèle des écarts par rapport aux prédictions du modèle (à courte portée) de la glace carrée. En comparant ces données à des simulations Monte Carlo, nos résultats indiquent que les interactions magnétostatiques à longue portée ne peuvent pas être négligées dans nos expériences, contrairement à ce qui était pensé jusqu'à présent.

Par la suite, ces glaces carrées artificielles ont été utilisées pour comprendre dans quelle mesure le protocole de désaimantation en champ que nous appliquons est un processus stochastique. Pour ce faire, nous avons étudié les configurations magnétiques obtenues après des protocoles de champ successifs. Nos résultats montrent que chaque micro-état magnétique obtenu diffère substantiellement du précédent, mais pas complètement. En analysant les configurations de spin et de vertex correspondantes, nous démontrons que notre protocole en champ est un processus stochastique, bien que nous observions également des signatures non ambiguës d'un déterminisme magnétique que nous attribuons à la présence d'un désordre résiduel. L'origine de ce désordre et du comportement aléatoire en champ sont discutés.

Enfin, nous explorons la physique d'une série de réseaux carrés convention-

nels (c'est-à-dire non décalés verticalement) désaimantés en champ tournant, dans lesquels le paramètre de maille est progressivement modifié afin d'ajuster l'intensité des interactions magnétostatiques. En comparant les populations de vertex et les corrélations de spin à des prédictions Monte Carlo, nous montrons que la série de réseaux est bien décrite par un Hamiltonien de spin unique, sondé à différentes températures effectives. En d'autres termes, le paramètre de maille peut servir de potentiomètre pour explorer la thermodynamique d'un modèle de spin donné.

Mots clés

Glace de spin artificielle, frustration géométrique, imagerie magnétique, désaimantation en champ

Abstrakt

V posledních dvou desetiletích se umělé systémy spinového ledu staly významnou experimentální platformou pro zkoumání kooperativních magnetických jevů často spojených s vysoce frustrovanými magnety. Ve srovnání se svými přirozenými protějšky nabízejí umělé systémy spinového ledu vytvořené z vzájemně interagujících magnetických nanostruktur několik klíčových výhod. Díky tomu, že jsou připravovány pomocí mikro nanotechnologických procesů, lze vytvářet rozsáhlou paletu geometrií. Kromě toho lze jejich magnetickou konfiguraci přímo vizualizovat na úrovni spinového stupně volnosti pomocí magnetických zobrazovacích technik. Lokální a globální veličiny lze pak pohodlně měřit v reálném prostoru a čase, a to při téměř libovolné teplotě.

Tato doktorská práce se zaměřuje na takové umělé spinové systémy, konkrétně na čtvercovou geometrii, která byla původně navržena jako dvourozměrný (2D) protějšek trojrozměrné (3D) krystalové struktury pyrochlorů. Tento 2D přístup však odstraňuje magnetickou frustraci přítomnou ve 3D a systém se uspořádává konvenčním antiferomagnetickým způsobem, místo aby vykazoval vysoce degenerovaný základní stav podobný spinové kapalině.

Na základě strategie navržené v literatuře byla vyrobena pole nanostruktur sestávajících ze dvou vertikálně posunutých submřížek, aby se obnovil účinek frustrace, což umožnilo experimentálně dosáhnout režimu spinové kapaliny. Zachycení magnetických konfigurací získaných po protokolu demagnetizace magnetickým polem odhalilo následující: analýza párových spinových korelací vykazuje odchylky od toho, co předpovídá model čtvercového ledu (krátkého dosahu). Srovnáme-li experimentální zjištění se simulacemi Monte Carlo, naše výsledky ukazují, že magnetostatické interakce dlouhého dosahu nejsou v našich polích, na rozdíl od původního názoru, potlačeny.

Poté byly tyto umělé struktury čtvercového ledu použity k pochopení toho, do jaké míry je námi aplikovaný protokol demagnetizace polem stochastickým procesem. Za tímto účelem jsme studovali magnetické konfigurace získané po jednotlivých aplikacích demagnetizačního protokolu. Naše výsledky ukazují, že každý zachycený magnetický mikrostav se podstatně liší od předchozího, ale ne zcela. Analýzou odpovídajících spinových a vertexových konfigurací jsme prokázali, že náš demagnetizační protokol je stochastický proces, ačkoli jsme také pozorovali jednoznačné známky magnetického determinismu, které přisuzujeme přítomnosti drobných nedokonalostí našich umělých systému. Následně diskutujeme možné zdroje náhodnosti v našem experimentu.

Nakonec zkoumáme chování řady konvenčních (vertikálně neposunutých) čtvercových mřížek demagnetizovaných magnetickým polem, u nichž se postupně mění

parametr mřížky, aby se ladila síla interakcí mezi elementy tvořící systém. Srovnáním experimentálních populací vertexů a párových spinových korelací s předpověďmi Monte Carlo ukazujeme, že mřížková řada je dobře aproximována jedinečným spinovým hamiltoniánem krátkého dosahu zkoumaným při různých efektivních teplotách. Jinými slovy, mřížkový parametr může sloužit jako jistý ovladač pro zkoumání termodynamiky daného spinového modelu.

Klíčová slova

Umělé systémy spinového ledu, geometrická frustrace, magnetické zobrazovací techniky, demagnetizace magnetickým polem

Acknowledgement

First and foremost, I would like to express my profound gratitude to my supervisors, Nicolas Rougemaille and Vladimír Kolařík. Your guidance, patience, and mutually complementary expertise, both from the field of artificial spin ice and micro and nanofabrication, have been instrumental in my doctoral studies. The support I received from both of you, especially in navigating the challenges of working between two workplaces, was invaluable and greatly contributed to my studies.

My gratitude also belongs to all the people who helped me, shared their expertise, trained me to operate various experimental devices or contributed to my work in other ways.

Namely on the "French side", I would like to thank Benjamin Canals for providing invaluable numerical software solutions that were used in this work, Yann Perrin for sharing his evaluation scripts, sample fabrication tips, and other codes developed during his PhD studies, Stefania Pizzini for her supervision during operation of Nanobeam Nb5 (electron beam writer at Institut Néel) and for sharing some fabrication tips, Isabelle de Moraes for sharing here tips regarding alignment procedures for the Nanobeam Nb5, Olivier Fruchart for supporting my access to the PTA facility and last but not least I would like to thank all members of the Nanofab staff for their help and expertise regarding various experimental techniques.

On the "Czech side", I would like to thank Stanislav Krátký for sharing his expertise regarding electron beam lithography and related fabrication techniques, Petr Meluzín for running my extensive list of exposure jobs, Jakub Sadílek for all the fabrication related tips, Jana Chlumská for her advice on various chemistry-related problems and for the help with navigating the administrative processes at our institute. I would also like to thank to all other members of the Electron Beam Lithography research team at the ISI, who have also helped me in various ways. Last but not least, I also thank all the members of the core team at CEITEC Nano, who have trained me on various experimental devices.

I also want to extend my gratitude to all the members of the informal group "Spin ice consortium": Nico, Benjamin, Johann, Lucien, Luca, Maria, and Vojta. I have enjoyed our meetings and the opportunity to freely discuss various aspects of our research. Special thanks go to Vojtěch Shánilec, my fellow co-tutelle companion, for all the discussions, tips, and shared advice.

My shared doctoral studies were possible due to the co-tutelle scholarship (Barrande Fellowship) granted by the French government. I am very grateful for the possibility of shuttling between Brno and Grenoble and for the advantages of combining the expertise from the two workplaces.

Finally, it is hard to find words for the level of gratitude that I feel towards my

family, who supported me in all my endeavours. I would especially like to thank Julie, who, during my studies, transitioned from girlfriend to fiancé and ultimately my wife and mother of our son while remaining my best friend along the way. Děkuji!

Ondřej Brunn

Declaration

I declare that I have elaborated my doctoral thesis on the theme of *Field demagnetised artificial square ice magnets: long-range interactions, origin of stochasticity and effective thermodynamics* independently, under the guidance of my thesis supervisors, Dr. Nicolas Rougemaille and doc. Ing. Vladimír Kolařík, Ph.D., using the literature and other sources of information, which are all quoted in the thesis and detailed in the list of literature at the end of the thesis. Contributions to the presented work originating from other than the author are dully noted throughout the thesis. This version of the thesis corresponds to the version submitted before the thesis defence. The final version, reflecting the reviewers' and committee members' comments and suggestions, is expected to be provided after the defence to the *HAL archive*.

Ing. Ondřej Brunn

CONTENTS

1 INTRODUCTION

1.1 Geometrical frustration

In physical systems, frustration is typically described as the inability to satisfy all interactions within the system simultaneously. This condition can stem from structural/chemical disorder, as seen in spin glasses, or from a specific combination of lattice geometry, type of spin, and the nature of spin-spin interactions in structurally/chemically ordered systems. The latter case is referred to as *geometrical frustration*, and this type of frustration is the underlying condition for the unconventional phenomena observed in frustrated magnets, be they artificial or natural.

The typical example for illustrating the geometrical frustration is considering a triangular plaquette that hosts Ising-like spins on its corners, and the pairwise spin-spin interaction is antiferromagnetic. Ising-like spins are restricted to one dimension and can point only in two opposite directions (e.g. up or down). The antiferromagnetic interaction between nearest neighbours then tends to align the neighbouring spins in an alternating fashion. While it is possible to satisfy the interactions for the first two spins placed to the triangular plaquette, it is not possible to do so when placing the third (see Fig. 1.1a).

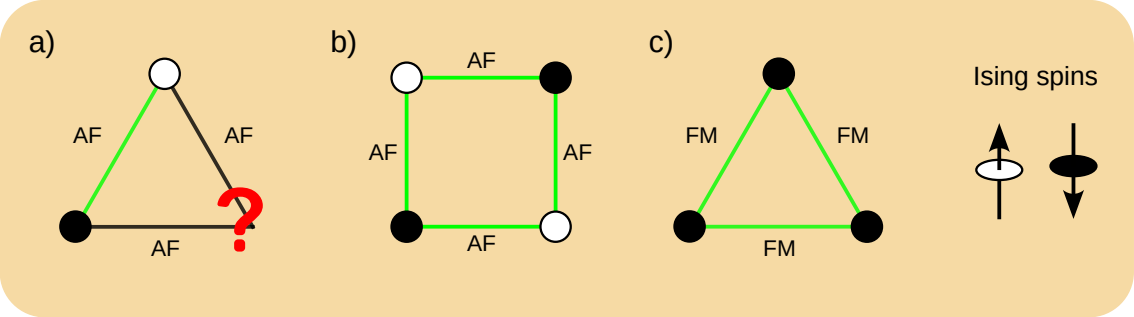

Fig. 1.1: a) Example of geometrical frustration: Ising spins placed on corners of triangular plaquette with nearest-neighbour antiferromagnetic (AF) interaction. Placing a third spin will inevitably lead to frustration in one interaction. b) If the geometry is changed to a square, it is possible to place all spins while keeping all nearest-neighbour interactions satisfied. c) If the geometry is maintained, but the nature of the interaction is changed to ferromagnetic (FM, i.e. spins tend to align parallel to each other), it is also possible to satisfy all interactions between nearest neighbours. White (black) dots represent spins pointing up (down). Green links indicate satisfied interactions.

Suppose the geometry of the problem is changed to a square. In that case, no frustration is present as placing the spins in alternating fashion is possible, and the nearest-neighbour antiferromagnetic interaction is fully satisfied (see Fig. 1.1b).

Similarly, suppose the nature of the interaction is changed to ferromagnetic while the triangular geometry is preserved. In that case, satisfying all interactions between the nearest neighbours is possible, and no frustration is present (see Fig. 1.1c). This simple example shows that geometrical frustration arises only if there is a specific combination of the lattice geometry, the nature of interaction and the type of spin (here, Ising-like). From this point onward, we will only focus on systems that effectively consist of Ising-like spins.

It is instructive to determine what are the possible configurations of a single triangular plaquette in which the Ising spins are coupled antiferromagnetically. The total amount of different configurations is $2^3 = 8$, as there are three spins, and each can have two different orientations. Essentially, there are two states: ground state configuration (six times degenerate, shown in Fig. 1.2a) in which one out of three bonds is frustrated and excited state (two times degenerate, shown in Fig. 1.2b) in which all three bonds are frustrated. If we continue the comparison with the square plaquette, the ground state configuration has no unsatisfied bonds and is two times degenerate (see Fig. 1.2c).

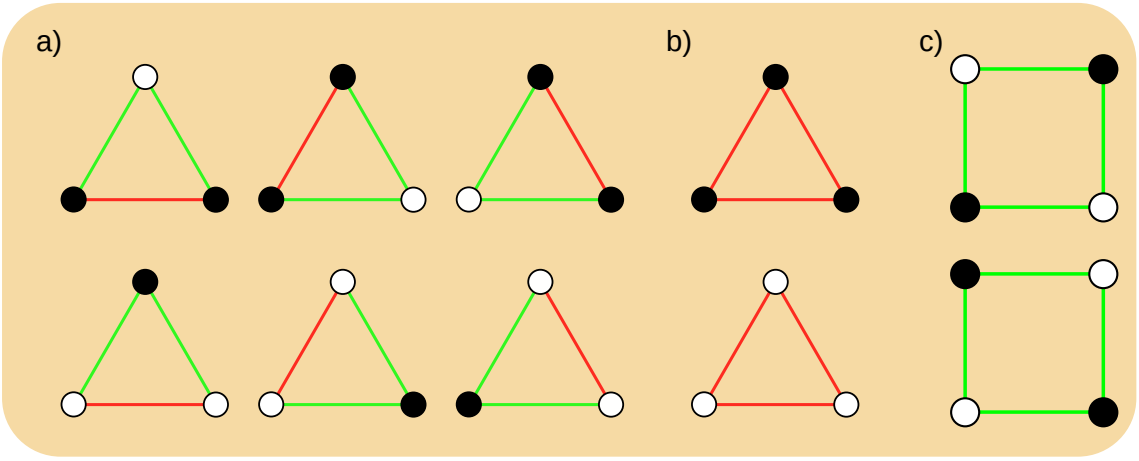

Fig. 1.2: a) Six lowest possible energy configurations (i.e., ground state configurations) for a triangular plaquette with antiferromagnetic interactions. b) Two possible higher-energy configurations for the same system. White (black) dots represent spins pointing up (down). Green (red) links indicate satisfied (frustrated) interactions. c) Two possible (not frustrated) ground state configurations for a square plaquette with antiferromagnetic interactions.

So far, we have restricted our discussion to evaluating the effect of frustration on the ground state configurations of a single triangular/square cell. Naturally, the next step is to examine what are the impacts of frustration on a network scale, focusing specifically on the lowest possible energy configurations. As a first step of building a network of corner-sharing triangles (this is effectively the kagome lattice),

one out of six GS configurations (shown in Fig. 1.2a needs to be selected. The subsequent addition of a triangular cell through a shared corner provides three possible orientations for the two undefined spins belonging to the new cell (when selecting from the available single triangle GS configurations). The building of such a chain is illustrated in Fig. 1.3. For example, for a chain consisting of only three triangles, there are $6 \times 3 \times 3 = 54$ possible ground state configurations and as the length of the chain is further extended, the degeneracy of the ground state increases faster than the system size. As all these states share the same energy, the ground state is macroscopically degenerate. Due to this extensive degeneracy of the ground state manifold, the residual entropy per site is a finite value. If the chain of triangles considered here is extended into a whole network, it forms the antiferromagnetic kagome lattice, for which it was shown that the residual entropy is $S_0 = 0.50183R$ [1], where R corresponds to ideal gas constant $R = N_A \cdot k_B$ (N_A is Avogadro's number and k_B is the Boltzmann constant).

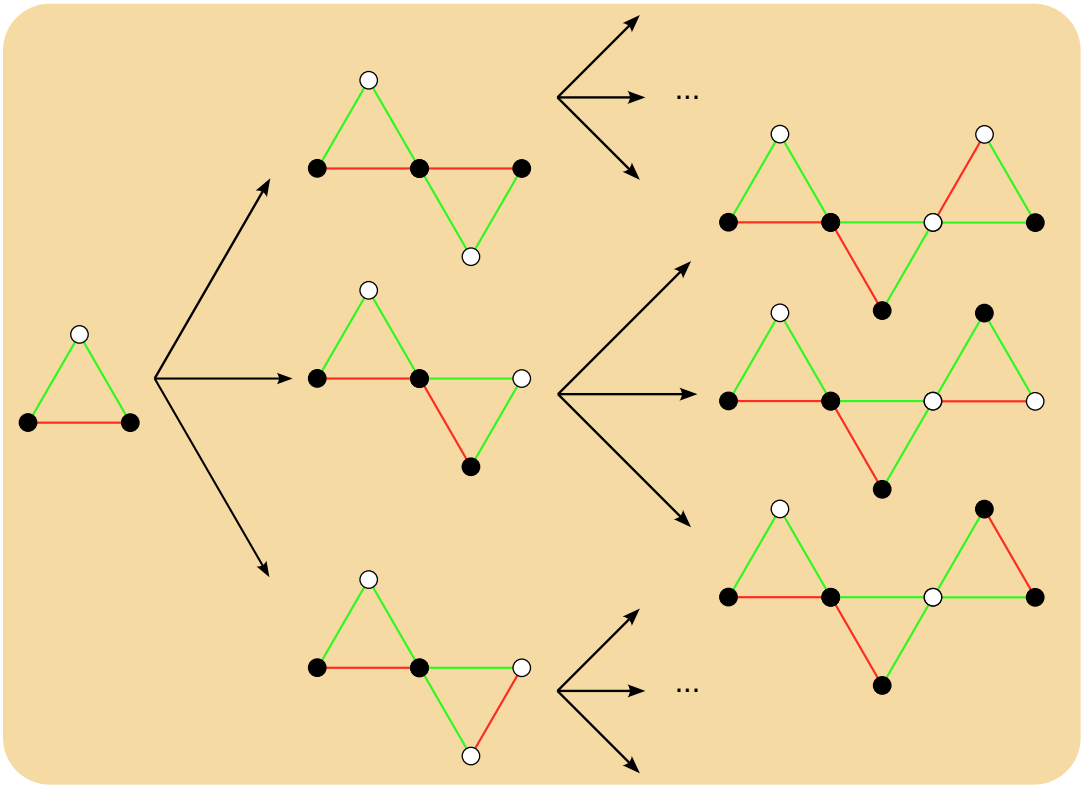

Fig. 1.3: Building a network of corner-sharing triangles out of available single triangle GS configurations. The number of possible configurations increases exponentially with the length of the chain.

To finish our comparison, if a chain or network of low-energy configuration is constructed from non-frustrated building blocks, such as square cells where the nearest-neighbour spins are antiferromagnetically coupled, the configuration becomes en-

tirely determined with the placement of the first block (selecting one of two possible ground state configurations). Consequently, there is only one way to connect subsequent blocks. In this scenario, the ground state degeneracy is unaffected by the system size, as the ground state always exhibits a twofold degeneracy. Hence, such a system does not exhibit any residual entropy.

At this point, we might conclude that geometrical frustration leads to extensive ground state degeneracy, subsequently leading to finite residual entropy (also called zero-point entropy). This behaviour contradicts the third law of thermodynamics, at least in the formulation provided by Planck, which states that: "When temperature falls to absolute zero, the entropy of any pure crystalline substance tends to a universal constant (which can be taken to be zero)." [2]. As frustrated systems generally lack a unique ground state ordering, they can explore the vast expanse of their ground state manifold with no energy penalty. This characteristic potentially allows for intensive fluctuations, even at low temperatures.

In this section, we have explored the impact of geometrical frustration on the low-energy states of theoretical spin models. In the next sections, we will show how such a phenomenon can be found in natural compounds, such as water ice and pyrochlore crystals.

1.2 Water ice

The seminal example of a frustrated natural compound is ordinary water ice. By the word ordinary, we refer to the hexagonal phase of water ice (I_h). In this phase, oxygen ions sit at the centres of a corner-sharing tetrahedron lattice. Thus, each oxygen ion is surrounded by four other oxygen ions. The bond between each pair of oxygen ions is facilitated by one hydrogen ion. Thus, each oxygen ion has a tetrahedral proton environment. As the electrostatic interactions between hydrogen ions are repulsive [3], one might conclude that the global energy would be minimised if the hydrogen ions occupy the middle position on each O – O line of contact. However, such a configuration does not maintain the integrity of water molecules, which exhibit strong chemical binding energy [4]. Consequently, the condition for minimising the global energy is that each oxygen has two hydrogen ions in a "close position" and two hydrogen ions in a "far position" (see Fig. 1.4). Therefore, the electrostatic interactions between hydrogen ions cannot all be minimised, leading to frustration. The two hydrogen ions in the close position correspond to covalent bonds of the water molecule, while the two in the far position are bonded via a hydrogen bond (they are bonded by covalent bonds to their respective neighbouring oxygen ions). The "two in, two out" condition, which reflects the water molecule

integrity constraint, is known as Bernal-Fowler "ice rules" [3].

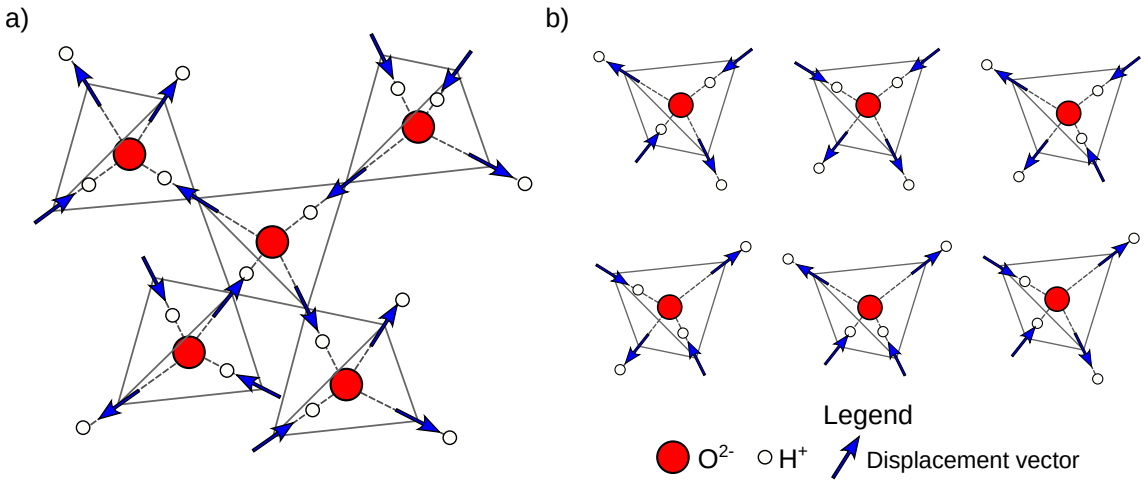

Fig. 1.4: a) Sketch of the internal structure of the low-energy arrangement of water molecules in ordinary ice (I_h). The arrows show the displacement vectors of hydrogen ions with respect to the centre point of each O – O line of contact. b) Sketch of six possible ground state configurations for an arrangement of four hydrogen ions surrounding one oxygen ion. Such configurations follow the *ice rules*.

During the 1930s, discrepancy (i.e., residual entropy) between the spectroscopic value of the entropy of water and that obtained by heat capacity measurements was reported [5, 6]. In 1935, Pauling [7] provided a description of water ice internal structure that accounts for the reported discrepancy. He emphasized that a large number of configurations respect the above-mentioned ice rules, and thus, the low-energy manifold of water ice exhibits extensive degeneracy. In other words, many different states can be built up by connecting the six tetrahedron cells that satisfy the two in, two out condition (see Fig. 1.4b).

Following Pauling's work, the total number of configurations for N oxygen ions is 2^{2N}, as there are $2N$ hydrogen ions, and each can be in two possible states (two positions per each O – O link). Out of these configurations, the ones in which the structure is built out of tetrahedron cells that respect the ice rules must be selected. There are $2^4 = 16$ possible configurations per tetrahedron, and six of those respect the ice rule constraint. Thus the number of possible states is $\Omega = 2^{2N} \cdot (6/16)^N = (3/2)^N$. All these states have the same lowest possible energy, therefore the ground state manifold is extensively degenerate. Thus the residual entropy of water ice is $S_0 = k_B \cdot \ln(\Omega) = 0.81\ \mathrm{cal} \cdot \mathrm{K}^{-1} \cdot \mathrm{mol}^{-1}$, which yields remarkable agreement with the experimental result reported by Giauque and Stout [6]: $S_0 = 0.82 \pm 0.05\ \mathrm{cal} \cdot \mathrm{K}^{-1} \cdot \mathrm{mol}^{-1}$.

1.3 Spin ice

Roughly sixty years after the consequences of frustration were described for water ice similar properties were discovered in rare-earth pyrochlore compounds at low temperatures: $Ho_2Ti_2O_7$ [8] and $Dy_2Ti_2O_7$ [9]. In those compounds, the magnetic ions (Ho^{3+} or Dy^{3+}) occupy the junctions of corner-sharing tetrahedron lattice and due to high crystal field energy their magnetic moments are constrained to a single axis (line connecting centres of the neighbouring tetrahedrons, same as the O – O line of contact in water ice), at low temperatures. Therefore, each spin is effectively Ising-like as it can only point towards or outwards with respect to the centre of one tetrahedron. Additionally, it was reported that the interaction between the rare-earth ions is effectively ferromagnetic [8] thus, the lowest energy state for each tetrahedron is when two spins point inwards and two outwards, which corresponds to the ice rules formulated for water ice. Therefore, a direct mapping between the displacement of hydrogen ions in water ice and the orientation of magnetic moments of magnetic ions in pyrochlore compounds is recovered. Thus, the pyrochlore compounds are essentially a magnetic analogue to water ice and are referred to as "spin ice" (see Fig. 1.5 for comparison).

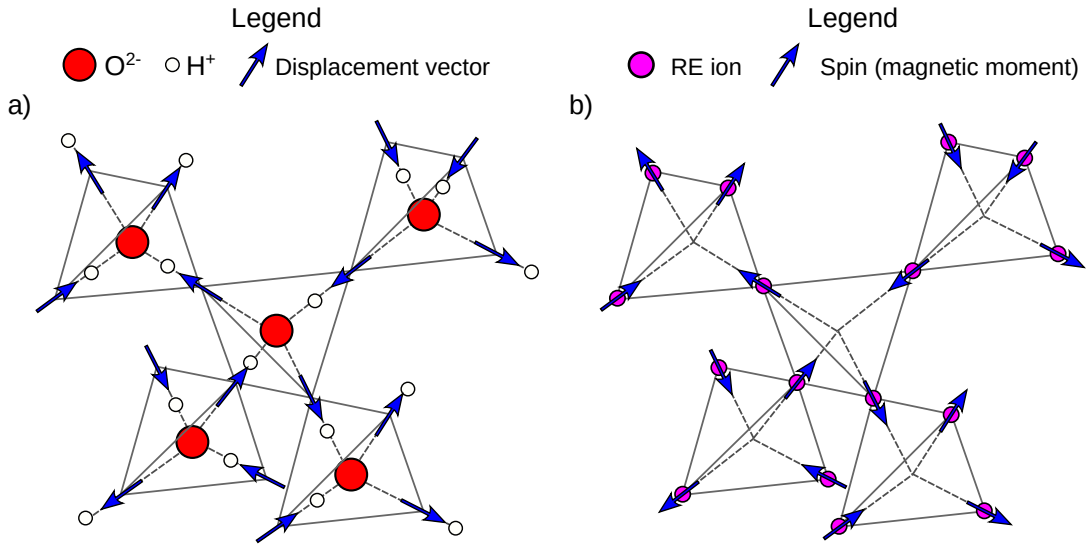

Fig. 1.5: a) Sketch of the internal structure of low-energy manifold of water ice (I_h). b) Sketch of the magnetic configuration of the low-energy state of the pyrochlore compound. Adapted (with significant modifications) from [10]

It is instructive to look in more detail at what leads to geometrical frustration in pyrochlore compounds. As the interaction between individual spins is effectively ferromagnetic, the interaction energy of a pair of spins is minimised when they point head-to-tail/tail-to-head. There are $2^4 = 16$ possible configurations per tetrahedron,

as there are four spins, and each can point inward/outward. The lowest possible energy per tetrahedron is achieved when two spins point inwards and two outwards. This condition is satisfied for 6/16 possible configurations per tetrahedron. However, in all six cases, two pairwise spin interactions out of six are frustrated (see Fig. 1.6). Thus, the system is geometrically frustrated.

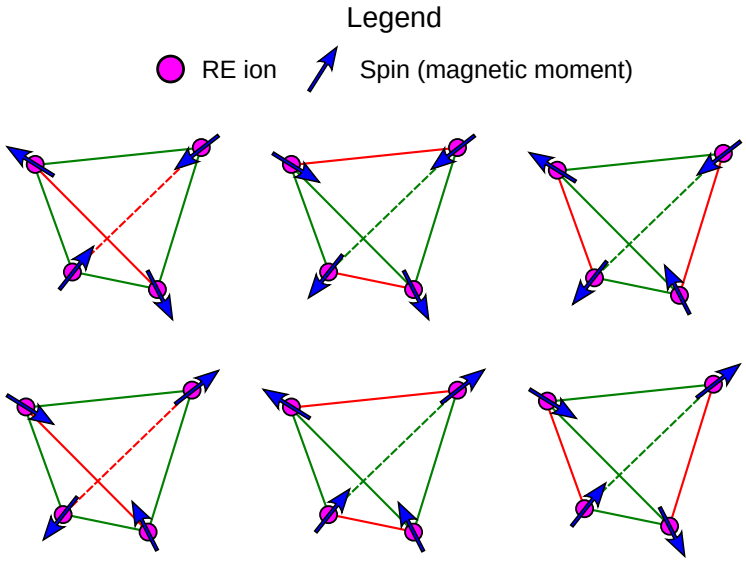

Fig. 1.6: Sketch of six possible ground state magnetic configurations for a single tetrahedron cell. There are six pairwise spin interactions that are all equally strong. In each case, the two out of those six interactions are frustrated (indicated by red lines), and four are satisfied (indicated by green lines).

Thus, the same as for water ice, the pyrochlore low-energy magnetic state exhibits extensive degeneracy, as there is a large number of states in which the ice rules (two-in, two-out) are respected. In fact, the level of degeneracy is the same as for water ice. Thus, the spin ice materials should also possess residual entropy as water ice. This was experimentally confirmed by Ramirez *et al.* [9] in 1999, and resulting residual entropy of $Dy_2Ti_2O_7$ agree with the Pauling's estimate for water ice to within a few percent, confirming the validity of the correspondence between water ice (I_h) and spin ice materials.

It is worth mentioning that in the case of spin ice materials, the extensive degeneracy arises from magnetic disorder, unlike in water ice, where it has a chemical origin. Therefore, from an experimental point of view, spin ice materials offer an additional degree of freedom in the possibility of applying an external magnetic field to access specific magnetic states. For example, the behaviour of kagome ice layers was investigated in $Dy_2Ti_2O_7$ in a magnetic field applied along the [111] direction [11].

However, experimental challenges are also associated with investigating magnetic states in pyrochlore compounds. To capture the exotic properties of interest, the

experiments must be conducted at very low temperatures (< 10 K, sometimes < 1 K), and the experimental techniques (such as neutron diffraction) yield only global information about the system's configuration. In other words, the obtained information is essentially averaged over the bulk of the sample, and resolving individual magnetic moments is not possible.

1.4 Artificial spin ice

Artificial spin ice systems were proposed as a two-dimensional counterpart to the three-dimensional magnetic structure of spin ice compounds. Some twenty years ago, pioneering works of Wang *et al.* [12] and Tanaka *et al.* [13–15] presented artificial arrays of nanomagnets patterned by electron beam lithography.

In the former work [12], arrays of single-domain ferromagnetic elongated islands were placed on a two-dimensional square lattice. After the application of field demagnetisation protocol, the captured magnetic configurations revealed the following: 1) each magnet is single-domain and due to the shape anisotropy Ising-like (magnetisation can point only in two opposite directions along the long axis of each nanomagnet) and 2) the captured configurations showed an excess of vertices obeying the ice rules. This work also introduced the term "artificial spin ice", which has been widely adopted.

In the case of the latter work [15], arrays of connected honeycomb networks were patterned, and their remanent state was measured. The magnetic imaging revealed the following: 1) the magnetisation of the wire segments between two vertex sites is effectively Ising-like (thus can point only outwards or inwards with respect to one vertex site), 2) these wire segments interact with each other at vertex sites, where domain walls are formed and 3) the captured configurations showed tendency to follow the ice rules (adapted to three magnet vertices: two-in/one-out or two-out/one-in).

It is instructive to outline the connection between the three-dimensional structure of spin ice materials and the two-dimensional geometries studied in the pioneering works mentioned above, as those are also the geometries that received major attention and were extensively studied. A two-dimensional square lattice can be deduced from the three-dimensional pyrochlore lattice (shown in Fig. 1.7a) if it is projected to a plane (looking downwards along the z-axis, shown in Fig. 1.7b). Then, if elongated nanomagnets are placed at the positions occupied by rare earth ions (shared corners of square cells) and are oriented such that their long axes point towards the centres of projected square cells, a two-dimensional analogue of the spin ice structure is obtained (see Fig. 1.7c).

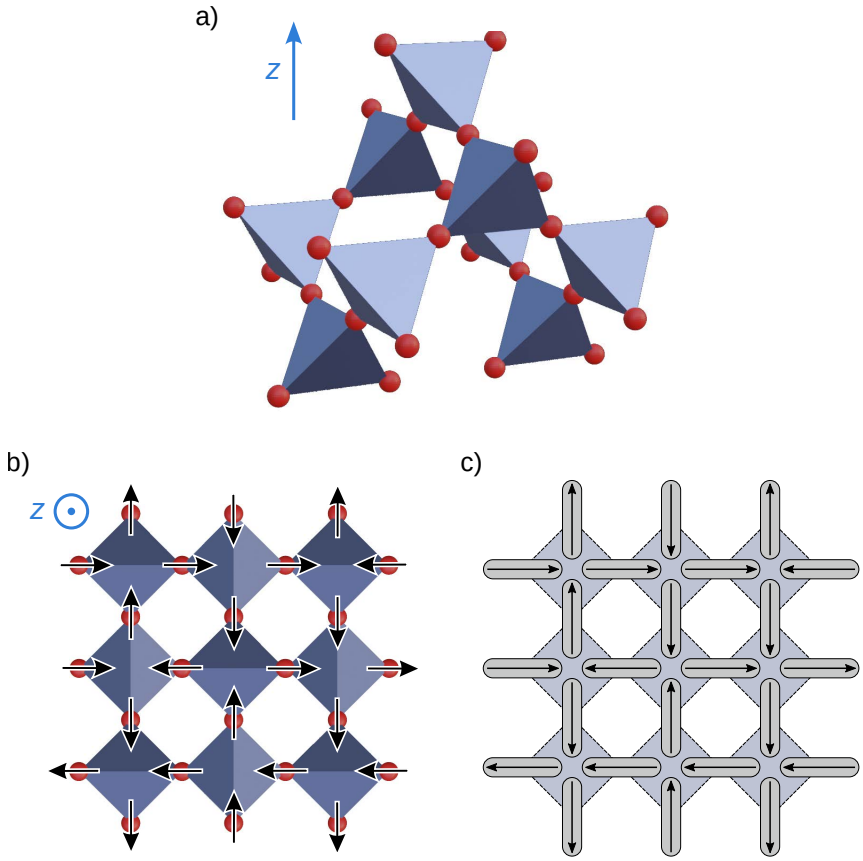

Fig. 1.7: a) 3D structure of pyrochlore compounds. The red balls indicate the positions of the rare earth ions. b) Projection of (a) to a plane (viewed from above, i.e. looking downwards along the z-axis). The arrows indicate the magnetic moments (also projected to a plane). c) Sketch of an artificial spin system consisting of elongated single-domain nanomagnets placed on a square lattice.

While the projection shown in Fig. 1.7 is quite illustrative, it is somewhat flawed as projecting the tetrahedron cell to a square cell introduces an imbalance between the six pairwise interactions belonging to one cell. In a square array of nanomagnets such as the one shown in Fig. 1.7c, the four interaction strengths of the perpendicular neighbouring magnets are stronger than the two of the collinear neighbouring magnets. Consequently, the six-fold ground state degeneracy per cell is lost, and the ground state consists of two configurations that satisfy the interactions between the perpendicular (nearest) neighbours, is two times degenerate and exhibits a conventional antiferromagnetic ordering. The frustration is present for the interactions between the collinear neighbours but does not effectively come into play. Meanwhile, all six pairwise interactions are equally strong in the tetrahedron cell. The consequences of this imbalance and how the balance can be restored in artificial systems will be addressed later in the text.

A two-dimensional kagome lattice can also be deduced from the three-dimensional structure of spin ice materials as a (111) plane intersection (shown in Fig. 1.8a and 1.8b). By the same approach as for the square lattice (mimicking the positions of spins by elongated nanomagnets), a two-dimensional kagome lattice built out of nanomagnets is obtained (see Fig. 1.8c).

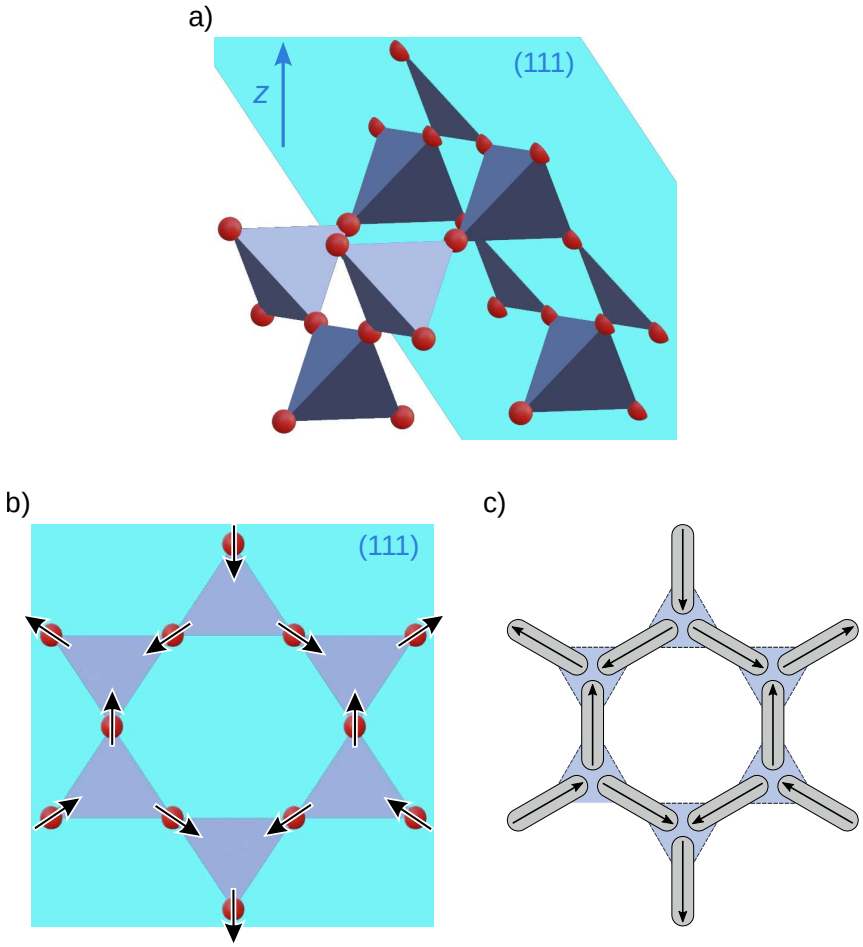

Fig. 1.8: a) 3D structure of pyrochlore compounds. The red balls indicate the positions of the rare earth ions. The (111) plane is shown in a light blue colour. b) A (111) plane intersection of (a), the arrows indicate the magnetic moments. c) Sketch of an artificial spin system consisting of elongated single-domain nanomagnets placed on a kagome lattice.

In the case of the artificial kagome spin system built out of elongated nanomagnets, the balance of the three pairwise interactions in the triangular cell (corresponds to one face of the tetrahedron cell) is maintained as the spins are just slightly tilted into a plane. Therefore, there is a six-fold ground state degeneracy per cell, in which one pairwise interaction is frustrated. Consequently, if only nearest-neighbour interactions are considered, the system exhibits extensive ground state degeneracy. Ar-

tificial systems of elongated magnets placed on the kagome lattice (such as the one shown in Fig. 1.8c) are sometimes referred to as hexagonal or honeycomb networks due to the dual relationship between the kagome and hexagonal lattices (elongated nanomagnets placed on the lattice points of kagome lattice corresponds to the links of the hexagonal lattice).

It is important to note that the term *artificial spin ice* has often been broadly applied to describe various systems consisting of arrays of nanomagnets. However, to be precise, this term should only be used for frustrated systems that feature a six-fold degenerate ground state per cell (i.e. vertex) and possess a geometry inspired by the structure of water ice (or spin ice materials). A more encompassing and accurate term would be *artificial spin systems*. Thus, while every artificial spin ice system is an artificial spin system, the converse is invalid.

1.4.1 Advantages of artificial spin systems

In the previous pages, we established the connection between spin ice materials and artificial spin (ice) systems. One might then ask what advantages the artificial spin systems offer for the experimental studies. The main advantages are: 1) tunability of the design, 2) direct accessibility of the local information about the configuration (at the scale of the spin degree of freedom) and 3) experiment temperature tunability.

Tunability of the design

Artificial spin systems consisting of nanomagnets are commonly fabricated by electron beam lithography combined with additive or subtractive microfabrication techniques (more details are provided in Sec. 2.2). Therefore, essentially any 2D or 2.5D[1] geometry (lattice) can be designed and patterned. Additionally, the shape, size and material of the nanomagnets can be selected at will. Usually, the nanomagnets are optimised to be a single domain, and their elongated shape defines their easy axis. In that case, their magnetisation (in-plane) can be considered "uniform", and each nanomagnet is effectively Ising-like, as the magnetisation can point only in two possible directions along with their easy axis. Therefore, each nanomagnet effectively emulates an Ising-like spin. If placed on a suitable lattice, one can consider the artificial spin systems as an experimental simulator of natural compounds or various theoretical spin models. It is worth pointing out that the artificial spin systems

[1] By 2.5D, we refer to geometries that are built by multi-step lithography, in which the structures patterned in the subsequent steps are supported by the ones fabricated in the previous step(s). No self-supporting structures can be fabricated by the most commonly adapted lithographic techniques. An example of a 2.5D structure is the vertically offset sub-lattices of a square lattice investigated in this work.

can also be built out of Ising-like nanomagnets with magnetisation perpendicular to the lattice plane [16–18]. Furthermore, artificial spin systems are not restricted to feature only Ising-like nanomagnets and systems consisting of XY magnets [19] or nanomagnets emulating Potts spins (four-state) [20] were presented.

The design flexibility can also be employed to apply different modifications to the considered lattice, such as: tuning the interactions strengths by changing the lattice parameter (as we do in Chapter 5), rotate the islands [21], add interaction modifiers [22], introduce two distinct nanomagnet sizes [23, 24], introduce topological defects [25] or create connected lattices with symmetric [26] or asymmetric modifications [27, 28] (subtracted material) at vertex sites. The design possibilities for artificial spin systems are virtually limitless and are essentially only limited by the capabilities and resolution of the fabrication techniques. Over the past twenty years or so, a wide variety of artificial spin system geometries and their modifications have been introduced (examples shown in Fig. 1.9).

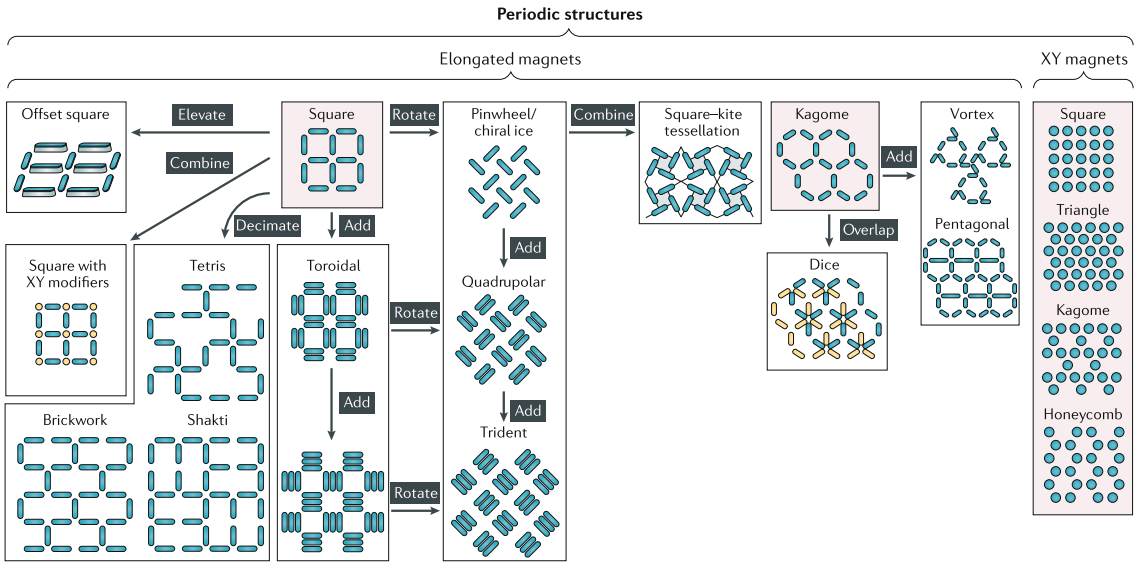

Fig. 1.9: Examples of the ever-growing family of artificial spin systems. The figure presents various modifications of the two seminal geometries (square and kagome). Adapted from [29].

Direct and local information accessibility

Magnetic imaging techniques employed for capturing the magnetic configurations of artificial spin systems consisting of single domain nanomagnets (e.g. magnetic force microscopy [12, 15, 27, 30, 31], x-ray magnetic circular dichroism photoemission electron microscopy [32, 33] or Lorentz transmission electron microscopy [34, 35]) allow for unambiguous determination of magnetisation direction for each nanomagnet. In other words, the orientation of each Ising-like pseudo-spin can be determined

directly in real space, which provides local information about the magnetic configuration of the system. At the same time, this locally-resolved information can be obtained across relatively large areas. For example, in this work, we use magnetic force microscopy to image entire lattices consisting of 840 or 1860 Ising-like pseudo-spins. Thus, the global information about the system's magnetic configuration is also obtained.

In contrast, the experimental techniques used to examine the magnetic configurations of spin ice compounds, such as neutron scattering [8, 36], are indirect and yield only a global perspective of the system. Consequently, while artificial spin systems provide the means to visualise how frustration is locally accommodated, studies of spin ice compounds are limited to interpretations based on global information. Additionally, the dynamics of local excitations within the disordered manifolds of artificial spin systems can be directly observed [37]. In contrast, for spin ice materials, one must rely on interpreting their effects as reflected in the global information [36, 38].

Experiment temperature tunability

The artificial spin systems consisting of single-domain nanomagnets can be designed to allow magnetic imaging to be conducted at or near room temperature. This is the case for the artificial spin systems in which the configuration is arrested after the application of the energy minimisation procedure (e.g., field demagnetisation [12, 26, 27, 30], at-growth thermalisation [21, 39, 40] or annealing through the Curie temperature of the constituent material [35, 41]). In such instances, the typical thickness of the nanomagnets ranges from 20 to 30 nm. Due to the volume of the nanomagnets, the blocking temperature is significantly higher than the room temperature, ensuring that the arrested magnetic configurations remain stable at room temperature, where magnetic imaging is usually performed. However, it is also possible to reduce the volume of the nanomagnets, which allows for tuning of the blocking temperature. This strategy allows for observation of real-space dynamics, assuming that temperature control of the environment is implemented *in-situ* within the imaging technique. For example, observation of the thermal relaxation of the artificial square spin system (with nanomagnet thickness of 3 ± 0.3 nm) at 350 K was reported [33].

In contrast, to observe exotic phenomena in spin ice compounds, very low temperatures are required (typically about our even below 1 K) [8, 9, 36]. One might then conclude that artificial spin systems built out of nanomagnets provide a more convenient window of experimental conditions.

Summary

For the reasons outlined above, artificial spin systems have received considerable attention in the last two decades (as evidenced by topical reviews [29, 42–44] and book chapters [45, 46]) and have provided a beautiful playground to experimentally investigate properties of various lattice spin models (whether inspired by natural compounds or not, whether frustrated or not). While artificial spin systems were initially introduced as an experimental simulator of frustrated spin models, their potential applications have also been explored. However, this topic is not a focus of this thesis and will not be discussed further (more details can be found in Ref. [29, 43, 47].

As a final point, it is worth mentioning that artificial spin systems are not restricted to feature nanomagnets as building blocks and different approaches were presented. For example, assemblies of colloidal particles [48–50] (also referred to as *particle ice*), arrays of macroscopic rotors [51], mechanical metamaterials [52] or nonmagnetic molecular assemblies [53] were presented.

1.4.2 The square geometry

In this work, we focus on the artificial spin systems built out of elongated nanomagnets placed on a square lattice. More specifically, we conduct experimental investigations of field demagnetised *conventional square lattices* (i.e., lattices in which all nanomagnets lie on the substrate) and *vertically offset square lattices* (i.e., lattices in which one sublattice is vertically offset with respect to the other one). Below, we describe these two systems and provide a brief overview of previous experimental works that have featured these types of artificial arrays of nanomagnets.

Conventional square lattice

The first experimental realisation of the conventional square lattice was reported by Wang *et al.* in 2006 [12]. In this work square arrays of elongated permalloy nanomagnets (size $220 \times 80 \times 25$ nm^3, lattice parameter 320–880 nm) were fabricated with intent to mimic the properties of spin ice materials (the relation between the 2D square lattice and 3D magnetic structure of pyrochlore compounds is provided in Fig. 1.7). Atomic force microscopy (AFM) topography image of a typical lattice fabricated in this work is provided in Fig. 1.10a, and Fig. 1.10b shows magnetic force microscopy (MFM) image showing the arrested magnetic configuration obtained for the same array after application of field demagnetisation protocol.

Utilising the vertex description (see Fig. 1.10c) Wang *et al.* reported that their captured magnetic configurations showed a tendency to locally respect the ice rule

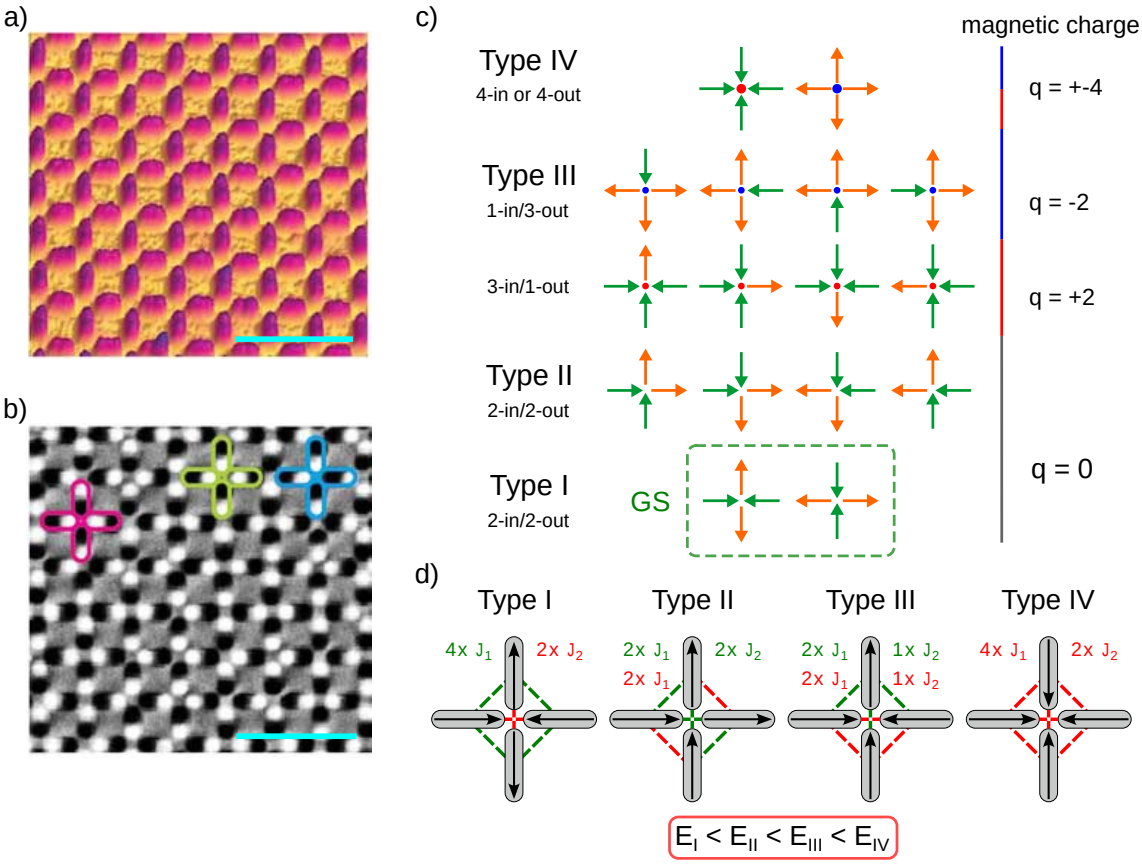

Fig. 1.10: a) AFM topography image of a conventional square lattice. b) MFM magnetic contrast taken for the same array as in (a). Each magnet is a single domain, as evidenced by black and white contrast on its extremities. The coloured outlines indicate examples of type I (pink), type II (blue) and type III (green). Both (a) and (b) are adapted from [12], and the blue bar represents 1 µm in both images. c) The possible 16 magnetic configurations per vertex site, divided into four topological types. d) Detailed look at satisfied and unsatisfied pairwise interactions at vertex sites for different vertex types. For a conventional square lattice consisting of elongated nanomagnets, the lowest possible energy configuration per vertex is type I, in which the four nearest-neighbour interactions (J_1) are satisfied at the expense of the next-nearest-neighbour interactions (J_2).

condition (two-in/two-out), evidenced by the excess of type I and type II vertices compared to what would be expected for an array of randomly oriented nanomagnets.

At this point, it is worth revisiting the consequences of projecting the 3D magnetic structure of spin ice materials into a 2D square array of nanomagnets (as shown in Fig. 1.7). We noted previously that this approach leads to an imbalance between the six pairwise interactions between the four magnets meeting at one ver-

tex site. In contrast, the six pairwise interactions between the four spins of one tetrahedron cell are equally strong in spin ice materials. For geometrical reasons, in a conventional square lattice vertex, the six pairwise interactions between the four magnets meeting at a vertex site are divided into four interactions between the nearest-neighbours (J_1, perpendicular pairs of magnets) and two interactions between the next-nearest-neighbours (J_2, collinear pairs of magnets) and $J_1 > J_2$. Interaction energy for a pair of magnets is minimised when they are oriented head-to-tail or tail-to-head. Consequently, the lowest possible energy configuration per vertex is reached when the interactions between the nearest-neighbours are satisfied at the expense of next-nearest-neighbours, which is the case for type I vertices (see Fig. 1.10d). The ground state manifold then corresponds to a perfect tiling of type I vertices in a chequerboard-like fashion, is two times degenerate and antiferromagnetically ordered.

In hindsight, it is clear that a conventional square array of elongated nanomagnets is not a suitable candidate to mimic the low-energy properties of spin ice materials[2] as the ground state configuration per vertex is only two-times degenerate, unlike in water ice or spin ice where it is six-times degenerate. The reason why the configurations reported by Wang *et al.* do not exhibit more prominent ordering can be attributed to the low efficiency of the demagnetisation protocol (this is supported by a relatively high fraction of type III vertices).

Even though this artificial spin system failed at mimicking the physics of spin ice materials, its well-defined antiferromagnetic ground state has become a sort of etalon for experimental studies. Conventional square arrays of nanomagnets were explored to evaluate efficiency of different field demagnetisation protocols [54–57] (more detailed comparison of those works is provided in Chapter 5), efficiency of at-growth thermalisation [39, 40, 58] or efficiency of annealing through Curie temperature [35, 41, 59]. Other experimental studies featuring conventional square lattices focused on effects of thermal fluctuations [33, 60], role of intrinsic disorder [45, 56], magnetisation reversal processes [61] or dynamics of charged excitations (type III vertices, see Fig. 1.10c) within uncharged but ordered backgrounds [62–64].

Vertically offset square lattice

In the preceding pages, we discussed why the conventional square lattice fails to replicate the properties of spin ice materials. For an accurate emulation, restoring the balance among the six pairwise interactions at each vertex site is essential, thereby preserving the six-fold ground state degeneracy per vertex site characteristic

[2] This statement might not be entirely accurate and will be revisited in Chapter 5.

of spin ice materials. Specifically, this requires modifying the square array of nanomagnets so that the interaction strengths at vertex are equalised ($J_1 = J_2$, referred to as "ice condition"), resulting in equivalent energies for type I and type II vertices ($E_{\mathrm{I}} = E_{\mathrm{II}}$).

A possible strategy to equalise the coupling strengths between the perpendicular (J_1) and collinear (J_2) neighbours at vertex site was proposed by Möller and Moessner in 2006 [65]. The main idea of this proposition is to shift vertically one of the sublattices forming the square array by a height offset h (shown in Fig. 1.11a). By doing so, the coupling strength between the perpendicular neighbours (J_1) is weakened, while the one between the collinear neighbours (J_2) remains the same. The height offset then enables for tuning of the J_1/J_2 ratio, and for a specific height offset h_{c}, the balance between the J_1 and J_2 is recovered (see Fig. 1.11c).

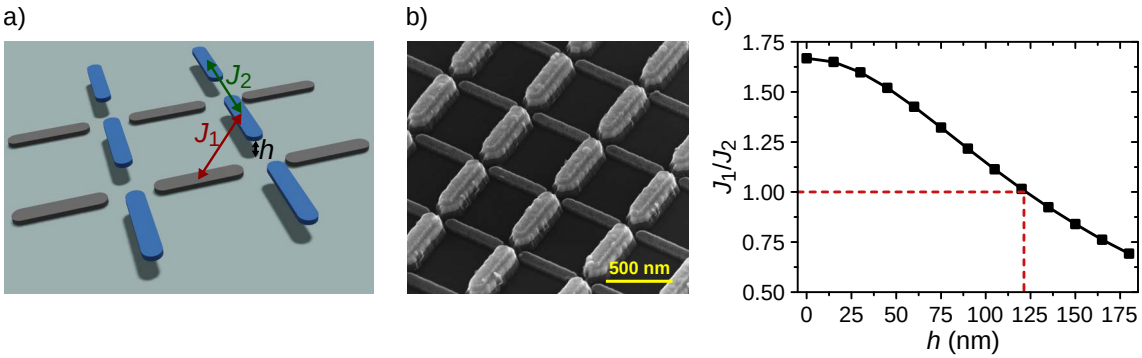

Fig. 1.11: a) Three-dimensional sketch of a vertically offset square lattice. The blue sublattice is shifted vertically by height offset h. The coupling strengths between perpendicular (J_1) and collinear (J_2) neighbours are indicated by red and green, respectively. b) SEM image of the vertically offset square lattice in which one sublattice is elevated due to placement of its nanomagnets on top of Ti/Au bases. c) Result of micromagnetic simulations showing how the J_1/J_2 ratio can be tuned by modifying the height offset h. At a critical (numerical) value $h_{\mathrm{c}}^{\mathrm{num}}$ close to 120 nm, the ice condition $J_1/J_2 = 1$ is obtained. Adapted from [30].

Experimental realisation of a vertically offset square lattice was presented by Perrin *et al.* in 2016 [31]. A two-step electron beam lithography process was utilised to achieve the height offset. The first step focused on preparing the Ti/Au bases and alignment marks. The second step was dedicated to fabricating the square arrays of permalloy nanomagnets. Thanks to precise alignment, the magnets of one sublattice rest directly on the substrate, whereas the magnets of the second sublattice are positioned atop the bases patterned during the first step (see Fig. 1.11b).

After applying a field demagnetisation protocol, the arrested magnetic configurations were imaged by magnetic force microscopy. Analysing the obtained real space

magnetic configurations revealed that for a height offset $h^{\text{exp}} = 100$ nm the configurations are highly disordered and the ratio between the type I and type II vertices approaches 1:2 (see Fig. 1.13b), which corresponds to their degeneracy numbers (two variants of type I vertex and four variants of type II vertex). This shows that for such a height offset, the balance between the six pairwise interactions at vertex is effectively approached ($J_1 = J_2 = J$) and considering only the nearest-neighbour interactions the type I and type II vertices have the same lowest possible energy and define the ground state (see Fig. 1.13c and 1.13d). A straightforward analogy with the six possible ground state configurations per tetrahedron cell in spin ice materials is thus retained (Fig. 1.6 vs. Fig. 1.13c). Therefore, such a system (vertically offset square lattice, $h^{\text{exp}} = 100$ nm) can be called artificial spin ice or artificial square ice.

One might then wonder, what are the characteristics of the captured magnetic configurations (for the height offset ($h^{\text{exp}} = 100$ nm). First, no clear ordering is evident when examining an example vertex map (as shown in Fig. 1.12). This is reflected in the experimental magnetic structure factor (MSF), which shows a diffused but structured magnetic diffraction pattern (see Fig. 1.12b), in which no Bragg peaks (indication of order) are present.

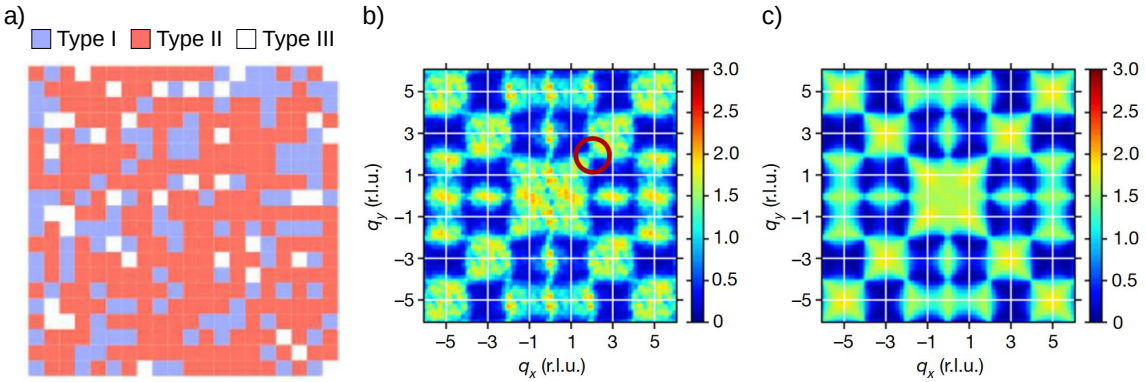

Fig. 1.12: a) Real space magnetic configuration (shown as a vertex map; the legend is provided above the map) of a vertically offset square lattice ($h^{\text{exp}} = 100$ nm). b) The magnetic structure factor computed from four magnetic configurations, similar to the one shown in (a). c) Numerical magnetic structure factor computed from 1000 random spin configurations, in which the ice rule constraint is strictly applied (i.e., only type I and type II vertices are permitted). The intensity scale bar is provided right next to each plot. (a) Adapted from [44], (b-c) adapted from [31].

Comparing this result with a numerical prediction (see Fig. 1.12c) indicates strong similarities, implying that the experimental magnetic configuration can be characterised as a *spin liquid* (disordered but correlated magnetic state, in which pairwise spin correlations are not zero, but decay to zero at large distances [44]). Furthermore, the experimental MSF exhibits distinct features (see red circle in

Fig. 1.12b, referred to as *pinch points*) that are indicative of algebraic nature of the pairwise spin correlations [31, 66] associated with the so-called *Coulomb phase* [67].

The Coulomb phase is an emergent state for certain lattice models featuring local constraints that can be mapped to a divergence-free "flux" [67]. Following the work of Henley [67], the lattice model has to satisfy three conditions for the Coulomb phase to emerge:

1. each variable (the spin in our case) can be mapped to a (discrete) signed (magnetic) flux $\mathbf{P}_i$, running along bond i (the bond is a line between two adjacent vertex sites in our case);
2. the variables obey hard constraints, such that the sum of the fluxes at each vertex is zero (this constraint corresponds to the ice rules in our case, two-in/two-out vertex configurations);
3. the system is in a highly disordered phase, without any long-range ordered pattern (i.e., liquid-like).

The three conditions mentioned above are valid assuming a vertically offset square lattice (with a critical height offset that recovers the ice condition), brought into its low-energy manifold (only type I and type II vertices are present). Even though the experimental spin configurations do not strictly obey the second condition (there are a significant fraction of type III vertices present; see white squares in Fig. 1.12a), indicating that the system has not been fully brought to its massively degenerate low-energy manifold, the experimental MSF exhibits features specific of a Coulomb phase (pinch points, highlighted by red circle in Fig. 1.12b). Therefore, the magnetic configurations can be described as a Coulomb phase with embedded local excitations (type III).

The nature of type III vertices

Following the work of Castelnovo *et al.* [68], the type III vertices are often referred to as *magnetic monopoles* in the context of artificial spin systems. The description, introduced for spin ice compounds, is based on substituting each spin by a pair of opposite magnetic charges (this description is often referred to as *dumbbell model*. Consequently, the six configurations that follow the ice rule (two-in/two-out) are characterised by a zero net magnetic charge at each (vertex) site. Conversely, the type III vertices (three-in/one-out or vice versa) have a net magnetic charge $q = \pm 2$ and type IV vertices (four-in or four-out) have a net magnetic charge $q \pm 4$ (see Fig. 1.13c). The magnetic charge q is defined as the sum of spins per vertex site ($+1$ for spins pointing inwards and -1 for spins pointing outwards).

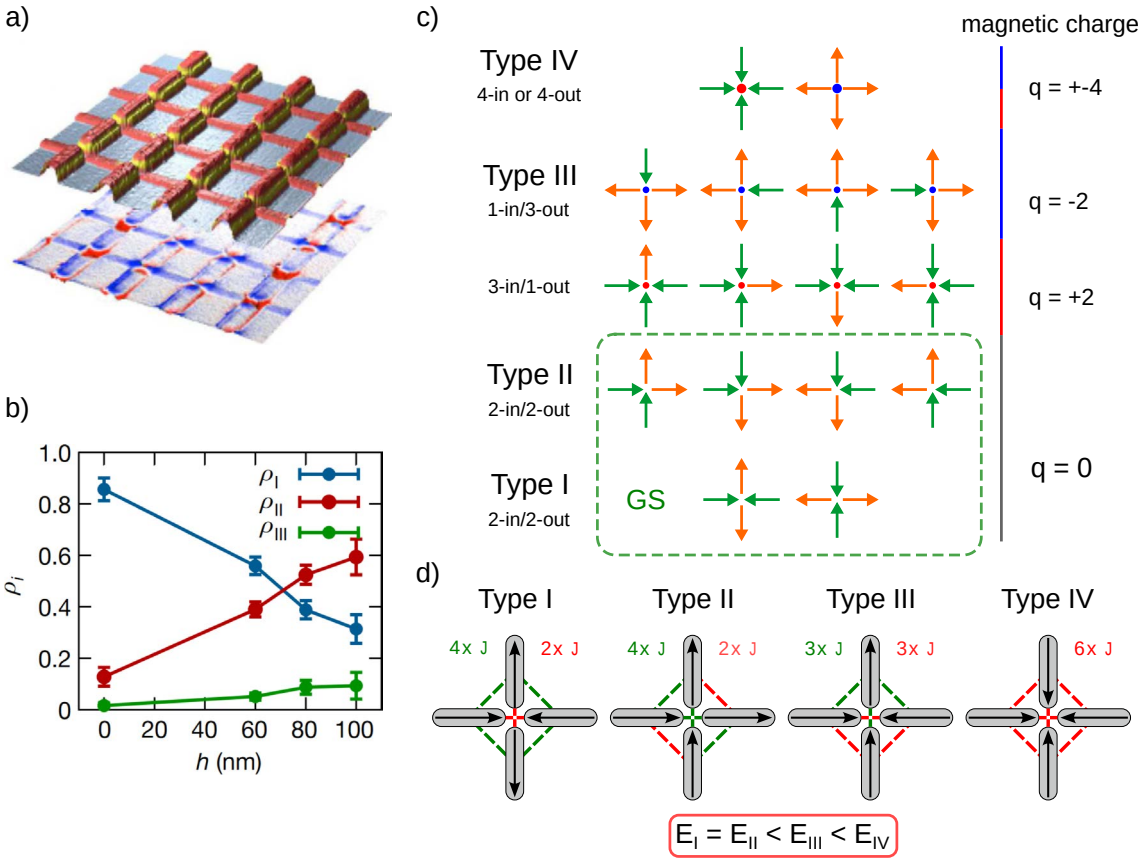

Fig. 1.13: a) AFM topography (top) and MFM contrast (bottom) images of a vertically offset square lattice. In the topography image, the nanomagnets are depicted in red, the bases that elevate one of the sublattices vertically are shown in yellow, and the substrate is represented in grey. In the magnetic image, the magnetic contrast is visualised with blue (red), indicating negative (positive) magnetic charges. b) A plot showing the density of type-i vertices as a function of the height offset h. The points represent mean values, and the error bars indicate the standard deviation (based on four demagnetisations). c) The possible 16 magnetic configurations per vertex site, divided into four topological types. d) Detailed look at satisfied and unsatisfied pairwise interactions at vertex sites for different vertex types. For a vertically offset square lattice (with critical height offset), there are six lowest possible energy configurations per vertex (type I and type II), in which four pairwise interactions between the nearest neighbours ($J_1 = J_2 = J$) are satisfied, and two are frustrated. (a) and (b) adapted from [31].

However, the properties of the type III vertices differ substantially based on their environment (i.e., in which configurations they are embedded). If they are embedded in an ordered and uncharged background (either type I or type II background), they act as confined quasi-particles and are typically linked to their oppositely charged

counterpart by a string tension [69, 70]. This string can be seen as a path that lead to their separation (trace of reversed spins) and is often referred to as *Dirac string*. In this case, when the type III vertices are embedded in ordered configurations, their nature can be characterised as charged defects (or charged excitations).

Examples of two possible configurations in which type III vertices are incorporated in mainly ordered backgrounds are shown in Fig. 1.14a and Fig.1.14b. In the first case (Fig. 1.14a), a pair of oppositely charged type III vertices is embedded in an ordered background of type I vertices. The two charged defects are connected by a chain of reversed spins corresponding to their possible annihilation path and forming a type II domain wall. Such a configuration corresponds to a system in which the ground state is formed by type I vertices, and the presence of type II and III vertices indicates that the system was not brought into its ground state configuration. Such configurations were reported for conventional square lattices after field demagnetisation [31, 56, 57] or thermal annealing [71]. In this scenario, the type III vertices are not free to move, and the only sustainable movement is the one that reduces the string length, potentially resulting in their annihilation, thereby further reducing the system's energy.

In the second case (Fig. 1.14b), a pair of oppositely charged type III vertices is embedded in a saturated background of type II vertices. The two charged defects are connected by a chain of reversed spins corresponding to their separation path and forming a type I domain wall. Such a configuration corresponds to a square spin system that was diagonally polarised by an external magnetic field, and subsequently, a field in the opposite direction was applied. Such a field treatment induces nucleation of the charged defects (type III vertices) that are propagated throughout the lattice via an avalanche process [62, 72]. Similar results were reported for a thermal relaxation of a conventional square lattice, in which the initial state was diagonally polarised by applying an external magnetic field [33]. In this scenario, the movement of the type III vertices is restricted by the constraints of the ordered background, and only sustainable movement is such that leads to further reduction of the system's energy (the type III vertices essentially mediates the field-driven reversal or stabilisation of the energetically more favourable configuration).

Conversely, if the type III vertices are present in a disordered liquid-like background (see Fig. 1.14c), their movement is not constrained, and they are free to evolve within a highly disordered manifold without energy penalty (movement of type III vertices leads to transformation of type I into type II vertices or vice versa, depending on the local configuration). In this scenario, the type III vertices can be referred to as magnetic monopoles, recovering the similarities with a low-energy manifold (with local excitations that break the ice rules) of spin ice compounds, for which the concept of emergent magnetic monopoles was initially introduced [68].

While in the case of the ordered magnetic backgrounds, one can identify the path of reversed spins that lead to the separation of the two oppositely charged type III vertices (shown in Fig. 1.14a and Fig.1.14b), the same is not possible in case of the type III vertices embedded in the magnetically disordered manifold. For a configuration shown in Fig. 1.14c, one can define many different paths to recombine the two magnetic monopoles. In other words, the path taken by the pair of monopoles is erased by the magnetic disorder, and in the case of a larger system with a finite density of monopoles, one cannot determine pairing for oppositely charged monopoles.

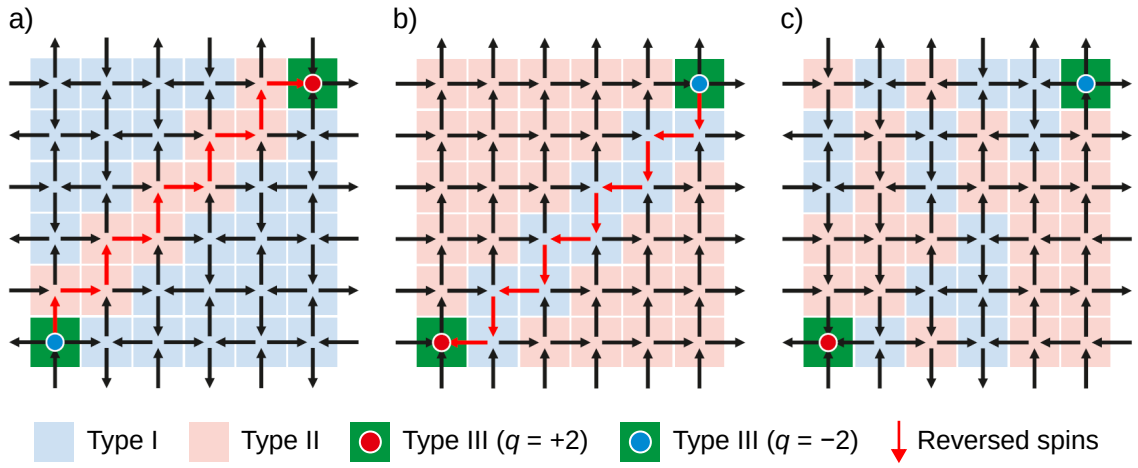

Fig. 1.14: Pair of oppositely charged type III vertices in: a) ordered type-I background (antiferromagnetic ordering), b) ordered type-II background (diagonally polarised state) and c) disordered (liquid-like) background. In the ordered backgrounds (a, b), the pair of type III vertices is linked by the path of reversed spins (red arrows). This path corresponds to a domain wall formed by type II vertices in (a) and type I vertices in (b). In the case of the disordered background (c), no apparent path of reversed spins can be identified (it was erased by the magnetic disorder). The legend for the maps is provided below. Adapted from [73].

To summarize, if the type III vertices are present in magnetically ordered backgrounds, their nature can be described as charged defects. If embedded within a highly disordered manifold, they behave as free-to-move magnetic monopoles, which interact via a magnetic Coulomb interaction [67, 68].

1.5 Motivation and overview

Over the past two decades, artificial spin systems have emerged as a robust experimental platform for exploring the properties of frustrated (Ising) spin models. The typical approach involves fabricating elongated nanomagnets on a lattice of interest and employing an energy minimisation procedure to stabilise the low-energy configurations of the spin system being studied. This approach proved fruitful and provided many intriguing experimental results, such as spin-liquid phases, magnetic Coulomb phases, emergent magnetic monopoles and many others. Unlike natural compounds, where the exotic physics associated with frustration was initially studied, artificial spin systems offer direct access to the system's configuration at the spin degree of freedom level. This accessibility allows for detailed observation of how frustration and local excitations are accommodated on a microscale, providing valuable insights into the underlying physics.

Artificial spin systems research is a fast-evolving field in which many different lattice geometries and associated phenomena are being investigated. However, the operating principle of those systems (i.e., the reason why and how they work) is sometimes overlooked. In fact, one could present compelling arguments as to why the approach of emulating spin models by arrays of magnetostatically coupled single-domain magnetic islands should fail. Strictly speaking, the nanomagnets are not point dipoles, Ising variables or macrospins as they are micromagnetic objects characterised by not uniform magnetic texture and exhibit magnetisation dynamics. Despite these limitations, the experimental results are well-approximated by Ising spin models.

In this work, we focus on field-demagnetised artificial square spin arrays (conventional square lattice and vertically offset square lattice) and investigate three separate problems (presented in three experimental chapters) that are all linked to the fundamental properties of artificial spin systems formed by elongated nanomagnets.

In Chapter 3, we investigate whether signatures of farther neighbour couplings can be detected experimentally in a spin liquid configuration retained in vertically offset square lattices (referred to as artificial square ice). This question is linked to the fact that artificial spin systems consisting of nanomagnets are dipolar by desing, thus considering nearest-neighbour interactions only to describe their physics is an approximation. While this short-range approximation showed good agreement with previously reported results for artificial square ice, we were able to detect subtle differences in the experimental magnetic structure factor that cannot be accounted for by the short-range model. We identify the origins of those additional features observed in the experimental magnetic structure factor, and utilising Monte Carlo

simulations, we show how they can be recovered numerically if interactions extending beyond nearest neighbours are considered. Our results thus indicate that interactions from farther neighbour couplings are at play in our field-demagnetised artificial square ice magnets, and they impact the magnetic correlations.

Chapter 4 reports the results of applying successive field demagnetisation protocols to artificial square ice magnets. The primary motivation for this work is to address to what extent the field demagnetisation we apply can be viewed as a stochastic process. Our results show that applying the field demagnetisation protocol multiple times to the same artificial square ice system results in magnetic configurations that are substantially different from each other, though not entirely. Analysing the obtained spin and vertex configurations, we demonstrate that our field protocol is a stochastic process, although some level of magnetic determinism is present in our results. We attribute the presence of magnetic disorder to intrinsic disorder (i.e., imperfections of the artificial spin systems that locally bias the magnetostatic interactions or reversal dynamics). This result illustrates one of the limitations of emulating spins by single-domain nanomagnets. We also explore potential sources of randomness in our experiment, including the intrinsic one associated with thermal fluctuations that affect the magnetisation reversal dynamics of the nanomagnets forming the artificial system. This highlights the importance of considering the micromagnetic nature of the building blocks of the artificial spin systems.

In Chapter 5, we investigate whether a series of field-demagnetised conventional square lattices, in which the lattice parameter is gradually varied to tune the interaction strengths, yield magnetic configurations corresponding to a unique spin model probed at distinct effective temperatures. In other words, is it possible to probe effective thermodynamics by tuning the interaction strengths of an artificial square spin system? By carefully comparing vertex populations and magnetic structure factors obtained by experiment and Monte Carlo simulations, we show this is generally the case. However, deviations for densely packed lattices are observed, showing the limitations of the single-model approximation. Moreover, for the densely packed lattices, we observe unexpected trend deviations that can be accounted for only if the coupling strengths of the spin model are significantly modified. Employing micromagnetic simulations, we show that this trend deviation can be attributed to the combination of micromagnetic effects and kinetic effects associated with the field demagnetisation protocol. This result again highlights the importance of considering the micromagnetic nature of the building blocks of the artificial spin systems.

2 METHODS

The primary purpose of this chapter is to provide detailed information about the experimental and numerical techniques employed in this work. The simplified research flow utilised in this work is provided in Fig. 2.1, and details about each method are provided later in the text.

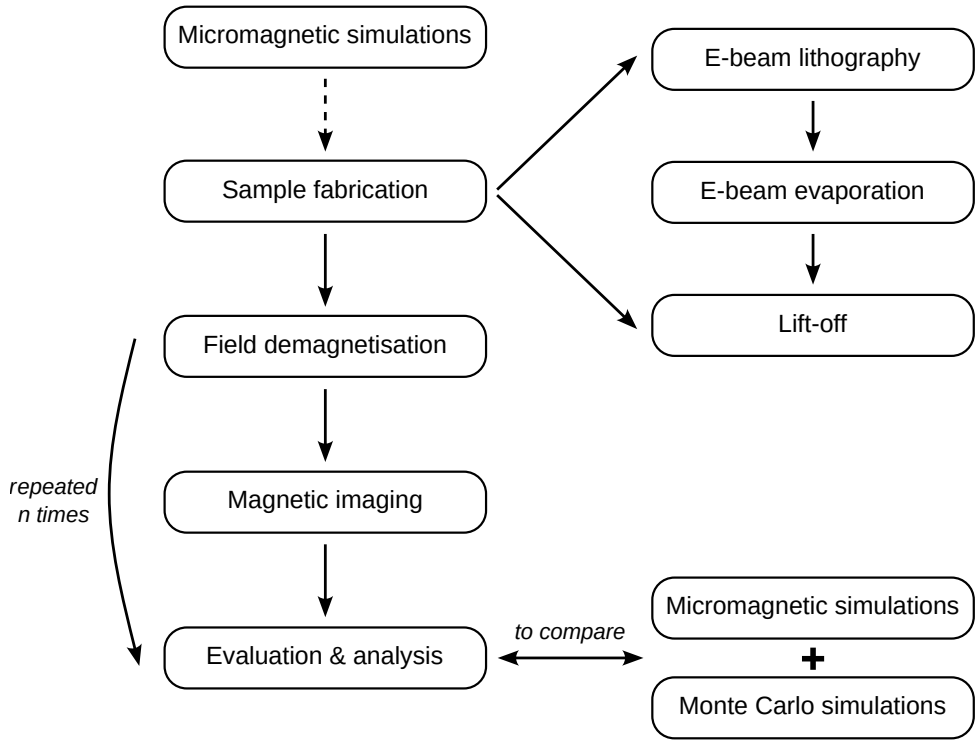

Fig. 2.1: An overview of the research flow implemented for the design, fabrication and characterisation of artificial spin systems.

Firstly, micromagnetic simulations are employed to assess the viability of the proposed concept for a selected artificial spin system and to optimise the design parameters. Typically, one or more 'free design parameters' are varied in the experimental study to modify the properties of the investigated system. For instance, in the case of the study presented in Chapter 3, the lattice parameter is varied, while the other parameters are fixed. Micromagnetic simulations allow us to model the impact of varying the free parameter, thereby providing insights into how the system might behave in experimental settings before conducting any empirical studies. This is particularly helpful, as the micromagnetic simulations are relatively fast to run in comparison to the sample fabrication and follow-up experimental steps.

As the idea for the experimental study was tested in the computational space via the micromagnetic simulations, the next step is to make the physical sample itself. To do so, we employ a conventional lift-off process utilising an electron beam writer

for the exposure of the process mask and an electron beam evaporator for the deposition of the material stack. After fabrication, the quality of the prepared structures is assessed by utilising scanning electron microscopy (SEM). As we usually fabricate the pattern with different exposure parameters at different locations on the sample, SEM imaging is used to select the regions of interest where the suitable quality of the structures is observed.

Both in our work and generally in the field of artificial spin systems, the interest lies in the low-energy configurations of the studied arrays. Therefore, it is necessary to employ experimental techniques that assist the system in reaching down to its low-energy manifold. For this purpose, we employ the field demagnetisation protocol. Upon completed demagnetisation, we conduct magnetic imaging by means of magnetic force microscopy, which allows us to determine the local magnetic properties of the lattices under study.

The final stage of the research flow is to analyse the captured configurations. In order to compare the experimental results with a numerical spin model, we employ Monte Carlo simulations. To align the Monte Carlo simulations with the experimental systems, we use micromagnetic simulations, which enable us to bring the properties of the numerical model close to what we probe experimentally. The field demagnetisation and subsequent steps may be repeated several times to improve the statistical reliability of the obtained results and to verify the reproducibility of the results.

The following text will provide details about each numerical or experimental technique utilised in this work. Should the method be carried out by someone other than the thesis author, it will be duly noted in the subsequent text. Otherwise, it is to be assumed that the author conducted the work.

2.1 Micromagnetic simulations

Micromagnetic simulations are nowadays a powerful tool of magnetism research, which allows not only for benchmarking/optimising of systems prior to their fabrication but also can provide valuable insights for interpretation of the experimental results. In this work, we used two different software packages for the micromagnetic simulations: OOMF [74] and MuMax^3 [75]. The OOMF package was used in Sec. 3.4 to model the effect of the height offset variation and to estimate magnetostatic coupling strengths in a square lattice with elevated sublattice. The MuMax^3 software was used in Sec. 4.3 to model the field-driven reversal of a single magnet or vertex consisting of four magnets. In the latter case, the difference between simulations run at 0 K and at room temperature was investigated. The MuMax^3 package was also used in Sec. 5.4 to estimate how the magnetostatic coupling strengths evolve

as the lattice parameter of square networks is varied.

As the OOMF simulations were conducted by Dr Nicolas Rougemaille, we will focus here on the MuMax^3 simulations that were carried out by the author of the thesis.

2.1.1 MuMax^3 simulations

MuMax^3 is a free, open-source micromagnetic simulation package developed by the DyNaMat team at Ghent University. One of the benefits of the MuMax^3 code is that some calculations are done by the graphical card (GPU), which allows for heavy computation task parallelisation, which significantly reduces the time needed to compute the simulations, compared to CPU based solutions such as OOMF. An NVIDIA GPU with a CUDA core is a necessary condition to run MuMax^3 software. The simulation is then defined using MuMax^3 API, which employs the Go programming language. The simulation execution can be then monitored via GUI.

MuMax^3 relies on the finite difference method for the discretisation of the simulation space. In other words, the simulation space is filled by equally sized cuboid-like cells, for which the relevant properties are calculated. This method's primary advantage lies in the significant reduction of the computation time. However, its drawbacks include the limitation in defining finer spatial subdivisions (which might be helpful to better approximate shape/region edges/boundaries) and a less precise approximation of curved shapes, which essentially results in a staircase approximation. The latter can lead to parasitic effects in the dynamics induced by the staircase approximation, such as the formation of pinning sites or nucleation centres. To suppress the artefacts induced by the discretisation, MuMax^3 has a built-in function *EdgeSmooth*, which recalibrates the saturation magnetisation of the cell in question. This adjustment is based on a further subdivision into subcells, enabling a more accurate approximation of the shape under consideration.

MuMax^3 is designed to calculate both the time- and space-dependent evolution of magnetisation in ferromagnetic elements [75, 76], such as, for example, permalloy nanomagnets considered in this work. In general, the two main use cases of MuMax^3 are either simulations of dynamics or energy minimisation computation. An example of the former case is the field-driven reversal of magnet or vertex, discussed in Sec. 4.3. In this case, we have also used the option to simulate the magnetisation dynamics at finite temperatures, which is implemented in MuMax^3 [75, 77]. An example of the latter case is the magnetostatic energy calculation of the distinct vertex types, discussed in Sec. 5.4. We will now focus on the latter case and provide a detailed description of how the simulations were designed and carried out.

The following text provides an example of how we define and execute the micro-

magnetic simulations using MuMax^3. In this example, we wish to investigate numerically how the total energy of different vertex types evolves as the gap between the magnets forming a single square lattice vertex is increased. The geometrical and material parameters are aligned with our experimental sample (see Tab. 5.1), and we aim to probe the $w = 150$ nm case.

Calculation of magnetostatic energy of vertex types

The first step is to define the size of the simulation world and the simulation mesh. As we plan to use a loop for probing the different gap sizes (i.e. magnet-to-magnet distance at the vertex centre), we select a simulation world size that comfortably fits the entire vertex geometry for the largest targeted gap. In the case considered here, the total in-plane size (both in x and y) of the square lattice vertex for the largest designed gap is $2 \times l + g = 2 \times 750 + 750 = 2250$ nm. We thus set sizeX = sizeY = 2400 nm to fit the considered geometry fully in x and y with some margins at the edge of the simulation box. For the z size of the simulation box, we set directly the height of the magnets considered in the experiment, thus sizeZ = 25 nm.

When selecting a number of cells (resp. the cell size), mainly two factors need to be considered. The first factor, a technical one, is that it is recommended to set the cell number to be power-of-two size (best for performance) or 7-smooth number (still good for performance) in order to optimise the software performance [75]. The second factor, a physical one, is that a sufficiently small cell size compared to the exchange length of the considered material shall be chosen [75]. In the case of permalloy ($Fe_{20}Ni_{80}$) $\Delta_d = \sqrt{2A/\mu_0 M_S^2} \approx 5$ nm, A is the exchange stiffness and M_S is the spontaneous magnetisation. Upon these considerations we set number of cells in x and y as Nx = Ny = 600, which sets the cell size in x, y to 4×4 nm^2. As the considered system is effectively two-dimensional, we set the cell size in z equal to the magnet height to reduce the computation time. A code snippet showing the setting of the simulation world size and the mesh size is provided in Lst. 2.1.

Listing 2.1: MuMax^3: Setting up simulation world size and mesh

```
//Simulation world parameters
Nx:=600; //number of cells in x
Ny:=600; //number of cells in y
Nz:=1; //number of cells in z

sizeX:=2400e-9; //size of simulation box in x
sizeY:=2400e-9; //size of simulation box in y
sizeZ:=25e-9; //size of simulation box in z

SetGridSize(Nx, Ny, Nz);
SetCellSize(sizeX/Nx, sizeY/Ny, sizeZ/Nz);
```

An intuitive way to test whether the simulation mesh is sufficiently fine is to repeat the same simulation with a finer mesh. If the results are not significantly different, the original size of the mesh is likely sufficient for the considered problem. In our case, we also tested finer mesh sizes $4 \times 4 \times 5$ nm^3 and $2 \times 2 \times 12.5$ nm^3, and we did not observe significant difference for the results, compared to the mesh size $4 \times 4 \times 25$ nm^3, indicating that the coarse disretisation in the z direction does not affect the quality of the results.

The next step is to specify other general simulation parameters, material parameters and fixed geometrical parameters (see code snippet in Lst. 2.2). We set *EdgeSmooth*=5 to obtain a more realistic approximation of the curved edges of the nanomagnets (*EdgeSmooth*=N means that N^3 subcells are used to rescale the saturation magnetisation of the considered cell). The value of *stime* is used later to specify the additional time for which we let the system evolve, after the energy minimisation is completed. Then the commonly used material parameters for permalloy are set (saturation magnetisation $M_S = 800$ kA m^{-1}, exchange stiffness $A = 10$ pJ m^{-1} and magnetocrystalline anisotropy is neglected). The damping is set to $\alpha = 0.5$ to speed up the convergence of the simulation. Finally, the fixed geometrical parameters: magnet width, aspect ratio, the value of initial gap size, magnet length, the radius of magnet ends and length of the rectangular part of the magnet are specified.

Listing 2.2: MuMax^3: Setting of global parameters

```
//Simulation parameters
smu:=5;
EdgeSmooth=smu;
stime:=5e-9;
snapshotformat="png"

//Material parameters
//permalloy
Msat=800e3; // saturation magnetisation
Aex=10e-12; //exchange stiffness
alpha=0.5; //damping

//Fixed geometrical parameters
w:=150e-9; //magnet width
ar:=5; //magnet aspect ratio
g:=60e-9; //initial value of gap
l:=w*ar; //magnet length
r:=w/2; //radius of magnet ends
lrect:=l-2*r; //length of magnet's rectangular part
```

As a next step, we specify the numerical outputs to be saved when specified in the simulation script (code snippet is provided in Lst. 2.3. Apart from the geometrical and simulation parameters, we specify that values of exchange, demagnetisation and total energy shall be recorded.

Listing 2.3: MuMax^3: Specifying the numerical outputs

```
//Table settings -- specifying the outputs
tableaddvar(smu, "Smooth", " ");
tableaddvar(stime, "simulation time", "s");
tableaddvar(w, "width", "nm");
tableaddvar(ar, "aspect ratio", "");
tableaddvar(g, "gap", "nm");
tableadd(E_exch);
tableadd(E_demag);
tableadd(E_total);
```

Then we define a loop (see Lst. 2.4) that cycles through the size of the gap from $g_{\text{in}} = 60$ nm to $g_{\text{fin}} = 750$ nm with step of $g_{\text{step}} = 30$ nm. Within the loop, we then define the geometry of the vertex, assign regions to individual magnets, specify their initial magnetisation and run the simulation. For clarity, we divide these tasks into individual code snippets, shown sequentially below.

Listing 2.4: MuMax^3: Loop definition (iterates over gap size)

```
//Start of the loop
gstep:=30e-9;
gmax:=780e-9;
for g=60e-9; g<=gmax; g+=gstep{
print(g)

//Geometry definition
...

//Region and initial magnetisation definition
...

//Core of the simulation
...

}
```

For the definition of the vertex geometry, we use the built-in shapes and transformation operations available in MuMax^3. Essentially, we merge the rectangular

part of the magnet's body with two circles at each end to obtain the stadium shape of the magnet. Subsequently, this shape is translated and rotated to define the four magnets, which form the square lattice vertex. The vertex is then set as the geometry to be used by the script. A code snippet used to define the geometry is provided in Lst. 2.5.

Listing 2.5: MuMax^3: Setting up the vertex geometry

```
//Geometry definition
mbody:=rect(w,lrect);
mhead:=circle(w);
magnet:=mbody.add(mhead.transl(0,lrect/2,0)).add(mhead.transl(0,-
    lrect/2,0));

tmagnet:=magnet.transl(0,l/2+g/2,0); //top magnet
bmagnet:=magnet.transl(0,-(l/2+g/2),0); //bottom magnet
rmagnet:=magnet.rotz(pi/2).transl((l/2+g/2),0,0); //right magnet
lmagnet:=magnet.rotz(pi/2).transl(-(l/2+g/2),0,0); //left magnet
vertex:=tmagnet.add(bmagnet).add(rmagnet).add(lmagnet); //vertex

setgeom(vertex); //set the full vertex as the simulation geometry
saveas(geom, "vertex");
snapshot(geom);
```

The next step is to define the initial magnetisation of the four magnets to recover the considered vertex type (here, type I is defined). To do that, we first define regions for each magnet and then set the magnetisation for a given region to obtain the type I configuration. A relevant code snippet is provided in Lst. 2.6. To simulate different vertex types, one must modify the magnetisation assignment accordingly.

Listing 2.6: MuMax^3: Definition of regions, assignment of magnetisation

```
//Region definition
defregion(1, tmagnet); //top magnet
defregion(2, bmagnet); //bottom magnet
defregion(3, rmagnet); //right magnet
defregion(4, lmagnet); //left magnet
save(regions);
snapshot(regions);

//Initial magnetisation definition, T1 defined
m.setRegion(1, uniform(0, -1, 0)); //top magnet
m.setRegion(2, uniform(0, 1, 0));  //bottom magnet
m.setRegion(3, uniform(1, 0, 0));  //right magnet
m.setRegion(4, uniform(-1, 0, 0)); //left magnet
```

At this point, we have fully initialised the studied problem and can proceed with running the simulation. For the purpose of energy minimisation for magnetostatic problems, the MuMax^3 code offers two options. The first option is to use the *relax()* command that attempts to find the minimum energy for the defined system by disabling the precession term in the LLG equation. The effective field, computed from the damping term, then directs the magnetisation toward a direction with lower energy, which, however, is not necessarily the global energy minima [75, 78]. The other option is to use *minimise ()* command, which employs the steepest descent method [79] to minimise the system energy. It is reported that the *minimise ()* method is faster, compared to the *relax()* method, but is less robust when the initial state is far from the energy minimum [78]. This is not true in our case, so both methods seem suitable for the problem considered here.

We used the *relax()* command, and the code snippet for running the simulation is provided in Lst. 2.7. We first record/snapshot the initial magnetisation of the system and simulated MFM contrast. Then, the energy of the system is relaxed, and the simulation is run for an additional 5 ns to ensure that a stable configuration has been reached. After that, we record/snapshot the final magnetisation state, simulated MFM contrast and numerical values specified in Lst. 2.3 are saved. Then, the script continues to sample through the specified gap values defined in Lst. 2.4.

Listing 2.7: MuMax^3: Core of the simulation

```
//Core of the simulation

//Snapshots of initial configuration
snapshot(m);
save(m);
MFMLift=sizeZ+50e-9;
snapshot(MFM);

//Energy minimisation
relax();
run(stime);

//Spapshots of final configuration and quantity save
snapshot(m);
save(m);
snapshot(MFM);
tablesave();
```

The above-provided code snippets (Lst. 2.1 to 2.7) can be merged together to obtain working MuMax^3 script as no parts were omitted. We note that it is a script,

not a configuration file, so the order of the snippets must be respected to recover a working file. To run the script, one can put the provided script into a .txt file and drag it on top of the MuMax^3 executable file or run it via the command line.

Results: magnetostatic energy of vertex types

Here, we report the results of the MuMax^3 simulations discussed in the previous pages. To probe all four possible vertex types, we have repeated the code presented above with different assignments of the initial magnetisation (in Lst. 2.6), to also recover the final configurations for the type II, III and IV vertices.

Fig. 2.2 shows the results of the micromagnetic simulations computed for a single vertex with magnet width $w = 150$ nm. In Fig. 2.2a, we plot the total vertex energy (normalised to the type I total energy) per vertex type as a function of the gap. This chart nicely illustrates how the increase in the gap size impacts the magnetostatic energy levels. For the small gaps, a distinct separation between the vertex energy levels is observed, with the energy levels of type III and IV vertices being significantly higher than those of type I and II. Conversely, for the large gaps, the

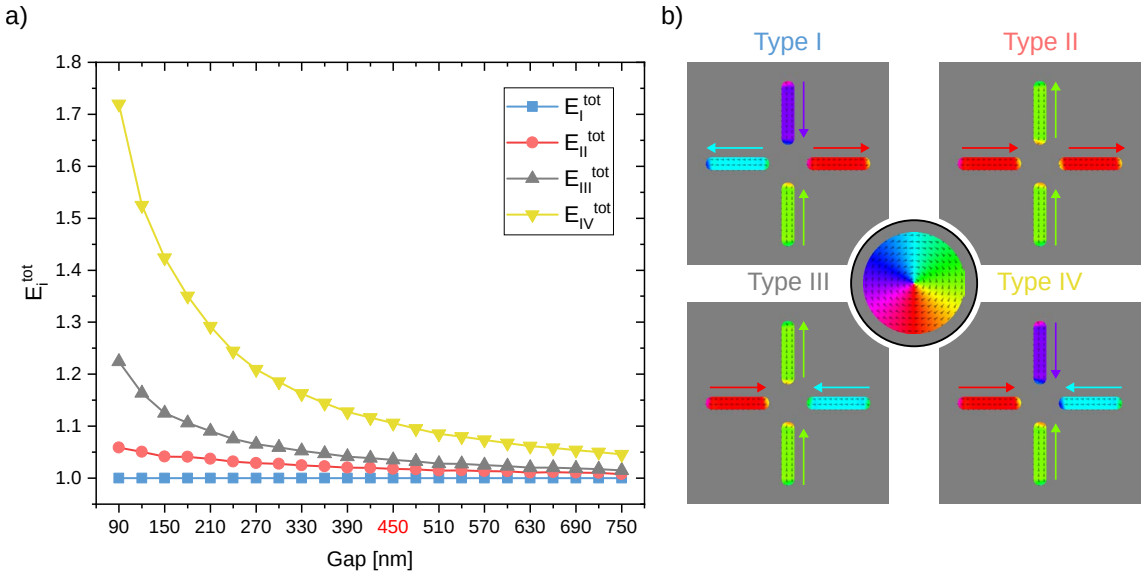

Fig. 2.2: Results of the micromagnetic simulations for the set of $w = 150$ nm magnets. a) Plot of the total vertex energy per type as a function of the gap. All energies are normalised with respect to the total energy of type I vertices. Data points are the results of the simulations, lines provide visual aid. The red label indicates the gap for which the snapshots of final micromagnetic states are provided in (b). b) Examples of final simulated magnetic configurations for a gap $g = 450$ nm. The colour indicates the local direction of magnetisation according to the provided colour wheel. The arrows next to individual magnets show the overall magnetisation direction to provide a visual guide.

energies of type I, II, and III vertices tend to converge, and the energy of type IV vertices also shows a tendency to approach this unified level. This is expected, as an increase in gap size results in diminished interaction strengths, consequently reducing the disparities among the energy levels under consideration. Fig. 2.2b then shows an example of the final micromagnetic states obtained for the four considered vertex types for a gap $g = 450$ nm.

Based on the estimated magnetostatic energies of the four vertex types, we calculated the estimation for the J_1 and J_2 coupling strengths and their ratio as a function of the gap. Those results are then used to select an approximate ratio for the Monte Carlo simulations. This process is detailed in Sec. 5.4. The same simulation set was also carried out for the magnet width $w = 100$nm, with the outcomes presented in the same section of the manuscript.

Simulating field-driven dynamics at finite temperature

In the previous pages, we provided a detailed description of how we approached the preparation of a MuMax^3 script for the purpose of magnetostatic simulations. In this work, namely in Sec. 4.3, we also used MuMax^3 to simulate a field-driven reversal of a single magnet and full vertex of the square lattice with high offset. In the latter case, we compare how the dynamics differ as the simulation is run at 0 K and at room temperature (300 K). We will now focus on this particular case, offering an overview of how the simulation was executed. We will not revisit the complete simulation definition to avoid redundancy, as it mirrors the description provided in the preceding pages.

To run the simulations at finite temperature, MuMax^3 includes implementation of stochastic (Brownian) thermal field $\vec{B}_{\text{therm}}$ as [75]:

$$\vec{B}_{\text{therm}} = \vec{\eta}(step)\sqrt{\frac{2\mu_0\alpha k_B T}{B_{\text{sat}}\gamma_{\text{LL}}\Delta V\Delta t}} \tag{2.1}$$

where μ_0 is the vacuum permeability, α the damping parameter, k_B the Boltzmann constant, T the temperature, B_{sat} the saturation magnetisation (in Tesla), γ_{LL} the gyromagnetic ratio (1/Ts), ΔV the volume of the cell, Δt the time step and $\vec{\eta}(step)$ a random vector drawn from a standard normal distribution whose value is changed after each time step. The code snippet used for setting up the temperature in the simulation is provided in Lst. 2.8.

Listing 2.8: MuMax^3: Setting up the temperature

```
temp.set(300) //set temperature to 300 K
Thermseed(2) //specify seed (optional)
fixdt = 0 //allow adaptive time-stepping
```

The first line sets the temperature to 300 K. In the second line, we specify the seed value for selecting the sequence of random numbers used to generate the thermal field. We can then compare the simulations' results with different seed values to evaluate whether applying "different" $\vec{B}_{\text{therm}}$ affects the results. Selecting the seed value also ensures reproducibility if the simulation needs to be repeated. In the last line, we specify that adaptive time stepping [77] is used, which generally reduces the time needed for the simulation.

We can then proceed with the simulation of the field-driven vertex reversal. To do so, we define a loop that increases the value of the external field by 1 mT and within each iteration, the simulation is run for 5 ns (the code snippet is provided in Lst. 2.9). It is important to note that for the purpose of simulating dynamics, the *run()* command must be used. During the simulation, the magnetisation configuration is saved every 100 ps, and the selected numerical quantities are saved every 10 ps.

Listing 2.9: MuMax^3: caption

```
snapshot(m) //capture the initial magnetisation configuration
AutoSnapshot(m, 100e-12) //capture every 100 ps
tableautosave(10e-12) //record values every 10 ps
Bmax := 80.0e-3 //max. value of external field
Bstep := 1e-3 //step for the external field
for B := 50.0e-3; B <= Bmax; B += Bstep { //start of the loop
    print(B) //print the value of external magnetic field
    B_ext = vector(-B/pow(2, 1/2), -B/pow(2, 1/2), 0) //external
       magnetic field in -(xy) direction
    run(5e-9) //run the simulation for 5 ns
    snapshot(m) //capture at the end of each iteration
} //end of the loop
```

The results of the field-driven reversal of the vertex of the square lattice with height offset simulated at 0 K and 300 K are reported and discussed in Sec. 4.3.

2.2 Sample fabrication

In most cases, artificial spin systems consist of sub-micron-sized elements. Such sizes require the utilisation of state-of-the-art nanofabrication techniques. If we focus on the research applications, one or two samples per designed system will usually be fabricated. Therefore, it is desirable to use direct-write techniques that allow for quick iteration of the fabrication process. Based on those requirements, the most suitable technique for patterning the artificial spin networks is electron beam lithography combined with additive or subtractive fabrication techniques to realise

the designed pattern in the magnetic material of choice. Different approaches might be taken depending on the details of the considered system to be made. Looking at the previous works, the following lithographic methods were used for the fabrication of artificial spin systems:

- e-beam lithography (positive resist, single layer) + lift-off [14, 26, 27, 39, 40, 56, 57, 62, 80],
- e-beam lithography (positive resist, double layer) + lift-off [12, 16],
- e-beam lithography (negative resist, single layer) + ion beam etching [81],
- e-beam lithography (positive resist) + lift-off (etching mask) + ion beam etching [82].

Schematics of the aforementioned fabrication approaches are provided in Fig. 2.3. While all four processes have similar capabilities and can yield similarly good results, there are distinct limitations for each of them. For the processes that form the final structures via the lift-off method (Fig. 2.3a and 2.3b), it is usually recommended to work exclusively with evaporation techniques for the deposition, due to more directional deposition. Using sputtering techniques, in this case, might lead to unwanted deposition of the material on the resist side walls, which might lead to a formation of collars at the proximity of the structure edges. This might be mitigated by using the double-layer resist mask (or single-layer mask of specific resists such as ZEP 520 or CSAR 62), which provides an undercut after the development. The lift-off technique is also sensitive to "cleanliness" of the developed areas, as any resist residuals might lead to increased shape roughness, lower surface adhesion or parasitic masking.

The processes that rely on ion beam etching to form the final patterns (Fig. 2.3c and 2.3d) might suffer from different effects induced by the ion beam etching itself. Collars (also referred to as fencing) might also form due to the re-deposition of the etched material to the mask side walls. Also, the magnetic properties of the structures might be impacted due to the plantation of the sputtering ions, intermixing of the substrate/structure materials or due to increased shape roughness, to name a few. Suppressing these effects might require careful process optimisation.

The list of possible fabrication approaches for artificial spin system patterning provided above is not extensive, and other approaches might be utilised. For example, the final structures can also be patterned by focused ion beam milling directly from a deposited film without the need for the resist process mask [83]. The main disadvantage of this approach is a relatively long procedure time, particularly for the systems in which the final structures cover a minority of the patterned area (which is often the case for arrays of elongated magnetic elements). The time needed for the FIB milling might be reduced by using a "Sketch and Peel" process, in which

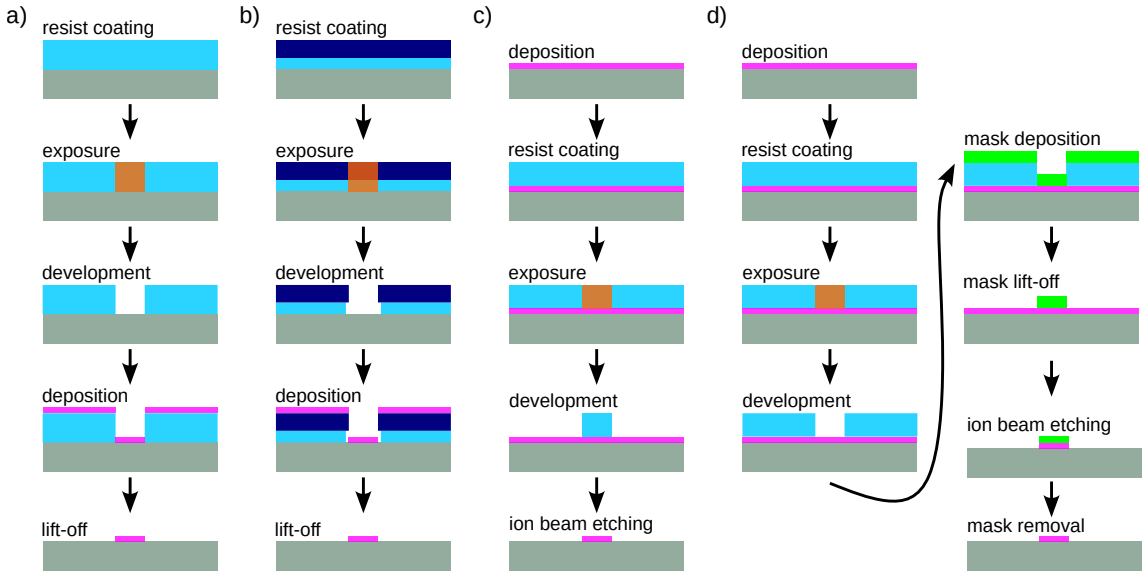

Fig. 2.3: Possible approaches for patterning of artificial spin systems utilising electron beam lithography to prepare a process mask. a) lift-off (single resist layer), b) lift-off (double resist layer), c) ion beam etching (negative resist mask) and d) ion beam etching (hard mask prepared by lift-off).

only the outlines of the targeted shapes are milled, and the unwanted material is removed using adhesion tape. It was shown that this method is capable of producing sub-100 nm gold structures [84]. Alternatively, it is possible to mask the outlines of the shapes using electron beam lithography and negative resist. After the deposition of selected material, an adhesive polymer is used to remove the "unsketched" shapes and the resist is subsequently stripped, leaving only the "sketched" pattern [85]. To the best of the author's knowledge, the Sketch and Peel technique has yet to be utilised for the fabrication of artificial spin systems.

To summarize, several fabrication processes are suitable for the fabrication of artificial spin systems. As each of them offers distinct advantages and limitations, the choice of the method to use must be based on careful consideration with respect to the desired system.

In this work, all of the studied samples were prepared using the lift-off method utilising electron beam lithography for the pattering of the process mask (a single layer of positive resist was used). This approach was selected as it is, in the author's point of view, the simplest one out of the methods mentioned above and its limitations can be mitigated by optimisation of fabrication parameters. Also, this process is well-known in our group, as it was successfully implemented in previous works by former students [31, 86].

In this work, we present three studies focused on the investigation of properties of field-demagnetised artificial square arrays of nanomagnets. In the two of them

(Chapter 3 and 4), a sample fabricated by a former PhD student of the group is utilised. In this sample, two types of square arrays are present: a conventional square lattice and a square lattice with an elevated sublattice. The latter was prepared by two subsequent lift-off steps, the first step being used to pattern non-magnetic bases and alignment marks and the second step being dedicated to pattering the magnets forming the lattice. Details about the sample fabrication can be found in Yann Perrin's PhD thesis (detailed description, in French) [87] or in this article (brief description) [31]. For the third study presented in this work (Chapter 5), the sample containing a series of conventional square lattices with varied lattice parameter was fabricated by the author of the thesis. We will now focus on this sample and provide a detailed description of the fabrication procedure. All tasks of the fabrication process were carried out by the author, if not indicated otherwise.

Note: During the PhD studies, the author of the thesis was responsible for fabricating several dozen samples with various artificial spin system geometries. Some of the works utilising those samples were already presented [26, 73, 88], while others are currently in progress. The fabrication was done either at Institut Néel (Grenoble, France) at the Nanofab facility, which features the Nanobeam Nb5 electron beam writer or at the Institute of Scientific Instruments of the Czech Academy of Sciences (Brno, Czech Republic), with the use of Raith EBPG 5000+ ES electron beam writer. When in Grenoble, the electron beam evaporation was done at the cleanroom facility of PTA. In the Czech Republic, the electron beam evaporation was done at the CEITEC Nano research infrastructure.

Therefore, the aim of the following subsections is not only to provide a detailed description of the fabrication of the sample investigated in this work but also to provide a well-tested recipe, which might be, hopefully, useful to future readers of the thesis.

2.2.1 Overview of the fabrication process

Here, we focus on the fabrication process employed for the preparation of the sample with conventional square lattices (with varied lattice parameters), which was probed experimentally in this work (in Chapter 5). This sample was prepared using the electron beam writer *Nanobeam Nb5* at the Nanofab facility at Institut Néel. All other process tasks (resist coating, development, lift-off etc.) were also conducted at the Nanofab cleanroom, with the exception of the electron beam deposition of permalloy, which was carried out by Vojtěch Schánilec at CEITEC Nano research infrastructure (the author had no access to suitable device at the time of the sample fabrication).

Even though it is not necessary for this particular geometry (there is no overlap

between two exposures required), we used a two-step lithographic technique (see Fig. 2.4), mainly for the convenience of the exposure execution. In the first step, we utilised the lift-off method to fabricate global registration/alignment marks (5 nm Ti / 50 nm Au), which are then used in the second step to place the pattern over the substrate precisely and to generate a focus map prior to electron beam exposure. The latter might slightly improve the fabrication quality. We also used the first step to pattern sample navigation features such as dose labels, region labels, orientation bar and sample ID. This approach allows us to position the labels in close proximity to the magnetic lattices with confidence that they will not affect the magnetic ordering of the lattices, as they are non-magnetic. The second step, another lift-off procedure, is then dedicated to the patterning of the magnetic arrays.

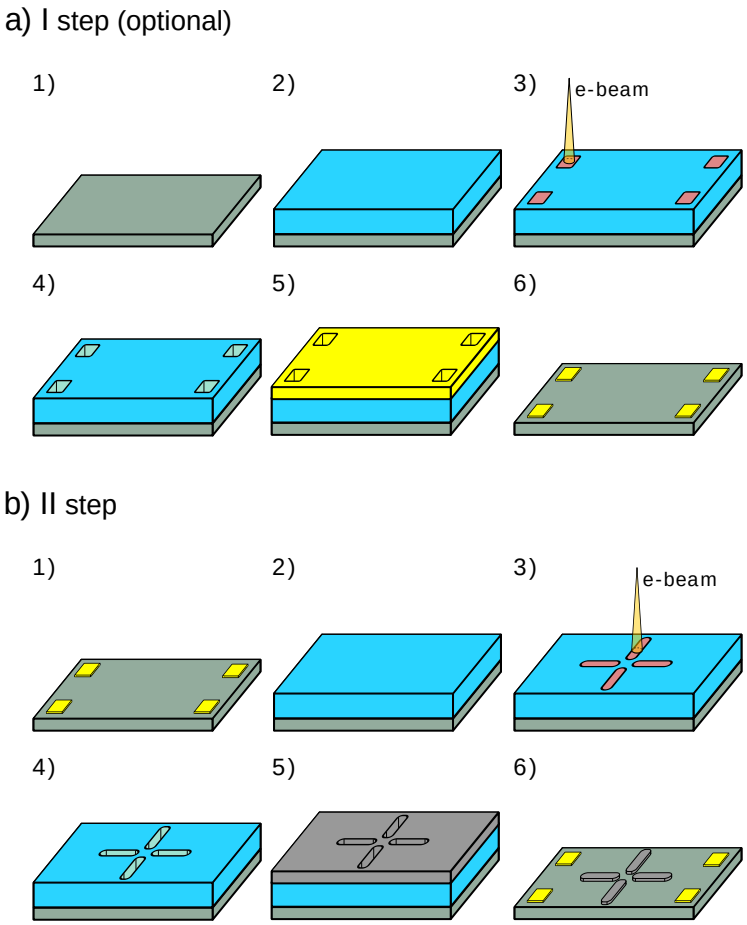

Fig. 2.4: Schematics of the two-step lithography technique used for sample fabrication in this work. Both the first (a) and second (b) steps consist of the same operations: 1) substrate preparation, 2) resist spin-coating, 3) electron beam exposure, 4) development, 5) material deposition and 6) lift-off. While the first step prepares registration marks and navigation features (labels, etc.), the second step is dedicated to patterning the magnetic lattices.

As mentioned above, the first step is optional, as there is no need to stitch precisely two consecutive exposures, and the focusing could be done, for example, by using paste with silver particles[1]. On the other hand, with the registration marks, the second step exposure execution is much simpler and less susceptible to placement errors. To be more efficient, we did the first step for a full 2" wafer, on which we can pattern nine 10×10 mm^2 chips at the same time. After lift-off, we cover the wafer with a protective layer of photoresist and use a wafer scriber to dice the wafer into individual chips. After stripping off the protective photoresist, the chips are ready to use for the second step.

In the following pages, we provide a detailed description of how the individual methods used for sample fabrication were carried out in this work.

2.2.2 Electron beam lithography

Electron beam lithography consist of the following steps:

1. Layout preparation.
2. Exposure data preparation.
3. Substrate preparation and resist spin-coating.
4. Electron beam exposure.
5. Development.

Each of the aforementioned steps can significantly influence the quality of the output, and process optimisation is a crucial task. The parameter space is rather extensive, and selecting the best recipe for a given task is based not only on conclusive testing but also on previous experience, previous works, discussion with colleagues, and the author's intuition. Therefore, some steps presented below cannot be justified by literature or tests and might be based on the author's subjective feelings.

Layout preparation

To prepare the layout defining the patterns for exposure, we utilised the open-source software KLayout Layout Viewer and Editor [89]. KLayout is 2D CAD software optimised for designing microfabrication templates. Shapes to be exposed are defined as squares or polygons placed on a fixed-spacing square grid (here, we use a grid size of 1 nm, which is typically used for patterns to be exposed by electron beam writers). There are two convenient features that are worth mentioning. First, the layout can be divided into layers that can be used to assign different fabrication

[1] The common practice is to apply a small amount of silver paste using a tiny brush close to the sample edge. The silver paste can then be used to optimise focus before the exposure.

parameters when preparing the exposure data (e.g., different exposure doses or different beam currents). Second, the layout can be built using a hierarchy, which is particularly handy if the layout consists of a repetition of the same shapes. In our case, we aim to design a layout consisting of individual magnets that are placed on a lattice. By using hierarchy, we can define the shape of the magnet only once and then specify the lattice positions to generate the lattice (in Klayout, a single object can be placed into *Cell* and the array is then generated via *Cell instance*). If the shape is to be modified, we can only modify its definition in the original *Cell*, and the changes will be reflected for all of its instances.

The snapshot of the single-chip of the full 2" wafer layout (in KLayout environment) used for the first lithography step is provided in Fig. 2.5. Different layers are used only to highlight different features of the design. On the border of the 10×10 mm^2 chip, scribing marks are designed. These dashed lines are filled with diffraction grating (period $\Lambda = 1$ µm) to improve the visibility after the fabrication. In the lower part of the chip, an orientation bar (also filled by the same grating) and sample label are placed. Both of those features are visible to the naked eye, which is helpful for the identification and manipulation of the sample. Two sets of global registration marks are placed on each diagonal, enveloping the central part of the chip, which is designated for the future placement of the magnetic arrays (in the second step). In each set of the registration marks, a 3×3 array of square marks is designed (each mark has size 8×8 µm^2, the period of the array is 200 microm in both directions). Finally, the regions to be filled by structures are labelled, and their boundaries are marked in the top left and bottom right corner. These features will be useful for navigating the finished sample during measurement.

The regions to be filled by the structures in the second step have size 500×500 µm^2, which corresponds to the size of the *main field (MF)* that will be used for the pattering (detail will be discussed later). Here, we designed an array of 6×6 regions, in which the rows are indexed by letters (A–F) and columns by numbers (1–6). In the second step exposure, we will assign a dose sweep across the rows and pairs of columns will be filled by lattices with different magnet widths.

For the second step, we prepared three separate layouts (for three selected magnet sizes), each containing a series of 24 conventional square lattices with varied lattice parameter. The geometry specification is provided in Fig. 5.1 and a list of designed lattices in Tab. 5.1. The strategy employed for geometrical parameter selection of the lattices is discussed in Sec. 5.1.

In Fig. 2.6, we show the layout for the second lithography step containing two identical series of square arrays with magnet's width $w = 100$ nm at different magnification. All of the lattices are built based on the same magnet shape, obtained by merging a rectangle with two appropriately positioned circles, which yields the

stadium shape of the magnet. Each magnet is essentially a polygon of 32 points.

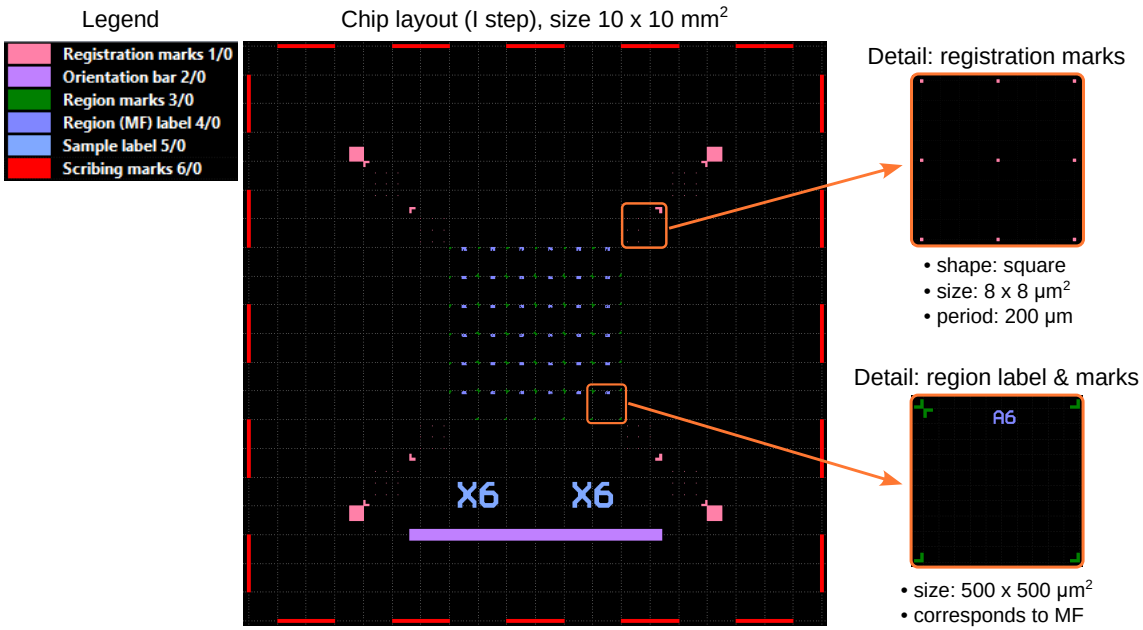

Fig. 2.5: Chip layout for the first lithography step of the sample studied in this work (Chapter 5). On the left, a legend describing different features of the design is presented. On the right, two details of the layout are shown.

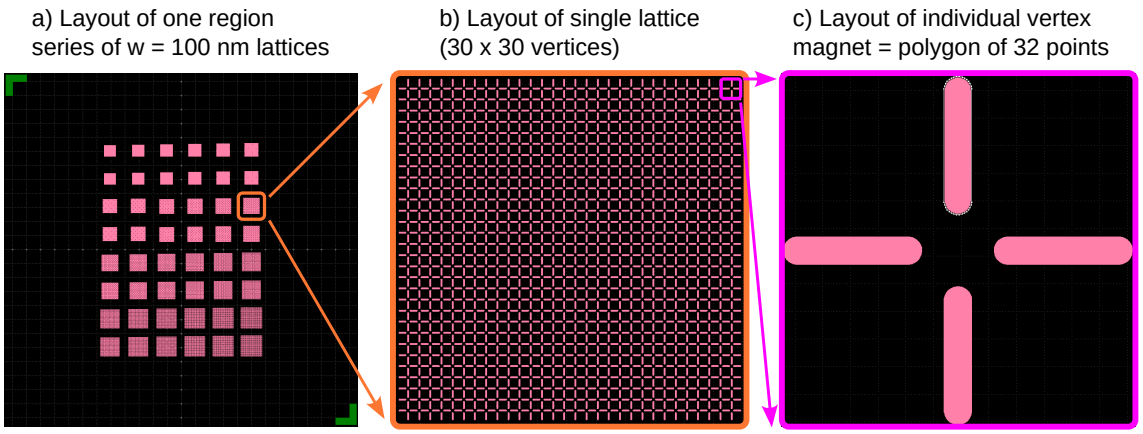

Fig. 2.6: Region layout for the second lithography step containing series of conventional square arrays consisting of stadium-shaped magnets of size 500×100 nm^2 at various magnifications: a) entire layout (2 series of 24 lattices), b) detail of one of those lattices and c) detail of single vertex of (b). In (c), for the top magnet, the 32 individual points defining its shape are shown.

The final step of the layout preparation is to export the designed patterns to a .GDS file, which will be used to prepare the exposure data.

Exposure data preparation

The next step is to prepare the exposure data, which essentially includes two steps: data fracturing and job file preparation. For this sample, the exposure was carried out by *Nanobeam Nb5* electron beam writer. To fracture the data, proprietary software of the Nanobeam company called *nbPat* was used. The input .GDS file is essentially translated into the native "language" of the writer pattern generator. In the case of this particular electron beam writer, the shapes to be exposed are approximated by pixels that correspond to the beam shot placements. The writing strategy for any defined shape (i.e. polygon) is first to write the outline of the shape and then subsequently fill the inner area of the shape. This writing strategy is a perfect fit for our application, as it allows for symmetrical and high-fidelity beam placement, particularly for the rounded ends of our magnets. A similar writing strategy is also available on other electron beam writers. For example, in the case of *RAITH* systems, comparable fracturing can be obtained using *sequence* method.

Field writing parameters, such as main field size (and offset) and subfield size (and offset), are specified during the fracturing. The main field corresponds to the physical movement of the writer stage. Each main field is then divided into subfields that correspond to a coarser beam deflection. Shapes within each sub field are written with finer deflection of the beam. General rules are to avoid placing critical structures at main field borders to avoid stitching errors. The stitching of the subfields yields much lower errors and is usually not critical for the pattern writing. Its effects can be suppressed by advanced writing strategies such as overpass (the writing is done in two or more passes with an appropriately scaled-down dose for each pass, and the subfield offset is changed between subsequent passes). However, as we did not observe any defects in our fabricated structures that would suggest subfield stitching errors being at play, we used the conventional single-pass writing technique.

In the case of the considered sample, we used main field size 500×500 µm^2 and subfield size 20×20 µm^2 for both lithography steps. In the case of the first step, the main field and subfield offsets were optimised with respect to the registration marks (the goal is to have main field and subfield borders not crossing the marks). For the second step, we centred the structures (series of lattices of one magnet width) within a single main field (see Fig. 2.6a). As the lattices within the series have varying sizes, it is impossible to optimise the subfield offset in a way that subfield borders do not cross the structures. However, as mentioned above, we did not observe any defects originating from the subfield stitching in the fabricated lattices.

The second task of the exposure data preparation is to prepare a job file that includes the definition of the exposure itself. This job file essentially includes the

set of instructions that the electron beam writer executes to carry out the exposure. In the case of the *Nanobeam Nb5* tool, the job file is a command-based script. The typical job file includes the following:

- Specification of the beam settings (e.g. focus setting).
- Specification of sample position with respect to the tool coordinates.
- Specification of patterns to be exposed (loading of the fractured pattern files).
- Dose setting for different block(s) of pattern(s).
- (Optional) Setting of the registration procedure (specification of the marks and their position).

We will now focus only on the second lithography step (dedicated to the fabrication of the targeted arrays) and briefly describe how the job file was designed. The fractured patterns (three separate layouts for lattices with different magnet widths $w = 100\,\text{nm},\ 150\,\text{nm}$ and $200\,\text{nm}$) are loaded. Each layout has a size of one main field, which is the same as the size of the labelled regions we prepared in the first step (see Fig. 2.5). We thus specified the positioning of the patterns (as blocks in the job file) as follows:

- $w100$ – columns 1 & 2,
- $w150$ – columns 3 & 4,
- $w200$ – columns 5 & 6.

This is then repeated in 8 rows, for which the exposure dose is increased from the bottom to the top (from $D = 600$ to $1300\ \mu\text{C/cm}^2$, with a step of $100\ \mu\text{C/cm}^2$). As we initially planned to have only six doses (for which we prepared the labelled region array in the first step), the lowest (highest) dose row is placed below (above) the prepared region array. By doing so, we specified the placement of all desired 48 blocks of patterns. To provide a fun fact, almost 4.3 million individual magnets are defined for writing on our sample.

For the global registration, four marks (one from each diagonal) are specified by their respective position. The left and right bottom marks are used to align the sample and tool coordinates. These four marks are also used to generate a focus map for the exposure.

We note that the selection of the exposure dose must consider the following: the resist to be exposed, the acceleration voltage of the electron beam writer and the nature of the lithography. We plan to use PMMA resist, which is positive (exposed areas are more easily dissolved during development), and the *Nanobeam Nb5* at Institut Néel is operated at 80 kV. The higher the voltage, the higher the exposure dose is needed to clear the resist in exposed areas after development. As we are interested in the fabrication of process mask, the lithography nature is binary (in exposed areas, we want to entirely remove the resist, in unexposed areas, the resist shall remain close to its original thickness). It is a common approach to slightly

overexpose the patterns in binary lithography to ensure uniform clearing of the exposed areas. Considering those aspects and reflecting on previous experience, we selected the dose sweep specified above. The reason for using several doses is to "broaden the process window" in order to make sure that some of the doses will yield the optimal result.

Substrate preparation and resist spin-coating

As we have designed the layout of our sample and prepared the exposure data, the remaining step to be done prior to the exposure is to prepare the substrate and coat it with suitable resist for the electron beam exposure. For both lithography steps, we used standard PMMA resist with molecular weight 950 K. For such a resist, a typical value of achievable resolution provided by manufacturers is approx. 6 nm, which is sufficient for patterns considered here.

The details of the substrate preparation and resist spin-coating for both lithography steps are provided below.

I step

- Substrate: 2" wafer, orientation: (100), type: P/Boron
- Substrate pretreatment: none, used "out-of-the-box"
- Resist: 4% PMMA 950 K (AR-P 679.04)
- Spin coating: 6000/4000/30 (RPM/acceleration/duration in seconds)
- Soft-bake: Hot plate, 180 °C, 5 minutes, with vacuum pumping
- Thickness measurement: approx. 230 nm
- Quality control via optical microscope

II step

- Substrate: 10×10 mm^2 chip (diced from the 2" wafer)
- Substrate pretreatment: cleaning/stripping of covering photoresist layer (used for scribing)
  - I bath: 5 min Acetone with ultrasonic agitation
  - II bath: 5 min IPA with ultrasonic agitation
  - Rinse with IPA (using wash bottle)
  - Dry with nitrogen
  - Hot plate (150 °C, 5 min), to evaporate any residual solvent/dehydrate the substrate
- Resist: 3% PMMA 950 K (AR-P 679.03)
- Spin coating: 4000/4000/30 (RPM/acceleration/duration in seconds)
- Soft-bake: Hot plate, 180 °C, 5 minutes, with vacuum pumping
- Thickness measurement: approx. 160 nm

- Quality control via optical microscope

The selection of resist concentration and spin-coating parameters is based on the desired thickness of the resist coating, which is based on what it will be used for. In our case, we are interested in a lift-off technique, for which the rule of thumb is to have at least a 1:3 (or better 1:5) ratio between the targeted thickness of the deposited material and the resist process mask. In the first step, we want to deposit approx. 55 nm (5 nm Ti / 50 nm Au), and in the second step, we wish to deposit approx. 30 nm (5 nm Ti / 25 nm NiFe). Thus, the resist concentration and spin-coating parameters were set accordingly. We verified the thickness in both cases by *Ocean Optics NanoCalc* spectroscopic reflectometer. So, for the first step, we have a ratio of approx. 55:230, and for the second step, approx. 30:160, both satisfying the "lift-off condition".

After the spin-coating, the substrate with coated resist is placed on top of a hot plate. This serves two purposes: 1) to evaporate the resist solvent and 2) to create a well-defined resist structure in the coated layer. A general rule is that the baking temperature should be above the polymer glass transition temperature $T_g^{\mathrm{PMMA}} = 125$ °C and significantly below its thermal degradation temperature ($T_c^{\mathrm{PMMA}} = 250$ °C. We thus opted to use $T_{\mathrm{bake}} = 180$ °C, which satisfies the criteria mention above and is also a "standard operation procedure" for PMMA resists at Nanofab facility at Institut Néel.

As a last step, the quality of the coated resist layer is investigated using optical microscopy. Particularly for the second step and the central area of the chip (where the structures will be placed), the cleanliness of both the substrate and the coated resist layer is critical, as any impurities present might result in defects. Thus, if any impurities were spotted in this area, we stripped/cleaned the sample and coated it again. Dark-field microscopy has proven very useful for spotting possible impurities, as they light up due to the light reflected from their edges and become clearly visible against the dark background generated by the uniform surface of the substrate.

Electron beam exposure

As we have prepared the substrate with suitable resist and the exposure data, we can proceed with the exposure itself. A simplified overview of the exposure procedure is as follows:

1. Load the sample into the electron beam writer.
2. Load the database with the selected electron beam current and working distance (this varies based on the substrate thickness).
3. Run a package of calibration procedures.
4. Locate and save positions of the marks, that specifies the sample coordinates.

5. Start the exposure job.

The selection of electron beam current has several implications for the pattern exposure. Firstly, the beam size differs based on the beam current. For the *Nanobeam Nb5* tool, the manufacturer estimates the beam size of approx. 4 nm for beam current of 1 nA, compared to approx. 20 nm for beam current of 30 nA. Therefore, lower beam currents are more suitable for writing small features, while large beam currents are more suitable for writing big features. We thus used beam current of 30 nA in the first step to write the exposure marks, labels and other chip features and beam current of 1 nA for the second step to write the square arrays of interest.

In the case of the *Nanobeam Nb5* tool, the writing step size is variable and depends on the exposure dose, beam current and writing clock rate. We did not prescribe the writing step size for the writing of our structures. Thus, the device uses the smallest possible step size that keeps the deflection rate below the limit of the writing clock (60 MHz). This resulted in writing step size of 2 nm for our square arrays patterned in the second lithography step. Compared to the size and shape of our features, the writing step is sufficiently small to provide an accurate representation. In fact, the writing step size is smaller than the beam size, which means that the beam shots will overlap, which is desirable for binary lithography, as it helps to achieve uniform clearing of the exposed areas.

Development

The final step of the lithography itself is to develop the sample. In the case of positive resist, which was used here, the interaction with the beam in the exposed areas leads to the breaking down of the resist molecules into smaller fragments that have lower molecular weight. This leads to their faster development rate compared to the unexposed areas, provided that a suitable solvent (also called developer) is used. The choice of the developer and development time is essential to optimise the process. As we wish to obtain a binary process mask after the development, which will be used for the lift-off technique, we need uniform clearing of the exposed areas, preferably without any resist residuals.

Upon testing and previous experience we used the following development procedure:

- I bath: MIBK:IPA [1:3], 60 s.
- II bath: IPA, 60 s.
- Rinse angled chip by IPA from wash bottle, 10 s.
- Dry with nitrogen.

After the development, we inspect the lithography results using an optical micro-

scope. Of course, we cannot inspect the structures themselves due to the technique's limited resolution, so one must trust the process (which is based on previous testing on larger features, where inspection by an optical microscope is possible).

2.2.3 Material deposition

For the material deposition, we used the electron beam physical vapour deposition (EBPVD) technique [90], also called electron beam evaporation, exclusively in this work. As we discussed previously, evaporation is preferable for the lift-off technique, as the more directional deposition prevents/limits the formation of collars at the mask side walls/structure edges.

The EBPVD operates on the principle of using a high-energy electron beam to vaporize a source material under UHV conditions, subsequently depositing a thin film onto a substrate/sample. The deposition rate (resp. layer thickness) is monitored during the deposition by a quartz crystal micro-balance monitor, which measures the frequency response of a quartz crystal to estimate the amount of the deposited material [91].

The deposition for the first lift-off was carried out using *Plassys electron beam evaporator* located in the Nanofab cleanroom at Institut Néel. First, 5 nm of Ti was deposited to improve the adhesion, and then 50 nm of Au was deposited to form the registration marks, labels and other chip features. The rate of deposition was approx. 1 $\text{Å}\,\text{s}^{-1}$ for Ti and approx. 0.5 $\text{Å}\,\text{s}^{-1}$ for Au.

The deposition for the second lift-off was carried out by Vojtěch Shánilec at CEITEC Nano research facility employing *BESTEC electron beam evaporator*. Again, 5 nm of Ti was deposited first to improve the adhesion, followed by 25 nm of NiFe deposition. Finally, 3 nm of Al was deposited as a capping layer. The rate of deposition was approx. 0.5 $\text{Å}\,\text{s}^{-1}$, 1 $\text{Å}\,\text{s}^{-1}$ and 0.5 $\text{Å}\,\text{s}^{-1}$ for Ti, NiFe and Al, respectively. The stage with the sample was continuously rotated at 5 RPM during the deposition.

2.2.4 Lift-off

The final procedure of the sample fabrication is to conduct the lift-off technique to remove the resist mask with the undesired material lying on top. In an ideal case, only the material deposited through the holes of the resist mask directly to the sample surface shall remain.

In the case of the sample fabrication presented here, the lift-off procedure is conducted slightly differently for the two lithography steps. For the first lift-off

(Ti/Au stack for the marks, labels, etc.) the procedure consists of the following steps:

- I bath: NMP solvent, heated to 80 °C via hot-plate (several hours).
  - Film release enhancement via pipette and removal of lifted film fragments from the bath via pipette.
  - Ultrasonic agitation (10 s, low-power).
- II bath: Ethanol.
  - Ultrasonic agitation (60 s, low-power).
  - Impurities release enhancement via pipette.
- Rinsing of angled wafer by Ethanol from wash bottle (10 s).
- Drying with nitrogen.

For both baths, the wafer was submerged in the appropriate solvent in glass through. For the first bath, the glass through was covered by an hourglass to suppress solvent evaporation. After the significant release of the material film was observed (during the first bath), the further film release was facilitated by the gentle blowing of the pipette (submerged in the solvent) from the sides of the substrate. By doing so, large fragments of the lifted-off material are fully released from the substrate. Subsequently, we removed those fragments from the bath by sucking them into the pipette. As the next step is to apply ultrasonic agitation, which breaks the film into tiny fragments, this step helps improve the process's cleanliness.

After the ultrasonic agitation, which helps to break any remaining connections between the structures and the material to be removed, the substrate is transferred into a second bath (Ethanol), followed by another ultrasonic agitation. Then another pipette release enhancement is carried out to release any remaining impurities from the substrate. Subsequently, the substrate is removed from the bath and thoroughly rinsed with Ethanol using a wash bottle. Finally, the sample's surface is dried by blowing the nitrogen gun.

For the second lift-off (Ti/NiFe stack for the square arrays), the procedure is slightly different and utilises an "hourglass trick", that in the author's experience leads to improved cleanliness of the final sample. This trick was suggested to the author independently by both Yann Perrin (former PhD student of the MNM group) and Bruno Fernandez (Nanofab staff member). The main idea is to place the sample into the lift-off solvent motive-down using an hourglass placed within the glass through. By doing so, the lifted-off material (particularly after it is fragmented by ultrasonic agitation) sediments at the bottom of the glass rather than on the sample, which further improves the process cleanliness. For the second lift-off, the procedure contains the following steps:

- I bath (motive-down): NMP solvent, heated to 80 °C via hot-plate (several

hours).
  - Ultrasonic agitation (60 s, ramped gradually from low- to mid-power).
  - Sedimentation (60 min).
- II bath (motive-down): Ethanol + ultrasonic agitation (30 s, mid-power).
- III bath (motive-up): Ethanol + ultrasonic agitation (30 s, mid-power) + impurities release via pipette.
- Rinsing of angled sample with Ethanol from wash bottle (10 s).
- Drying with nitrogen.

This concludes the process of sample fabrication. The next step is to image the patterned structures by scanning electron microscopy, which will provide information about the micro-quality of the fabricated structures. As one cannot inspect the influence of every decision taken during the fabrication process, it is hard to provide evidence for every process parameter. Particularly, the above-described implementation of the lift-off process might seem unnecessarily complex. The one thing we tested, and it is worth stressing, is that applying ultrasonic agitation is crucial for obtaining clean structures, which, combined with a suitable exposure dose, produces sharp structure edges without (almost) any collar defects present. We also note that we (for other samples) tested different solvents for the lift-off (Aceton or Dioxolan), which also produced nice results. However, the quality of the lift-off was slightly inferior compared to when NMP was used.

2.2.5 Results

Due to the sub-micron size of the magnets, only the macro-quality can be assessed by optical microscopy, and scanning electron microscopy (SEM) has to be used to image their micro-quality. From the macro point of view, the fabrication quality is excellent, and no macro defects are present. By macro-defect, we mean missing parts of the layout that could originate, for example, from particle contamination (either in resist or prior to the material deposition). This would cause missing parts of the designed structures of irregular shape. The absence of this type of defect suggests that the overall cleanliness of the fabrication process was maintained.

On the micro-scale, we observe a very low amount of defects. By micro-scale defects, we refer to defects on the lattice element level, such as missing magnets (see the example provided in Fig. 2.7a). For example, for the 4 series of $w = 100$ nm lattices investigated in Ssec. 5.3.1, only 4 out of 84 considered lattices are observed to have a micro-defect. In the case of the four lattices referred to above, we observe that, at most, 3/1860 magnets are missing. We note that for the micro-defects, we mostly observe missing magnets, which suggests that these defects originate from

the lack of adhesion between the substrate and the magnet. We can only speculate what caused the lack of adhesion for those missing magnets. Possible explanations are either not completely cleared resist after development or the presence of micro-impurities on the substrate. In both cases, it is likely that the magnet is then "ripped off" during the lift-off (particularly during the ultrasonic agitation), leading to a vacant site in our artificial array.

On the nano-scale level, we understand defects as a shape variation that is more prominent than the shape roughness, which is always present. In the case of our sample, we typically observe nano-scale defects characterised by missing material at the edge of the patterned shapes (see the example provided in Fig. 2.7c). The likely origin of those defects is not perfectly cleared resist at the substrate after the development. These resist residues then act as parasitic mask, leading to the removal of the chunk of the deposited material, resulting in a magnet with missing volume.

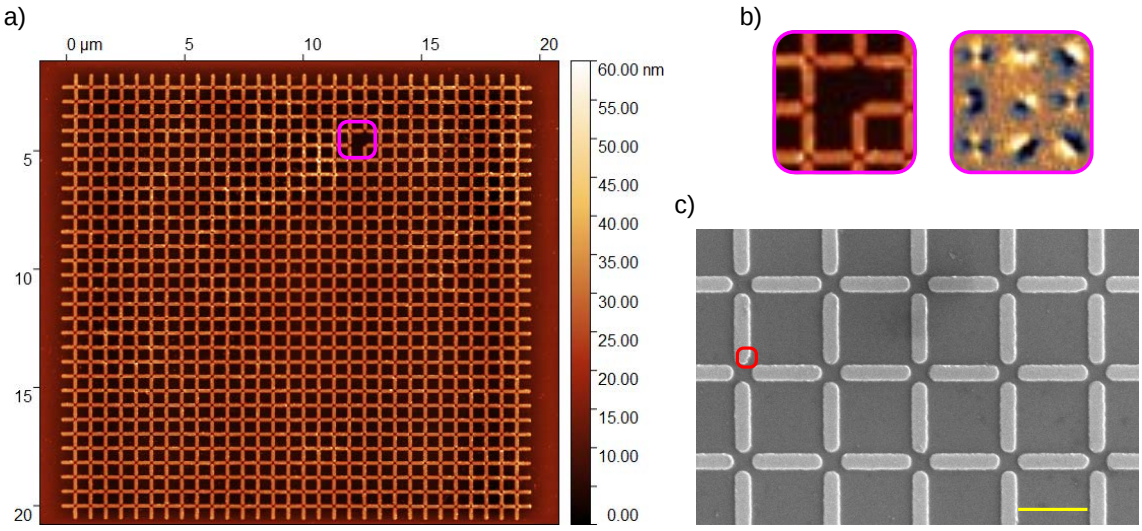

Fig. 2.7: Examples of fabrication defects observed in our artificial square arrays. a) AFM topography image of an incomplete square lattice. The pink box highlights two missing magnets. b) The detail of the defect site highlighted in (a). The left image shows AFM topography, and the right image shows the magnetic contrast. The contrast of the incomplete vertices is distinguishable from the complete ones, as they do not consist of four "poles". c) SEM detail of fabricated square lattice. The red box highlights nano-scale defect. Part of the magnet's volume is missing, and the shape variation is significant compared to the magnet's roughness.

In the case of the lattices with micro-scale fabrication defects, for which we mainly observe an entire magnet body missing, the defects sites are easy to identify in the topography and magnetic images obtained by AFM/MFM (see Fig. 2.7b). For this type of defect, we then assign a missing spin in the evaluation. A defect of

this type affects the spin configuration in the vicinity of the defect site, as there are missing pairwise spin-spin interactions.

The nano-scale defects (example shown in Fig. 2.7c) are essentially not visible in the AFM/MFM images, as they are below the resolution at which we scan the images. These defects may slightly influence the interaction strengths and/or the magnets reversal dynamics, but it is hard to establish how strong their impact is. In this work, we consider those defects as intrinsic property of the fabricated arrays.

Other important task to be done during the SEM imaging is to identify which exposure doses yields structures suitable for the experimental study. To do so, we imaged the same lattice patterned with different exposure doses. The results of this analysis are provided and discussed in Sec. 5.20.

2.2.6 Summary

In this section, we provided a detailed description of how we approached the design and fabrication of artificial square arrays consisting of nanomagnets arranged on a square lattice. This sample is then experimentally investigated in Chapter 5.

The fabrication recipe provided above is a well-tested recipe and was also used for fabricating other samples, with only minor optimisation of the process parameters. As the fabrication results are fairly good, we show that it is not always necessary to use double resist layers for the lift-off technique, provided that the resist thickness, exposure dose and development parameters are suitably optimised.

2.3 Field demagnetisation

Both in this work and generally in the field of artificial spin systems research, the interest lies in the low-energy configurations of the studied arrays. So far, two main approaches to minimise the system's energy have been employed: field or thermal demagnetisation. The intended demagnetisation protocol must be chosen before the sample fabrication, as there are distinct requirements for sample compatibility. For example, the thermal approach requires a specific substrate or intermediate layer to mitigate substrate-sample inter-diffusion [71], smaller magnet volume (compared to the field approach) [22, 92] or specific magnetic material choice [35]. The discussion comparing the two approaches and their performance is provided in the introduction of Chapter 4. Here, we focus only on the field demagnetisation protocol, which was used exclusively in this work.

Typical samples that will be demagnetised by field protocol consist of arrays that are thermally stable at room temperature. The usual thickness of the magnets is in the range of 20 to 30 nm, which leads to their Blocking temperature

being significantly above the room temperature. In other words, due to the volume of the magnets, the energy barrier for the magnetisation reversal is so high that spontaneous reversal (driven by thermal fluctuations) never occurs. Therefore, the magnetic configurations of the arrays can be altered only by applying the external magnetic field, which yields arrested configurations that do not change in time. The magnetic imaging can then be conducted at room temperature, which is always convenient.

The typical adaptation of a field demagnetisation protocol for arrays of ferromagnetic nanomagnets relies on application of external magnetic field, which amplitude decreases in time [12, 31, 54, 55, 57], although use of protocol with fixed field amplitude was also reported [56]. In the case of systems with in-plane magnetisation, such as ours, the field direction is also applied in-plane. Furthermore, the field or rather the sample, is rotated in-plane to ensure effective demagnetisation of the multi-axial systems.

Use of different decaying field profiles to demagnetise square arrays of nanomagnets was reported: linear decrease [54, 57], step decrease [54], step decrease with polarity alternation [12, 54, 55] or sine function with linearly-decreased amplitude [31]. Without taking into account the different lengths of the applied protocols, the closest approach to the ground-state ordering for conventional square arrays was reached by using the sine function with linearly decreased amplitude in Ref. [31]. A more detailed comparison of the reported performance of different field demagnetisation protocols is provided in the introduction of Chapter 5.

In this work, we exclusively employ the sine function with a linear decrease in amplitude as the field profile for the demagnetisation, following the previous work of Perrin *et al.* [31]. Schematic of the field demagnetisation protocol utilised in this work is provided in Fig. 2.8a, and the experimental set-up used for demagnetisation is shown in Fig. 2.8b. This set-up was designed by V. Schánilec during his master studies [93] and was later refurbished by the author of the thesis. The image provided in Fig. 2.8b shows the current (refurbished) version of the device.

The sample is placed in a sample holder pocket and secured by double-sided tape. The sample holder is then mounted on top of the brushless dc motor, which is positioned below the air gap of the electromagnet. In our experiment, the sample rotation was typically set to $f_{\mathrm{sample}} = 20$ Hz, if not specified otherwise. Then, the magnetic field driven via coil excitation controlled by a waveform generator and a KEPCO power supply was applied. The typical field profile used in this work consists of the sine wave ($f_{\mathrm{field}} = 250$ mHz) modulated by a linear function with a negative slope, which is adjusted based on the targeted total length of the protocol. To be precise, the modulation function consists of the liner function with a negative slope, to which a zero function is appended. In this work, we typically used 72

h long demagnetisation protocols. The coil excitation is set such that the initial amplitude of the external magnetic field is approx. 100 mT, which is well above the coercive field of the investigated lattices. Then, the field amplitude gradually decreases towards zero, following the field profile specified above. As the rotational frequency of the sample is much faster than the frequency of the sine wave, only minor changes in the field amplitude occur during one complete revolution of the sample.

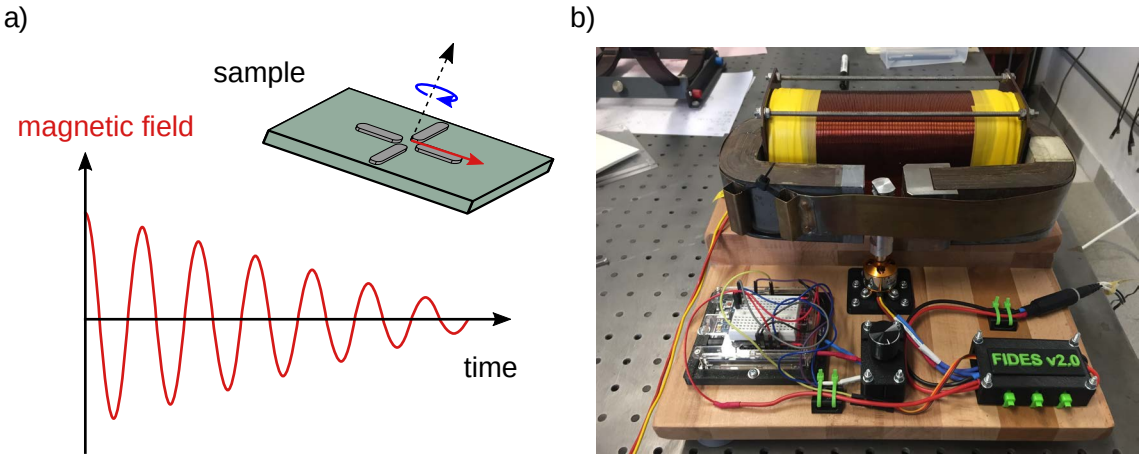

Fig. 2.8: a) Schematic of a field demagnetisation protocol. The sample is rotated within an external magnetic field defined as a sine wave with linearly decreasing amplitude in time. The field direction is in-plane with respect to the sample. b) Image of field demagnetisation set-up used in this work. The samples are placed in a sample holder mounted on a brushless dc motor. The sample holder is located within the air gap of the electromagnet consisting of copper coil and iron pole pieces. A waveform generator and KEPCO power supply drive the excitation of the coil. The motor rotation is controlled via a potentiometer connected to an Arduino board and electronic speed control module.

The field demagnetisation protocol is essentially a black-box process. One might know only the initial configuration of the sample prior to the demagnetisation and then the final configuration after the demagnetisation is conducted. However, an intuitive description of what happens during the field protocol can be provided. During demagnetisation, each magnetic element within the array experiences an effective field that combines the external driving field with the cumulative dipolar fields of the neighbouring magnets. Magnet reversal occurs when this effective field surpasses the coercive field strength of the magnet in question and is oriented in the opposite direction to the current magnetisation direction of the magnet being considered.

If the amplitude of the driving field exceeds the coercive fields of the lattice mag-

nets, the magnetisation of the nanoislands aligns with the direction of the applied external field. In this regime, the magnetic configuration of the lattice can be described as a diagonally polarised state, and the net polarisation tracks the direction of the external field. Once the maximum field amplitude is below the coercive fields of the lattice magnets, the configuration is frozen as the field is not strong enough to facilitate any magnet reversal. At this point, the final configuration that will be subsequently imaged is arrested. The field protocol is then effective only when the amplitude of the external field is comparable to the coercive fields of the lattice magnets. In this regime, the external field provides the additional push to overcome the reversal barrier but does not overpower the contribution of dipolar fields from the neighbouring magnets, which steers the system towards its low-energy manifold. The level of energy minimisation is then essentially limited by single-spin flip dynamics, as collective spin updates such as loop flips are not available experimentally.

2.4 Magnetic imaging and data evaluation

Once the sample is demagnetised, the arrested magnetic configurations are measured by magnetic imaging. In this work, we exclusively use magnetic force microscopy to probe the magnetic configurations of our arrays. This technique offers enough resolution to resolve the orientation of each nanoisland forming the lattices, providing fully resolved real space information about the magnetic configuration. Once this configuration is extracted from the measured image, different quantitative data can be computed to characterise the captured configuration. Below, we describe how the magnetic imaging was performed and how we process the captured images.

2.4.1 Magnetic force microscopy

Magnetic force microscopy (MFM) [94, 95] is a two-pass scanning probe microscopy technique that enables probing of magnetic properties of the sample based on its interaction with a sharp tip coated with a thin film of magnetic material. The tapping mode, wherein the cantilever with the tip oscillates near its resonance frequency, is predominantly employed for magnetic force microscopy nowadays. This mode was also utilised in this work.

The first pass is essentially a conventional atomic force microscopy (AFM), and the probe measures the topography of the sample by scanning across it (see Fig. 2.9a). In the tapping mode, the amplitude of the probe oscillations is such that at the lower turning point, the tip encounters intermittent contact with the sample. The tapping mode thus operates at the transition between the repulsive and attractive force regime. During the scan, the microscope maintains the set oscillation amplitude (also called set point). Suppose there is a change in the sample-tip

distance. In that case, the oscillation amplitude changes and its recorded value is passed to a feedback loop that adjusts the Z scanner piezo element to maintain the set amplitude set point. The sample topography is then reconstructed from the Z scanner movement. The topography recorded at the given line scan in the first pass is then used as an input for the subsequent second pass.

For the second pass, the tip is lifted to a specified height above the sample surface and mimics the previously measured topography profile. Thus, a constant distance between the tip and the sample surface is maintained (see Fig. 2.9b). Therefore, the tip mostly experiences the interaction between the magnetic stray field emerging from the sample and the magnetic coating of the tip. This leads to a difference between the driving phase and the detected phase of the tip oscillations. If the stray field attracts the tip towards the sample, the resulting phase shift is negative and vice versa (see Fig. 2.9b). The recording of this phase shifts throughout the scanning process and then yields a magnetic image.

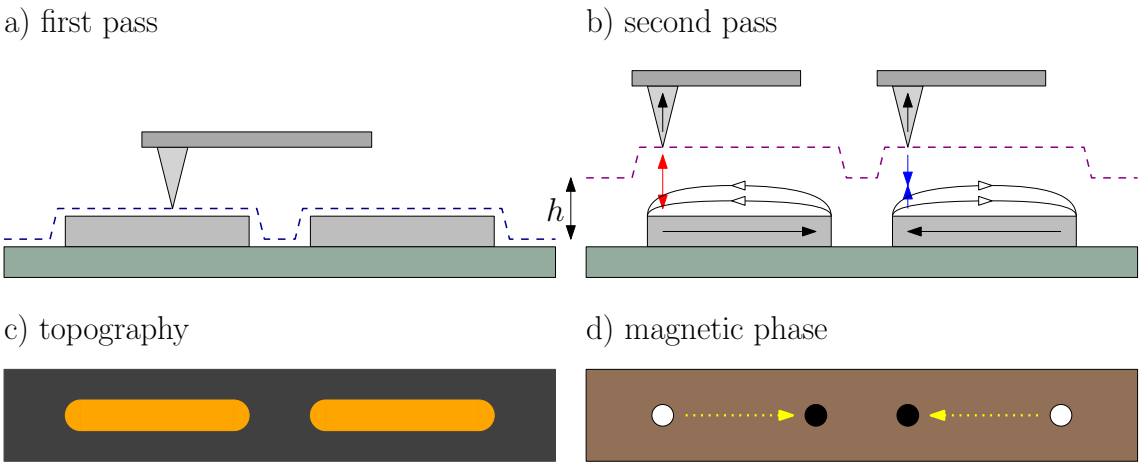

Fig. 2.9: Illustration of the two-pass magnetic force microscope technique scanning across in-plane oriented single-domain stadium-shaped nanomagnets. a) The sample's topography is acquired during the first pass (a blue dashed line illustrates the tip trajectory). The second pass (b) then measures the phase shift induced by the interaction of the tip with the stray field emerging from the magnets. During the second pass the tip is shadowing the topography profile recorded during the first pass at specified lift height h above the sample surface (shown by magenta dashed line). The spatially resolved image of the topography (c) and magnetic phase shift (d) is acquired by composing several adjacent line scans together. The colour scales of these illustrations mimic the *Gwyddion* and *Sky* colour scales that we use in this work for the topography and magnetic phase, respectively. Both colour scales are available in the *Gwyddion* [96] SPM data analysis software that we use to visualise the AFM/MFM images in this work.

In Fig. 2.9c, we show an illustration of how a perfect topography image of

two stadium-shaped magnets might look like. In reality, scanning artefacts will be present, particularly at the magnet edges. In fact, the topography is only a helpful byproduct of the measurement as we are primarily interested in acquiring the magnetic phase image. Having the topography for all measured lattices is, of course, practical, as we can check that no micro-scale fabrication defects are present, such as missing magnets.

Fig. 2.9d then shows how a perfect magnetic phase image of two oppositely oriented single-domain magnets should look like. The MFM essentially measures the interaction of the magnetic tip with a stray field emerging from the magnets. Provided that the magnetisation is oriented as shown in Fig. 2.9b, the negative phase shift (illustrated by black dots) occurs at the magnet heads. Accordingly, the positive phase shift (illustrated by white dots) occurs at the magnet tails. This allows for the reconstruction of the magnetisation direction for each nanoisland in the imaged array.

Measurement details

The MFM measurements reported in this work were carried out either utilising *NT-MDT Ntegra* microscope at the MFM platform at Institut Néel or utilising *Bruker Dimension Icon* microscope at the AFM platform of Institute of Scientific Instruments of the CAS. In the case of the measurements carried out at the Institut Néel, in-house coated AFM tips were used. The tips were typically coated with a thin film of CoCr alloy deposited by magnetron sputtering. The usual thickness of the CoCr layer was approx. 50 nm. In the case of the measurements carried out at the Institute of the Scientific Instruments, commercial probes with a medium moment MESP-V2 from the device manufacturer were used. Following the optimisation of scanning parameters, suitable magnetic contrast was achieved, enabling the complete resolution of the magnetisation orientation for each magnet within the measured arrays. As this was accomplished routinely for both probe choices and both devices mentioned above, we will not distinguish between the tip/device used for the magnetic images reported in this work.

The main aim of the MFM imaging in the scope of this work is to obtain sufficient magnetic contrast, which allows for unambiguous determination of the magnetisation direction of each magnet forming the array while minimising the scan acquisition time and maximising the tip lifetime. To do so, the typical scanning parameters were set as follows:

- Scan resolution: 512×512 points.
- Scan rate: 0.2 to 0.4 Hz.
- Lift height: 60 to 80 nm.
- Set point: approx. 30 nm.

The scan size was set to fully envelope the measured lattice. The set point was optimised so the tip correctly tracks the measured lattices, and the gain(s) was/were optimised to minimise the amplitude error while ensuring a fast reaction of the feedback loop to the topography variation. The lift height was set to a relatively high value to minimise the possible contact of the tip with the sample during the second pass. By following this methodology, we were typically able to record several dozens of scans before the magnetic coating of the tip was worn out, which led to insufficient contrast of the magnetic images.

For the measurements of conventional square arrays with varied lattice parameter (results reported in Chapter 5), we used the automatic measurement capability of the *Bruker Dimension Icon* microscope. This is done via a *Programmed move* for which the centres of the targeted lattices are specified, and then the microscope runs a sequence of MFM measurements with fixed pre-set parameters for each of them. After the capture is done, the tip is withdrawn from the sample, the position of the motorised stage is changed to the previously specified position (centre of the next lattice to be measured), the tip is landed, and the next scan is conducted. Using the *Programmed move* allowed us to acquire a considerable amount of measurements in a time-effective manner.

Measurement results

Here, we show typical AFM/MFM images acquired for artificial arrays considered in this work. We also discuss the challenges of obtaining MFM contrast that allows for a clear evaluation of the arrested magnetic configuration. Fig. 2.10 shows examples of AFM and MFM scans obtained for a conventional square lattice of nanomagnets investigated in this work. As the lattice spacing is relatively dense (the magnet-to-magnet distance at the vertex site is only 140 nm), the contrast of individual "poles" at the vertex site slightly diffuse together, particularly for the type II and type III vertices. However, the contrast is sufficient to allow for unambiguous determination of the magnetisation orientation for each magnet (see the detail provided in Fig. 2.10b).

In Fig. 2.11 we show the AFM and MFM images of another conventional square lattice with the same size of the magnets as in Fig. 2.10, only difference being significantly larger lattice parameter (the magnet-to-magnet distance at the vertex site is 500 nm). Due to the bigger separation between the magnets, the MFM contrast is much easier to interpret, as the "poles" of the four magnets meeting at the vertex site are nicely separated (see the detail in Fig. 2.11b). In fact, the clarity of the MFM contrast is so good that it allowed us to use a relatively simple image processing technique to automate the evaluation of the coarsely packed lattices. The details about this automated evaluation method will be provided later.

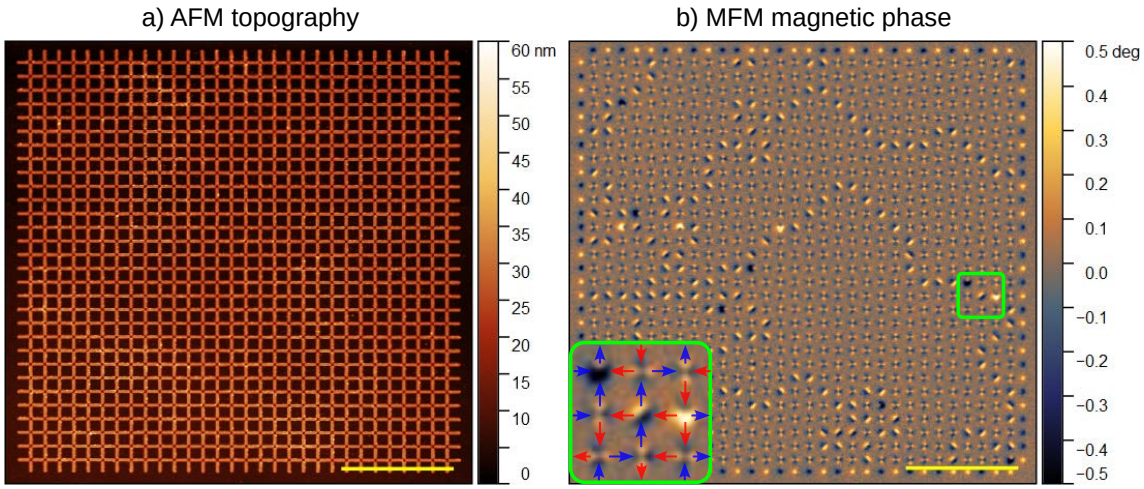

Fig. 2.10: Example of AFM (a) and MFM (b) image of a conventional square array of nanomagnets investigated in this work. The nominal size of the magnets is $500 \times 100 \times 25$ nm^3, and the lattice spacing is relatively dense (magnet-to-magnet distance at vertex site is 140 nm). In (b), a detail of 3×3 vertices shows the evaluation of the magnet's magnetisation (spins are drawn from white to black "pole" for each magnet). We use the convention to draw spins pointing in two principal directions of the lattice in blue (red) colour for positive (negative) direction, respectively. This convention is maintained throughout this work. The scale bar represents 5 µm in both images.

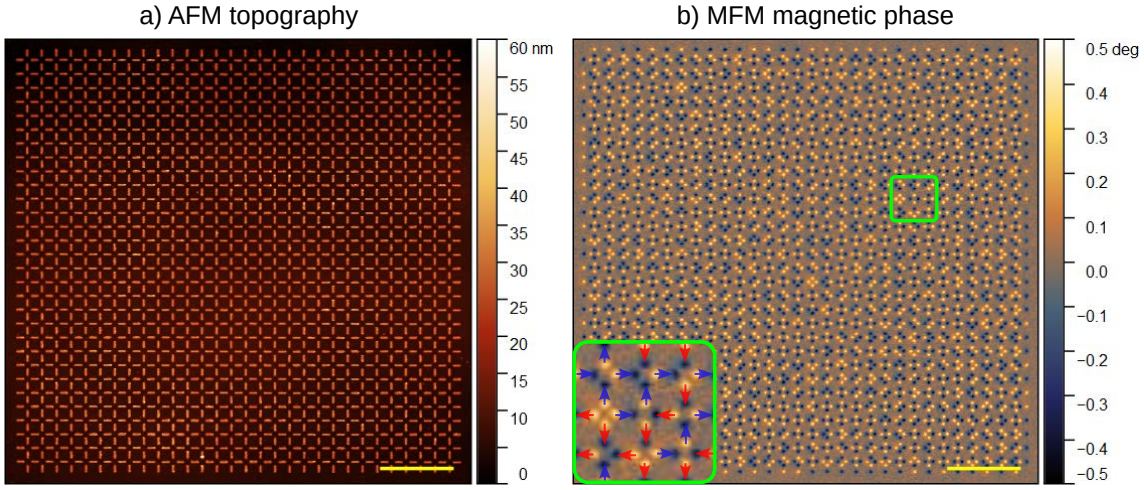

Fig. 2.11: Example of AFM (a) and MFM (b) image of a conventional square array of nanomagnets investigated in this work. The nominal size of the magnets is $500 \times 100 \times 25$ nm^3, and the lattice spacing is relatively coarse (magnet-to-magnet distance at vertex site is 500 nm). In (b), a detail of 3×3 vertices shows the evaluation of the magnet's magnetisation (spins are drawn from white to black "pole" for each magnet). The colour code for the spins is the same as in Fig. 2.10b. The scale bar represents 5 µm in both images.

In the case of the square lattice with elevated sublattice, both the measurement and the MFM contrast interpretation proved to be much more challenging than when all of the magnets lie directly on top of the surface. An example of measurement of such lattice is provided in Fig. 2.12. The height offset for the vertical magnets leads to much less clear contrast at the vertex sites, and the signal from the magnets lying on top of the substrate is slightly screened by the elevated ones (see Fig. 2.12b).

Also, there are sometimes edge artefacts that lead to parasitic signals (sometimes the tip touches the edge of the elevated magnets, which leads to a very strong negative phase shift at the considered pixel). What proved to be a handy trick was to average the forward and backward MFM phase signals. As the parasitic edge signal was typically present at the leading edge of the magnets, averaging together the two oppositely scanned passes helped to filter out the parasitic contrast. We note that Fig. 2.12b shows the backward MFM phase signal only, so the interpretation of the magnetisation direction of each magnet is challenging. However, the different vertex types have different overall intensities and distinct characteristic shapes. Thus, by careful evaluation, which also considers the neighbouring vertices, the contrast at each vertex site can be evaluated.

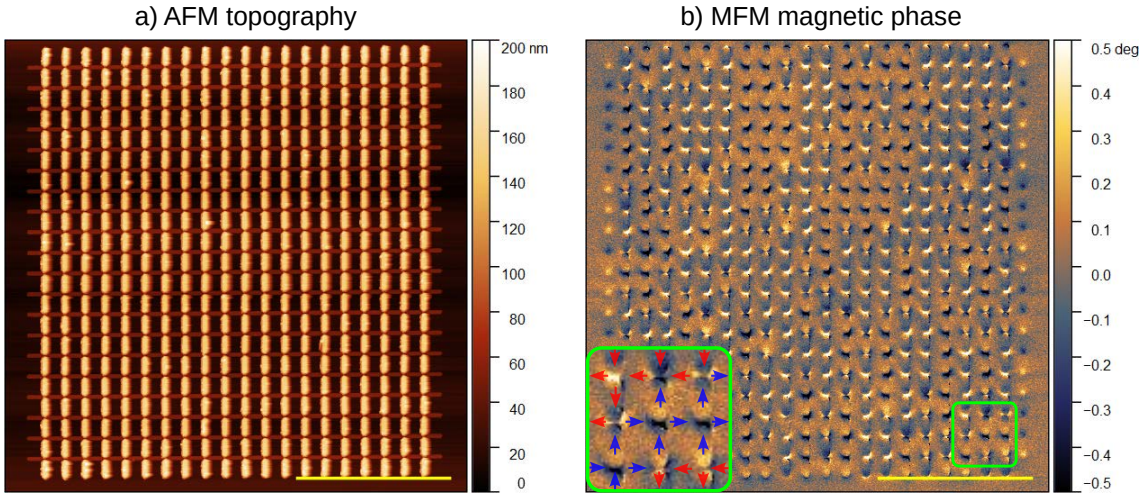

Fig. 2.12: Example of AFM (a) and MFM (b) image of the square lattice with elevated sublattice. The nominal size of the magnets is $500 \times 100 \times 30$ nm^3, the lattice spacing is relatively dense (magnet-to-magnet distance at vertex site is only 150 nm), and the nominal value of the height offset is $h = 100$ nm. In (b), a detail of 3×3 vertices shows the evaluation of the magnet's magnetisation (spins are drawn from white to black "pole" for each magnet). The colour code for the spins is the same as in Fig. 2.10b. The scale bar represents 5 µm in both images.

2.4.2 Data evaluation

The primary goal of the MFM data evaluation in this work is to extract qualitative information regarding the magnetisation orientation of each nanomagnet in the imaged array and to generate a numerical matrix suitable for visualisation and analysis. Essentially, the visual information captured by the MFM needs to be converted into an array of numerical values in a manner that is convenient for further processing.

The first step of the data evaluation is to obtain a levelled and corrected magnetic phase image from the raw data produced by the microscope. For this step, we relied on free open-source SPM data analysis software *Gwyddion* [96]. Typically, we levelled the scanned images using the mean plane subtraction method, aligned the scan rows using the median method, adjusted the range of the data, such as the mean value corresponding to zero, and optimised the scale range to improve the image contrast. We also corrected the data to "unrotate" the image and applied scanner drift or distortion compensation when necessary. We also used the option to remove the polynomial background to further improve the contrast for the evaluation. During this operation, we always verified that the subtraction of the polynomial background did not induce any errors affecting the targeted contrast emerging from the individual nanomagnets. Finally, the image obtained with the above-described pre-treatment was saved and used as an input for the evaluation script(s).

For the magnetic phase images with contrast that is challenging to interpret (conventional square lattices with dense lattice spacing and square lattices with elevated sublattice), the evaluation was done manually with the help of *MATLAB* script developed by the thesis author during his master studies. The main principle of the code operation is that the magnetic phase image of the considered lattice is sliced into individual images that include the magnetic contrast of individual vertex sites. The script then cycles through all the vertex sites of the lattice, and the user classifies the vertex configuration. As the user also evaluates the contrast at the lattice borders, each spin is essentially evaluated twice, which is used to verify the integrity of the spin configuration. If contradictory information arises from the two vertices to which each spin belongs, the user is prompted to provide a correction. The details about the *MATLAB* evaluation code implementation and execution are provided in [97].

The evaluation script produces a numerical array specifying the direction of each spin, with the output format tailored to comply with the input requirements of a visualisation and analysis toolkit developed by Yann Perrin during his doctoral studies [87]. The scripts of the *Perrin toolkit* are then subsequently run using a batch file that is automatically executed at the end of each evaluation script execution. This

produces a wide range of outputs that we use to describe and analyse the captured configurations, such as vertex population statistics, vertex and spin maps or magnetic structure factor intensity plots.

For the magnetic phase images with "easy-to-read" contrast (mostly conventional square lattices with a coarser lattice spacing), a new automatic *MATLAB* evaluation script was developed in this work. The operating principle of the code is essentially the same. However, the evaluation of the contrast at individual vertex sites and lattice edges is done automatically employing a relatively simple median threshold method to classify each individual "pole" (see Fig. 2.13). Essentially, the code determines whether the "single-pole" region (see the subset of Fig. 2.13b) is significantly more white/black with respect to the global mean value of the image pixels. If the threshold criteria are not met or contradicting information about the spin direction between the two neighbouring vertices is obtained, the user is prompted to evaluate the direction of the considered spin.

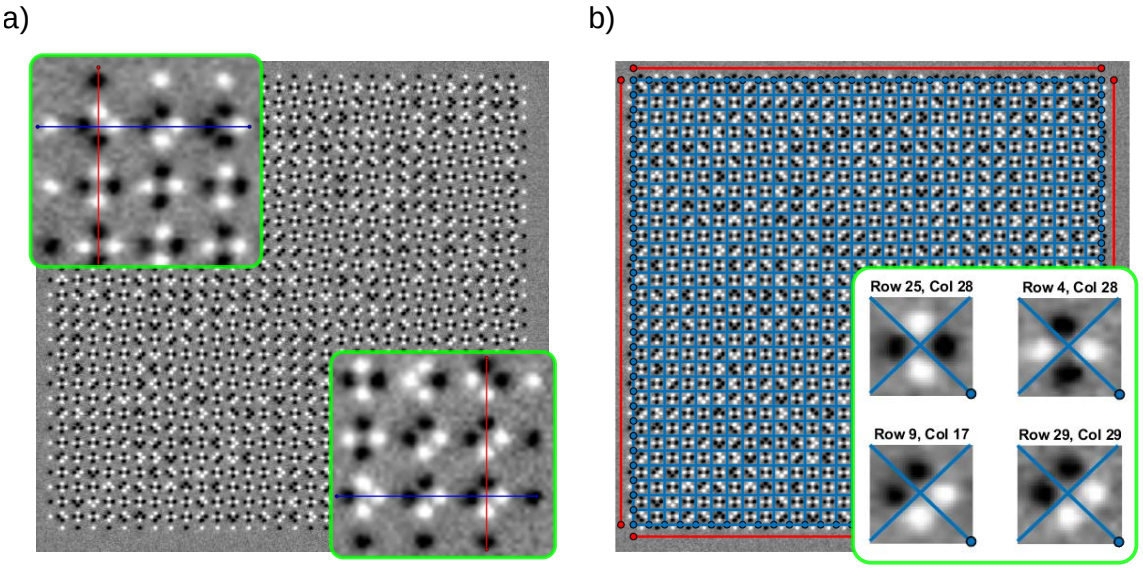

Fig. 2.13: Operation of the *MATLAB* auto evaluation code. a) The user specifies the position of the top-left and bottom-right vertex sites. This information is used to generate slicing lines, as shown in (b). b) For each identified vertex site, the image is dissected into four sectors in which the individual "poles" are located (shown in the subset). Then "polarity" (black/white) of each "pole" is classified using a median threshold method.

After the evaluation is completed, the code again yields a spin matrix formatted accordingly to meet input requirements of the *Perrin toolkit*. Upon the toolkit execution, the same outputs as for the manual option are acquired.

2.4.3 Statistical analysis of the captured spin configurations

In the previous pages, we described how the arrested magnetic configurations of artificial square arrays of nanomagnets can be measured and evaluated to obtain the complete spin configuration (in the form of a spin matrix). The question then arises regarding how the extracted spin configurations can be analysed. Below, we give an overview of different statistical metrics that can be calculated from the extracted spin matrices.

Residual magnetisation

One of the first proposed methods to analyse the captured configurations is to calculate total residual magnetisation as:

$$m_x = (N_x - N_{-x})/(N_x + N_{-x}), \tag{2.2}$$

$$m_y = (N_y - N_{-y})/(N_y + N_{-y}), \tag{2.3}$$

$$m_{\mathrm{tot}} = \sqrt{m_x^2 + m_y^2}/\sqrt{2}, \tag{2.4}$$

where N_x (N_{-x}) is the number of horizontal spins pointing right (left), N_y (N_{-y}) is the number of vertical spins pointing up (down), m_x (m_y) is a magnetisation in x (y) direction and m_{tot} is a total residual magnetisation of the considered array. Under this definition, $m_{\mathrm{tot}} = 1$ would indicate fully magnetised configuration (i.e. perfect ferromagnetic ordering) and $m_{\mathrm{tot}} = 0$ would indicate perfect antiferromagnetic ordering. While this metric has its merit and was used in previous works to measure the efficiency of different field demagnetisation protocols [54, 55], it is somewhat coarse, thus we have not employed it in this work.

Vertex populations

Another commonly implemented method is to analyse the captured configurations based on the density of different vertex types [12, 26, 30, 31, 56, 57]. In the case of a square lattice, there are 16 possible configurations per vertex, which can be divided into four topological types (see Fig. 2.14a). One can then count the number of occurrences per vertex type and calculate vertex populations (expressed as a percentage or fraction relative to the total number of vertices in the considered array). Furthermore, as the information about vertex types is spatially resolved during the evaluation, vertex and spin maps can be plotted, which is a helpful tool to analyse the captured configurations visually (see Fig. 2.14b and 2.14c).

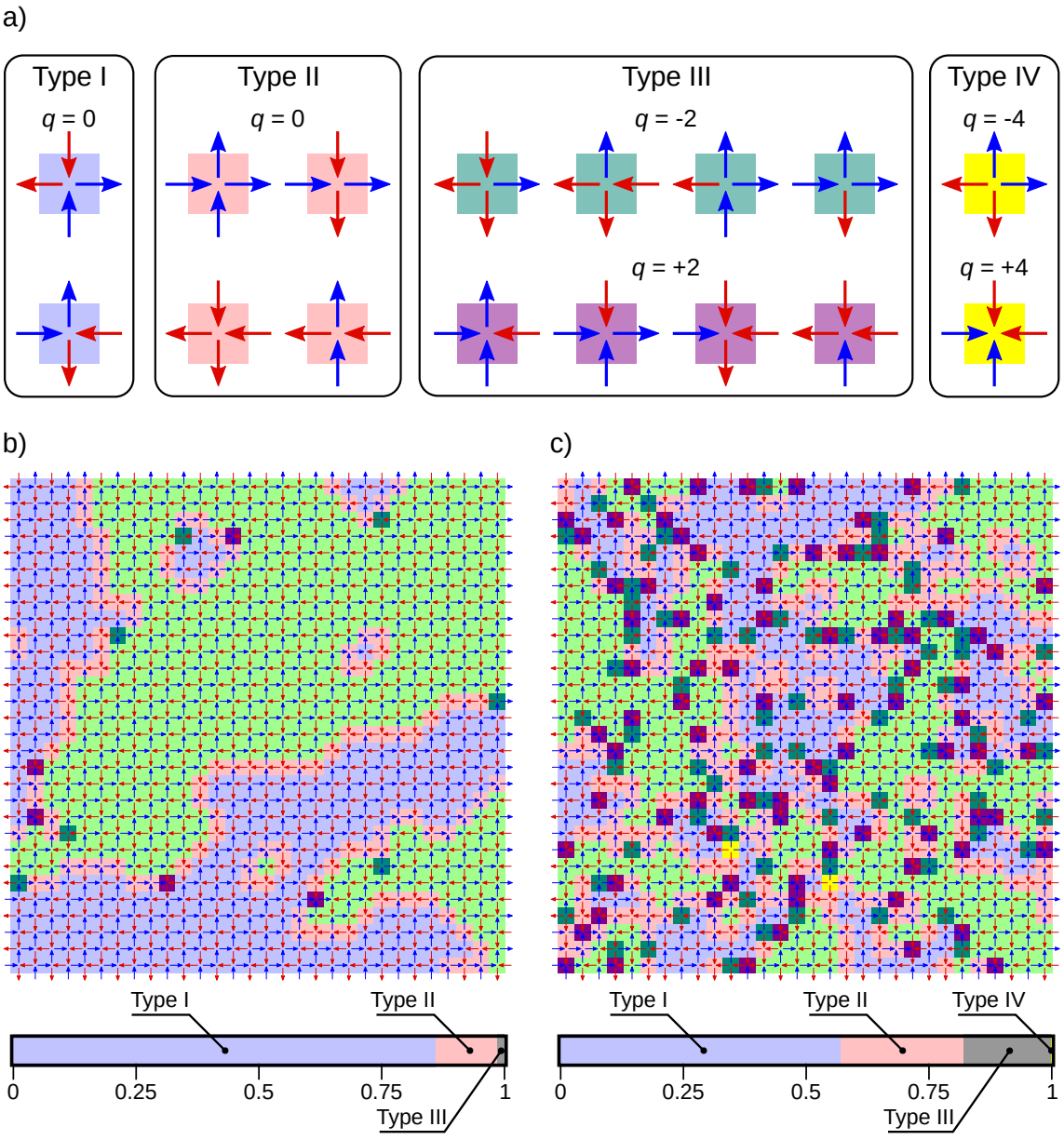

Fig. 2.14: a) The 16 possible vertex configurations per square lattice vertex site, divided into four topological types (type I, II, III and IV). Different vertex types are distinguished by distinct colours, which are used to create vertex maps. For type III vertices, dark green (magenta) colour indicates a negative (positive) charge. The spins pointing in positive (negative) directions are shown as blue (red) arrows. This colour scheme for vertex and spin maps is used throughout the thesis with minor modifications. b), c) Spin and vertex maps obtained by evaluation of the measured magnetic configurations of conventional square lattices, (b) has more dense lattice spacing than (c). Vertex populations are indicated below each map as a horizontal stacked bar chart. Type I vertices are shown as light blue or light green to indicate distinct domains.

The vertex populations are quite indicative when the investigated system has a magnetically ordered ground state. For example, the ground state of a conventional square array of nanomagnets is antiferromagnetically ordered and consists of perfect tiling of type I vertices. In that case, the vertex populations can provide information on how close the ground state ordering is being approached in the experiment. To provide an example, Fig. 2.14b shows the vertex and spin map obtained for a conventional square lattice. The vertex populations for this configuration are 86 %, 12.7 % and 1.3 % for type I, II and III, respectively. Therefore, one can conclude that the ground state configuration is being approached relatively closely (this is also supported by the vertex map, which shows large domains of type I vertices).

However, the vertex populations are a global metric, and they essentially only tell what percentage of the configuration belongs to distinct vertex types. Therefore, this metric does not reflect how the vertices are spatially distributed over the lattice. This can be visually evaluated based on the vertex maps, but the vertex populations themselves are insensitive in this regard. A more sensitive way to analyse the configurations is needed, especially when the configurations are disordered (or close to being disordered).

Pairwise spin correlations and magnetic structure factor

A more sensitive approach how to analyse the level and nature of order or disorder present in the captured configurations is to calculate pairwise spin correlations. There are essentially two options for how to approach the correlations analysis. The first option involves calculating the real space correlations, also known as correlation coefficients, for defined pairs of spins and then averaging these over the entire network. In the case of a square network, the typical approach is to define the correlation function based on the distance and orientation of neighbouring magnets relative to the magnet under consideration. In that way, correlations can be calculated for nearest neighbour pairing, next nearest neighbour pairing, and further neighbour pairings if necessary. The usual approach is to define a correlation C, such that $C = +1$ ($C = -1$) if a pair of spins is aligned in a way that minimises (maximises) their interaction energy. In this way, the mean correlation values between distinct neighbouring pairs can be measured, which helps quantify the level and nature of the ordering present in the system. Examples of the works that employed analysis of the real space correlations can be found in Ref. [12, 55].

The other option is to conduct the correlation analysis in the reciprocal space. This can be done by computing a Fourier transform of the pairwise spin correlations (deduced from the real space configurations), which provides the *magnetic structure factor* (MSF). All of the experimental MSFs presented in this work were calculated

by a script belonging to the *Perrin toolkit*, in which the MSF is calculated in such a way that the resulting intensity plot corresponds to a magnetic diffraction pattern (similar to those obtained in neutron scattering experiments on spin ice materials). More details about the implementation of the MSF calculation can be found in Yann Perrin's PhD thesis (detailed description, in French) [87] or in Ref. [31] (brief description). All numerical MSFs (deduced from Monte Carlo simulations) presented in this work were calculated using scripts provided by Dr. Benjamin Canals. Both the experimental and numerical MSFs were then plotted by a code developed by Dr. Benjamin Canals to ensure the same visual appearance.

An intuitive way how to interpret the MSF intensity plots is that if the magnetic configuration is ordered (i.e., strongly correlated), MSF will exhibit strong Bragg peaks (the nature of ordering corresponds to Bragg peaks at different locations in reciprocal space). Conversely, if the magnetic configuration is entirely random, MSF will be completely flat. There is also an intermediary regime in which the magnetic configuration is disordered but correlated. In this case, the MSF will show a low-intensity diffused but structured pattern. These three cases are shown in Fig. 2.15.

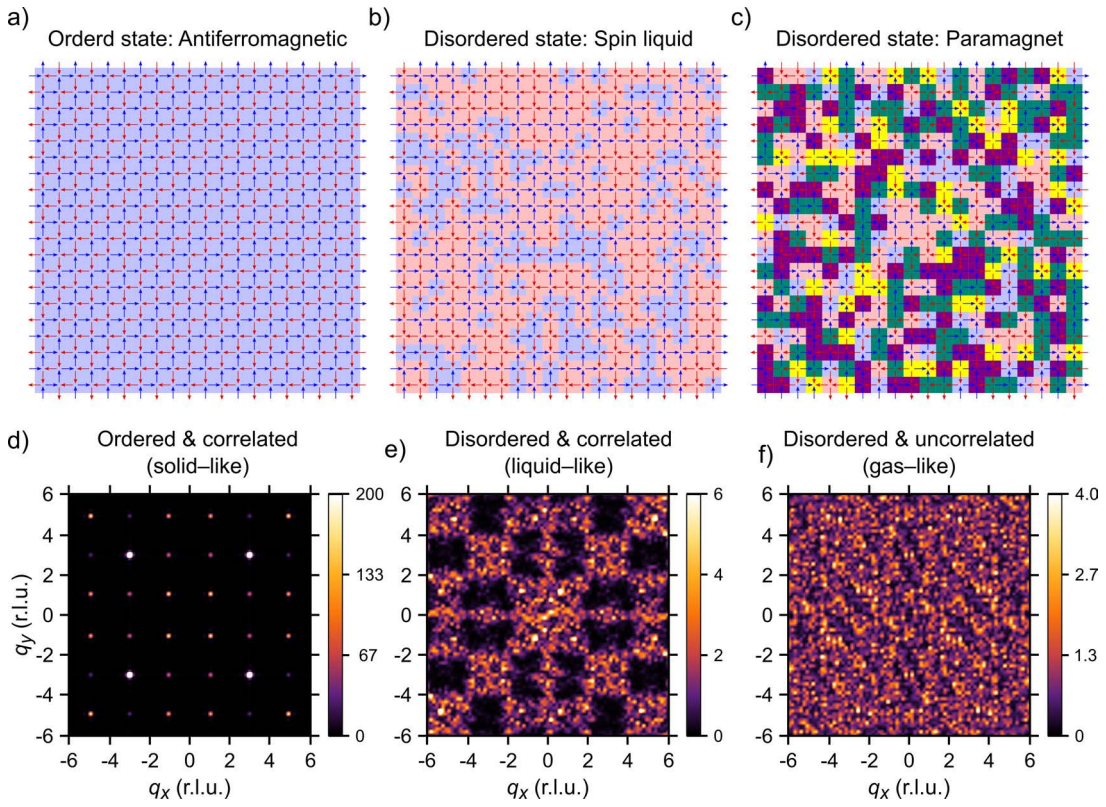

Fig. 2.15: a-c) Examples of three different magnetic configurations for a square spin system. d-f) Associated magnetic structure factors. All MSFs are computed for 81×81 points covering the area of $\pm 6 \times \pm 6$ $(\pi/a)^2$ in reciprocal space. The intensity scale bar is provided right next to each plot.

We note that the three magnetic configurations presented in Fig. 2.15a–2.15c were arbitrarily defined (i.e., they are not the experimental results). Fig. 2.15a shows an antiferromagnetically ordered state consisting of the perfect tiling of type I vertices. As this state is perfectly ordered, associated MSF (shown in Fig. 2.15d) shows strong Bragg peaks. Fig. 2.15b shows a spin liquid (a vertex paramagnet of type I and II vertices). As this state is disordered but correlated, the associated MSF (shown in Fig. 2.15e) shows a diffused but structured pattern characteristic of a spin liquid state on a square lattice [66]. Fig. 2.15c then shows a random arrangement of spins on a square lattice (vertex paramagnet of type I, II, III and IV vertices). As this state is disordered and completely uncorrelated, the associated MSF (shown in Fig. 2.15f) shows a fully diffused background. Utilising an analogy with the three conventional states of matter, the three magnetic configurations presented in Fig. 2.15a–2.15c can be described as solid–like, liquid–like and gas–like (from left to right).

The Fig. 2.15 shows three very different examples that are easy to distinguish (and one might argue that the MSF analysis is unnecessary for that). However, the interpretation of the obtained MSFs can be much more nuanced in the experiment. For example, suppose the spin liquid phase is being approached experimentally, and some residual ordering is present. In that case, the MSF will exhibit Bragg peaks with slightly higher intensity than the diffused background. The location of the peaks in the reciprocal space is then linked to the nature of the ordering present in the system. This is a strategy that we employ in Chapter 3.

In this work, we primarily use the vertex populations and MSF to analyse the spin configurations extracted from the magnetic images of the investigated lattices. In other words, the input is in the form of a numerical array that specifies the spin configuration. Thus, the same analysis methods can also be applied to configurations obtained by Monte Carlo simulations. One can then compare experimental results obtained by magnetic imaging of artificial spin systems and numerical results obtained by probing the thermodynamic properties of a given spin model(s). This is a strategy that we use in Chapter 5.

2.5 Monte Carlo simulations

The Monte Carlo simulations presented in this work were performed by Dr. Nicolas Rougemaille, utilising custom software solutions developed by Dr. Benjamin Canals, a theoretician from the Condensed matter theory research team at Institut Néel. As the author of the thesis was merely using the outputs of those simulations, we will not provide an in-depth technical description of how those simulations are designed. Instead, we will focus on the simulations' outputs and discuss how these might be utilised to analyse the experimental results. General technical details regarding the implementation of Monte Carlo simulations for artificial spin systems can be found in the appendix of Ioan-Augustin Chioar's doctoral thesis [98].

The great benefit of the Monte Carlo simulations is that they allow for probing of finite thermodynamic properties of the considered spin model. Provided that the model is aligned with the experimentally studied system, the results of the Monte Carlo simulations are useful reference, to which the experimental results can be compared. This is particularly helpful in the case of the field demagnetised artificial arrays, as one essentially obtains only one image of the arrested configuration per demagnetisation procedure.

The comparison with the Monte Carlo simulations can then help to answer the fundamental question of whether the experimentally captured configuration is representative of physics at thermodynamic equilibrium or if an out-of-equilibrium physics is present. Additionally, by comparing the numerically modelled properties with the experimental results, one can assign a fictitious effective temperature to the experimentally captured magnetic configuration. By doing so, one can determine whether the captured microstate is representative of an ordered or disordered phase at thermodynamic equilibrium.

The use cases of the Monte Carlo simulations in the context of artificial spin system research are not limited to providing a reference for experimental results. For example, application of Monte Carlo simulations to probe numerically the low-energy properties and predict the possible ground-state configurations of different models were reported [65, 99, 100].

In this work, we employ Monte Carlo simulations in two separate studies. In Chapter 3, we use Monte Carlo simulations to show that further neighbour couplings must be considered if the experimental results obtained for artificial square ice magnets shall be accurately reproduced. In Chapter 5, we use Monte Carlo simulations to show that effective thermodynamics can be observed in a conventional square spin system, and the effective temperature reached depends on the lattice spacing. The details about how the simulation parameters were set are provided in the aforementioned chapters of the manuscript.

3 FARTHER NEIGHBOUR COUPLINGS IN ARTIFICIAL SQUARE ICE MAGNET

In general, artificial spin systems are composed of single-domain ferromagnetic islands arranged on a given lattice and are coupled together via magnetostatics. Thus, they are essentially dipolar systems and employing short-range models (considering only nearest-neighbour interactions) to describe their physics is an approximation. In the case of artificial kagome systems, both consisting of in-plane (artificial kagome ice) or out-of-plane magnets (kagome Ising antiferromagnet), this approximation captures only some of the physics observed experimentally [16, 101]. Other low-energy physics, such as spin liquid 2 phase [32, 82, 102, 103] or spin-fragmentation [103, 104] can be accounted for only if long-range (dipolar) couplings are considered.

Conversely, the physics of artificial square ice systems seems to be well approximated utilising the short-range model [31, 37]. Even though there is no strong discourse between experimental results and short-range model, the question of whether we can detect signatures of farther neighbour couplings experimentally is still relevant. For example, dipolar interactions are known to lift the extensive degeneracy of the square ice manifold, leading to the ordering of the system at low temperatures [65, 70].

A sample with an artificial square ice magnet was fabricated to probe whether the signatures of farther neighbour couplings can be detected experimentally. In order to recover the ice regime experimentally, we resorted to a previously studied square spin system, the z-shifted square lattice [31, 87]. The sample was exposed to a field demagnetization procedure several times, and arrested magnetic configurations were imaged in real space utilizing the magnetic force microscopy technique. The experimental magnetic structure factor (MSF) averaged over the different experiments was computed based on spin configurations extracted from the magnetic imaging and compared to a numerical one (deduced from the Monte Carlo simulations). In accordance with previous works [31, 37], the experimental magnetic structure factor resembles the one corresponding to the low-energy manifold of the square ice model. However, careful inspection of intensity profiles in peculiar wave-vector directions of the average MSF reveals distinct features that differ from the numerically deduced MSF. In the following pages, we will discuss the origins of those features and how they can be recovered if long-range magnetostatic interactions extending beyond the nearest neighbour are included in the theoretical model.

3.1 Designing the system

Artificial square ice magnets were patterned by two-step electron beam lithography (employing the lift-of process). The first step was dedicated to fabricating the non-magnetic bases (Ti/Au), which create the desired height offset for one sublattice of the square array. The nominal value of the height offset is set to $h^{exp} = 100$ nm, for which the liquid phase was already observed in a field demagnetized system [31]. Subsequently, a second lithography step was employed to fabricate simultaneously the nanomagnets on top of the bases and also directly on the substrate surface, which ensures the fidelity of the pattern on the lattice level.

One array then consists of 840 stadium-shaped nanomagnets (NiFe) with nominal dimensions of $500 \times 100 \times 30$ nm^3 for the length, width and thickness, respectively. The 30-nm-thick NiFe layer is capped with 3-nm-thick Al film to limit oxidation of the magnetic material. The nominal magnet-to-magnet distance at the vertex is set to 150 nm, resulting in a lattice parameter of $a = 650$ nm. SEM image of the entire lattice (consisting of 20×20 vertices) and tilted image showing the realisation of the vertical offset within our artificial system are provided in 3.1.

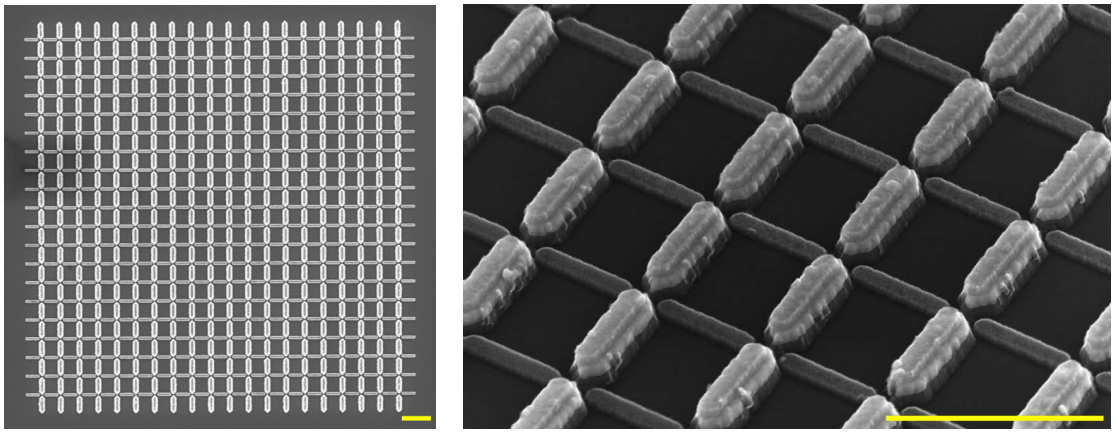

(a) Full lattice (b) Detail, tilted

Fig. 3.1: SEM images of an artificial square ice system in which one sublattice is elevated by height offset h. a) full lattice of 840 nanomagnets (all vertical magnets have elevated bases) and tilted detail (b). In (b), one can clearly see the Ti/Au beds supporting one-half of the magnets. Yellow bar represents 1 µm in both images.

The choice of the geometrical parameters mentioned above, together with the choice of the magnetic material, has several implications necessary for realising the artificial square ice system. The first consequence is that every magnet in our grids is effectively single-domain (i.e. magnetisation texture is close to uniform, and no magnetic wall or vortex is present within a single magnet). Therefore, their moments can be considered as Ising-like spins. Secondly, the blocking temperature is

several orders above the room temperature due to the magnet volume, rendering the spontaneous magnet reversal practically impossible. In other words, the magnetic configuration of our lattice is stable at ambient temperature and can be modified only by applying an external magnetic field. Lastly, all these parameters together are a collective recipe to experimentally recover the spin liquid phase. If only one is changed, one might obtain an ordered configuration instead. For example, even if the height offset is kept at $h^{exp} = 100$ nm and only the lattice parameter is reduced by 50 nm, the resulting configuration will be approaching ferromagnetic order instead. Thus, we chose the geometrical parameters of our lattices to be the same as in the previous work [31], which succeeded in observing the liquid phase.

3.2 Experimental results

The artificial magnets were brought to their low-energy magnetic configurations through field demagnetization protocol, which was used four times in total, each time followed by magnetic imaging of the selected lattices. Three out of four times, we have employed a 72-hour-long protocol. Once, a 168-hour-long procedure was used. We note that we have not detected a significant difference in the arrested configurations obtained with the longer protocol. The magnetic image of one of the demagnetized configurations is shown in Fig. 3.2a. A careful classification of the magnetic contrast at each vertex site (see legend above Fig. 3.2a) yields a determination of the global spin configuration (shown in Fig. 3.2b), provided there are no structural or imaging defects present. MSF is then computed from the extracted spin configuration (see Fig. 3.2c).

Consistent with the previous work [31], the experimental MSF exhibits distinct features of the low-energy manifold of the square ice model: the intensity pattern is diffuse but structured and displays emergent pinch points for specific wave vectors in the reciprocal space [31, 37]. We note that in our experiment, we systematically recover (over four demagnetizations and two layout-wise identical lattices) spin configuration and associated MSF consistent with the characteristics of the spin liquid state. This is also evidenced by the experimental vertex populations (approx. 29 %, 62 % and 9 % for the Type I, II and III vertices, respectively), which are approaching the ratio of 1:2 for Type I and II vertices expected for the ground-state manifold of the square ice model. The presence of a considerable fraction of Type III vertices, which is also in line with previous studies [31, 37], indicates that the captured spin configurations are not in the ground-state manifold. In other words, the energy of the system was minimized substantially, but not entirely.

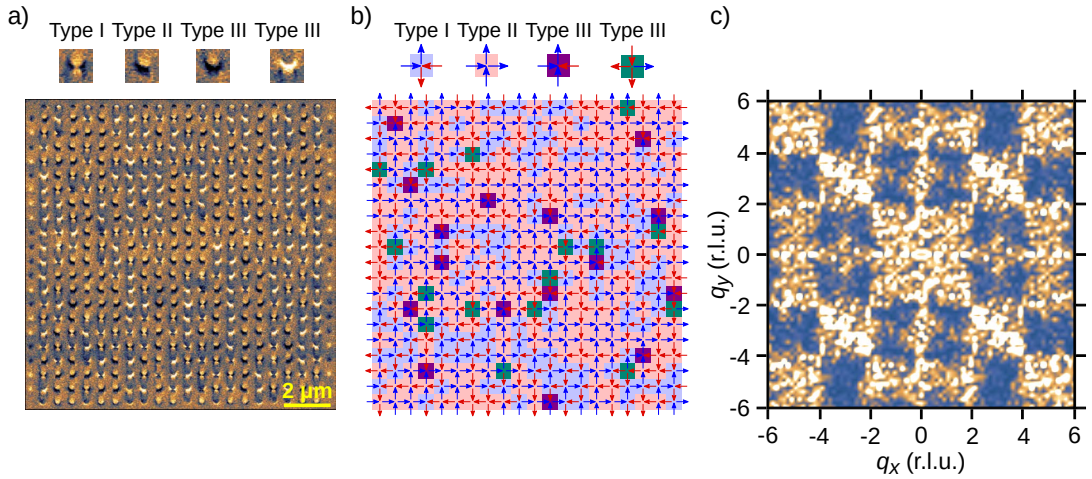

Fig. 3.2: a) Magnetic image of a square lattice with a height offset $h^{\text{exp}} = 100$ nm. A legend with examples of four distinct vertex types' contrasts is provided above the image. b) Spin configuration extracted from (a) with colour code highlighting the vertex type (see the legend above the map). The arrows indicate the direction of the magnetization within each nanomagnet. d) The magnetic structure factor computed from (b). This magnetic structure factor strongly resembles that of the square ice. Adapted from [30].

3.2.1 Comparison with the (short-range) square ice model

We have established that our experiment reproducibly recovers spin liquid configurations approaching the ice regime. Naturally, the next step is to compare the results obtained by our artificial lattices with the relevant theoretical model – the square ice model. We calculated the average experimental MSF (see Fig. 3.3a) based on eight individual measurements. The average MSF's intensity plot is smoother and more symmetrical, compared to the individual one reported in Fig. 3.2c, whilst preserving its shape. At first glance, the physics captured in our experiment strongly resembles that of the square ice model (see Fig. 3.3b). Nevertheless, careful inspection of the experimental magnetic structure factor reveals additional features that the square ice model cannot reproduce. Specifically, line scans along the $q_x = 3$ and $q_x = 5$ directions (see red and purple dashed lines in Fig. 3.3a and 3.3b) show features that are not present in the theoretical MSF (see Fig. 3.3c).

At this point, it is worth pointing out that the square ice model is a short-range model, which considers only interactions from the nearest neighbours. Provided that the coupling strengths of the nearest perpendicular and collinear neighbours are tuned to be equal ($J_1 = J_2$), there are six equally strongly bound nearest neighbours in a square lattice (see Fig. 3.3d) and direct analogy with the structure of spin ice materials can be drawn (see Fig. 3.3e). However, as described in the preceding

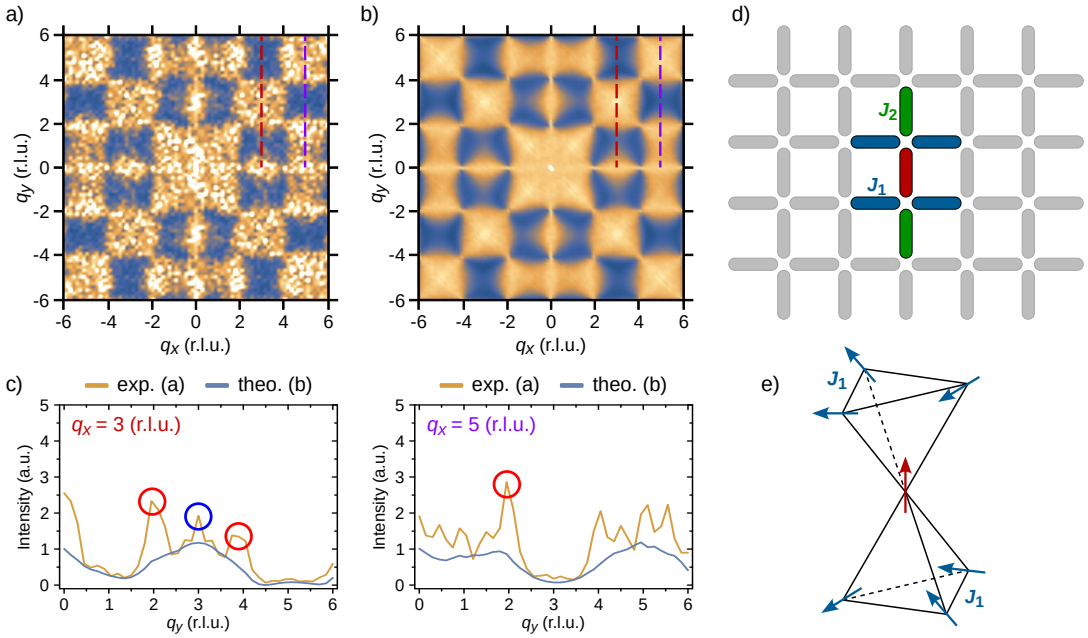

Fig. 3.3: a) Averaged (over four demagnetizations of two lattices) experimental magnetic structure factor. b) Magnetic structure factor corresponding to the low-energy manifold of the square ice model (obtained by numerical simulation). c) Intensity profiles obtained from (a) (in orange) and (b) (in blue) for the two q directions $q_x = 3$ and $q_x = 5$. The scan directions are depicted in (a, b) as red ($q_x = 3$) and purple ($q_x = 5$) dashed lines. Blue and red circles mark additional features observed experimentally. d) Two-dimensional map of coupling strengths in the square spin system. The short-range model includes only J_1 and J_2 couplings. e) Sketch of spin ice material structure showing six equally distanced neighbouring spins. (a-d) adapted from [30].

paragraph, this (short-range) square ice model shows limitations in capturing the physics observed experimentally.

The following questions naturally arise. Is it possible to trace the origin of those additional features present in the experimental magnetic structure factor? Furthermore, can we modify our theoretical model to better account for the experimental results? We will show below that these features emerge due to dipolar interactions, extending beyond nearest neighbours and being at play in our lattices.

3.3 Origin of the additional features

It is worth recalling that numerical studies of square arrays with height offset have shown that dipolar interactions are expected to order the system at low temperatures ultimately [65, 70, 105]. The character of the ground state thus strongly depends on the value of the height offset, and ice regime is an intermediate phase

that is terminated at low T by an ordering transition [65].

When the height offset h is smaller than the critical value h_c, the ground state is two-times degenerate and exhibits an antiferromagnetic ordering in the sense of Rys-F model [106, 107]. Corresponding spin configuration and magnetic structure factor are provided in Fig. 3.4. Suppose the h is bigger than the critical value. In that case, the ground state is also antiferromagnetically ordered (in a manner of Slater-KDP model [108]). It is comprised of antiferromagnetic alternation of adjacent fully polarized lines[1]. Associated spin configuration and magnetic structure factor are provided in Fig. 3.5.

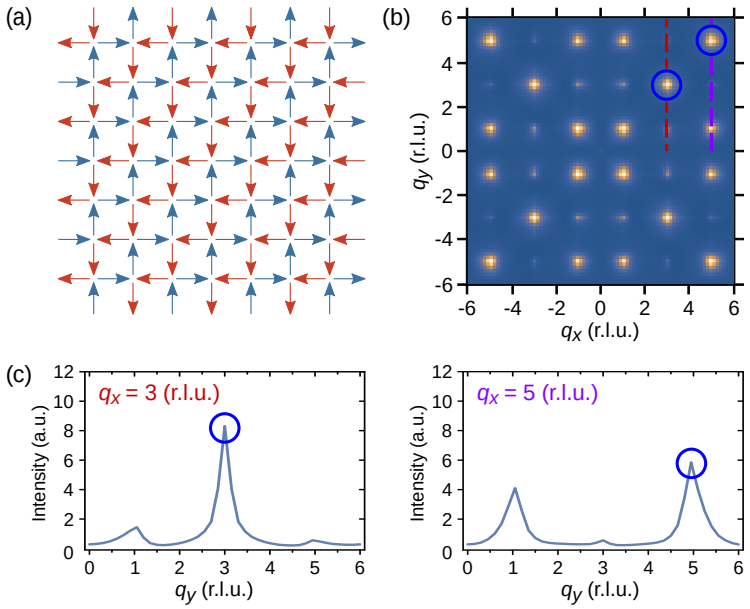

Fig. 3.4: a) Spin configuration and (b) magnetic structure factor representing the ordered ground state of the Rys-F model. c) Intensity profiles are taken from (b) for the $q_x = 3$ and 5 r.l.u. directions (indicated by red and purple dashed lines, respectively). The blue circles highlight specific positions in the reciprocal space for which features corresponding to the experimental MSF are observed. The MSF shown in (b) is obtained at finite temperature to widen the Bragg peaks. Adapted from [30].

Notably, the two ground states exhibit magnetic Bragg peaks in reciprocal space exactly at the positions where the additional features are located in the experimental MSF (see Figs. 3.3c, 3.4c and 3.5c). For example, the Rys-F model or-

[1] This is true if we consider the antiferromagnetic coupling between adjacent lines being present, i.e. $J_3 > 0$. This assumption is, in fact, both reasonable and instructive as we are looking for signatures of coupling strengths that go beyond J_2. For the sake of completeness, without the antiferromagnetic coupling between neighbouring lines, the ground state consists of a random arrangement of ferromagnetic lines.

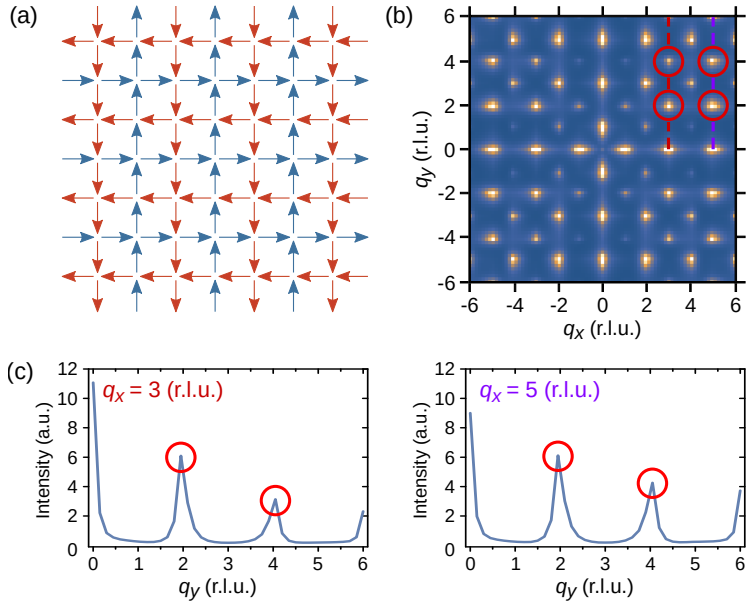

Fig. 3.5: a) Spin configuration and (b) magnetic structure factor representing the ordered ground state of the Slater-KDP model with an antiferromagnetic coupling between adjacent lines. c) Intensity profiles are taken from (b) for the $q_x = 3$ and 5 r.l.u. directions (indicated by red and purple dashed lines, respectively). The red circles highlight specific positions in the reciprocal space for which features corresponding to the experimental MSF are observed. The MSF shown in (b) is obtained at finite temperature to widen the Bragg peaks. Adapted from [30].

dered ground state induces Bragg peak at $(q_x, q_y) = (3, 3)$, which can be directly linked to an experimental feature marked by blue circle in Fig. 3.3. Likewise, the Slater-KDP ordered ground state induces Bragg peaks at positions $(q_x, q_y) = (3, 2)$, $(3, 4)$ and $(5, 2)$. This fits nicely with the experimental features marked by red circles in Fig. 3.5c. Remarkably, also the intensity asymmetries between the pairs of peaks marked in Fig. 3.5c are observed in the experimental MSF (see Fig. 3.3c). The additional experimentally recovered features thus can be linked with the ground-state properties of the *dipolar* square ice [65, 70].

These additional features point towards the presence of additional antiferromagnetic spin-spin correlations on top of the pure square ice manifold. To put it differently, the imaged low-energy magnetic configurations are not an entirely random arrangement of Type I and Type II vertices. Consequently, the Type I vertices (shown as blue squares in Fig. 3.2b) form slightly bigger patches than expected from pure statistics. Similarly, the Type II vertices (shown as red squares in Fig. 3.2b) belonging to lines in the square array are more likely to have opposite adjacent line(s) around them (see alternating red and blue polarized lines on top of red domains in Fig. 3.2b).

3.4 Beyond the nearest-neighbour description

In the previous section, we traced the origins of additional experimental features back to the ground state properties of the dipolar square ice model. One can wonder whether it is possible to recover those features numerically by including interactions beyond the nearest neighbours in the theoretical model. In order to do so, we carry out Monte Carlo simulations with the Ising spin Hamiltonian, in which the magnetostatic coupling strengths are derived from the material properties and actual dimensions of nanomagnets used in the experiment. In this work, we have examined the effects of adding farther neighbour couplings to the spin Hamiltonian up to the tenth-nearest neighbours (see Fig. 3.6).

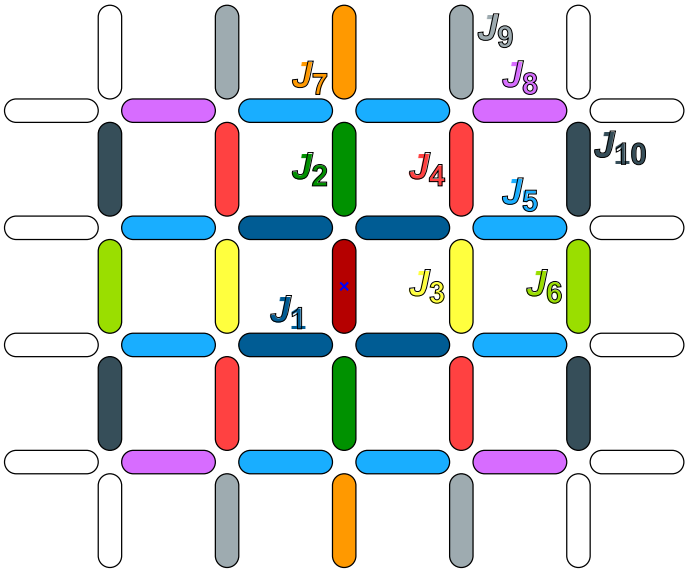

Fig. 3.6: a) Two-dimensional map of a square lattice with colour code highlighting the ten coupling strengths (concerning the central red magnet) considered in this work. Adapted from [30].

3.4.1 Estimating the coupling strengths

Even though single-domain nanomagnets are often considered as Ising pseudo-spins in artificial spin systems, they are micromagnetic objects with magnetisation texture which is not exactly uniform, especially at both ends of single island [86, 109–113]. Therefore, it is necessary to estimate coupling strengths, representative of our real physical system, in a way that accounts for the micromagnetic effects.

For that reason, we computed the micromagnetic energy of pairs of nanomagnets corresponding to the first to tenth nearest neighbours, using the OOMMF code [74]. The numerical simulation follows all the geometrical parameters of the fabricated lattices (lattice parameter: $a = 650$ nm, stadium-shaped magnets of size:

$500 \times 100 \times 30$ nm^3) and material parameters corresponding to NiFe are selected (the spontaneous magnetisation M_S is such that $\mu_0 M_S = 1.0053$ T, the exchange stiffness is set to $A = 10$ pJ m^{-1} and magnetocrystalline anisotropy is neglected). The simulations are run at 0 K. Thus, no thermal fluctuations are present. To minimise finite difference effects, the simulation mesh size is set to $1 \times 1 \times 15$ nm^3. Small cell size in x and y is selected to provide a good approximation of the semicircular ends of the magnets, while coarse mesh size in z helps to reduce the simulation time, as it does not affect the estimate of the coupling strengths substantially. The actual coupling strengths J_i ($i = 1 \ldots 10$) are deduced from the energy difference between antiferromagnetic (head-to-head) and ferromagnetic (head-to-tail) arrangement of the associated pair of magnets (see Fig. 3.7a).

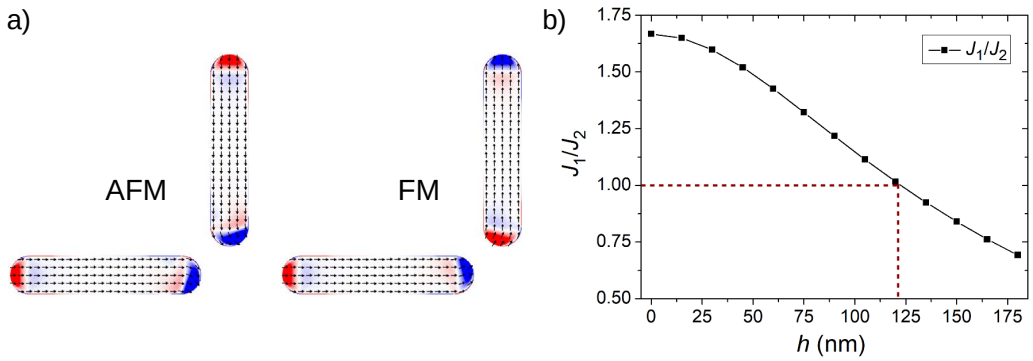

Fig. 3.7: a) Three-dimensional simulated micromagnetic configurations for a pair of orthogonal nanomagnets. In the left pair, the two magnets are coupled antiferromagnetically, while in the right pair, they are coupled ferromagnetically. The red and blue contrast represents the divergence of the magnetization vector, while the arrows indicate the local direction of magnetization. The energy difference between those two configurations corresponds to the J_1 coupling strength. b) Sweeping the height offset h in the micromagnetic simulations allows the calculation of the J_1/J_2 ratio as a function of h. For a critical (numerical) value $h_c^{\text{num}} \approx 120$ nm (indicated by red dashed lines), the square ice condition $J_1/J_2 = 1$ is recovered. The data points represent the results of the simulation. The line is provided only to guide the eye. (b) adapted from [30].

In a square lattice with a height offset as ours, the J_1, J_5 and J_8 coupling strengths are derived from pairs of magnets from the two sublattices (see Fig. 3.6). The two considered magnets are located within the same sublattice for the remaining coupling strengths. Therefore the height offset h matters only when estimating the J_1, J_5 and J_8. We then computed J_1 as a function of the height offset in the range from 0 to 180 nm with steps of 15 nm. In line with previous work [31], the J_1

coupling weakens as the height offset increases and for critical value $h_c^{\text{num}} \approx 120$ nm it is equal to J_2 (which is independent of the height offset). Further increase of the h beyond the critical value then leads to J_1 being weaker than J_2. The evolution of the J_1/J_2 ratio as a function of height offset h is provided in Fig. 3.7b.

Our goal, however, is to estimate the coupling strengths for our experimental system, which has height offset $h^{exp} = 100$ nm. The results of coupling strengths up to tenth nearest neighbours J_i $(i = 1 \dots 10)$ calculated for the experimental value of the height offset are reported in Tab. 3.1.

Tab. 3.1: Estimated micromagnetic coupling strengths J_i for the first ten neighbours $(i = 1 \dots 10)$ of square array with height offset $h^{\text{exp}} = 100$ nm. All values are expressed in arbitrary units (a.u., 1 a.u.$= 1.05 \times 10^{-18}$ J).

i	1	2	3	4	5	6	7	8	9	10
J_i	2.220	1.933	-0.333	0.045	0.104	-0.052	0.132	0.073	0.058	-0.018

3.4.2 Probing the thermodynamic properties

Thanks to the obtained estimates of magnetostatic coupling strengths, we can now probe numerically finite temperature properties of a (spin) square ice model with farther neighbour interactions included. The main hope is to obtain agreement between the theoretical model and the experimental system. We thus carried out Monte Carlo simulations utilizing the Ising spin Hamiltonian, defined as:

$$H = -\sum_{i,j|r_{i,j}<\alpha} J_{i,j}\sigma_i\sigma_j \tag{3.1}$$

where σ_i and σ_j are Ising variables on sites i and j of a square lattice, separated by distance r_{ij}. The parameter α then defines the distance to which coupling strengths are included. In this work, we examined the effects of including the interactions of up to the first ten neighbours ($\alpha_{\text{max}} = \sqrt{5}a$, a is the lattice parameter). The simulations were carried out for $12 \times 12 \times 2$ lattice sites[2] with periodic boundary conditions and utilizing single spin-flip algorithm. The cooling-down procedure starts at $T/J_1 = 100$ and ends as the single spin-flip dynamics freezes. After each temperature step-down, first 10^4 modified Monte Carlo steps (mmcs) are used for reaching the thermal equilibrium and then measurements follow (also computed with 10^4 mmcs). The magnetic structure factor is computed as a function of the effective temperature

[2]To check that the simulation results do not depend on the system size, we run (in selected cases) simulations for $12 \times 12 \times 2$, $20 \times 20 \times 2$ and $30 \times 30 \times 2$ lattice sites and no substantial difference was observed.

(T/J_1), with the same parameters as the experimental one (density of points, area in reciprocal space).

3.5 Results and discussion

Below, we report our findings of comparing Monte Carlo simulations with experimental results by taking the following steps:

1. We first assume that the square ice condition is strictly obeyed ($J_1 = J_2$).
2. We then examine the thermodynamic properties of the square ice model with additional coupling strengths originating from further neighbours step-by-step. In other words, we start with the short-range model (only J_1 and J_2 included), and we run a series of simulations where we add coupling strengths from further neighbours one by one. The last simulation then considers all ten coupling strengths provided in Tab. 3.1.
3. For all these simulations, we extract the intensity profiles along the $q_x = 3$ and $q_y = 5$ r.l.u. directions, for which the distinct experimental features are observed (see Fig. 3.3c).
4. For each simulation (i.e. range of included coupling strengths), we determine the Monte Carlo temperature that provides the best fit against the experimental data.
5. We then detune the ice condition to validate the robustness of our findings.

3.5.1 Ice condition obeyed: $J_1 = J_2$

First, we consider the case where $J_1 = J_2$ and proceed with points (2-4) as laid out above. Even though the magnetostatic micromagnetic simulations yield uneven values for the first two couplings for the experimental value of height offset $h_{\text{exp}} = 100$ nm (see Tab. 3.1), this is reasonable assumption as we are approaching the ice phase in the experiment (as evidenced by vertex populations and experimental MSF). We take $J_1 = J_2 = 2$, and for other coupling strengths, we use the estimates obtained by the micromagnetic simulations (reported in Tab. 3.1) to maintain the proportionality.

The results for the complete set of considered coupling strengths (up to J_{10}) are reported in Fig. 3.8. Curves extracted from the experimental MSF are shown in orange, while the theoretical ones are shown in blue. The left and right columns correspond to $q_x = 3$ and $q_x = 5$ r.l.u. directions, respectively. For each subplot (Fig. 3.8a to 3.8h), the range of coupling strengths included in the spin Hamiltonian is provided on the left, together with the Monte Carlo temperature which provides the best fit of the experimental data.

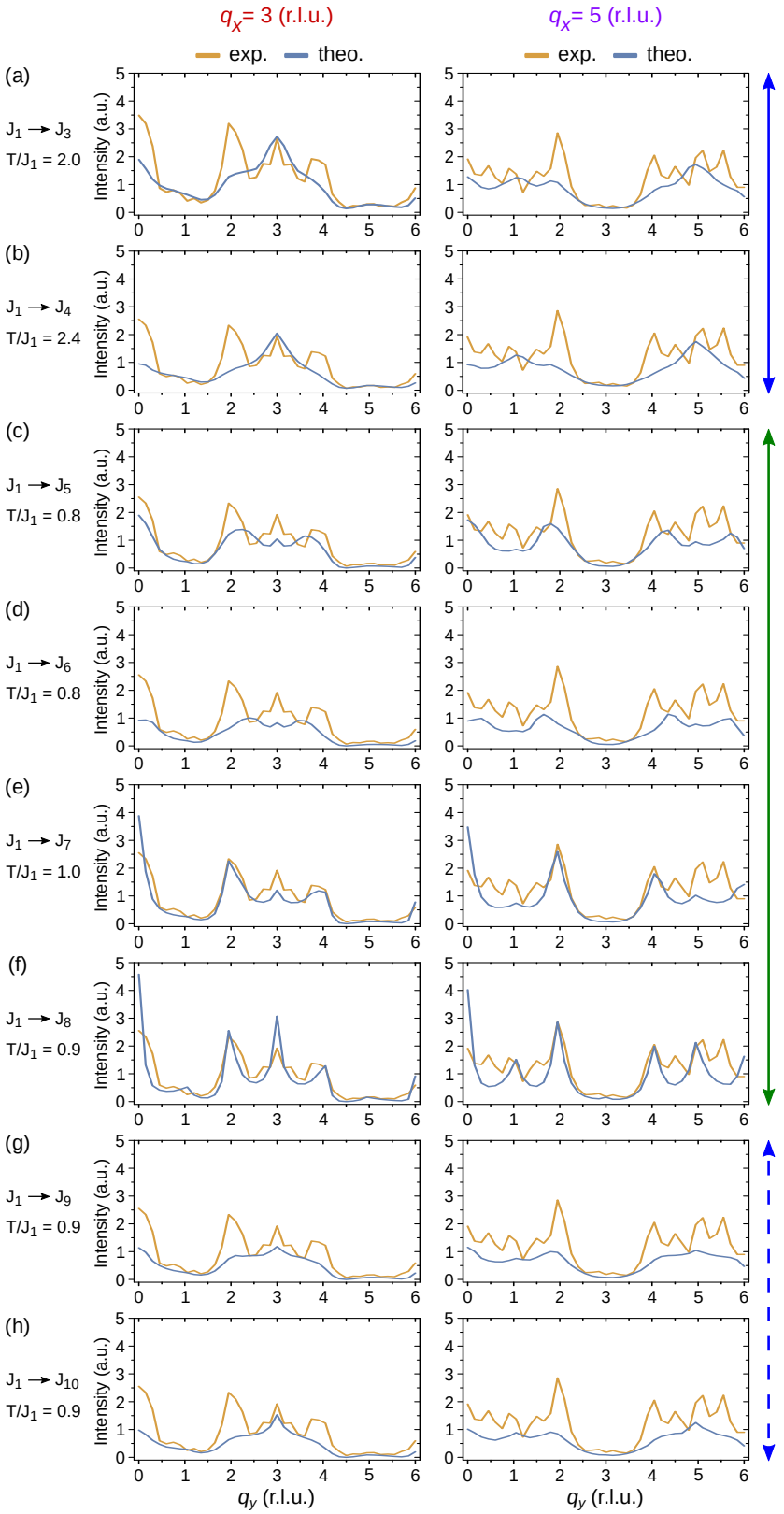

Fig. 3.8: Comparison of intensity line scans (along $q_x = 3$ and $q_x = 5$ r.l.u. directions) of the experimental (orange lines) and theoretical (blue) magnetic structure factors. The range of interactions included in the theoretical model and the Monte Carlo temperature, which provides the best fit to the experimental data, are indicated on the left. Adapted from [30].

Essentially, the set of reported simulations can be divided into three groups (indicated by a coloured arrow on the right side in Fig.3.8. In the first subset (solid blue arrow), the main impact of the coupling interactions added to the model (J_3 and J_4 is to amplify antiferromagnetic correlations between spins belonging to the same sublattice. This is evidenced by the strengthening of the peaks located at $(q_x, q_y) = (3, 3)$ and $(5, 5)$, which corresponds to ordering in the sense of Rys-F model (peaks highlighted by blue circles in Fig.3.4c). In the second group (green arrow), coupling strengths from J_5 to J_8 affect both the antiferromagnetic correlations between spins of the same sublattice and the antiferromagnetic correlations between adjacent polarized lines. The latter is evidenced by intensity increase for peaks located at $(q_x, q_y) = (3, 3)$, $(3, 4)$ and $(5, 2)$, $(5, 4)$, which originates from ordering in a sense of Slater-KDP model (peaks highlighted by red circles in Fig.3.5c). Finally, for the last two simulations (blue dashed arrow), which goes up to J_9 and J_{10}, only the antiferromagnetic correlations between spins belonging to the same sublattice are present.

To summarize, the results reported in Fig. 3.8 show that by including interactions that extend beyond nearest-neighbours into the theoretical model, it is possible to reproduce the experimentally observed features. Specifically, when considering interactions up to J_7 (Fig. 3.8e) or J_8 (Fig. 3.8f), the theoretical curve approaches the experimental one (semi)quantitatively. We note that at least some features of the experimental MSF are observed for all considered ranges of included coupling strengths. In other words, the qualitative agreement between the model with farther couplings included seems always better than the short-ranged model.

One might then wonder why the agreement obtained for coupling interactions extending up to J_8 gets lost after including farther coupling strengths (namely J_9 and J_{10}). At this point, it is worth recalling the results of previous theoretical/numerical works on dipolar square systems with height offset [65, 70, 105], which reports that full dipolar treatment of the spin Hamiltonian (i.e. considering all interactions in the system) leads to ordered ground state. The nature of the ground state is critically sensitive to the height offset h value. Therefore, determining the ground state configuration for the case where $h = h_c$ is not an easy task and in Ref. [105], it is stated that it depends on the algorithm that is used for the "cooling-down" in the Monte Carlo simulation.

3.5.2 Ice condition detuned: $J_1 < J_2$

In the text above, we discussed the results under the assumption that the ice condition ($J_1 = J_2$) is strictly obeyed. This is unlikely to be achieved in the experiment, especially if we consider that the nature of the ground state is susceptible to the

height offset h value. It is then natural to wonder whether the conclusions drawn above are robust when the $J_1 = J_2$ condition is detuned.

Obviously, the ice condition can be detuned in two ways, either having $J_1 > J_2$ or $J_1 < J_2$. In the former case, both the detuning condition and the long-range magnetostatic interactions will favour the ordering in the sense of the Rys-F model (see Fig. 3.4). In this case, the agreement between the experimental MSF and the modelled one could only worsen. However, the latter case ($J_1 < J_2$) will amplify the antiferromagnetic correlations between the adjacent polarized lines (see Fig. 3.5). Detuning the ice condition in this way will thus lead to a competition between the correlations originating from the long-range interactions and those amplified by the detuning.

Indeed, when selecting $J_1 = 2$, $J_2 = 2.1$ and $J_3 = -0.333$ we recover semi-quantitative agreement with the experimental data (see Fig. 3.9a). We note that for $J_1 = J_2 = 2$ the agreement was rather poor (as shown in Fig. 3.8a). Similarly, when one more coupling strength is included ($J_4 = 0.045$), it is possible to recover a nice agreement with the experimental data when setting $J_1 = 2$ and $J_2 = 2.2$ (see Fig. 3.9b). The same approach can be extended to include additional coupling strengths from further neighbours.

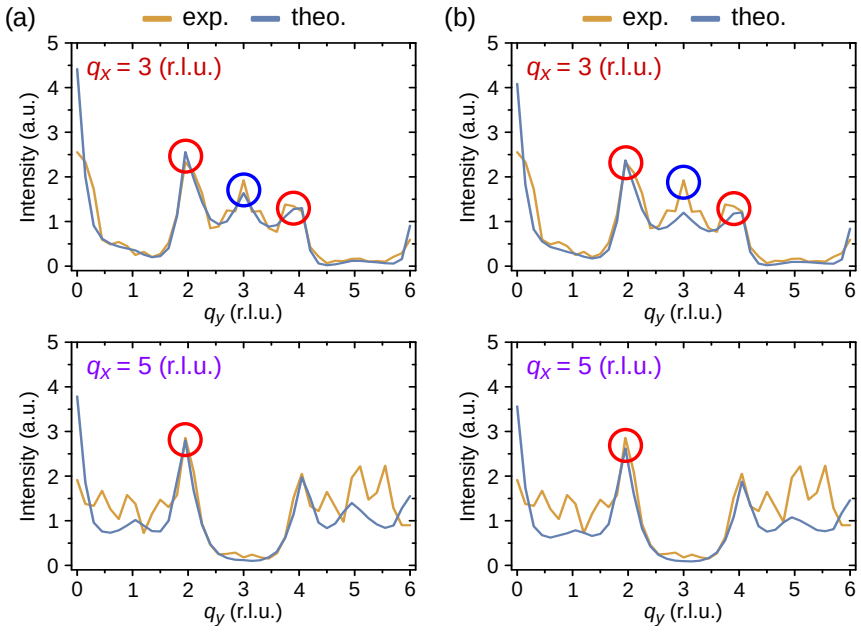

Fig. 3.9: Intensity line scans (along $q_x = 3$ and $q_x = 5$ r.l.u. directions) comparing experimental data and two models with following set of coupling strengths: (a) $J_1 = 2$, $J_2 = 2.1$, $J_3 = -0.333$, and (b) $J_1 = 2$, $J_2 = 2.2$, $J_3 = -0.333$, $J_4 = 0.045$. The Monte Carlo temperature is $T = 1.5\,J_1$ for both simulations. The blue and red circles highlight the experimentally observed features. Adapted from [30].

The origin of the additional features we observe experimentally is, therefore, further validated as being associated with magnetostatic interactions that extend beyond nearest neighbours. These findings are robust, as the argumentation holds whether the ice condition is obeyed or detuned. The next question is whether the detuning of the ice condition such as $J_1 < J_2$ can occur in our experiment. This could be, in principle, justified in two cases:

1. if the experimental height offset would be above the numerical critical value $h_c^{\text{num}} \approx 120$ nm, which is not the case as $h_{\text{exp}} = 100$ nm and
2. if the field demagnetisation procedure would amplify the impact of J_2 coupling strength due to associated kinetic effects. This is likely the case, as the magnetisation during the field demagnetisation procedure (the sample is essentially exposed to a rotating magnetic field) reverses via an avalanche process, favouring the formation of straight lines in the lattice. This is conveniently illustrated by numerical simulations of the field demagnetisation protocol provided in Supplementary Information (namely Videos 1 and 2) of Ref. [31].

3.5.3 Ordering vs dynamical freezing

The final point we want to address is why our artificial magnet does not order, and the obtained MSF strongly resembles the one of the square ice model instead. Looking at the Monte Carlo temperatures that provide the best fit to the experimental data (see Fig. 3.8 or 3.9) reveals that the experimentally measured spin configurations correspond to an effective temperature in the order of J_1. Our field demagnetization protocol is thus unable to fully minimize the system's energy, and we obtain configuration respective of a higher energetic manifold. At this point, it is instructive to recall reported findings of numerical studies of dipolar square systems with height offset [65, 70, 105]. Namely, Ref. [65] predicts that in such a system, the ice regime is an intermediate phase that is terminated at low T by an ordering transition (the ground state is h-dependent). This allows the interpretation of our results. The field demagnetization is unable to reach the ground state configuration, and the intermediate ice regime is captured. However, the emergence of Bragg peaks in our experimental MSF indicates that the ordered configuration is slightly approached. The fact that we cannot reach a very low-energy state in our experiment is consistent with previous works. In general, exploring the ground-state manifold of artificial frustrated magnets experimentally, whether using field or thermal demagnetization, is rather challenging [44] both due to intrinsic (e.g., dynamical freezing [27, 114]) or extrinsic (i.e., quenched disorder) effects.

3.6 Summary

In this study, we focused on further examination of the properties of field-demagnetised artificial square ice magnets. By carefully inspecting the magnetic structure factor derived from measured magnetic configurations, we identified additional features that cannot be accounted for by the short-range square ice model. We then traced down the origins of these distinct features and showed that they are in agreement with the ground-state properties of the dipolar square ice model. To further support our findings, we report how these features can be recovered numerically by including additional coupling strengths that extend beyond the nearest neighbours into the model. We check that our findings are valid not only when the ice condition is strictly obeyed, but also when it is detuned. We thus conclude that considering longer-ranged couplings is necessary to interpret our results accurately.

As a consequence, an artificial system such as ours is expected to undergo an ordering transition at (very) low temperature [65]. However, this ground state is not reached in the experiment, as the field demagnetisation procedure is not able to fully minimise the energy of the system due to the dynamical freezing. On the other hand, the field demagnetisation protocol is sensitive enough not to wash out the signatures of long-range dipolar interactions.

Interestingly, our findings also have implications for the properties of magnetic monopoles.In a pure ice manifold (i.e., square ice with only nearest neighbour interaction), magnetic monopoles are deconfined quasiparticles that are free to move (without energy penalty; the energy cost is associated only with their nucleation) and interact via effective Coulomb interaction that has entropic origin [67]. On the other hand, in a square ice manifold perturbed by long-range interactions, the magnetic monopoles additionally interact via genuine magnetic Coulomb interaction [67, 69]. Additionally, if the long-range interactions are considered, the energy landscape is no longer entirely flat (as for the short-range description), leading to additional binding of the monopole pairs [69]. In other words, the magnetic monopoles we observe in our experiments are not fully deconfined and should behave as weakly bound, as the string tension bounding the pairs of oppositely charged monopoles do not entirely vanish (even within the ice manifold) [70].

4 IS FIELD DEMAGNETIZATION OF ARTIFICIAL SQUARE ICE MAGNET A STOCHASTIC PROCESS?

Bringing artificial magnets into their ground-state or low-energy manifolds remains a major experimental challenge. Being able to lower the system energy sufficiently is a crucial ingredient, as a majority of the exotic and intriguing behaviour emerges only at low effective temperatures. So far, two main approaches have been employed to bring artificial frustrated magnets into their low-energy states. Both approaches are illustrated in Fig. 4.1 and discussed in the following paragraphs.

The first one, field demagnetization protocol, is in detail described in Sec. 2.3 together with how we implement it in our experiments. In this method, the sample is exposed to an external magnetic field, the amplitude of which slowly decays in time. In the case of in-plane artificial magnets, the sample is often rotated to compensate for the multi-axial symmetry of the studied systems. This method has been used in a number of previous studies with minor differences [12, 16, 17, 24, 26, 27, 30, 31, 54, 82, 86, 115], mostly in how the magnetic field amplitude is reduced/stepped down.

The second approach relies on thermal activation of the magnetization dynamics, either by annealing the sample above the Curie temperature of the constituent magnetic material [32, 35, 41, 59, 71, 103, 116, 117] or by approaching the blocking temperature of individual magnets [33, 37, 92, 118]. A special case of the latter approach is a single-shot technique, in which the magnetic configuration develops only in the early stages of the magnetic material deposition in a magnetic field-free environment [21, 39].

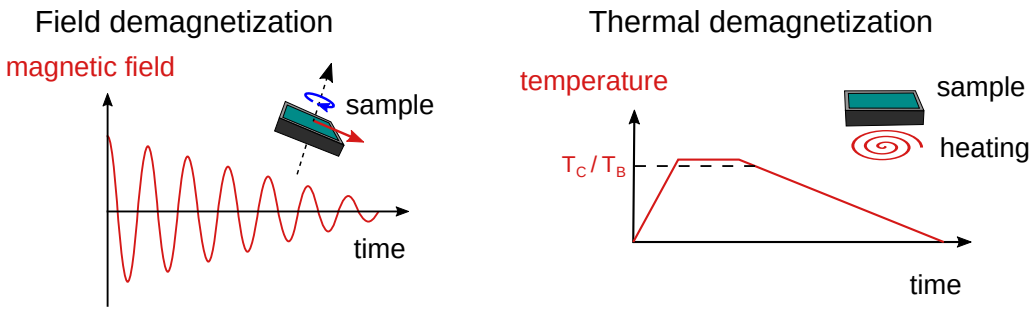

Fig. 4.1: Schematics of field and thermal demagnetization approaches.

The two approaches presented above offer distinct advantages but share the same experimental limitations. In practice, both protocols seem to be similarly efficient in reaching down to low-energy configurations of degenerate artificial systems [44].

For example, in the case of the experimental studies of kagome dipolar spin

ice, both approaches are unable to reach down to very low-energetic configurations, which are characterized by magnetic charge crystallization, and only partial emergence of the charge ordering is observed [32, 35, 71, 82, 103, 117]. This behaviour is not unique for the kagome dipolar spin ice and was also reported for kagome Ising antiferromagnet [32, 99] and Shakti spin system [41, 119]. Even though the experimentally reached effective temperatures remain relatively high, detecting signatures of phenomena associated with lower-energetic states is still possible. Prime example is the spin fragmentation process [104], which was partially observed in dipolar kagome spin ice [103].

Similarly, both field-demagnetised [31] and thermally active [22, 37] artificial magnets were successfully used to capture the physics of the square ice model. Here, as well, the effective temperature of the system remained relatively high, and very low-energy ordering was also not reached. However, its signatures were detected experimentally [30], as we discussed in detail in the previous Chapter (Chapter 3).

To summarise, both field and thermal demagnetisation, at least in systems studied so far, were unable to explore the (very) low energetic configurations[1]. Both approaches are, in fact, limited by the same mechanism, which is the freezing of the single spin-flip dynamics. This intrinsic effect prohibits reaching low-energy manifolds in the systems we are interested in, as they become loop models in their low-temperature regimes [44]. Therefore, the experimentally available single spin flip events are not able to further minimise the system energy at some point, both when using a field or thermal approach.

In the text above, we discussed the effectiveness of both protocols and their shared limitations. There is, however, a fundamental difference between them. In the case of the thermally active arrays, we can intuitively understand that the thermal fluctuations act as a source of stochasticity. On the other hand, one might then wonder whether a field protocol is not a source of determinism, especially when both the blocking temperature and Curie temperature of the constituent material are well above the demagnetisation/measurement temperature. Without any thermal fluctuations at play, one might think that field demagnetising the very same lattice several times will repeatedly yield the same configuration. This is in contrast with thermally active systems, in which one can repeat the same protocol several times and hope to obtain different states after each demagnetisation of the same array.

This has practical implications for how one should approach artificial magnets in the experiment. Usually, such artificial systems have limited size, both for fabrication and measurement reasons. A common approach is then to average several

[1] With the exception of recently reported approaches that reduce the degeneracy at the vertex level and bias the system towards reaching the targeted low-energy configurations [24, 27, 28].

measurements to improve the statistics (for example, see Fig. 3.3) and test the experiment's reproducibility. If one assumes that successive field demagnetisation protocols applied to the same lattice would yield the same configurations, it would be necessary to average different lattices (i.e. *ensemble average)* to capture the physics at stake better. On the other hand, if the field demagnetisation proves to be stochastic, one would obtain a different configuration each time the protocol is applied, and it would be sensible to average over the different demagnetisations (i.e. *time average*).

The main aim of this work is to address the following questions: What will be the result of applying field demagnetization protocol several times to the very same *athermal*[2] artificial square ice magnet? Would we obtain the same arrested magnetic configuration repeatedly, or will we capture essentially a series of uncorrelated configurations that share similar macroscopic properties? Alternatively, can we view a field demagnetization protocol applied to an *athermal* artificial magnet as a stochastic process? If so, what could be the potential origins of stochasticity (or determinism) in such an experiment? This work thus aims to complement previous studies that reported presence [18] or absence [63] of stochasticity in artificial spin systems and consequences of the presence of quenched disorder in such arrays [56, 120, 121].

In order to address the questions specified above, we studied the response of artificial square ice magnets to successive field demagnetisation procedures. After each demagnetisation protocol, the magnetic configuration of lattices of interest was imaged using magnetic force microscopy and the spin configuration of the lattices was extracted from the captured images. We note that the sample was always aligned in the same way for the imaging after each demagnetisation. The spatial distribution of vertices and spins within the same lattice were then compared across the demagnetisations. As the lattices examined in this study belong to the same sample as the ones used in the previous section, we will rely on the sample description provided there (see Sec. 3.1). Nevertheless, we want to emphasise that due to the volume of the nanomagnets, their magnetic moments are stable and do not reverse at ambient temperature unless the field protocol is applied.

We note that the dataset for the lattices with height offset $h_{\mathrm{exp}} = 100$ nm is shared with the previous section. Thus, the findings of this and the previous section can be applied to each other. However, this section will also analyse the results for one lattice with no height offset, which is also present on the sample. This lattice has the same geometrical parameters as the lattices with elevation and was fabricated

[2]In accordance with previously reported studies, we use the term *athermal* to refer to systems that have stable remanent magnetic state (orientation of the nanomagnets does not change as a function of time).

in the same (second) lithography step.

4.1 Experimental results

All of the lattices of interest in this study belong to one sample, so they all share the same field history. In order to experimentally investigate the questions raised above, we demagnetised the sample four times in total. After each application of the demagnetisation protocol, we conducted magnetic imaging employing magnetic force microscopy and extracted the complete spin configuration of each lattice. The resulting captured configurations of one artificial square ice magnet (i.e. square lattice with elevated sublattice, height offset $h_{\mathrm{exp}} = 100$ nm) demagnetised for times are provided in Fig. 4.2a. As usual, we also computed the magnetic structure factor for each captured configuration (see Fig. 4.2b).

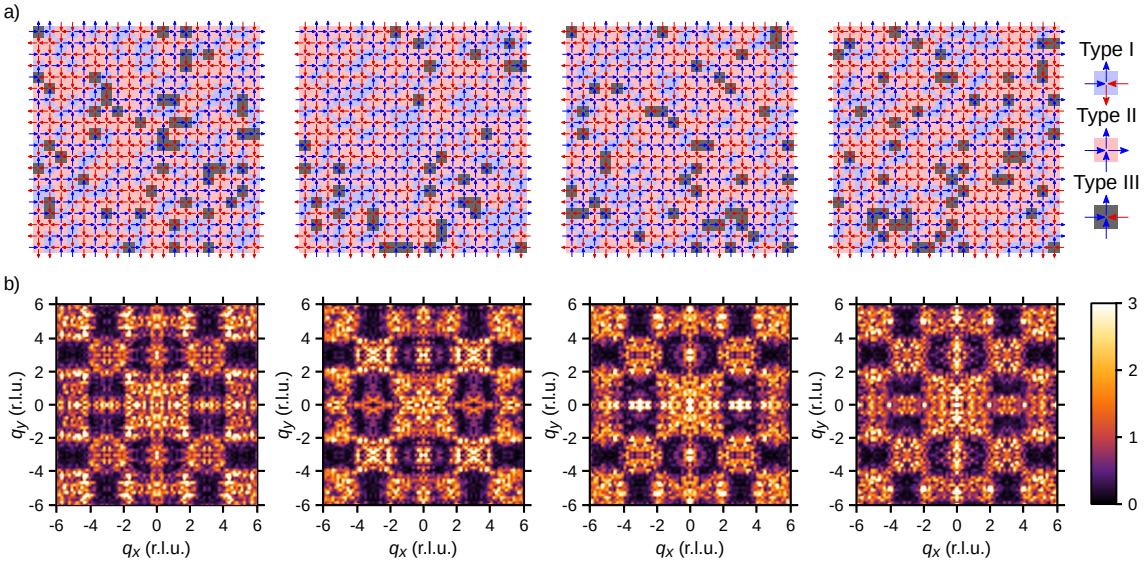

Fig. 4.2: a) Spin and vertex maps showing real space configurations of the same artificial square ice magnet after applying field demagnetisation protocol four times. The vertices are represented by blue, red and grey squares for type I, II and III vertices, respectively (see the legend on the right). The arrows indicate the local spin directions. b) Corresponding magnetic structure factors computed from the spin configurations provided in (a). All four plots have identical intensity (i.e., the scale bar on the right belongs to all four images) and are computed for 81×81 points in reciprocal space.

Several conclusions might be drawn from the above-presented series of measurements: 1) All four configurations are different, and no obvious pattern appears systematically in all of them. 2) Although they are different, they share similar macroscopic properties (e.g. vertex populations). 3) All four captured configurations are liquid-like, as evidenced by their associated magnetic structure factors (see

Fig. 4.2b, where all four plots have characteristic disordered but structured pattern associated with low energy-manifold of the square ice model).

At this point, it is worth pointing out that an artificial square ice magnet is a particularly well-suited system for our study, as the low-energetic state is a disordered phase. Its configuration can be described as a vertex paramagnet of type I and type II vertices, assuming no excitations (type III) are present. Therefore, any fixed repeating pattern should be easily identified in a series of measured configurations belonging to the same lattice. Similarly to previous work [31], we observe approx. 9 % of type III vertices (emergent magnetic monopoles) present in our lattices. Their presence reflects the fact that the field demagnetization protocol is not able to minimize the system energy fully. As mentioned above, no repeating pattern (e.g. patches of fixed vertices) appears when comparing the four liquid-like configurations. Similarly, the positions of magnetic monopoles are not fixed and vary across the four demagnetizations.

4.1.1 Exploring the level of stochasticity/determinism

We have established above that no obvious pattern is repeating in the four captured magnetic configurations. However, by only looking at the four spin/vertex maps, it is hard to resolve whether the arrested configurations are genuinely independent of each other or if there is some level of correlation between them. In order to be more quantitative and to also ease the visual evaluation, we have generated vertex density maps (see Fig. 4.3), in which each vertex site, represented by a coloured square, is shaded according to a frequency of occurrence of a given vertex type.

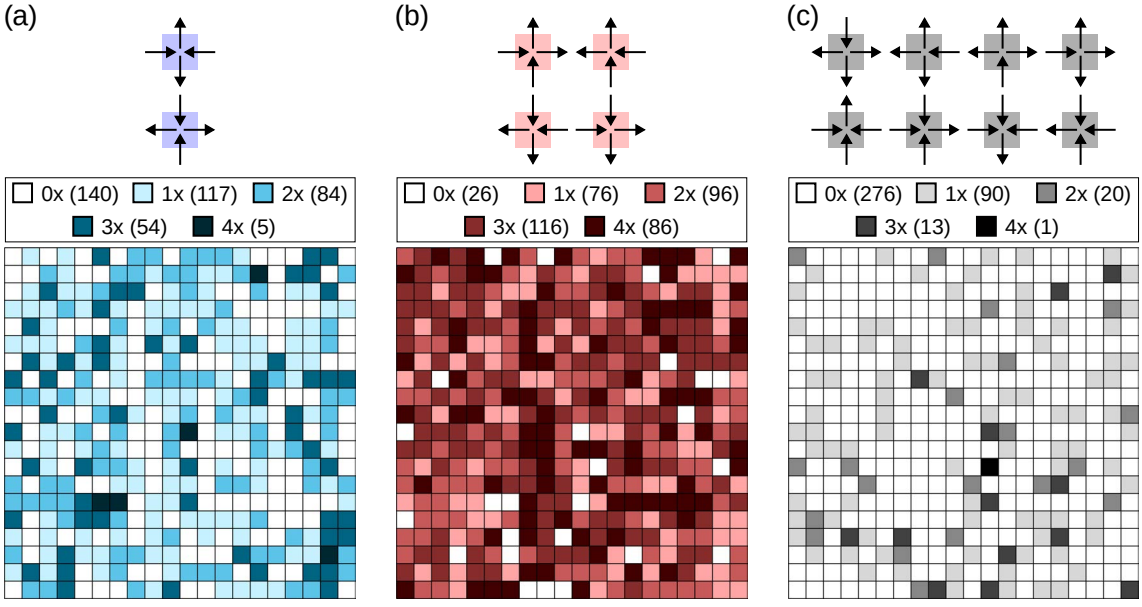

Fig. 4.3: Vertex density maps for type I (a), type II (b) and type III (c) vertices. Shading corresponds to the frequency of occurrence (see legend above each map).

For example, Fig. 4.3a shows a density map for type I vertices, compiling the four measured magnetic configurations (presented in Fig. 4.2a). If type I was never present at a given vertex position, the corresponding square is coloured as white. If type I was present at a given vertex position, the corresponding square is coloured as blue, and the shade corresponds to a frequency of occurrence. By looking at the legend above the Fig. 4.3a we can see that type I was never present at 140 vertex sites and was present once, twice, three times, or four times at 117, 84, 54, and 5 vertex sites, respectively. Density maps for type II (Fig. 4.3b) and type III (Fig. 4.3c) are constructed accordingly. It is worth mentioning that only the vertex type is considered when compiling the density maps, regardless of the associated spin configuration of the given vertex (e.g. density map do not distinguish between the eight possible type III spin configurations, and all will appear as a grey square).

The vertex density maps thus provide a visualisation of the spatial distribution of vertex types across the four demagnetisations of one lattice. We note that the lattice was always aligned the same way prior to magnetic imaging. Looking at the legend boxes above the density maps (see Fig. 4.3), one can see lattice positions at which the same vertex type appeared four times (i.e. after every demagnetisation). Namely, there are 5 locations for type I, 86 locations for type II and 1 location for type III, in which the same vertex type appears. One may wonder whether this amount of vertex type overlap originates from pure statistics or if there is a local preference for a given vertex type at some lattice positions. In other words, do sample imperfections (structural and/or magnetic disorder) lead to creation of pinning sites, that prescribe which vertex type is more favoured at a given location?

To probe this issue, we have calculated vertex overlap probabilities P_i to find vertex type i $[i = (\mathrm{I}, \mathrm{II}, \mathrm{III}, \mathrm{IV})]$ n times at the same lattice site after n demagnetisations (the resulting plot is provided in Fig. 4.4c). For $n = 1$, there are four data points which correspond directly to the four imaged configurations. When $n = 2, 3$ and 4, there are six, four and one points, respectively (as we explore all possible combinations, there are six pairs, four triplets and one quadruplet available for selection). All possible combinations are plotted as open circles, whereas the average values are shown as full circles (see Fig. 4.4c). Example of an overlap (i.e. intersection) of pair ($n = 2$) of vertex maps (obtained after first and second demagnetisation) is provided in Fig. 4.4a, whereas example of intersection of triplet ($n = 3$, maps obtained after first three demagnetisations) is shown in Fig. 4.4b. Comparing these two overlap maps reveals that the number of vertices located in the same lattice positions decreases gradually for all vertex types as n increases. This trend is further evidenced when looking at the series of full circles (average values for all possible combinations) in Fig. 4.4c. Therefore, we can conclude that the field demagnetisation protocol is not a purely deterministic process.

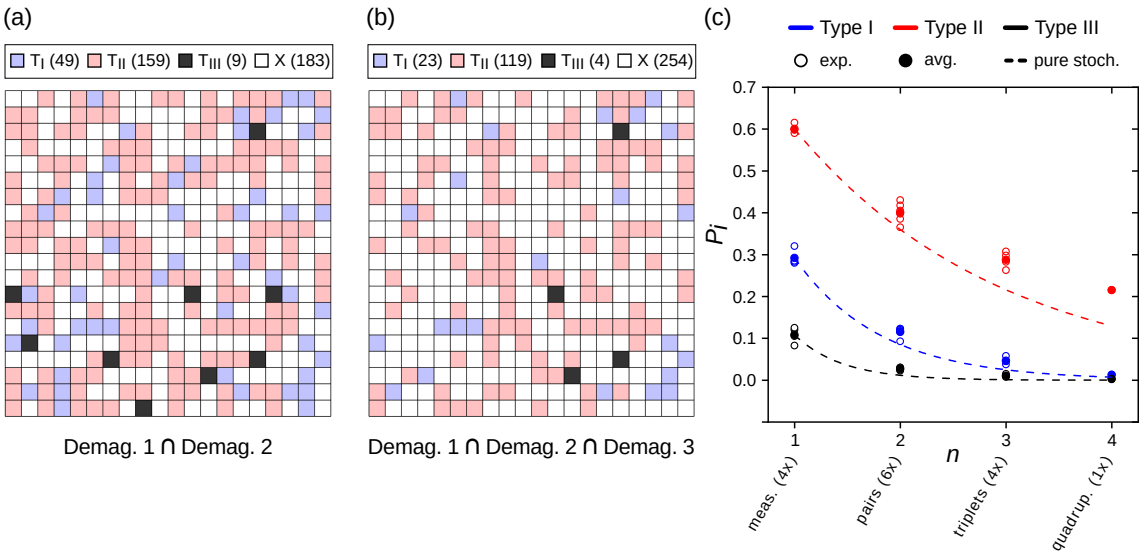

Fig. 4.4: Example of vertex overlap maps obtained as the intersection of two (a) and three (b) experimentally observed configurations [(a) is the intersection of first two and (b) of first three configurations reported in Fig. 4.2, taken from left to right]. c) Probability P_i to find a type i vertex at the same lattice position n times after n demagnetisations. Open circles are the values obtained by all possible combinations. Full circles are the average values. The dashed lines show the expected probabilities for a purely stochastic process.

To compare the experimental results with probabilities expected for a purely stochastic process, we calculated the expected probabilities as $P_i = (N_i/N)^n$ where N_i are the average vertex populations observed experimentally for type i vertices, and N is the total number of vertices of single lattice ($N = 400$). By design, a perfect match is obtained for $n = 1$. When $n \neq 1$, we find fairly good agreement between the experiment and the predictions. However, the agreement cannot be considered quantitative since the stochastic description consistently underestimates the probabilities of type I and II vertices. (see the blue and red dashed lines in Fig. 4.4c). In other words, more overlap is present in our experiment compared to a purely stochastic regime. This effect is particularly evident for type II vertices (which make up the majority of configurations), for which the deviation between experimental data and prediction increases substantially as n increases. One might wonder whether this behaviour is specific to the studied lattice or if a similar trend would also be observed in other lattices of the same type. To explore this further, we conducted the same experiment and analysis on a different lattice, which shares all nominal properties and also the field history, as it is located on the same sample.

4.1.2 Examining another artificial square ice magnet

We have repeated the same analysis for another artificial square ice magnet on the same sample to test whether the results are robust and reproducible. We note that both lattices were imaged after the same demagnetisation procedures. As the second lattice has identical nominal geometrical parameters and the fabrication process parameters, they can differ only due to intrinsic deviations of the fabrication process itself. Specifically, both lattices are even located within the same main-field window. Therefore, they share the same local alignment marks for the lithography steps. The only conceivable difference originating from the fabrication process could be a slight shift between the first and second lithography layer (i.e. the non-magnetic elevated beds and magnets on top of them), as the precision of the alignment might differ based on spatial position within the main-field window. However, we note that for neither of the two lattices, SEM imaging revealed magnets that would not sit fully on the bases or bases that would interfere with magnets of the lower layer (i.e. magnets directly on the substrate). However, it should be acknowledged that the magnets on top of the bases are relatively close to their edges. Therefore, determining that the whole volume of the magnet is on the base is not entirely certain.

The resulting arrested configurations of the second artificial square ice magnet obtained after the very same four demagnetisation protocols are shown in Fig. 4.5a.

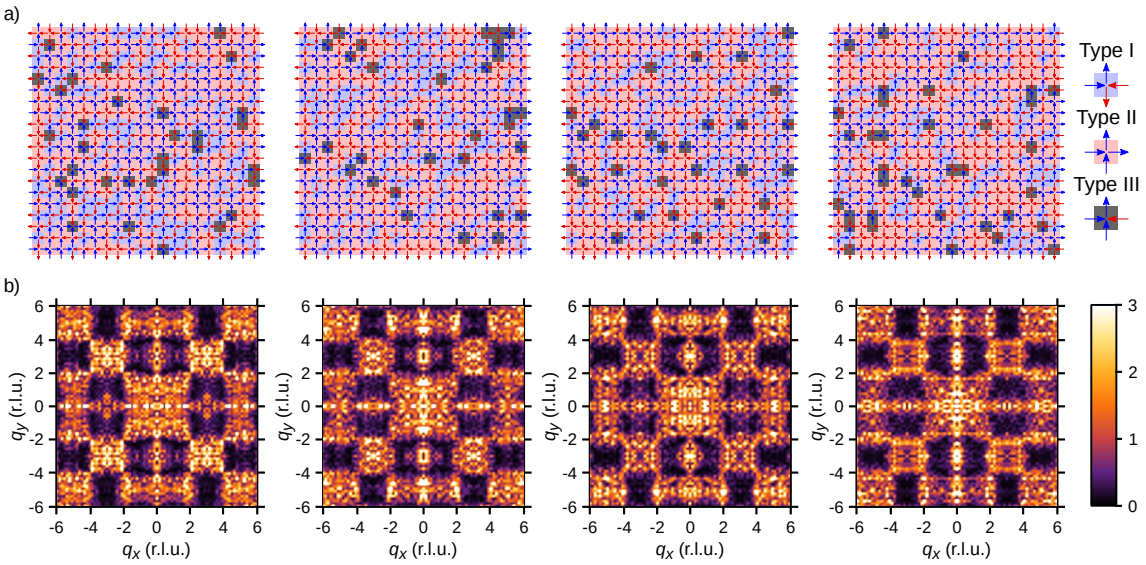

Fig. 4.5: a) Spin and vertex maps showing real space configurations of another artificial square ice magnet after applying field demagnetization protocol four times. The colour code is the same as in Fig. 4.2. b) Corresponding magnetic structure factors computed from the spin configurations shown in (a). All four plots have identical intensity (i.e., the scale bar on the right belongs to all four images) and are computed for 81×81 points in reciprocal space.

We have also calculated the magnetic structure factor for each captured configuration (shown in Fig. 4.5b). By looking both at spin/vertex maps and associated magnetic structure factors, we can confirm that the findings formulated for the first lattice (no apparent repeating pattern in the configurations, the configurations are all different but share similar macroscopic properties, all configurations are liquid-like) are valid for the second lattice as well.

Following the analysis of the first artificial square ice magnet, the next step is to compute the vertex density maps to visualise the spatial distribution of vertex types as a function of successive demagnetisation protocols. The vertex density maps for the second artificial square ice magnet are provided in Fig. 4.6. As we repeat essentially the same process, we will rely on the detailed description provided previously and focus only on the results and their comparison with the first lattice.

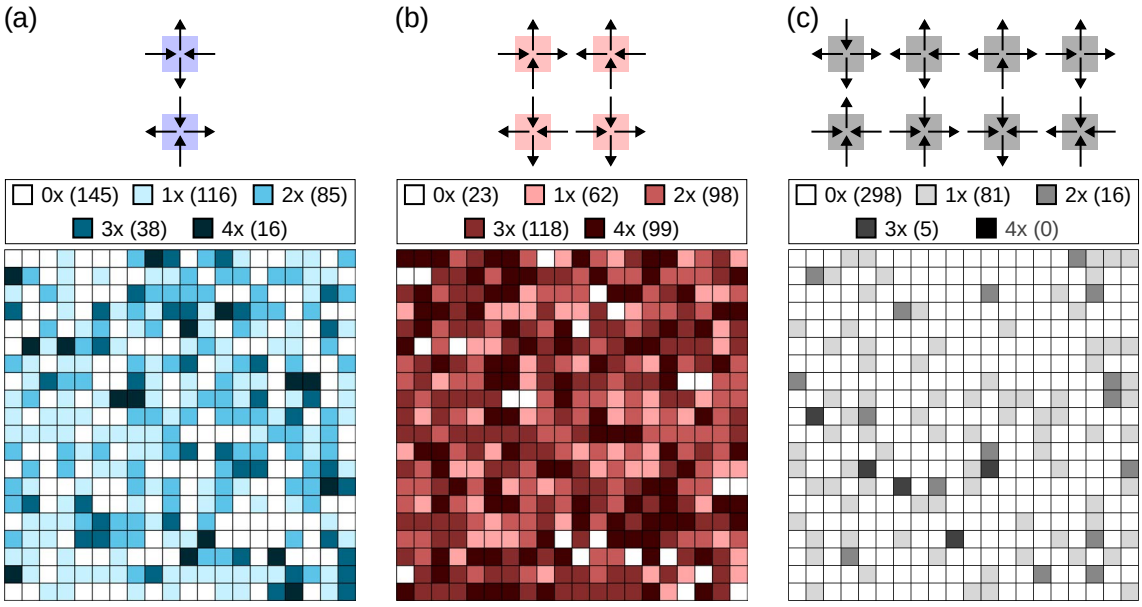

Fig. 4.6: Vertex density maps for type I (a), type II (b) and type III (c) vertices. They are computed from the four measurements of the second lattice. Shading corresponds to the frequency of occurrence (see legend above each map).

Comparing the two sets of vertex density maps of both lattices does not reveal any significant differences, as the frequency of occurrence per vertex type distribution is rather similar. The only observation that comes to mind is that there are slightly fewer type III vertices being present in the second lattice on average (about 3 % less), which naturally leads to a less dense map for type III vertices in general and, consequently, more dense maps for type I and type II vertices, compared to the first lattice.

To complete the analysis of the second lattice, we have also calculated the vertex overlap probabilities (shown in Fig. 4.7c). As for the first lattice, one can see the

same trend for the deviation between the experimental data and probabilities expected for the purely stochastic regime. Therefore, we confirm that our findings are not specific to a single realisation of an artificial square ice magnet, thus indicating the robustness and reproducibility of our results. To conclude, we see more vertex type overlap for both lattices than expected for purely stochastic demagnetisation protocol, showing that some determinism is present in our experiment. The possible source of determinism and other signatures of its presence will be discussed later.

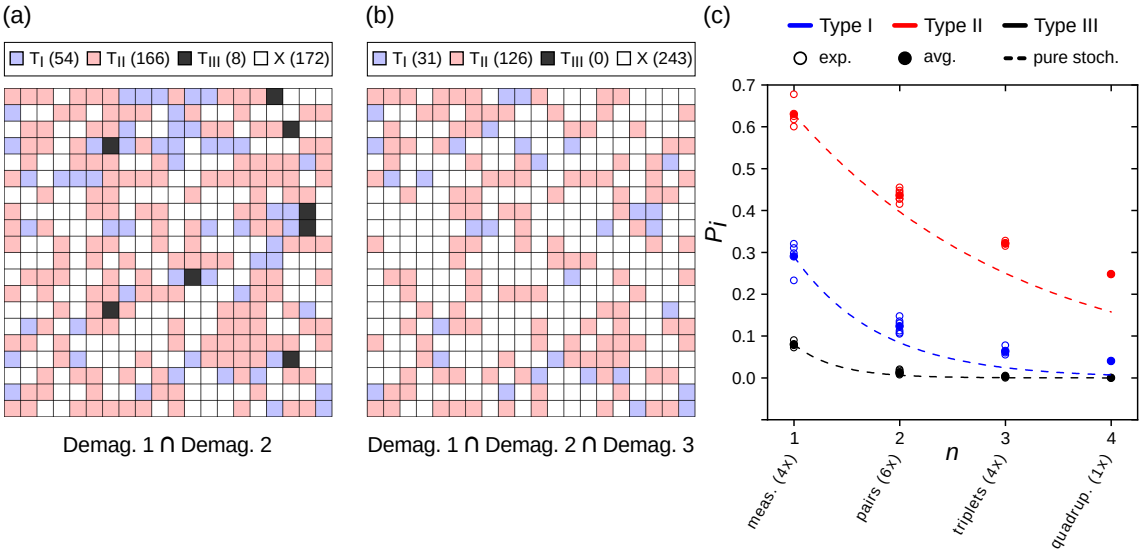

Fig. 4.7: Example of vertex overlap maps obtained as the intersection of two (a) and three (b) experimentally observed configurations of the second lattice [(a) is the intersection of first two and (b) of first three configurations reported in Fig. 4.5, taken from left to right]. c) Probability P_i to find a type i vertex at the same lattice position n times after n demagnetisations. Open circles are the values obtained by all possible combinations. Full circles are the average values. The dashed lines show the expected probabilities for a purely stochastic process.

The question then arises whether these findings can be generalised to other artificial spin systems with different physics at play.

4.1.3 Examining another system: conventional square lattice

We conducted the same experiment and analysis for a conventional square spin system (i.e. square lattice with no height offset) to probe this idea. We emphasise that the conventional square lattice shares the same nominal geometrical parameters as the two artificial square ice magnets discussed above. The only difference is the absence of the non-magnetic bases. Of course, the absence of elevation of one sublattice has significant consequences for the energy landscape of the system.

Specifically, the system is unfrustrated, resulting in an ordered ground state that is only two times degenerate (two possible tiling of type I vertices).

We note that the conventional square lattice is located on the same sample and was imaged after the very same demagnetisation protocols as the two artificial square ice arrays discussed in detail above. For the sake of consistency, we will follow the same steps for analysing the captured configurations (provided in Fig. 4.8a), as with the two previous lattices.

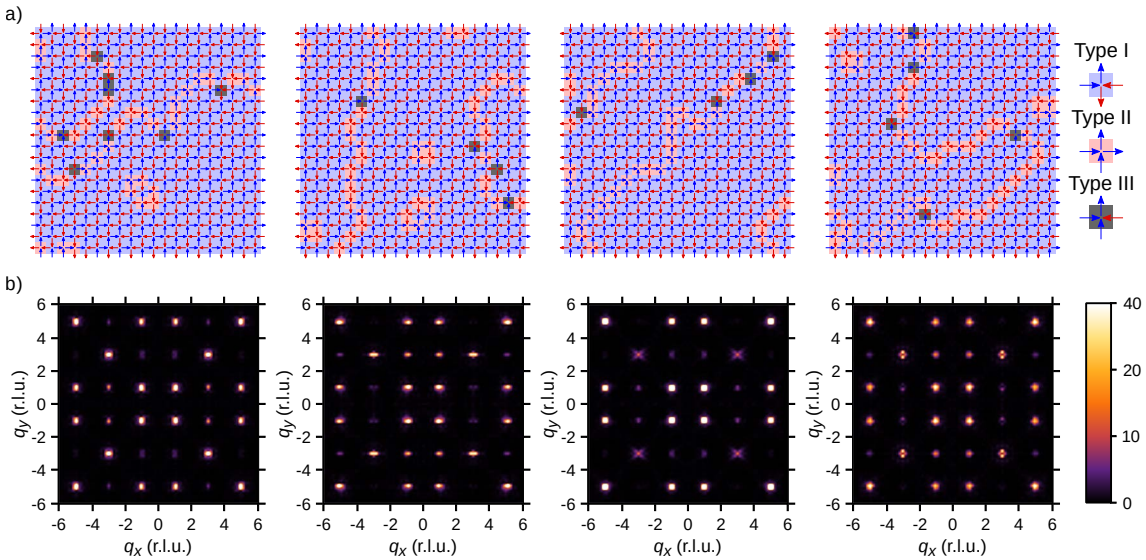

Fig. 4.8: a) Spin and vertex maps showing real space configurations of the conventional square spin system after applying field demagnetisation protocol four times. The colour code is the same as in Fig. 4.2. b) Corresponding magnetic structure factors computed from the spin configurations shown in (a). All four plots have identical intensity (i.e., the scale bar on the right belongs to all four images) and are computed for 81×81 points in reciprocal space.

As expected, the four arrested magnetic configurations of the conventional square spin system exhibit large domains of type I vertices separated by meandering type II domain walls. Only a tiny fraction (approx. 1.3 %) of charged defects (type III vertices) is observed, all incorporated within the type II domain walls. Interestingly, neither the charged defects nor the domain walls appear systematically at the same locations within the lattice. To be more quantitative and visually represent the vertex type spatial distribution across the four demagnetisations, we have again compiled the vertex density maps (shown in Fig. 4.9). As the vertex populations are dominated by type I vertices (approx. 86 % on average), their density map (see Fig. 4.9a) naturally shows many of them appearing on the same lattice position. Notably, every lattice position was at least once hosting type I vertex.

As we are interested in examining the level of stochasticity/determinism, it is

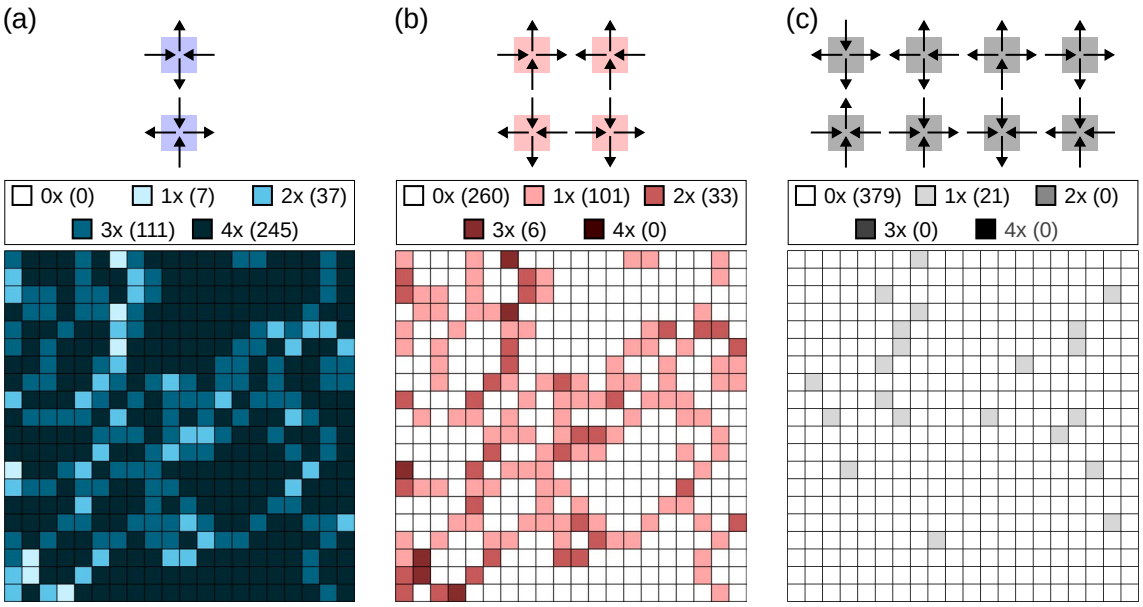

Fig. 4.9: Vertex density maps for type I (a), type II (b) and type III (c) vertices. They are computed from the four measurements of the conventional square spin system. Shading corresponds to the frequency of occurrence (see legend above each map).

more convenient to look at the position of type II and III vertices. The density map of type II vertices (see Fig. 4.9b) reveals that there is not even one lattice site that would always host a type II vertex. In other words, our lattice has no predetermined pathway for a domain wall. In general, the type II density map shows that the domain walls enter the lattice at similar positions, as evidenced by lattice sites close to the edges with a high frequency of occurrence (3x), and then take different routes through the bulk of the lattice. Interestingly, the type III density map (see Fig. 4.9c) shows that we never observed them more than once at a given lattice site.

To finalise the analysis of the conventional square lattice, we also plotted the vertex overlap probabilities (provided in Fig. 4.10c). A comparison of the experimental data with probabilities expected for a purely stochastic process (dashed lines) reveals that the deviation between them is considerably narrower compared to the two artificial square ice magnets. As for the two former lattices, the experimental vertex overlap probabilities decay slower than expected based on pure statistics. Considering that the type II density map shows that the sites with a high frequency of occurrence are found close to the lattice edges (six sites that host the type II three out of four times), one might wonder whether cropping of the lattice to remove the edges will improve the agreement between the experiment and the prediction. Removing the edges from the captured spin configurations is not unreasonable. First, the vertices at the edges have fewer neighbouring vertices, which unambiguously af-

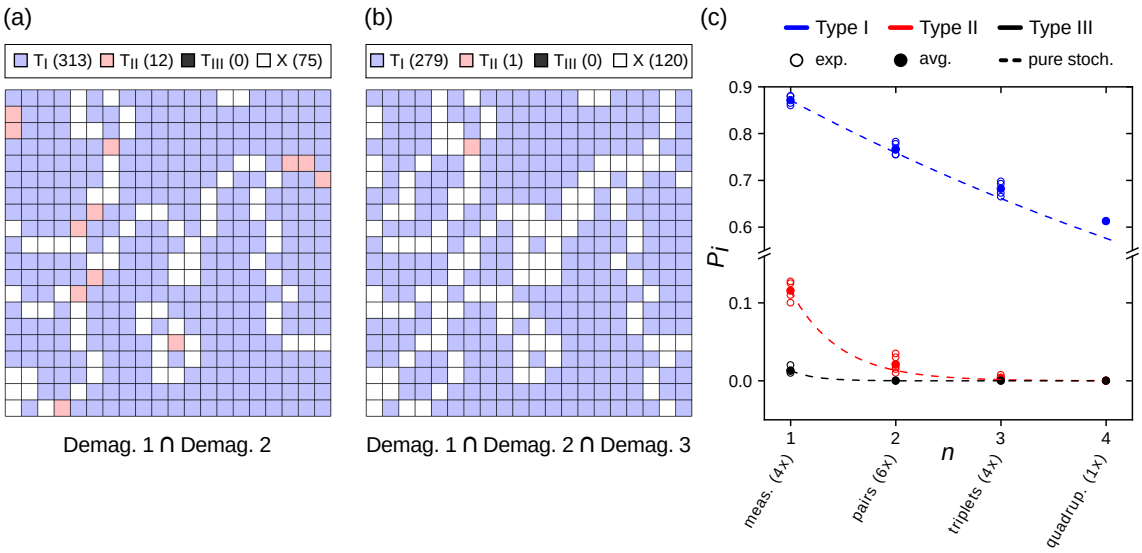

Fig. 4.10: Example of vertex overlap maps obtained as the intersection of two (a) and three (b) experimentally observed configurations of the second lattice [(a) is the intersection of first two and (b) of first three configurations reported in Fig. 4.8, taken from left to right]. c) Probability P_i to find a type i vertex at the same lattice position n times after n demagnetisations. Open circles are the values obtained by all possible combinations. Full circles are the average values. The dashed lines show the expected probabilities for a purely stochastic process.

fects their dynamics. Second, due to the proximity effect, the magnets at the edges might receive a lower exposure dose during the electron beam lithography, resulting in slight differences in fidelity and fabrication quality.

The results of the step-by-step symmetrical cropping of the lattice edge layer/s of the captured configurations are provided in Fig. 4.11. We see that as the edge layer/s are cropped out (not considered for the analysis), the agreement between the experimental data and the prediction improves. This trend continues further when the width of the crop is increased an almost perfect agreement is found for the cropped-out centre of the lattice of size 12x12 vertices.

These observations allow us to conclude that quenched disorder does not play a significant role in the conventional square lattice, as the deviations between the experiment and stochastic prediction of the vertex overlap probabilities for large n originate from the lattice edges. In other words, when only the bulk of the lattice is considered for the calculation of vertex overlap probabilities, they agree with a prediction for a purely stochastic demagnetisation process.

We note that the cropping of the measured configurations of the two artificial square ice magnets (i.e. lattices with height offset), which were discussed in detail previously, did not result in improving the agreement between the experiment and

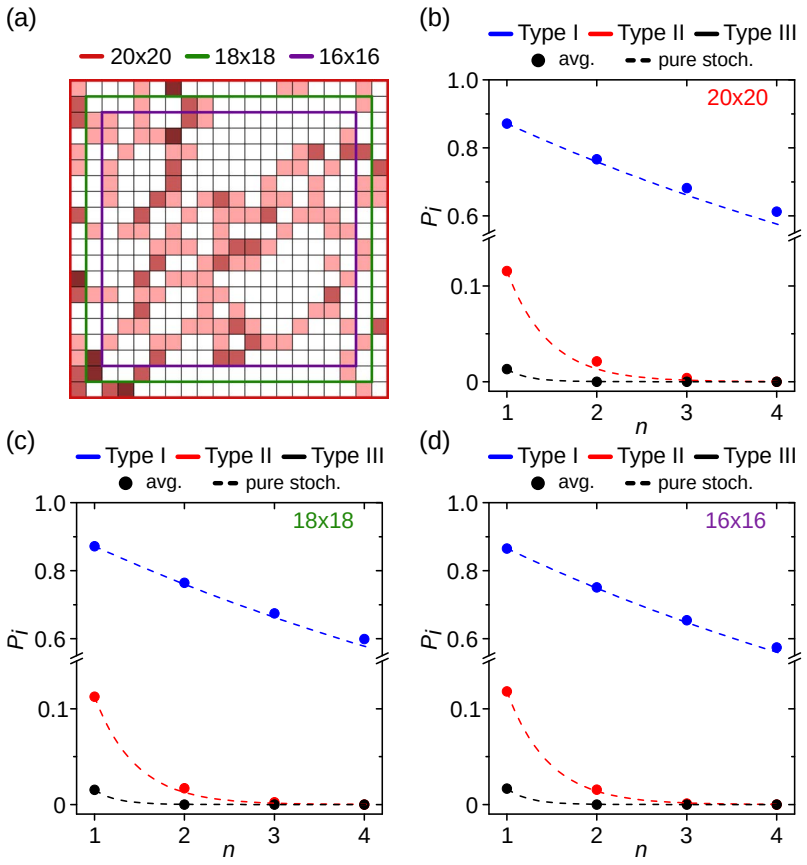

Fig. 4.11: a) Density map for type II vertices, compiled from the four measurements of the conventional square spin system. The coloured frames indicate the cropping for the analysis of the vertex overlap probabilities. (b-d) Probability P_i to find a type i vertex at the same lattice sites n times after n demagnetisations, calculated for the entire lattice (b) and symmetrical cropping of one (c) and two (d) vertex edge layer/s. Full circles are the average values. The dashed line shows the expected probabilities for a purely stochastic process.

prediction, even for cropping up to the centre of the lattice of size 12x12 vertices.

4.2 Discussion: footprints of quenched disorder

We have established above that the quenched disorder does not play a significant role in the conventional two-dimensional square lattice, as removing the lattice edges leads to recovering the agreement between the experiment and the stochastic prediction. Conversely, the same approach did not work on the artificial square ice magnets. One might wonder whether we can identify footprints of quenched disorder within the experimentally captured liquid-like configurations. In order to test this idea, we will pivot back to the first artificial square ice magnet (results provided

in Fig. 4.2) and continue the analysis not on the vertex level but at the spin level. Specifically, we will focus on the lattice sites that hosted type III vertices three (13x) or four (1x) times (highlighted in the density map of the type III vertices provided in Fig. 4.12a). As discussed before, the MFM imaging enables us to resolve the magnetisation orientation of each nanomagnet. Therefore, we can extract the exact spin states of the lattice sites that hosted type III three or four times. Comparing these local configurations (across the demagnetisations) leads to an intriguing discovery: the monopoles have a strong tendency to have the same spin state repeatedly (see Fig. 4.12).

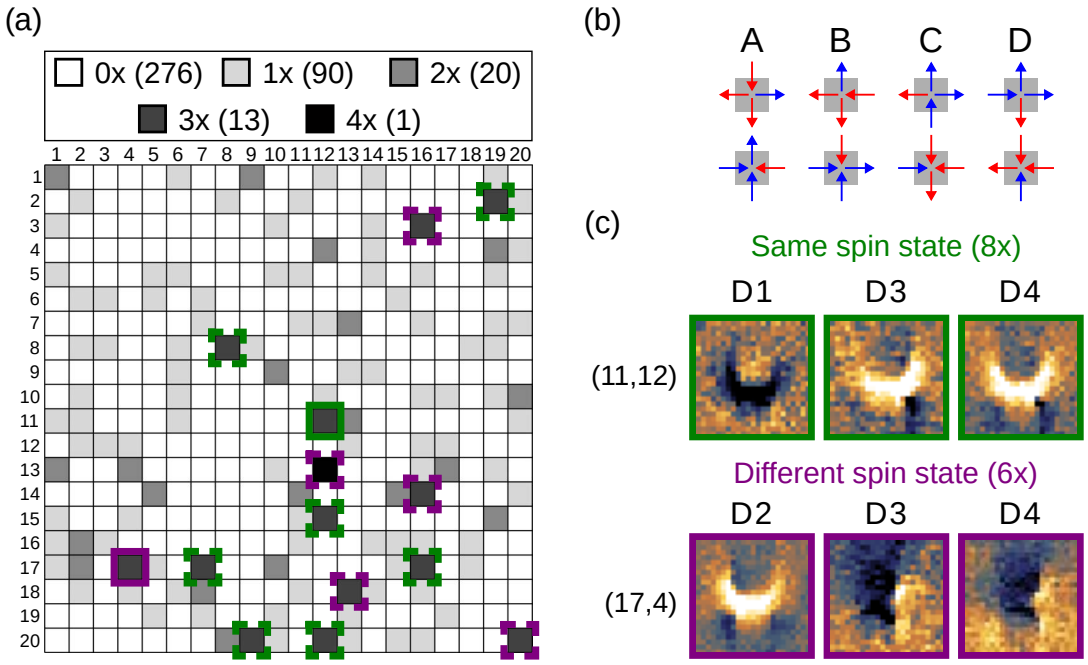

Fig. 4.12: a) Density map for type III vertices, compiled from the four measurements (demagnetisations) of the first artificial square ice magnet (results shown in Fig. 4.2). The numbers on the left (above) index the rows (columns). Lattice sites that hosted T3 vertices three or four times are highlighted by green and purple frames for sites with the same and different spin states, respectively. MFM contrast recorded at the two sites highlighted by solid colour frames is provided in (c) as an example of lattice position with the same and different spin states. b) All eight possible type III vertices divided into four spin states (A-D) based on spin-reversal symmetry. The other variant of the same spin state is obtained by reversing all spins (i.e., from red to blue and vice versa). c) Example of lattice sites hosting three times the same spin state [at lattice position (11,12)] and different spin states [at lattice position (17,4)]. Numbers above the cropped images (D1 to D4) refer to the demagnetisation protocol.

This discovery is somewhat surprising as there are eight possible monopoles

(i.e., a ±2 charged defects), which can be divided into four spin states (each being two-time degenerate, see Fig. 4.12b). Thus, each monopole spin state has a 25% probability to occur. The probability of observing three times the same spin state (out of four possible) for a monopole is only 6.25 %. Strikingly, in our experiment, 9 of the 14 considered monopoles have three times the same spin state[3]. This statistic is incompatible with the assumptions for a purely stochastic process, and quenched disorder is present and biasing our experiment.

One might then wonder what distinguishes these vertex sites, that repeatedly hosted the same monopole spin state, from the rest. To investigate this issue, we performed detailed SEM imaging of those lattice sites to evaluate whether structural defects are present. Fig. 4.13 shows a comparison of two lattice sites that hosted monopole three out of four times, whereby one hosted same monopole spin state (Fig. 4.13a) and the other different monopole spin states (Fig. 4.13b).

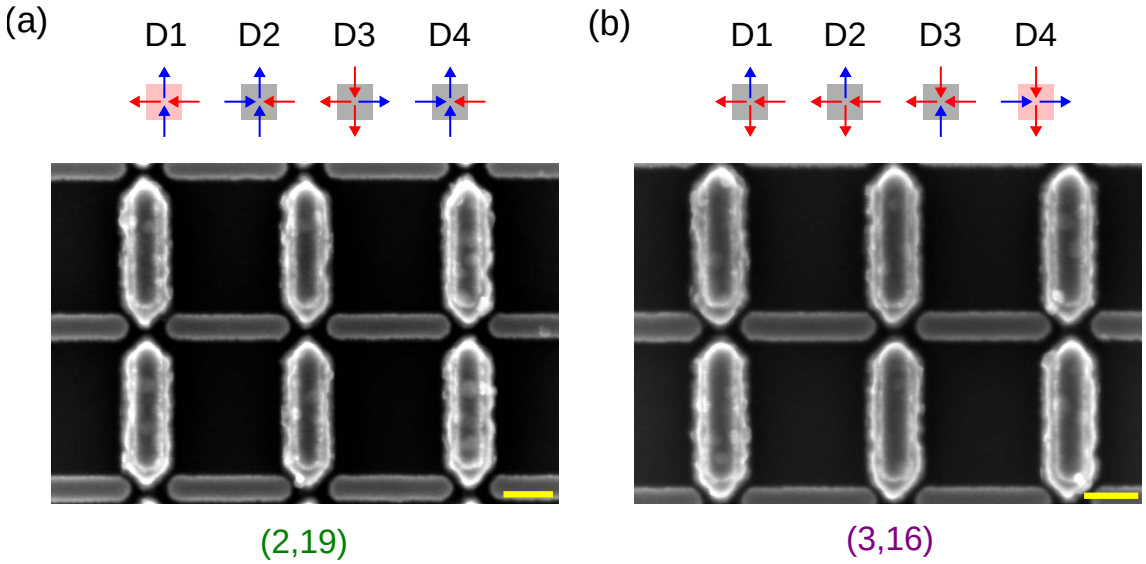

Fig. 4.13: SEM details of vertex sites of the artificial square ice magnet that hosted monopole three out of four times. a) Lattice site (2,19) that hosted monopole of same spin state. b) Lattice site (3,16) that hosted monopole of different spin states. Above each image are the local spin configurations obtained at that vertex site across the four demagnetisations (D1 to D4). The yellow scale bar represents 200 nm. The indexing of rows/columns is as in Fig. 4.12.

A comparison of those two SEM details does not reveal a significant difference between them (e.g. missing part of a magnet, magnet not aligned on top of its base, base interfering with the magnets on the substrate, etc). In other words, there seems

[3]The one lattice site at which type III was observed four times hosted three times the same spin state. Therefore, we have a total of 9 sites that hosted three times a monopole of the same spin state.

to be no structural reason why one should host monopoles of the same spin state and other monopoles of different spin states. We note that we conducted such detailed imaging for all of the lattice sites that hosted monopole three or more times (indicated in Fig. 4.12a), and we did not observe any structural features that would explain why we often observe monopoles of same spin state at a given lattice site. As we did not observe any structural defects, we speculate that the source of the quenched disorder has a magnetic origin.

4.2.1 Extending the spin state analysis to type II vertices

One might wonder what the results of the spin state analysis, which we did for type III vertices often observed at the same lattice position, will be if we consider type II vertices instead. There are four possible type II vertices that can be divided into two spin states (each being two-time degenerate, see Fig. 4.14b). As the type II vertices prevail in the artificial square ice vertex populations (approx. 60 %), a significant number of them are found at the same lattice site. To be precise, the density map provided in Fig. 4.3 shows that 86 lattice sites hosted type II vertex after each of the four demagnetisations. We will now focus on those 86 lattice sites and examine their associated spin state. The analysis results are summarised in Fig. 4.14.

Based on the analysis provided in Fig. 4.14 following observations can be made:

1. In our experiment, the probability of finding the same type II spin state four times at the same lattice site is overweighted compared to prediction (coming from pure statistics). Proportionally, the probability of having two times both spin states at a lattice site is underweighted. Both shown in Fig. 4.14c.
2. Lattice sites that host four times the same spin state are spatially distributed across the lattice. We do not see clustering of such sites.

Therefore, similar to the type III spin state analysis, we observe a local preference for type II spin state at lattice sites, further confirming that quenched disorder is present and biasing our experimental results. We note that the spin state analysis cannot be extended to type I vertices, as they have only one two-time degenerate spin state.

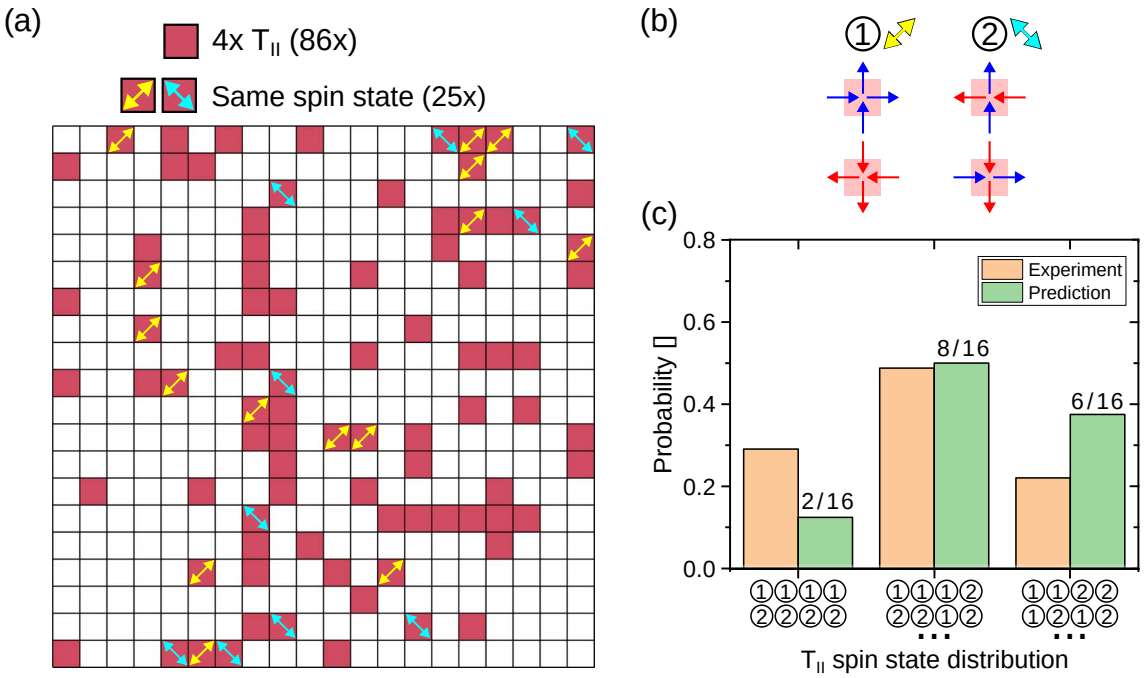

Fig. 4.14: a) Map showing the 86 sites where type II was observed after each demagnetisation. Out of those sites at 25, type II of the same spin state was observed. Those sites are highlighted by the double-headed arrows that show which spin state was present. b) Division of possible type II vertices into two spin states. The double-headed arrows illustrate the net moment direction of those spin states. c) Comparison of experimental spin state probability distribution compared with that coming from pure statistics.

4.2.2 Summary

So far, we have limited our analysis of the footprints of the quenched disorder to the first artificial square ice magnet. We note that we did the same analysis also for the second lattice with the height offset. The results are essentially in agreement, with the following minor deviations:

1. For the second lattice, we observed type III at the same lattice site less frequently (5 sites where type III was present three times, none where it would appear four times). The same spin state for type III was observed twice at those five sites. The effect of observing the same spin state is, therefore, slightly weaker (2/5) than for the first lattice (9/14) but still above the expectations for pure statistics. Detailed SEM imaging of the five considered lattice sites also revealed no structural defects, consistent with the first lattice.
2. Interestingly, the spin state analysis of type II vertices observed four times at the same lattice site for the second lattice shows a stronger preference for hosting the same type II spin state (43/99 vs. 25/86, see Fig. 4.14a for reference).

4.3 Discussion: what is the source of randomness?

We have established above that the experimental vertex overlap probabilities for both examined artificial square ice magnets decay slower than the expectation for a purely stochastic process (reported in Fig. 4.4c and 4.7c). We then discussed footprints of the quenched disorder in the spin configurations captured for those two lattices. Combining those results, we conclude that if the field demagnetisation protocol we apply to our lattices is at least partly a stochastic process, quenched disorder likely adds some determinism.

At the beginning of this section, we discussed the two approaches used for bringing the artificial spin systems to their low energy configurations: field and thermal demagnetisation. We stated that in the case of thermal demagnetisation, one might intuitively understand that the thermal fluctuations act as a source of stochasticity. We also stated that the field demagnetisation protocol might be considered a deterministic process, especially when the demagnetisation is carried at temperatures well below both the blocking temperature of the individual magnets and the Curie temperature of the constituent material. This is, however, in contrast with our experimental results.

One might then ask, what is the source of randomness in our experiments? We acknowledge variations in our field demagnetisation protocols may exist between successive demagnetisations, even if we set the same parameters for each protocol (same strength of the initial field, same voltage for driving the motor rotation, etc.). This variability could be attributed to *extrinsic* sources of randomness, such as magnetic noise generated by the electromagnet power supply, fluctuations in the rotation speed of the sample, and variability in the initial field direction, among others. Assuming that these sources of variation can be eliminated, there is still an *intrinsic* source of stochasticity, which has a micromagnetic origin.

At this point, it is worth recalling that considering nanomagnets of the size considered in this work as Ising pseudospins is a rough approximation, and the relevance of their micromagnetic texture in artificial spin systems was previously reported [86, 109–113]. This has important implications for the dynamics in our lattices, as the magnetization reversal in considered nanomagnets is expected to proceed via nucleation and propagation of vortex domain walls [122].

To illustrate how the magnetisation texture evolves during reversal, we conducted micromagnetic simulations using the MuMax3 software [75]. The nanomagnet has the same shape (rectangle with two semicircular heads) and dimensions ($500 \times 100 \times 30$ nm^3) as the ones forming our experimentally investigated lattices.

For the simulation, material parameters commonly used for permalloy are selected (spontaneous magnetisation $M_S = 800$ kA m^{-1}, exchange stiffness $A = 10$ pJ m^{-1}, magnetocrystalline anisotropy is neglected and damping is set to $\alpha = 2 \times 10^{-2}$). The simulation mesh size is set to $2 \times 2 \times 30$ nm^3. The simulations are run at 0 K, therefore, no thermal fluctuations are present. The external magnetic field is oriented at an angle of 45° with respect to the long axis of the nanomagnet, and its amplitude increased by steps of 1 mT when approaching the reversal field. Snapshots of the magnetisation texture upon reversal are shown in Fig. 4.15.

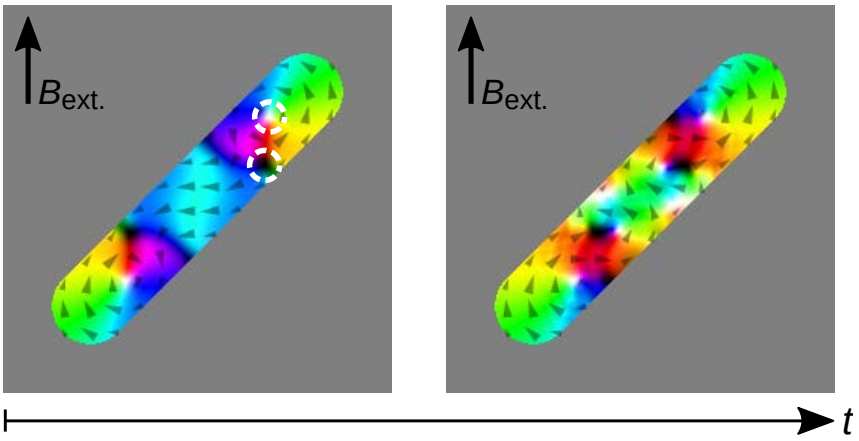

Fig. 4.15: Snapshots of a micromagnetic simulation illustrate the magnetisation reversal in a nanomagnet considered in this work. The white dashed circles in the left snapshot highlight vortex/antivortex cores.

The prominent feature we wish to emphasise is the emergence of vortices and antivortices, denoted by the appearance of the white and black cores, respectively. White dashed circles highlight a pair of vortex and antivortex cores in the left snapshot provided in Fig. 4.15. These vortex/antivortex cores are nucleated at the edges of the nanomagnet and then move towards its centre. The eventual annihilation of vortices/antivortices triggers the magnetisation reversal.

It was reported previously that thermal fluctuations at room temperature (i.e. 300 K) significantly influence field-driven domain wall dynamics in permalloy stripes, particularly for the fields above the Walker field [123]. Notably, this study reports stochastic effects being present for defect-free magnetic wires and also for stripes with notch-like pinning site or stripes with roughness (i.e. randomised defects on the wire edges). Consequently, similar effects could be at play during our field demagnetisation protocols of artificial spin systems (carried at room temperature), as the field necessary for triggering the nanomagnet reversal is much larger than the Walker field.

It is worth pointing out that our lattices consist of 840 interacting nanomagnets,

where each magnet is influenced by an effective field combining both the external magnetic field and the fields originating from the neighbouring nanomagnets. Thus, any probabilistic effects at the single magnet magnetisation dynamics level can propagate through the lattice via the kinematic effects associated with the field demagnetisation protocol.

To explore how the thermal fluctuations might introduce a source of stochasticity in our experiments, we conducted micromagnetic simulations emulating the field-driven reversal of square lattice vertex at 300 K, utilising the stochastic thermal field B_{therm} implemented in the MuMax3 software [77]. Material parameters are the same as for the single magnet reversal simulation (described above). All geometrical parameters closely follow the nominal parameters of lattices in the experiment (magnets size $500 \times 100 \times 30$ nm^3, lattice parameter $a = 650$ nm and height offset $h_{\text{exp}} = 100$ nm). The simulation mesh is set to $4 \times 4 \times 10$ nm^3, enabling the correct height offset setting while keeping the simulation time reasonably low. The initial configuration is type II vertex, in which net magnetic moment points in the +xy direction (i.e. magnetisation of the horizontal magnets points to the right and magnetisation of vertical magnets points to the top). Then, the magnetisation of the top magnet is reversed, and an external magnetic field is applied in the -xy direction. The amplitude of the external field is then increased by steps of 1 mT. The simulation was repeated 10 times with different seeds for the thermal field selected for each one of them. For reference, the simulation was also run at 0 K. The results of the simulation set (11 simulations in total) are summarised in Fig. 4.16.

Interestingly, the flipping order of magnets is observed to be dependent on the seed value of the stochastic thermal field B_{therm} emulating the room temperature (i.e. 300 K), at which the field demagnetisation protocols were carried out in the experiment. For the two seeds out of ten (shown in Fig. 4.16a), the left and bottom magnet flip first simultaneously, similar to when the simulation is run at 0 K. The only difference is that the reversal starts at a lower value of the external field. The remaining eight simulations show reversal starting either with the left magnet (three times, see Fig. 4.16b) or the bottom magnet (five times, see Fig. 4.16c). For both cases, the reversal of the first magnet starts at a lower external field than the reversal at 0 K. Even if the flipping order is the same, there are additional differences, such as the total time of the reversal, as shown in Figs. 4.16b and 4.16c (compare the blue/green curve against the grey curves). We ran the same simulation to improve the statistic for 20 additional seeds, increasing the total number to 30. The distribution of the branching (i.e. what magnet(s) are reversed first) for all simulations that have been run is provided in Fig. 4.17. Notably, it shows that the bottom or left magnet is reversed first equally likely and less likely that they are reversed together at the same time.

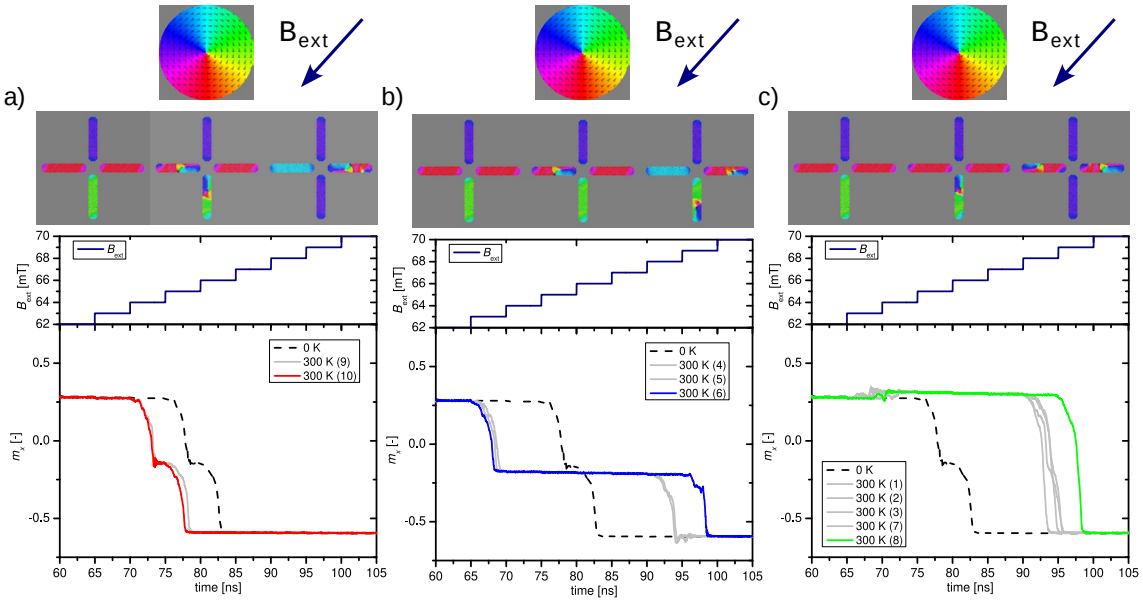

Fig. 4.16: Micromagnetic simulations of field-driven reversal of artificial square ice magnet vertex considered in this work (i.e. there is vertical offset $h_{\text{exp}} = 100$ nm between the horizontal and vertical magnets). The magnets' flipping order depends on the seed selection for the stochastic thermal field B_{therm}. The results are divided based on flipping order: (a) left and bottom magnets flip first at the same time (similar to when the simulation is run at 0 K), (b) left magnet flip first and (c) bottom magnet flip first. Three representative snapshots are shown for each case: initial configuration, first reversed magnet(s), and last reversal step. These snapshots correspond to the coloured curve in the respective plot below. The plots show the magnetisation m_x as a function of time for the different seeds (indicated in the brackets within the plots legend). The black dashed line corresponds to the simulation run at 0 K. Above each magnetisation plot is also a plot showing the stepping of the external field B_{ext}. The direction of the external magnetic field B_{ext} and magnetisation colour wheel are indicated above the snapshots.

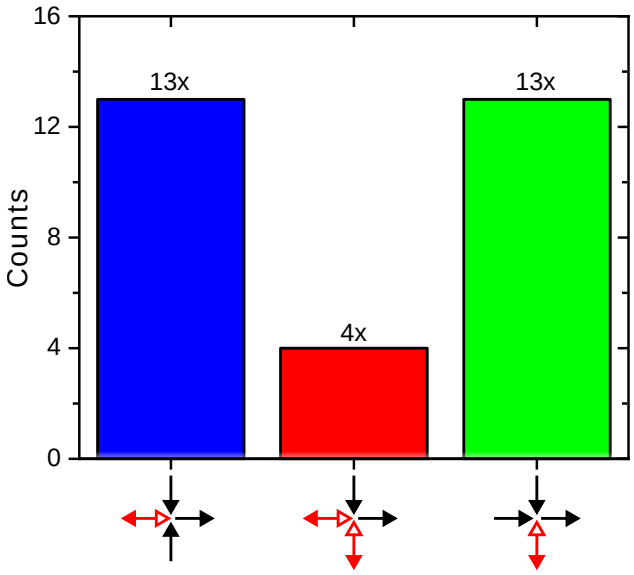

Fig. 4.17: Distribution of the flipping order for 30 different seeds. Below each column, the magnet(s) that flip first is shown in red (the empty arrowhead shows the initial orientation and the full arrowhead shows the final configuration. The colours of the bars correspond to coloured curves in Fig. 4.16.

We can then speculate that the branching effect we have demonstrated above can act as a source of randomness for the avalanche processes present during the field demagnetisation procedure. In other words, thermal fluctuations might influence the reversal pathways taken during the field demagnetisation protocol when the external field's strength approaches the magnets' reversal fields for at least some external field angles. This may eventually lead to capturing different (almost) uncorrelated configurations after applying the field demagnetisation protocol several times to the very same lattice.

4.4 Summary

In this study, we have focused on comparing the results of applying field demagnetisation protocol four times to several lattices located on the same sample. We show that the configurations obtained for a given lattice after successive field demagnetisations share similar macroscopic properties but differ substantially in the spatial distribution of vertices. By analysing the vertex density maps and associated vertex overlap probabilities, we show that the amount of vertex type overlap is in qualitative agreement with a prediction for a stochastic demagnetisation process. However, the agreement is not quantitative, as we see slightly more overlap than expected across the studied lattices.

We attribute these differences to the presence of quenched disorder. In the case of the conventional square spin system (i.e. lattice with no height offset), the difference between the experiment and prediction for the stochastic process can be suppressed by removing lattice edges from the analysis. Conversely, in the case of the artificial square ice magnet (i.e. lattice with properly tuned height offset), the same approach does not close the gap between the experiment and the prediction. The analysis of the spin-states of often overlapping type III and type II vertices reveals local preference to host the same spin-state at those lattice sites repeatedly. Thus providing direct evidence of quenched disorder being at play. Interestingly, the detailed examination of those lattice sites through electron microscopy has not revealed any noticeable structural defects, which leads us to speculate that the quenched disorder has a magnetic origin.

However, the most interesting outcome of this work is that the field demagnetisation protocol is not a purely deterministic process, as the response of the very same lattice to several demagnetisations yields different arrested configurations. Using micromagnetic simulations, we show that the square lattice vertex's field-driven reversal is sensitive to room-temperature thermal fluctuations, and the reversal order differs with the stochastic thermal field seed. Those simulations lead us to believe that the room-temperature thermal fluctuations are not negligible for consideration of field demagnetisation dynamics.

We note that describing artificial spin systems, which are thermally stable at remanence, as athermal systems, as is often done in the literature, might be misleading. Even though the blocking temperature of individual nanomagnets and the Curie temperature of the constituent material is well above the temperature at which the demagnetisation is carried out, the thermal fluctuations are still present and might influence the demagnetisation dynamics.

Lastly, we would like to note that plotting the vertex density maps provides interesting insights regarding the level of stochasticity/determinism, as they conveniently highlight the regions that retain the same configuration after successive demagnetisations. The vertex density maps might help spot the areas that shall be removed from the analysis as we did for the conventional square spin system or in interpreting deviations from the at-equilibrium state. For example, one can imagine that the monopoles present in the spin-liquid phase can originate either from the freezing of the single spin-flip dynamics or from quenched disorder. By doing several demagnetisations, one can then distinguish between them, as the "true" monopoles will appear at different sites, and the "pinned" ones will appear at the exact locations.

5 EFFECTIVE THERMODYNAMICS IN ATHERMAL, FIELD-DEMAGNETISED ARTIFICIAL SQUARE SPIN SYSTEMS

Artificially made spin systems offer great flexibility in the lattice design. This flexibility enables not only the fabrication of a large palette of lattice geometries, but also lattices of the same geometry with varying lattice parameters. This was employed already in the first study that reported an experimental investigation of an artificial square spin system [12]. In this work, a series of square lattices consisting of nanomagnets of the same size but with different lattice parameters (i.e. periods) was prepared, and the configurations obtained after an ac field demagnetisation protocol were imaged. Comparing the vertex populations and pairwise spin correlations as a function of lattice spacing revealed that magnetic ordering develops preferentially in densely packed lattices. Accordingly, the lattices with larger lattice spacing are less correlated, and uncorrelated spin arrangements are obtained for the largest studied lattice spacing. This is expected as the increase of the lattice spacing significantly reduces the strength of the magnetostatic interaction coupling neighbouring nanomagnets. However, even for the smallest studied lattice spacing, the fraction of type I vertices was approx. 33 %, indicating that the arrested configuration is far from the ground state configuration (perfect tiling of type I vertices only).

More details on the ac field demagnetisation protocol used in the aforementioned study were provided in a work authored by the same group [54]. Here, it was reported how the field was stepped down during the demagnetisation. The provided information makes it possible to estimate the total duration of the demagnetisation protocol as approx. 1 min. This work also compared different field profiles used for the demagnetisation, concluding that ac demagnetisation was more efficient (measured by total remanent magnetisation extracted from captured configurations) than linear or monotonous stepping-down of the applied field. This work was later supplemented by the study originating from the same group [55], which also investigated the role of the fineness of the magnetic field step size during the ac field demagnetisation procedure. Apart from showing that the correlations continue to develop even after the global magnetisation is minimised, which essentially advocates for using finer field step size to increase the demagnetisation efficiency, this work also reports that smaller lattice spacing yields more strongly correlated configurations. This work does not directly report the maximum value of the type I vertex population reached but reports values of spin-spin correlators. The highest value for the nearest-neighbour pairwise spin correlator is reported as approx. $\langle C \rangle = 0.49 \pm 0.03$. To provide a reference, the value of $\langle C \rangle = 1$ is expected for ground-state configura-

tion (tessellation of type I vertices only). Looking at the values of the minimal field step size given, one can estimate the duration of the finest demagnetisation protocol as approx. 66 min.

Response of artificial square spin systems to other field profiles used during the field demagnetisation was also investigated. Interestingly, configurations with a type I population of approx. 50 % were obtained using a protocol with fixed amplitude of the applied magnetic field [56] and notably, arrested configurations with maximum type I vertex fraction of approx. 63 % were obtained using linearly ramped down field profile [57]. In accordance with the previous work that used the ac field profile [55], the recipe for approaching the ground-state ordering is to have strong interactions (i.e. small lattice parameter) and fine-stepping of the field. In the work with linearly-ramped down field profile [57], the total duration of the demagnetisation protocol for the finest ramping rate can be estimated as approx. 72 min. As all studies with decaying external fields mentioned above share similar starting values of the external field (approx. 130 mT), it is reasonable to use the total duration of the protocol to illustrate how much time the configurations were given to evolve. For clarity, all the studies mentioned here employed sample rotation to compensate for the multi-axial symmetry of the lattices (different rotation speeds in the range of approx. 2500—1000 RPM were used). To provide the time frame, the works mentioned above were published in 2006–2013.

In 2011, a novel way of approaching the ground-state configuration in artificial square lattice by single-shot at-growth thermalisation was presented [39]. This approach leverages the fact that during the early stages of the material deposition, the magnetisation of the islands can switch due to their low volume while accommodating the effective field from the neighbouring magnets. Assuming no external magnetic field is present, the as-grown state can closely approach the ground-state configuration. The arrested configuration imaged by MFM then showed GS-ordered domains of type I with a width of approx. 10 µm, significantly surpassing the results of field demagnetised lattices formerly reported. Two years later, a study from the same group reported results of applying the at-growth thermalisation process to a series of square lattices with varying lattice parameters [40]. Notably, it was shown that the captured populations of different vertex types can be tuned by modifying the lattice constant. Similar to what was reported previously for the field demagnetised lattices, smaller lattice constant results in more correlated configurations with a higher fraction of type I vertices. For the most densely spaced lattices studied even achieving population of 100 % of type I vertices over five MFM images of size 13×13 µm^2 taken at different places of the same lattice is reported. The effective temperature is determined from experimentally observed vertex populations, following the formalism presented previously [124]. Interestingly, it is shown that varying

the lattice parameter yields configurations with distinct effective temperatures and strong agreement with a vertex model (vertex energies estimated by a point-dipole approximation) is reported. In other words, it is possible to scan across magnetic microstates with distinct effective temperatures by fabricating a series of square lattices with different lattice parameters, which are at-growth thermalised.

In this work, we aim to investigate whether this approach of varying the lattice parameter to obtain configurations characterised by different effective temperatures can be employed when working with athermal, field-demagnetised artificial square spin system. This issue has already been mentioned in a previous work [124], which, however, mainly focused on the effect of the magnetic field step on the achieved effective temperature, even though some effect of varying the lattice parameter can also be identified from the experimental data reported. It is worth mentioning that the maximum population of approx. 50 % for type I vertices is reported, similar to the earlier studies working with the field demagnetisation. However, we know that the ground-state configuration (full tiling of type I vertices) can be approached more closely with a field demagnetisation, as populations with approx. 86 % for type I vertices were repeatedly reached previously in our group for artificial square arrays [31]. Our goal is thus to complement the previous work [124] with more efficient demagnetisation, which, in principle, should enable us to obtain magnetic states with lower effective temperatures. Ideally, approaching what was reported for the at-growth thermalised arrays [40].

We believe this is an important matter that can provide more insights for comparing the effectiveness of field and thermal approaches for equilibrating the artificial arrays. It is our understanding that field demagnetisation is often considered an obsolete or inferior process compared to thermal activation. We aim to show that field demagnetisation can yield similarly good results, and it is still a relevant method for exploring low-energy manifolds of artificial spin systems. Our study also has practical implications. Assuming it is possible to scan across different effective temperatures by field demagnetising athermal square arrays with varying lattice parameter, one can even envision to probe a phase transition, provided it lies in the experimental window of the effective temperatures reached.

To experimentally investigate the abovementioned matter, a sample with a series of artificial conventional square arrays [12] with varying lattice parameter was fabricated. The sample is then field demagnetised and arrested configurations of individual lattices imaged by magnetic force microscopy. Captured magnetic images were evaluated to obtain spin and vertex maps. The evolution of vertex populations as a function of varying lattice parameter was then compared against the results of Monte Carlo simulations with short-range (J_1,J_2) model. A good agreement between the experiment and the simulation is observed, suggesting that adjusting

the strength of the interactions in the square arrays makes it possible to probe microstates that are representative of distinct (fictitious) effective temperatures.

5.1 Sample design

This work studies the effects of varying the lattice parameter of artificial conventional square arrays. By conventional, we mean a square lattice that has all magnets placed directly on the substrate (i.e. there is no height offset engineered). When designing such an artificial array, one can essentially choose all the geometrical parameters defining the lattice and also the constituent material. This enables the design to be optimised in a convenient way for the planned experiment. For the purpose of this work, the sample must be designed to fulfil the following requirements: 1) the magnetic configurations of the arrays are stable at remanence (at room temperature), 2) the individual magnetic elements forming the grids are single-domain, 3) arrays provide strong enough contrast for the magnetic force microscopy allowing evaluation of each island and 4) for small lattice parameters the arrays are strongly interacting to allow for approaching the ground-state ordering.

Considering the requirements listed above and the experience gained from the previous works, we have opted for the following nominal values of geometrical parameters for our sample:

- magnet width: $w = 100\,\text{nm},\ 150\,\text{nm}$ and $200\,\text{nm}$,
- magnet length: $l = 5 \times w$,
- gap sweep: $g = 0.4 \times w$ to $5 \times w$ (with step $0.2 \times w$),
- magnetic material: 25 nm NiFe,
- nanomagnets shape: stadium (rectangle with two semicircular ends, see Fig. 5.1b),
- lattice size: 30×30 vertices.

.

The choice of the magnet's width, length, thickness, and constituent material is mostly based on our previous works (and those of a former student in our group). Namely the square lattices with magnet width of 100 nm were investigated in [30, 31, 87] and for width of 150 nm in [97]. In those works, the same shape, aspect ratio (i.e. $l = 5 \times w$) and magnetic material (NiFe, thickness 25 or 30 nm) were used. Based on the results obtained therein, we expect the closest approach towards GS ordering (between 80 to 90 % of type I vertices) for gaps in the range $g = 1 \times w$ to $2 \times w$. The gap refers to the distance between opposite magnets at a vertex site. Therefore, the designed gap sweep corresponds to a sweep of the lattice parameter in the range of $a = 5.4 \times w$ to $10 \times w$ ($a = l + g$), yielding a series of 24 lattices for each designed width.

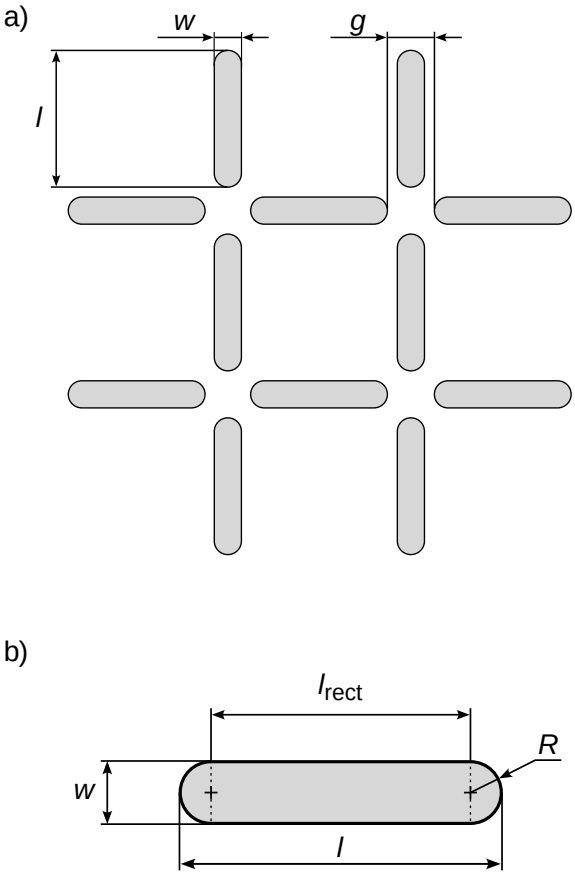

Fig. 5.1: a) Sketch of a conventional square lattice of size 2×2 vertices, with plotted geometrical parameters. b) Detail of single stadium-shaped magnet with defining geometrical parameters.

Tab. 5.1: Overview of designed lattices

w [nm]	**100**	**150**	**200**
Lat. nr.	g [nm]	g [nm]	g [nm]
1	40	60	80
2	60	90	120
3	80	120	160
4	100	150	200
5	120	180	240
6	140	210	280
7	160	240	320
8	180	270	360
9	200	300	400
10	220	330	440
11	240	360	480
12	260	390	520
13	280	420	560
14	300	450	600
15	320	480	640
16	340	510	680
17	360	540	720
18	380	570	760
19	400	600	800
20	420	630	840
21	440	660	880
22	460	690	920
23	480	720	960
24	500	750	1000

Such a gap sweep should enable us to closely approach the GS ordering for the small gaps and also to capture significant changes in vertex populations as the interaction strengths are weakened by increasing the gap. In fact, we start the sweep from $g = 0.4 \times w$ for which the magnet's semicircular heads are in contact (for the perpendicular neighbouring magnets at the vertex site) to ensure that we probe the smallest possible gaps. The first four lattices in each series have a gap smaller than the magnet width, which was not reported in the literature, as per the understand-

ing of the author of this thesis.

To finish the description of the sample design, we note that we have opted for lattice size 30×30 vertices. Such a lattice then consist of 1860 individual magnets and each vertex constitutes of 4 magnets (there are no incomplete vertices at lattice edges). Maximum array size ($w = 200$ nm, $g = 1000$ nm) is 61×61 µm, ensuring that even the largest lattice can be imaged by a single MFM scan, which is convenient both for the measurement and also the evaluation.

5.2 Sample fabrication and SEM characterisation

The sample considered here was fabricated by our usual lift-off process, with the lithography carried out by 80 kV electron beam writer *Nanobeam Nb5* at Institut Néel. Series of conventional square lattices with varied gaps (listed in Tab. 5.1) were patterned with eight different exposure doses (from $D = 600$ to 1300 µC/cm^2, with step of 100 µC/cm^2) and each series for given magnet width and dose was repeated four times. We note that all the lattices were patterned on a single 10×10 cm^2 Si substrate. The reasoning for replicating each series four times serves two primary purposes. First, once the optimal dose that produces high-quality structures is determined, we can gather data from multiple series of design-wise identical lattices. This approach enhances the statistical reliability of the results without the necessity to repeat the demagnetisation protocol several times. Second, replicating each series across different locations on the sample reduces the risk of encountering damaged lattices. This precaution accounts for potential local fabrication flaws, which could arise from impurities or insufficient adhesion.

The dose sweep was designed according to previous experience in a way that it starts with a dose which is on the lower limit of the optimal dose window ($D_1 = 600$ µC/cm^2) and slowly progresses towards the higher doses for which we expect higher quality of the fabricated structures. However, a higher dose generally leads to a slight enlargement of structures (essentially positive bias of the design), which might lead to undesirable (and undesigned) melting of the magnets at the vertex sites for small gaps. With the designed dose sweep, we aim to find an optimal dose(s) that yields high-quality structures and ensures that unconnected individual islands still form the lattices with small gaps.

In order to assess the fabrication quality and to evaluate the smallest achieved lattice spacing (i.e., the smallest gap for which no melting is present), we have conducted detailed SEM imaging across the lattices fabricated with different exposure doses. Fig. 5.2 shows SEM details of fabricated conventional square lattice

($w = 100$ nm, $g = 140$ nm) captured with a stage tilt of 60°. The best shape quality is observed for the highest dose ($D_8 = 1300$ µC/cm^2). On the other hand, for the dose $D_2 = 700$ µC/cm^2, the shape quality is rather poor. For this study, we have decided to work with lattices exposed with doses ranging from $D_5 = 1000$ µC/cm^2 to $D_8 = 1300$ µC/cm^2, which yield nanomagnets of acceptable shape quality. The structures exposed with lower doses mostly suffer from lower edge quality and show less smooth top surfaces.

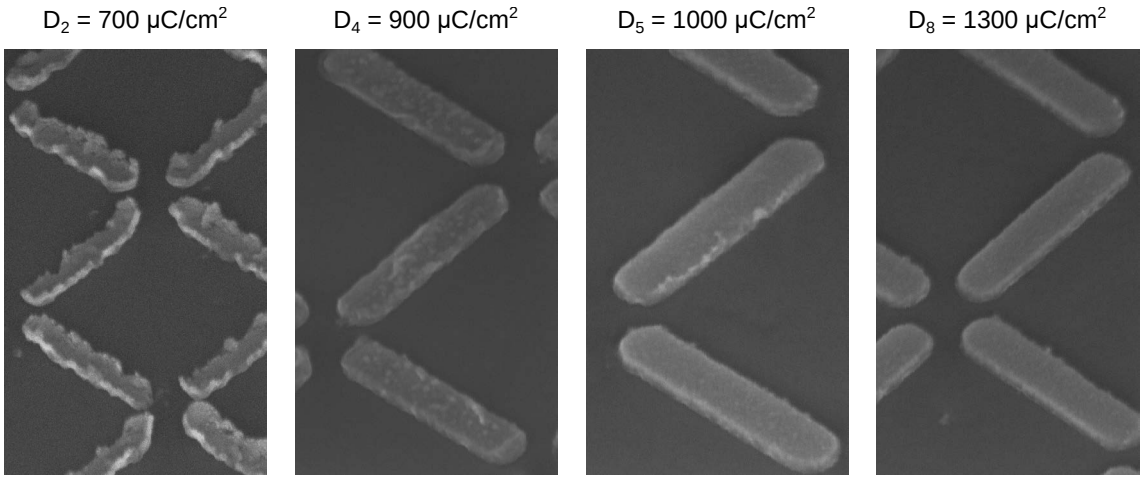

Fig. 5.2: Tilted (60°) SEM details of lattices with nominal width $w = 100$ nm and nominal gap $g = 140$ nm (lat. nr. 6) for different exposure doses (indicated above each image).

The next step is to evaluate for which designed gap the melting together of the nanomagnets at the vertex site will occur and to establish whether this critical gap will differ across exposure doses. Fig. 5.3 shows SEM details taken at the approximate centre of lattices with magnet width $w = 100$ nm for previously selected dose range D_5–D_8 and for lat. nr. 4–6. The red circles highlight observed tiny connections between neighbouring magnets at the vertex site (to be on the safe side, we consider even the tiniest connections).

This analysis allows us to conclude that for the dose range D_5–D_8 lattices with nr. 6–24 are indeed formed by individual (unmelted) islands. Lattices with nr. 4 and 5 can be considered as transition between individual and melted islands (we will show later that these tiny connections do not significantly alter the vertex populations). For the lattices with nr. 3, the connecting bridges between perpendicular magnets are more evident. For the lattice nr. 2, we observed the formation of an essentially connected square grid with holes at the vertex site (similar to the geometry we studied elsewhere [26]. Lattices with nr. 1 also forms connected square grids, but defects are present at the vertex sites (resist masking the "hole" is either not lifted-off or fell to the side, leading to missing magnetic material).

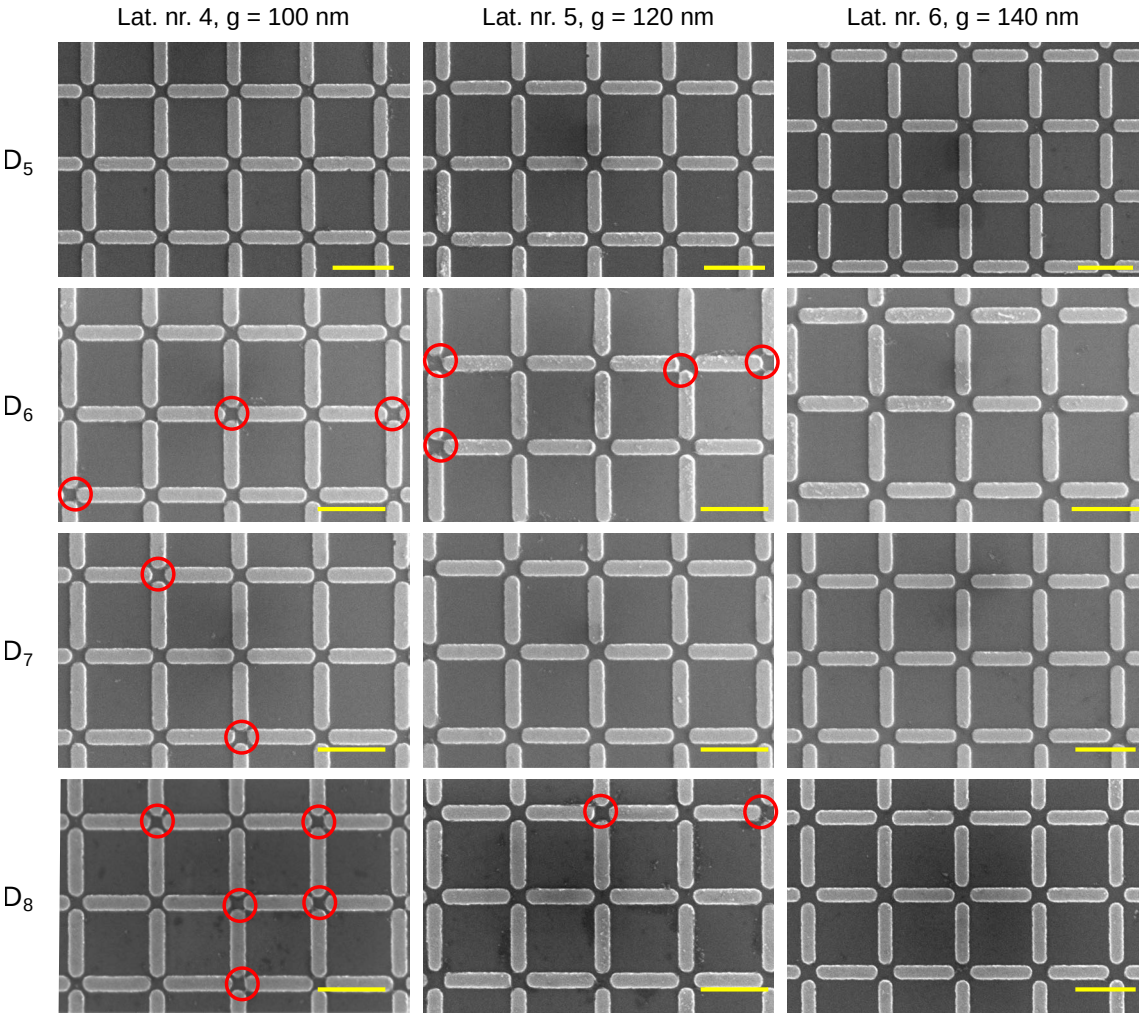

Fig. 5.3: SEM details taken approximately at lattice centres of lattices with width $w = 100$ nm. Rows correspond to different exposure doses (indicated on the left) and columns to different nominal gaps/lattice numbers (indicated above). Yellow bar represents 500 nm in all images. Red circles highlight magnets in contact (i.e. there is a tiny bridge connecting perpendicular neighbours at the vertex site).

We have conducted the same assessment for the lattices with nanomagnet width $w = 150$ nm, the results are provided in Fig. 5.4. For those lattices, we observe that the lattices nr. 4–24 are formed by individual nanomagnets. For the lat. nr. 3, we observe melting for doses D_6–D_8, while for the D_5, we observe that the magnets are still not in contact. For the lat. nr. 2, we again observe the formation of fully connected square grids with holes of varied pillow-like shapes. The lat. nr. 1 shows the same connected grids with defects as for lattices with the magnet width $w = 100$ nm.

To conclude, we have established that the majority of the fabricated series are formed by individual nanomagnets (lat. nr. 6–24 for the width of magnets 100 nm and lat. nr. 4–24 for the width of 150 nm). These ranges are valid for exposure

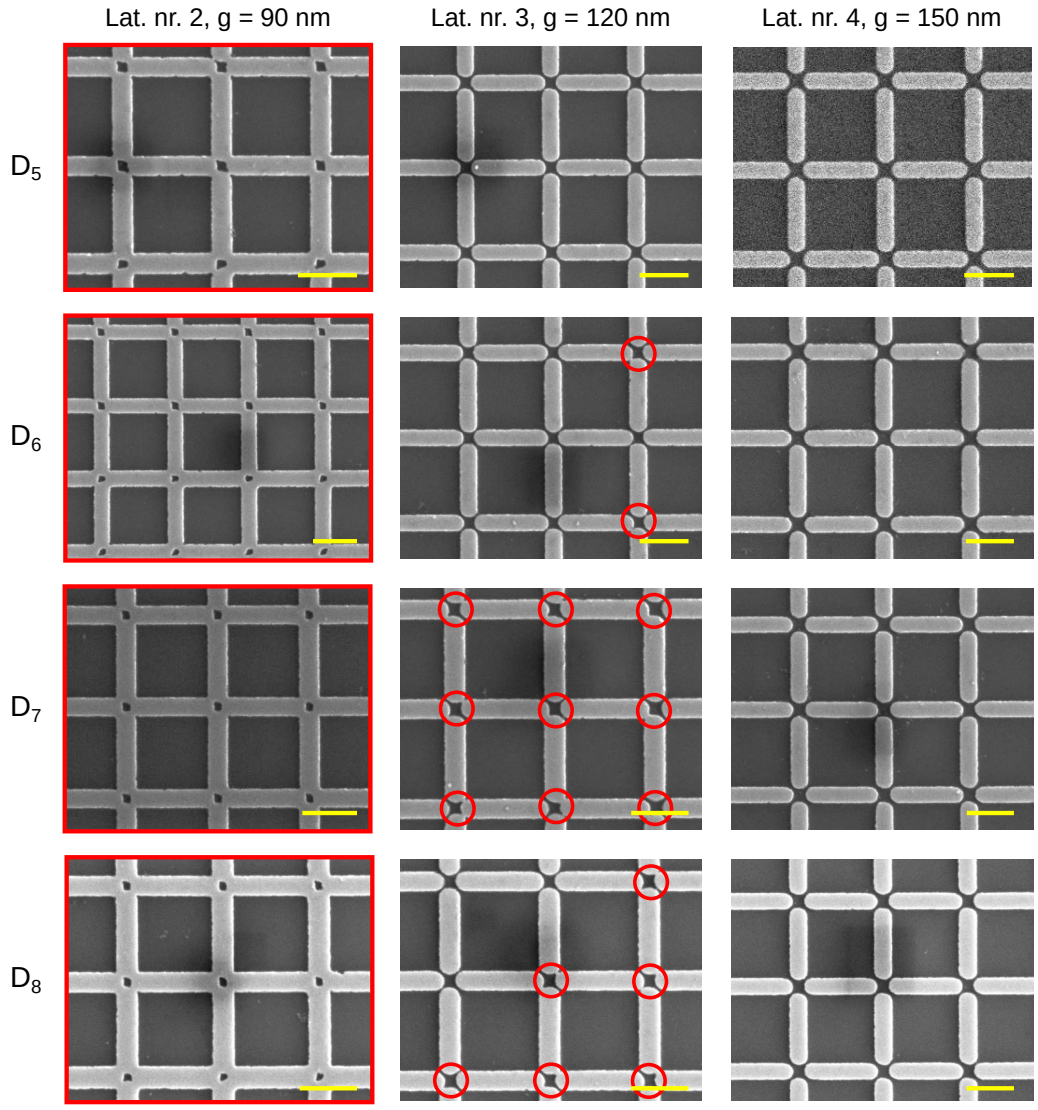

Fig. 5.4: SEM details taken approximately at lattice centres of lattices with width $w = 150$ nm. Rows correspond to different exposure doses (indicated on the left), and columns to different nominal gaps/lattice numbers (indicated above). Yellow bar represents 500 nm in all images. Red circles highlight magnets in contact (i.e. there is a tiny bridge connecting perpendicular neighbours at the vertex site). Red frames highlight fully melted lattices with holes at the vertex sites.

doses D_5–D_8. Hence, using SEM imaging, we have identified the area of interest with lattices suitable for our experiment.

5.3 Experimental results

In order to bring the lattices to their low-energy manifolds, we have employed a 72h long ac field demagnetisation protocol (with sample rotation). Lattices belonging

to the area of interest (based on the SEM assessment described above) were then imaged by magnetic force microscopy. The spin configurations were then evaluated based on the obtained MFM images, which enabled us to extract all characterising quantities of our lattices, such as vertex populations or spin correlations. As the collected dataset is quite extensive (we have measured more than 340 different lattices across different widths and exposure doses), we will provide only selected representatives of the series in the text and complete example series in the Appendix of the thesis. In the following, we will primarily focus on the global properties, such as the vertex populations as a function of the gap.

5.3.1 Lattices with magnet width 100 nm

Fig. 5.5 shows three measured magnetic configurations and their associated spin and vertex maps. These three configurations are selected as representatives of the entire gap sweep series (magnet width $w = 100$ nm), full series is provided in Sec. A.1. Fig. 5.5a shows the image of lat. nr. 6, the smallest gap, for which the lattice consists of individual (unmelted) islands. Fig. 5.5c shows the image of lat. nr. 24, which is the largest gap in the designed series, and Fig. 5.5b shows the image of the lat. nr. 15, which is in the middle of the suitable gap sweep range (for convenience, the images are shown as equal size).

At this point, it is instructive to recall what is the ground-state configuration of a conventional square lattice. Regardless of the gap size or magnet width, the magnetostatic coupling strength between the perpendicular neighbouring magnets J_1 is always stronger than between the collinear magnets J_2. This means that the type I vertices have the lowest energy and the ground state is antiferromagnetically ordered, two times degenerate, and consists of a tessellation of type I vertices.

Looking at the vertex/spin map obtained experimentally for the gap $g = 140$ nm (see Fig. 5.5d), one can see that the ground-state configuration is approached. The lattice is dominantly populated by type I vertices (approx. 85 %), which form large domains (highlighted by light green and light blue colours to ease the recognition of separate domains). These type I domains are separated by domain walls, formed by mostly type II vertices (approx. 14 %). A small fraction of type III vertices (approx. 1 %) is present and exclusively incorporated within the domain walls. This result is consistent with what we reported above for different sample (see Fig. 4.8) and with previous studies originating from our group [30, 31]. Our result surpasses other reported studies which employed various field demagnetisation protocols [55–57, 124], judged by achieved type I vertex fraction (or nearest-neighbour pairwise spin correlator). However, our result still somewhat underperforms what was reported for the at-growth thermalisation equilibration [40].

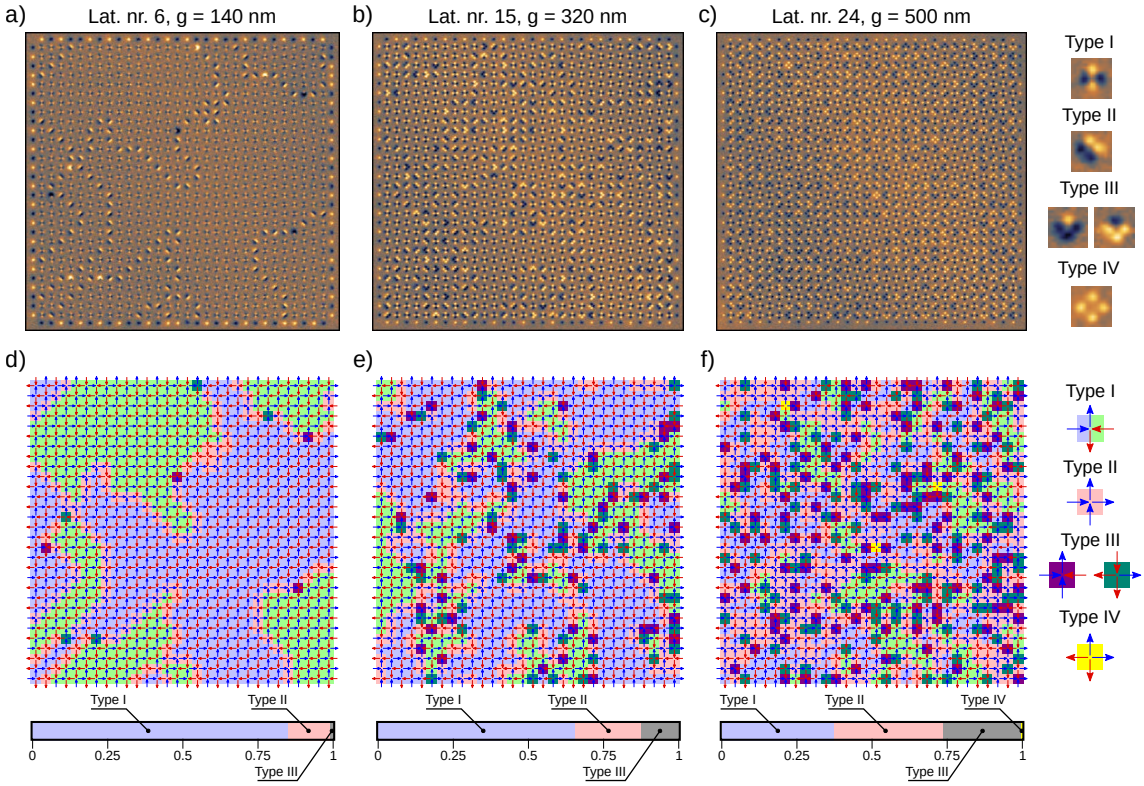

Fig. 5.5: a-c) Magnetic images of conventional square lattices ($w = 100$ nm) with gaps $g = 140\,\text{nm}$, $320\,\text{nm}$ and $500\,\text{nm}$ (corresponding lat. nr. 6, 15 and 24, from left to right). d-f) Spin and vertex maps extracted from (a-c), each map is below its respective magnetic image. The legends for interpreting the magnetic images and spin/vertex maps are provided on the right. Below each spin/vertex map is a stacked bar chart indicating the vertex populations of the respective map above. The images belong to one series of lattices exposed with exposure dose $D_7 = 1200\ \mu\text{C/cm}^2$.

Pivoting back to the results provided in Fig. 5.5, one can see how the increase of the gap, which leads to the weakening of the coupling strengths, affects the captured configurations. For the gap $g = 320$ nm (see Fig. 5.5e), the type I population exhibits an approximate 20% reduction, along with a decrease in the average domain size and an increase in their overall number. Correspondingly, the type II population has increased by approx. 9 % and type III population by approx. 11 %. While the type II vertices form mostly one-vertex-wide domain walls again, similar to the gap $g = 140$ nm, the type III vertices start forming small clusters that connect the type II domain walls. For the largest gap in the series $g = 500$ nm (see Fig. 5.5f, the population of type I vertices is further reduced by approx. 28 % at the expense of type II and type III vertices. Type I domains are further divided into smaller patches, and type II vertices start to form patches as well (or this can be described as widening of the domain walls). Type III vertices then form larger clusters or

appear as single vertices and are generally more evenly distributed over the whole lattice. Even three type IV vertices are observed, showing a significant weakening of the coupling strengths, as those never appear for the lattices with small gaps.

Henceforth, our analysis will shift towards examining the collective characteristics of the entire series under study. To facilitate this, we have plotted the vertex populations derived from individual MFM images belonging to one series of lattices with varying gaps (see Fig. 5.6, $w = 100$ nm, $D_7 = 1200$ µC/cm^2).

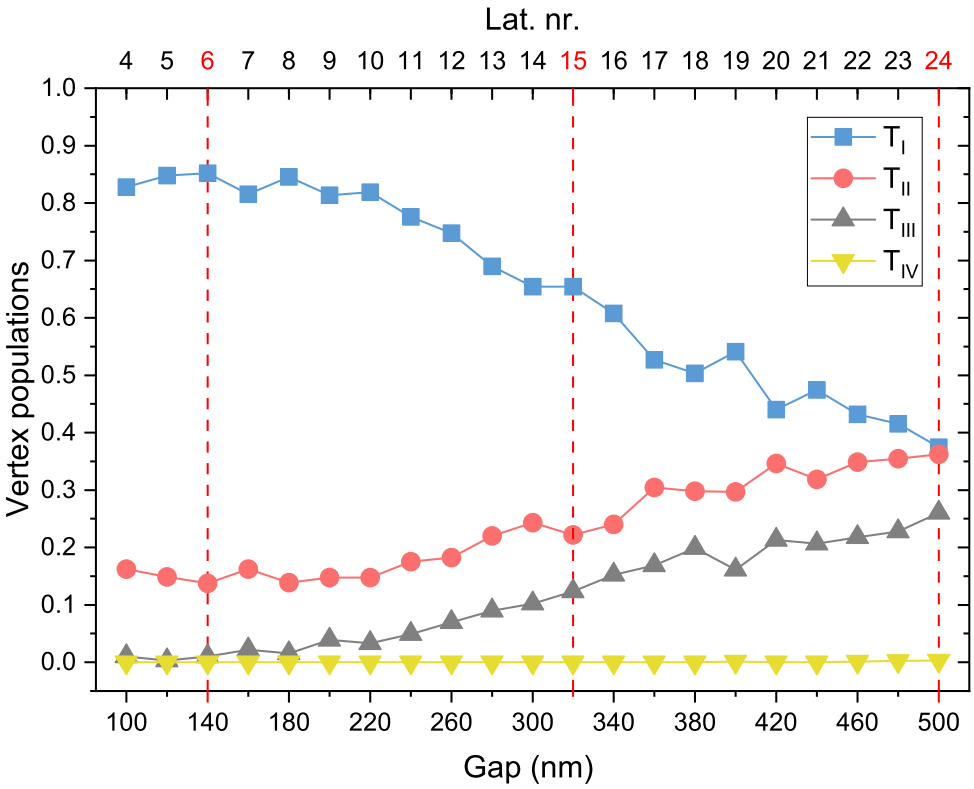

Fig. 5.6: Evolution of the vertex populations as a function of gap for one series of conventional square lattices ($w = 100$ nm, $D_7 = 1200$ µC/cm^2). Three lat. nr./gaps, for which MFM images and spin/vertex maps are presented in Fig. 5.5 are indicated by red dashed lines. The full symbols denote experimental data. The lines serve solely as a visual guide.

It is worth noting that the series under discussion is the same from which we have presented the exemplar of the three lattices in Fig. 5.5. Notably, within this series of 21 lattices (lattice numbers 4 to 24), we observe an absence of defects at the spin level (i.e. missing magnets). This absence of missing spins is a testament to a well-tuned fabrication process and also showcases the capabilities of the electron beam writer, the *NanoBeam nB5*.

Looking at the trends for the vertex populations as a function of gap (Fig. 5.6),

we observe how the weakening of the coupling strengths leads to significant changes of the vertex type distribution. In most of the gap range (lat. nr. 8–24), we observe a linear-like reduction of type I population at the benefit of type II and III vertices. However, even for the largest gap in the series (lat. nr. 24, $g = 500$ nm), the system is still correlated, as the vertex populations are far from what is expected for the uncorrelated (paramagnetic) configuration. For such a configuration, the vertex fractions correspond to the vertex degeneracy (i.e. 12.5 %, 25 %, 50 % and 12.5 % for type I, II, III and IV, respectively).

Interestingly, the vertex population of type I seems to saturate for the gaps smaller than approx. $g = 200$ nm and further reduction of the gap does not lead towards increasing the type I population. Even if we exclude the lat. nr. 4 and 5 from the consideration[1], we observe that for lat. nr. 6–8, the type I fraction essentially plateaus at approx. 80-85 %, which starkly contrasts with the rest of the series (lat. nr. 9–24). This is an unexpected result, which we will discuss later. We will also show that for the lattices with magnet width $w = 150$ nm, the trend change for the small gaps becomes even more pronounced.

As we have measured and evaluated three additional series that have identical fabrication parameters (same design, same dose) as the series presented in Fig. 5.6, it is natural to aggregate the results to improve the statistical reliability. The aggregated plot of the vertex populations as a function of the gap for the four series is provided in Fig. 5.7. The data for the individual series are shown as open symbols, and the averaged data are denoted by full symbols with lines to guide the eye. The chart shows strong agreement across the four series and only minor variations between them. Some variation is expected, as we are working with lattices of limited size (30×30 vertices). We note that for the 84 lattices belonging to the four series, we observe only four having a defect on a spin level (i.e. missing magnet; at most, 3/1860 spins are missing). This low rate of defects means that the structural disorder in our lattices is essentially negligible.

Looking at the aggregated chart of vertex populations provided in Fig. 5.7, we clearly observe the saturation of type I vertices for the small gaps, as we did for the individual series (Fig. 5.6). We marked the lat. nr. 8 ($g = 180$ nm) by green dashed line as a threshold at which the linear increase of the type I vertices, observed for the majority of the series (lat. nr. 9–24) changes to a flat value. By a green dashed line, we marked the lattices (4 and 5) for which we observed the formation of minute

[1] For lattice number 4, we detected the formation of minute connections between perpendicularly neighbouring magnets at vertex sites for dose D_7 (refer to Fig. 5.3). In the case of lattice number 5, the formation of such connections for dose D_7 was not observed; however, this phenomenon was noted for doses D_6 and D_8. Consequently, to err on the side of caution, we also consider the potential for bridge formation in lattice number 5 for dose D_7.

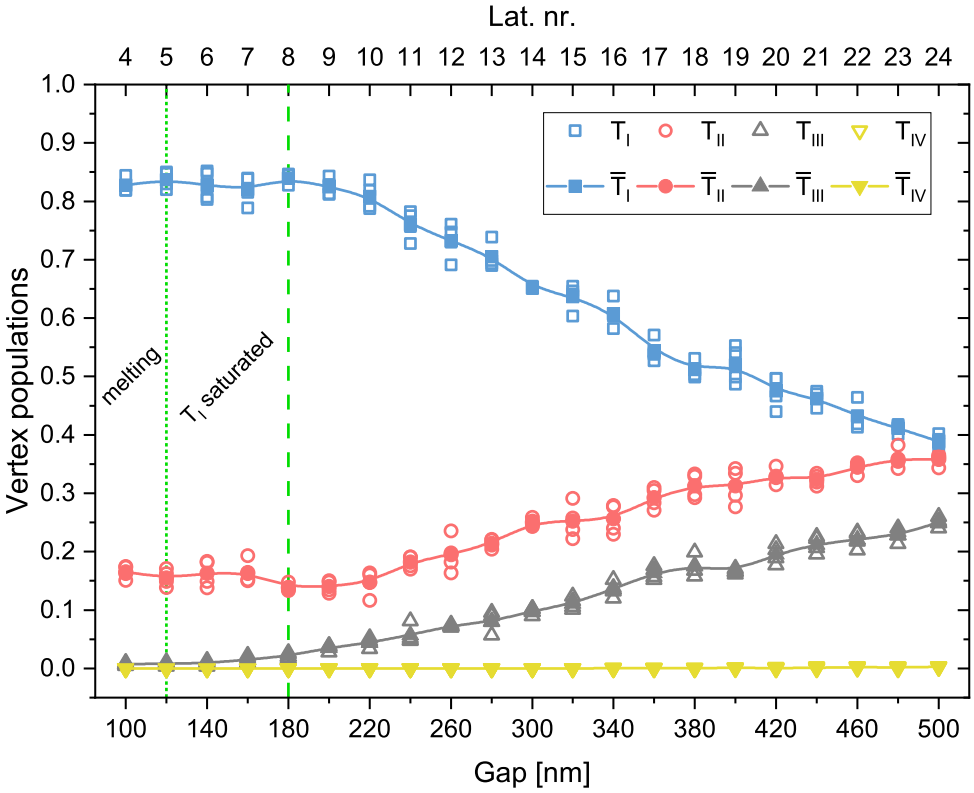

Fig. 5.7: Evolution of vertex populations as a function of a gap for a set of four design-wise identical series of conventional square lattices (w = 100 nm, D_7 = 1200 µC/cm^2). The open data markers denote experimental results for the four series. The full markers show the average values. The lines connect the average values and are provided as a visual aid.

connections between the magnets. We will now focus on the outcomes observed for lattices featuring a magnet width of w = 150 nm. We will discuss potential explanations for the occurrence of type I vertex population saturation for narrow gaps later.

5.3.2 Lattices with magnet width 150 nm

In the following, we report the results obtained magnet width $w = 150$ nm. We will follow the same steps as for the lattices with magnet width $w = 100$ nm, for which we have reported the results above. Fig. 5.8 shows three MFM images and associated spin/vertex maps as representatives of the gap sweep series, full series is provided in Sec. A.2. Generally, we observe a similar effect of the gap increase on the captured configurations.

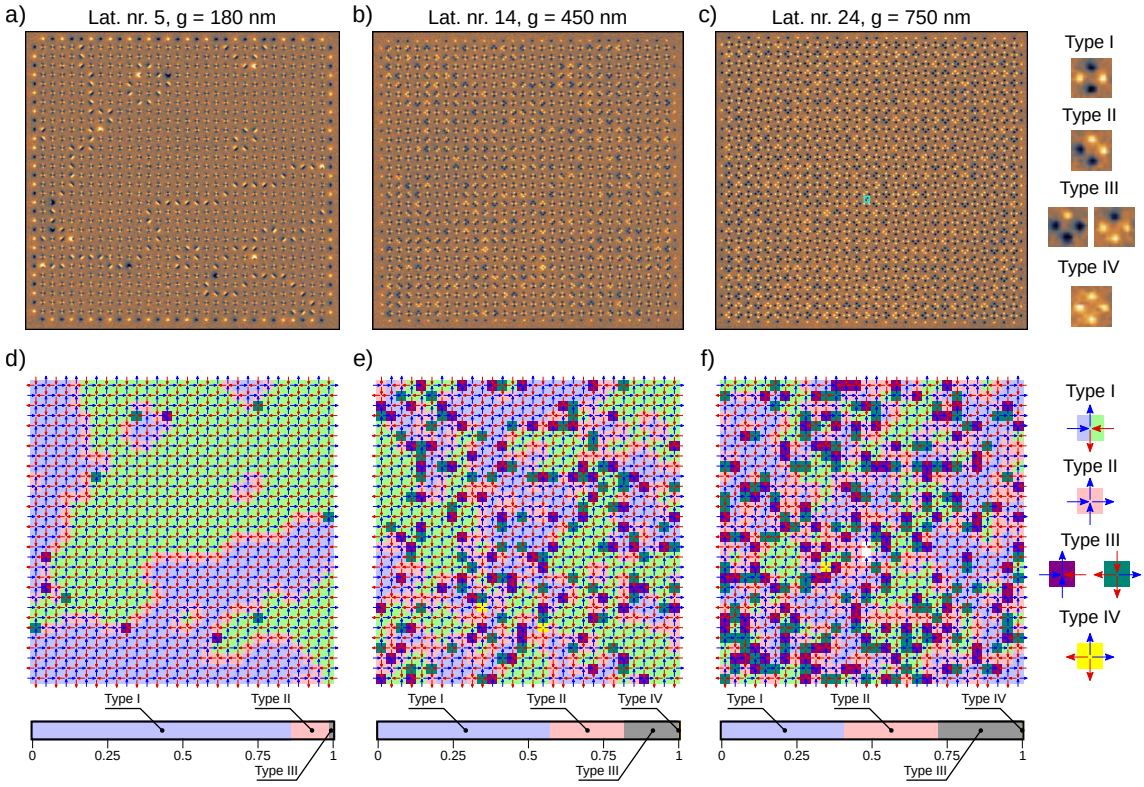

Fig. 5.8: a-c) Magnetic images of conventional square lattices ($w = 150$ nm) with gaps $g = 180\,\text{nm}$, $450\,\text{nm}$ and $750\,\text{nm}$ (corresponding lat. nr. 5, 14 and 24, from left to right). d-f) Spin and vertex maps extracted from (a-c), each map is below its respective magnetic image. One multi-domain magnet is observed in (c), highlighted by a cyan frame. As we cannot assign an Ising value to it, there is one missing spin in (e). The legends for interpreting the magnetic images and spin/vertex maps are provided on the right. Below each spin/vertex map is a stacked bar chart indicating the vertex populations of the respective map above. The images belong to one series of lattices exposed with exposure dose $D_5 = 1000\ \mu\text{C/cm}^2$.

For the gap $g = 180$ nm (Fig. 5.8d), we again observe configuration that approaches the ground-state ordering. The ratio between type I, II and III vertices is similar to what we reported for the lat. nr. 6 ($w = 100$ nm, see Fig. 5.5d). Again, we observe large domains of type I vertices, separated by type II domain walls, that

occasionally host type III vertices. The only difference compared to lat. nr. 6 ($w = 100$ nm) is that all domain walls are not connected to the lattice edges, and we observe a few small type II domain loops encapsulating small type I domains within large type I domains. The amount of charged defects (type III vertices) is only slightly higher (9 counts for $w = 100$ nm and 12 counts for $w = 150$ nm).

Looking at the opposite end of the gap series (see Fig. 5.8f), we observe configuration that is very similar to what we observed for the largest gap in the $w = 100$ nm series (Fig. 5.5f, both in vertex populations and in how the vertices are spatially distributed over the lattice).

Noticeably, for the gap $g = 450$ nm (Fig.5.8e), we observe a different balance between the vertex types compared to lat. nr. 15 ($w = 100$ nm, Fig. 5.5e). With the increase of the gap size, we observe a faster reduction of type I vertices at the expense of type II and III vertices for the lattice with magnet width $w = 150$ nm. Additionally, we also see a faster increase in the type III vertex population. We note that both lattices under comparison belong roughly to the centre of the studied gap series.

The next step is to examine the evolution of the vertex populations as a function of the gap sweep. Fig. 5.9 presents a chart depicting the vertex populations, derived from individual MFM images, within a single series of lattices with varied gaps ($w = 150$ nm, $D_5 = 1000$ µC/cm^2). From this series, we provided the three exemplars MFM images with their respective spin/vertex maps in Fig. 5.8. For this series as well, we do not observe any structural defect on the spin level. However, for large gaps, we rarely observe magnets forming multi-domain states (three lattices have one or two multi-domain magnets). For reference, each lattice is formed by 1860 spins, so the multi-domain defect level is very low. As we cannot assign an Ising value to those multi-domain magnets, we treat them as a missing spin when evaluating the spin configurations (an example is provided in Fig. 5.8f). Looking at the provided plot of the vertex populations, we observe a similar trend as for the $w = 100$ nm series. There are, however, several differences.

Firstly, we do not observe a saturation for type I vertices for small gaps, but we observe a reversal of the trend (for which the magnets are still not melted together, see Fig. 5.4). This effect is unexpected and will be discussed later. Secondly, we observe that the decrease of the type I population as the gap is increased is faster for the part of the range (lat. nr. 5–10) than for the rest of the series (lat. nr. 11–24). We note that for the $w = 100$ nm series, the decrease of type I vertices seemed linear-like. Thirdly, we observe a smaller separation between the type II and type III trendlines, compared to the $w = 100$ nm series. These three observations show that the change in the width of the magnets has significant effects on the observed vertex populations, even though the magnet's aspect ratio remains the same.

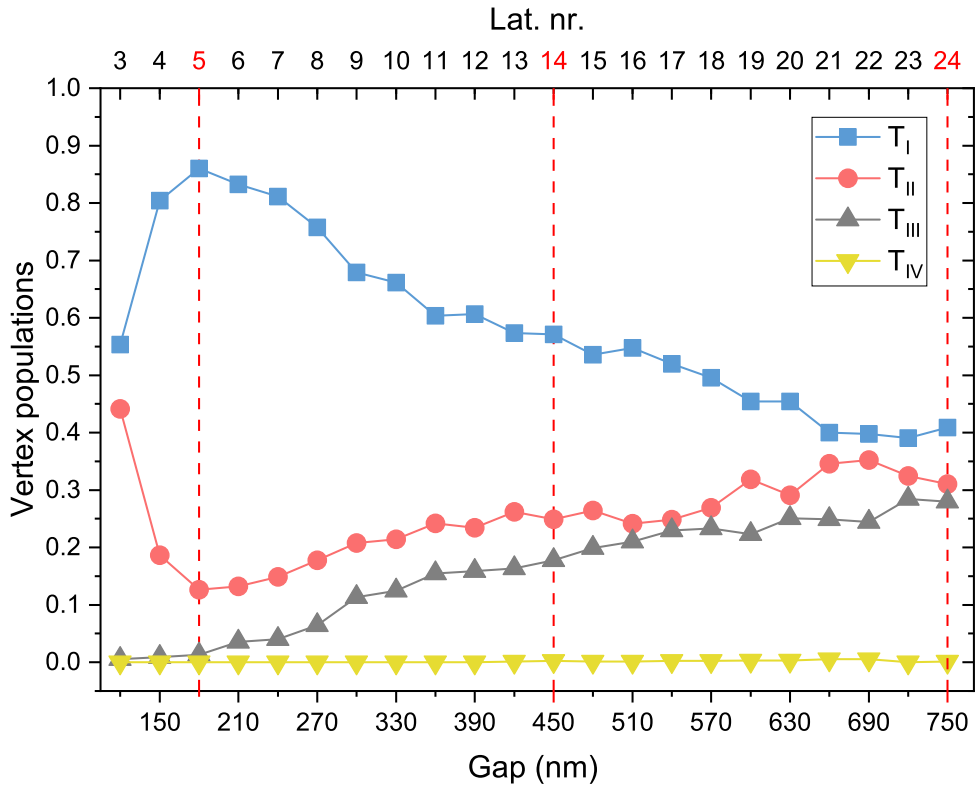

Fig. 5.9: Evolution of the vertex populations as a function of gap for one series of conventional square lattices ($w = 150$ nm, $D_5 = 1000$ µC/cm^2). Three lat. nr./gaps, for which MFM images and spin/vertex maps are presented in Fig. 5.8 are indicated by red dashed lines. The symbols denote experimental data. The lines serve solely as a visual guide.

Similar to the $w = 100$ nm series, we have accumulated measurements of three additional design-wise identical series for the magnet width $w = 150$ nm (all for the same dose $D_5 = 1000$ µC/cm^2). In two of the series, lat. nr. 3 and 4, measurement was not conducted due to observed defects. Besides, the vast majority of lattices were found to be defect-free. Only for 10 lattices out of 84, we could not extract the orientation of each spin, mostly due to the multi-domain state or impurities preventing us from obtaining readable magnetic contrast. In the most severe cases among these 10 lattices, the orientation of 5 out of 1860 spins could not be determined.

Establishing the overall sound quality of the lattices within the four series, we have aggregated the results to improve their statistical reliability. The composite graph of the vertex populations as a function of gap for the four series ($w = 150$ nm, $D_5 = 1000$ µC/cm^2) is shown in Fig. 5.10. Open symbols denote data points for the individual series, while the full symbols show the average values. The lines connect the average values to provide a visual guide. Orange labels highlight the two lattice numbers (3 and 4), as they were measured only for two series (in the other two

series, significant defects were observed for those lattices).

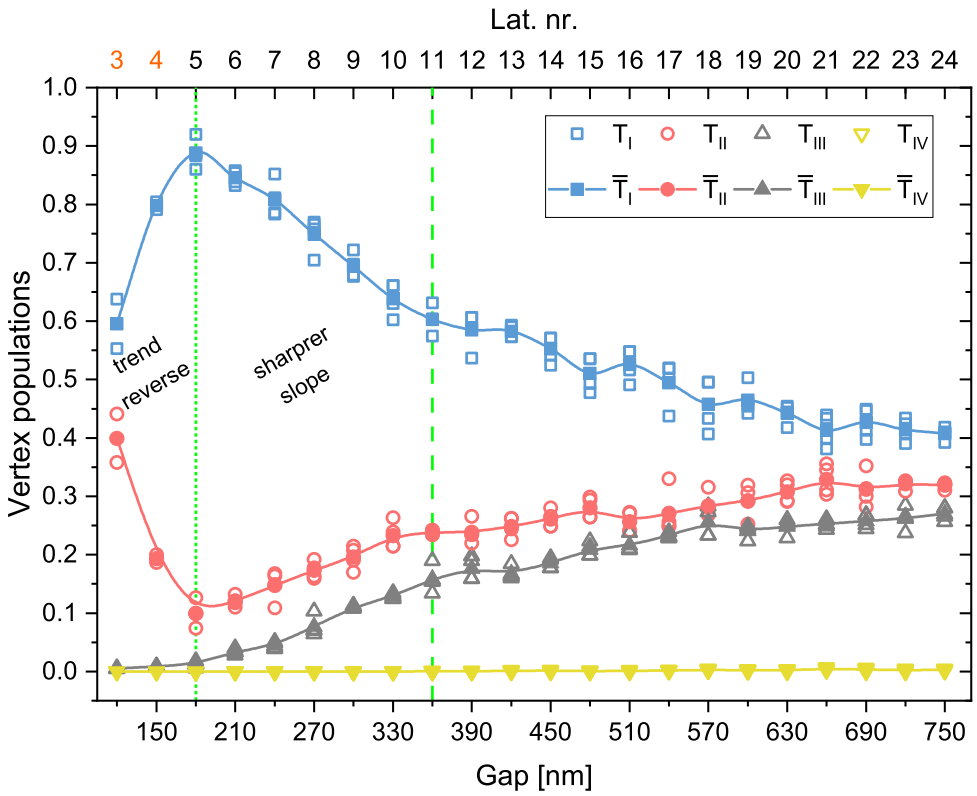

Fig. 5.10: Evolution of the vertex populations as a function of a gap for a set of four design-wise identical series of conventional square lattices (w = 150 nm, D_5 = 1000 μC/cm^2). The open symbols denote experimental results for the four series. The full symbols show the average values. The lines connect the average values and are provided as a visual guide. The two lattice numbers (4 and 5) measured only from two series are highlighted by orange labels.

Looking at the composite chart, we observe robust agreement across the four series, and the observations we made for the individual series plot (in Fig. 5.9) are also valid here. The green dotted line highlights the gap for which a reversal in population trends is observed, whereas the green dashed line indicates a shift in the trend's steepness.

5.4 Comparison with thermodynamics

The scientific question we want to address is whether it is possible to probe configurations representative of different effective temperatures by tuning the coupling strengths of athermal, field-demagnetised artificial square spin system. In other words, can the evolution of the captured magnetic configurations as a function of lattice parameter be viewed as a series of at-equilibrium states with different effective temperatures?

In order to address this question, we carried out Monte Carlo simulations with an Ising spin Hamiltonian, which enabled us to sample through the at-equilibrium thermodynamic properties of the chosen model. In this work, we decided to use the short-range model. Thus, only coupling strengths of the first and second neighbours (J_1 and J_2) are considered. This is an approximation, as our systems of single-domain islands are dipolar in nature. However, previous works studying similar conventional square lattice systems (at-growth thermalised) show that the captured physics is well described by a short-range model [39, 40]. In those works, the point-dipole approximation was used to estimate the vertex type energies (only six pairwise interactions between the four dipoles forming the vertex contribute to its energy).

Provided that the numerical model is aligned with our experimental system, we can then compare the properties of a series of experimentally studied lattices with increasing gaps against the thermodynamic evolution of the model.

5.4.1 Coupling strength estimation

To align the numerical model with the actual physical system, we performed a series of micromagnetic simulations, which enable us to estimate the values of the coupling strengths as a function of the lattice parameter. Compared to estimating the interactions based on the magnetic charges (dumbbell model) [68, 124] or point-dipole approximation [39, 40], the micromagnetic approach accounts for the magnetisation texture of the islands, which is not exactly uniform, particularly at their both extremities [86, 109–113].

We thus computed the micromagnetic energy of type I, II and III vertices with increased magnet-to-magnet distance, utilising the MuMax3 software [75]. The simulations are designed to closely follow both the geometrical and the material parameters of the lattices studied experimentally. Thus for the series of $w = 100$ nm lattices the magnets have size $500 \times 100 \times 25$ nm^3 and the magnet-to-magnet distance (i.e. gap) is varied from $g = 0.6 \times w$ to $5 \times w$ (with step of $0.2 \times w$). The simulation mesh is set to $2 \times 2 \times 25$ nm^3, and the simulation space is set to fit completely the full vertex for the largest gap value. Correspondingly, for the series of $w = 150$ nm

lattices, the magnets have size $750 \times 150 \times 25$ nm^3 and the gap is increased in the same fashion as for the $w = 100$ nm lattices. In this case, the simulation mesh is set to $4 \times 4 \times 25$ nm^3. For both simulation series, the nanomagnets have the stadium shape, as in the experiment. For the material definition, parameters commonly used for permalloy are set (saturation magnetisation $M_S = 800$ kA m^{-1}, exchange stiffness $A = 10$ pJ m^{-1} and magnetocrystalline anisotropy is neglected). The damping is set to $\alpha = 0.5$, and simulations are run at 0 K with no external field applied.

The coupling strengths between perpendicular neighbours J_1 and collinear neighbours J_2 are then calculated as follows:

$$J_1 = -(E_1 + E_2 - 2 \times E_3)\ /4, \tag{5.1}$$

$$J_2 = -(E_2 - E_3)\ /2, \tag{5.2}$$

where E_i ($i = 1,\ 2$ and 3) are the total vertex energies of type I, II and III, respectively (description of the energy calculation and results are provided in Methods in Sec. 2.1). Fig. 5.11 shows the results of the MuMax3 simulations for the $w = 100$ nm series of lattices. Fig. 5.11a shows an example of the geometry definition for two cases: $g = 100$ nm and $g = 500$ nm. The white areas correspond to the individual magnets, and for those areas, the material parameters corresponding to permalloy are defined. In the bottom panel, we show the six pairwise couplings ($4 \times J_1$, $2 \times J_2$) that contribute to the vertex energy. Fig. 5.11b shows the snapshots of final micromagnetic states (after the system is relaxed in the simulation) of the type I, II and III vertices (from left to right) for the two gaps (same as in Fig. 5.11a). The total energies of those three configurations are saved as an output of the simulation and are used to calculate the coupling strengths.

Fig. 5.11c then shows the plot of coupling strengths J_1, J_2 as a function of the gap. As expected, increasing the gap leads to reducing the coupling strengths, and the coupling strength for the perpendicular neighbours is always stronger than that of the collinear neighbours (i.e. $J_1 > J_2$) in the sampled range of gap values.

It is instructive to plot the ratio J_2/J_1 as a function of the gap (provided in Fig. 5.11d), as it provides clear insight on what is the expected ground-state ordering of the system. Interestingly, we observe that for small gaps, the ratio increases towards the ice condition ($J_2/J_1 = 1$). However, even for the smallest possible gap, for which the magnets do not touch ($g = 45$ nm, not shown in the chart), the condition is not reached ($J_2/J_1 = 0.85$) and stays on the side of $J_1 > J_2$. Therefore, from the magnetostatic point of view, the expected ground-state ordering is type I tiling for all studied gaps.

If we consider the range of gaps for which we observe unmelted magnets in the experiment ($g \leq 140$ nm), the values of the J_2/J_1 ratio lie in the interval

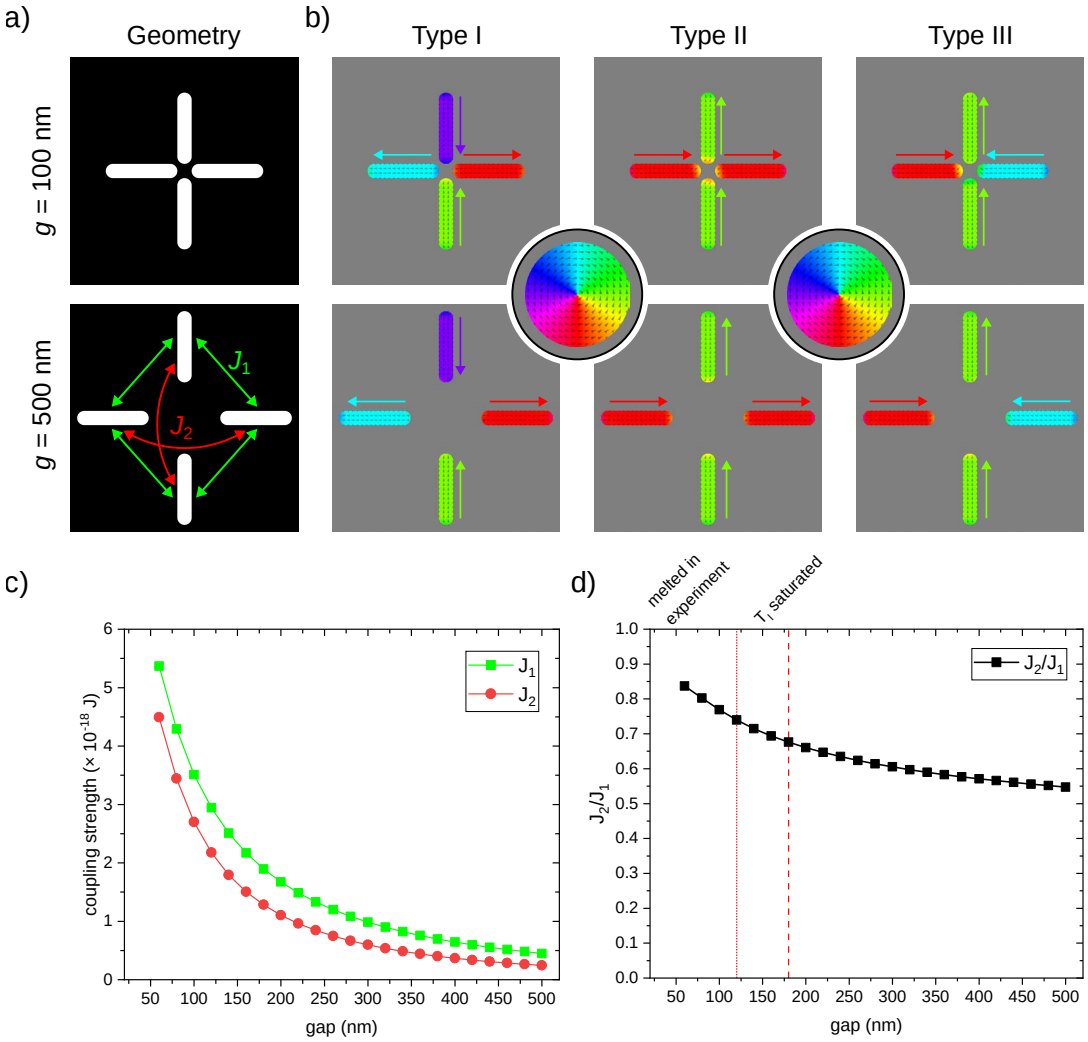

Fig. 5.11: a) Two examples of geometry definition for micromagnetic simulations for the lattices with magnet width $w = 100$ nm. In the bottom image the J_1, J_2 coupling strengths are illustrated. b) Snapshots of the final micromagnetic simulated states for type I, II and III vertices. The local direction of magnetisation is indicated by colour according to the provided colour wheel. The arrows next to individual magnets show the overall magnetisation direction to provide a visual guide. c) Plot of coupling strengths J_1 and J_2 as a function of the gap. The values of coupling strengths J_1, J_2 are computed using eq. 5.1 and 5.2, respectively. d) J_2/J_1 ratio as a function of the gap. The red dotted line indicates the gap for which we observed melting of the magnets in the experiment, while the red dashed line indicates the gap below which the population of type I vertices does not increase in the experiment.

$< 0.55; 0.71 >$. This is the interval of interest that will be probed in the Monte Carlo simulations (the $J2/J1$ ratio is used to define the coupling strengths for the model). At this point, it might seem that our effort to describe the experimental results by a single model is a lost battle, as the J_2/J_1 ratio is not constant across the

studied gap range. In fact, one could consider viewing our series of lattices as a set of different models, as for each gap, the value of J_2/J_1 ratio is different. However, we will show later that our approach (fitting the experimental data with a single model) works and provides a good agreement.

We now shift our focus to the series of $w = 150$ nm lattices, for which we have followed the same micromagnetic approach to obtain the estimates for the coupling strengths, as for the $w = 100$ nm lattices. As we have followed the same steps as above, we report only the results for the J_1 and J_2 coupling strengths and their ratio (see Fig. 5.12). Looking at the charts, the results are similar to the ones obtained for the $w = 100$ nm lattices. Naturally, the absolute value of the J_1, J_2 coupling strengths is slightly higher as the magnets have a larger volume (see Fig. 5.12a). The plot of the J_2/J_1 ratio (shown in Fig. 5.12b) reveals a trend very similar to the one of the $w = 100$ nm lattices. If we consider the range of gaps for which we do not observe the trend reversal of the vertex populations, we obtain an interval for the J_2/J_1 ratio $< 0.60; 0.76 >$.

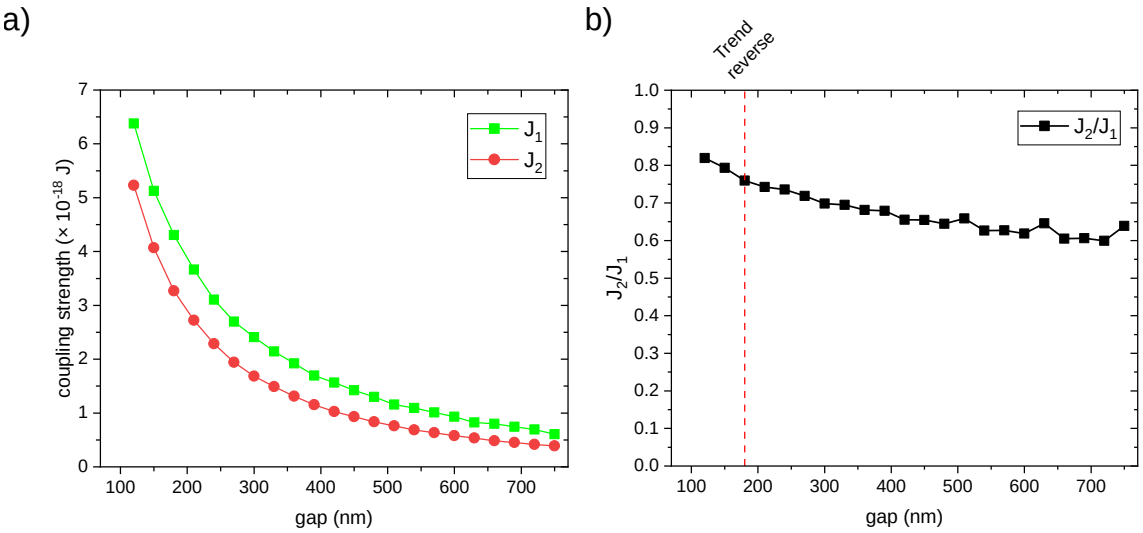

Fig. 5.12: Results of the MuMax3 simulations for the $w = 150$ nm lattices. a) Plot of coupling strengths J_1 and J_2 as a function of the gap. The values of coupling strengths J_1, J_2 are computed using eq. 5.1 and 5.2, respectively. d) J_2/J_1 ratio as a function of the gap. The red dashed line indicates the gap for which the trend of the vertex populations is reversed in the experiment.

To conclude, we have estimated the $J_2/J1$ ratio for both series of lattices studied experimentally ($w = 100$ and 150 nm) using micromagnetic simulations. This lets us know what J_2/J_1 ratio values to focus on with Monte Carlo simulations. The question of what happens for the small gaps (trend saturation for the $w = 100$ nm lattices and trend reversal for the $w = 150$ nm lattices) remains unanswered for now, and we will address it later in the discussion.

5.4.2 Probing the thermodynamic properties

The next step is to probe numerically finite temperature properties of the short-range square spin model using Monte Carlo simulations. The idea is to compute a series of simulations with different J_2/J_1 ratios sampling the interval estimated by micromagnetic simulations. Subsequently, we plan to compare the results of Monte Carlo simulations against the experimental data. We proceed as follows:

1. We compute a set of Monte Carlo simulations for different values of J_2/J_1 ratio (ranging from 0.50 to 1.00 with a step of 0.05). This range covers the interval of J_2/J_1 ratios estimated from the micromagnetic simulations.
2. We fit the above reported experimental data to the vertex populations obtained with the Monte Carlo simulations. Essentially, we fit a series of experimental quadruplets (vertex populations of all four vertex types for a series of lattices with varied gap) to the vertex population curves obtained by Monte Carlo simulations employing the least-square method.
3. We establish what value of J_2/J_1 ratio provides the best fit for each of the two averaged experimental series ($w = 100$ nm and $w = 150$ nm lattices).
4. We then compare the experimental averaged magnetic structure factors to the ones obtained with Monte Carlo simulations for the J_2/J_1 ratio selected in the previous point.
5. If the experimental data and Monte Carlo simulations agree both in the vertex populations and magnetic structure factors, we can consider our series of lattices with varied gap as a series of at-equilibrium states with different effective temperatures.

For the Monte Carlo simulations, we define the short-range Ising spin Hamiltonian as:

$$H = -\sum_{i,j|J_1,J_2} J_{i,j}\sigma_i\sigma_j, \tag{5.3}$$

where σ_i and σ_j are Ising variables on sites i and j of a square lattice, and only interactions between magnets coupled by J_1, J_2 coupling strengths are considered. The simulations were carried out for lattice size 30×30 vertices, equalling the lattice size used in the experiment. The simulations utilise a single-spin flip algorithm and open boundary conditions. The cooling-down procedure starts at $T/J_1 = 100$ and ends as the single spin-flip dynamics freezes. After each temperature step-down, first 10^4 modified Monte Carlo steps (mmcs) are used for reaching the thermal equilibrium and then measurements follow (also computed with 10^4 mmcs). Thus, at each temperature step of the simulation, we collect a large set of statistically independent configurations (10^4), from which we compute the mean values of vertex

populations and associated standard deviations (both per-vertex type).

Fig. 5.13 shows results of Monte Carlo simulations for two exemplar J_2/J_1 ratios out of the sampled interval. As expected, in both cases, the vertex population curves start from the value corresponding to the vertex degeneracy in the high-temperature limit. Similarly, we observe that pure type I ground state is closely approached in the low-temperature limit for both cases. However, we observe significant differences in how the vertex population evolves, especially for type II and III vertices, for the Monte Carlo temperature around units of T/J_1. As the effective temperature of field demagnetised lattices such as ours generally approximates the magnitude of J_1, selecting the J_2/J_1 ratio will be crucial to finding a good agreement between our experimental data and the Monte Carlo simulations.

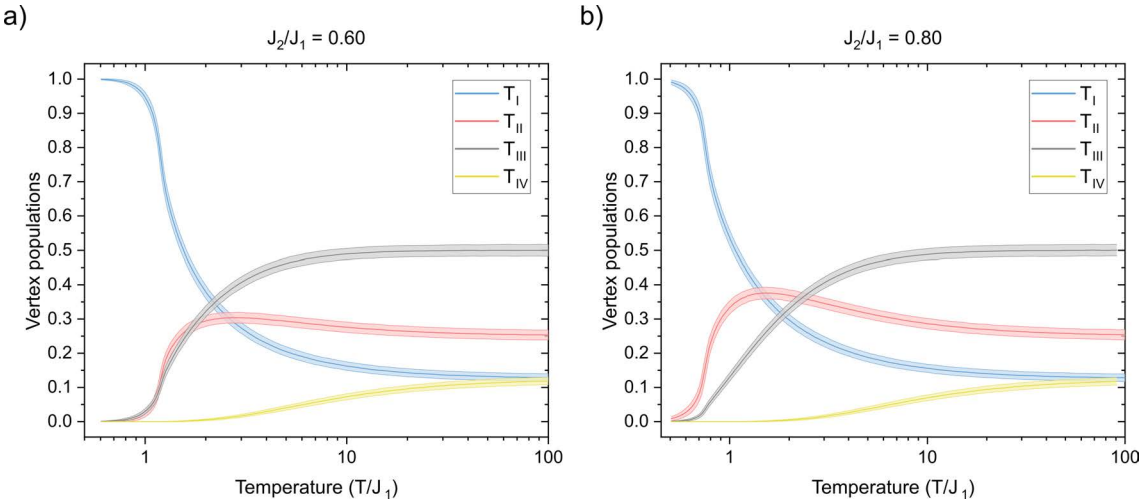

Fig. 5.13: Results of Monte Carlo simulations for a short-range square spin system for two distinct $J_2/J1$ ratios: (a) $J_2/J_1 = 0.60$ and (b) $J_2/J_1 = 0.80$. The vertex populations and their standard deviations are plotted as lines with enveloping error bands.

5.4.3 Results: $w = 100$ nm series

We thus proceed by comparing the experimental results (averaged series obtained for $w = 100$ nm, $D_7 = 1200$ µC/cm^2 lattices, see Fig. 5.7) against the vertex population curves obtained by Monte Carlo simulations to find what J_2/J_1 ratio provides the best fit. For now, we restrict the experimental data to lattices for which we do not observe the type I saturation (lat nr. 8–24, $g =$ 180 nm to 500 nm).

Fig. 5.14 shows the results of fitting the experimental data against the Monte Carlo simulated vertex population curves. For each experimental quadruplet (i.e., vertex populations of all four types per given gap), the best fit against the experimental data was found using the least-square method. The overall quality of the fit is determined as the average of the root mean square error calculated for

each quadruplet.

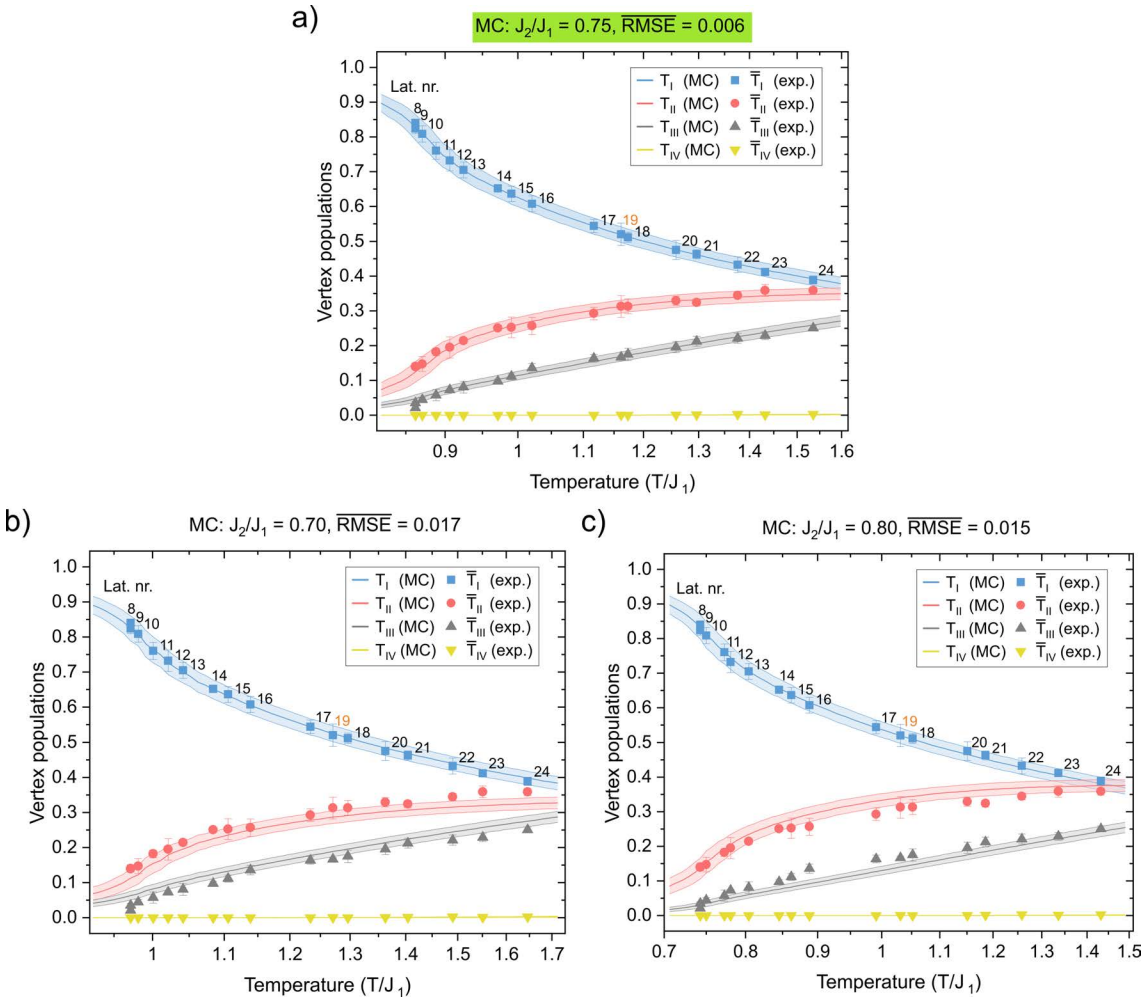

Fig. 5.14: Results of comparing the experimental data averaged over four series ($w = 100$ nm, $D_7 = 1200$ µC/cm^2) against Monte Carlo population curves for three different J_2/J_1 ratios: (a) $J_2/J_1 = 0.75$, (b) $J_2/J_1 = 0.70$ and (c) $J_2/J_1 = 0.80$. MC simulated populations are shown as lines with enveloping 1σ error bands. Experimental data are shown by symbols with their associated error bars indicating standard deviation. For data points belonging to type I experimental data, the lat. nr. is provided as a label next to each respective point. The mean RMSE indicates the quality of the agreement above each chart. The best fit is observed for the MC ratio $J_2/J_1 = 0.75$.

The figure shows that the best fit is reached for the MC set with ratio $J_2/J_1 = 0.75$ (see Fig. 5.14). The agreement between the experiment and the Monte Carlo simulation is remarkable in two ways. First, we observe that almost all experimental data points, except for the T_{III} vertices for the lat. nr. 8, fits within the 1σ bands of the simulated vertex population curves. We note that the simulations were carried out for lattice sizes identical to the experiment. The results indicate that our

experimental data can be well approximated by a single short-range model within the selected range of considered gaps.

Secondly, the ordering of the lattices in the sense of gap variation is preserved, except for one data point (lat. nr. 19, highlighted by the orange label in the chart). This means that we can view the gap as an experimental knob that allows for probing states characterised by different effective temperatures associated to a single model. This is quite a striking result if we take into account that the J_2/J_1 ratio, estimated by micromagnetic simulations for the $w = 100$ nm magnets (see Fig. 5.11d), dependents on the gap.

If we compare the J_2/J_1 value that provides the best fit ($J_2/J_1 = 0.75$) against the estimation based on micromagnetic simulations for the same range of lattices (lat. nr. 8–24, $J_2/J1 \in < 0.55; 0.71 >$), we see that the value that provides the best fit is above the estimated interval. At this point, it is worth noting that the estimated coupling strengths J_1 and J_2 are magnetostatic, as the simulations were carried out with no external magnetic field applied. However, the field demagnetisation is driven by an external magnetic field. The possible explanation for the quantitative disagreement is that J_2 is artificially increased due to the kinetic effects of the field demagnetisation protocol (during the field demagnetisation protocol, magnetisation reverses via an avalanche process, which favours the formation of polarised lines in the lattice, see numerical simulations of field demagnetisation protocol in Ref. [31], namely Videos 1 and 2 in the Supplementary Information).

Looking back at Fig. 5.14, we observe that increasing/decreasing the J_2/J_1 value by 0.05 (which is the step we used to sample through the J_2/J_1 ratio in the Monte Carlo simulations) leads to recovering lesser agreement between the experimental data and the simulations. In both cases (see Fig. 5.14b and 5.14c), we observe that especially the populations of T_{II} and T_{III} vertices are out of balance.

5.4.4 Results: $w = 150$ nm series

One might then wonder whether a similarly good agreement can also be found for the $w = 150$ nm series. We thus repeat the analysis of comparing the Monte Carlo simulations against the experimental data for the averaged series of $w = 150$ nm lattices (4 series, $D_5 = 1000$ µC/cm^2). The results are provided in Fig. 5.15.

Looking at the provided charts, we observe that the best fit is reached for the MC set with ratio $J_2/J_1 = 0.675$, as evidenced by the mean RMSE value provided above each chart (see Fig. 5.15). Even though we computed this additional MC set, the overall series agreement is slightly worse than observed for the $w = 100$ nm lattices. This is mainly due to a deviation of the experimental data from the Monte Carlo prediction observed for the low lattice numbers (i.e. smaller gaps).

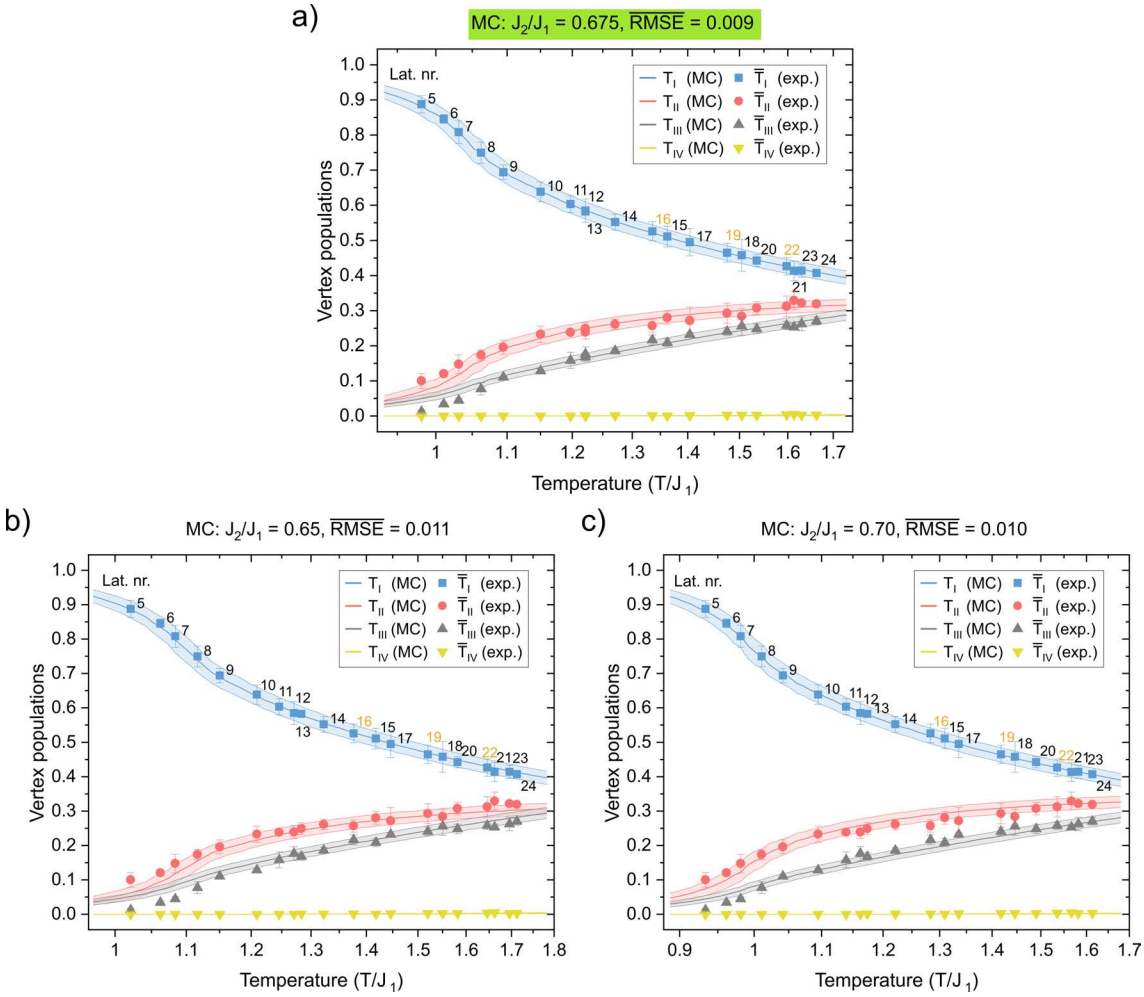

Fig. 5.15: Results of comparing the experimental data averaged over four series ($w = 150$ nm, $D_5 = 1000$ μC/cm^2) against Monte Carlo population curves for three different J_2/J_1 ratios: (a) $J_2/J_1 = 0.675$ (b) $J_2/J_1 = 0.65$ and (c) $J_2/J_1 = 0.70$. MC simulated populations are shown as lines with enveloping 1σ error bands. Experimental data are shown by symbols with their associated error bars indicating standard deviation. For data points belonging to type I experimental data, the lat. nr. is provided as a label next to each respective point. The quality of the agreement is indicated by the mean RMSE above each chart. The best fit is observed for the MC ratio $J_2/J_1 = 0.675$.

It is worth recalling that the estimate of the J_2/J_1 ratio obtained by micromagnetic simulations (see Fig. 5.12b) shows dependence on the value of the gap (smaller gap value corresponds to higher J_2/J_1 ratio). Thus, a more accurate representation of the data points for the low gap values could be reached only at the expense of lesser agreement for the rest of the series. This shows that our approach of representing the experimental data with a single model (single J_2/J_1 value) has limitations.

We have established above that the main deviation between the experimental

data and the simulations is observed for the low gap values (lat. nr. 5–7). Considering the quality of the agreement in the rest of the series, we have selected the ratio $J_2/J_1 = 0.675$ as the best fit (see Fig. 5.12a), as it most accurately represents the experimental data in the remainder of the studied range.

Even though the overall quality of the agreement is slightly lower for the $w = 150$ nm lattices compared to the $w = 100$ nm lattices ($\overline{\text{RMSE}} = 0.009$ in Fig. 5.12a compared to $\overline{\text{RMSE}} = 0.006$ in Fig. 5.11a, respectively), we still observe that the majority of the experimental data points lie within the 1σ bands of the Monte Carlo simulations, indicating good overall agreement for the series. Also, similar to the $w = 100$ nm lattices, we observe that the ordering of the lattices in the sense of gap variation is mostly preserved, except for three lat. nr. (indicated by orange labels in Fig. 5.12a). This shows that for the wider magnets, the tuning of the gap value also allows for the probing of states characterised by different effective temperatures corresponding to a unique spin model.

5.4.5 Results: correlation analysis

In the previous pages, we have reported robust agreement when comparing the experimental vertex populations with Monte Carlo simulations. One may wonder whether such agreement is sufficient to demonstrate that we probe at-equilibrium physics at different effective temperatures.

At this point, it is instructive to recall that spin configurations sharing similar (or even the same) vertex populations can have different properties. In other words, how the vertex types are distributed over the lattice matters. Calculating the magnetic structure factor is a convenient tool to obtain a global picture of how the system is ordered (see examples of distinct patterns for similar vertex populations in Fig. 4., Ref.[44]). Thus, to fully prove that the experimental results can be seen as a series of at-equilibrium states with distinct effective temperatures, it is necessary to observe not only the agreement with the vertex populations but also with the magnetic structure factors (i.e., the magnetic correlations).

Therefore, we have computed the magnetic structure factor as a function of temperature for the J_2/J_1 ratios, which provided the best fit for the experimental series ($J_2/J_1 = 0.75$ for the $w = 100$ nm lattices – see Fig. 5.14a and $J_2/J_1 = 0.675$ for the $w = 150$ nm lattices – see Fig. 5.15a). Similar to the vertex populations, the Monte Carlo MSF is averaged over a large number of configurations (10^4) for each temperature step. The simulated MSF can then be compared against the experimental MSF, averaged over four series, for both $w = 100$ nm and $w = 150$ nm lattices.

Fig. 5.16 compares the magnetic structure factors obtained by numerical simulation and those computed from the measured configurations. For both simulated

and experimental MSFs, three are shown, and the complete series of experimental MSFs is provided in the Appendix (see Fig. A.5 and A.6). The numerical MSFs are obtained for the ratio $J_2/J_1 = 0.75$, which provided the best fit for the vertex population curves (see Fig. 5.14a).

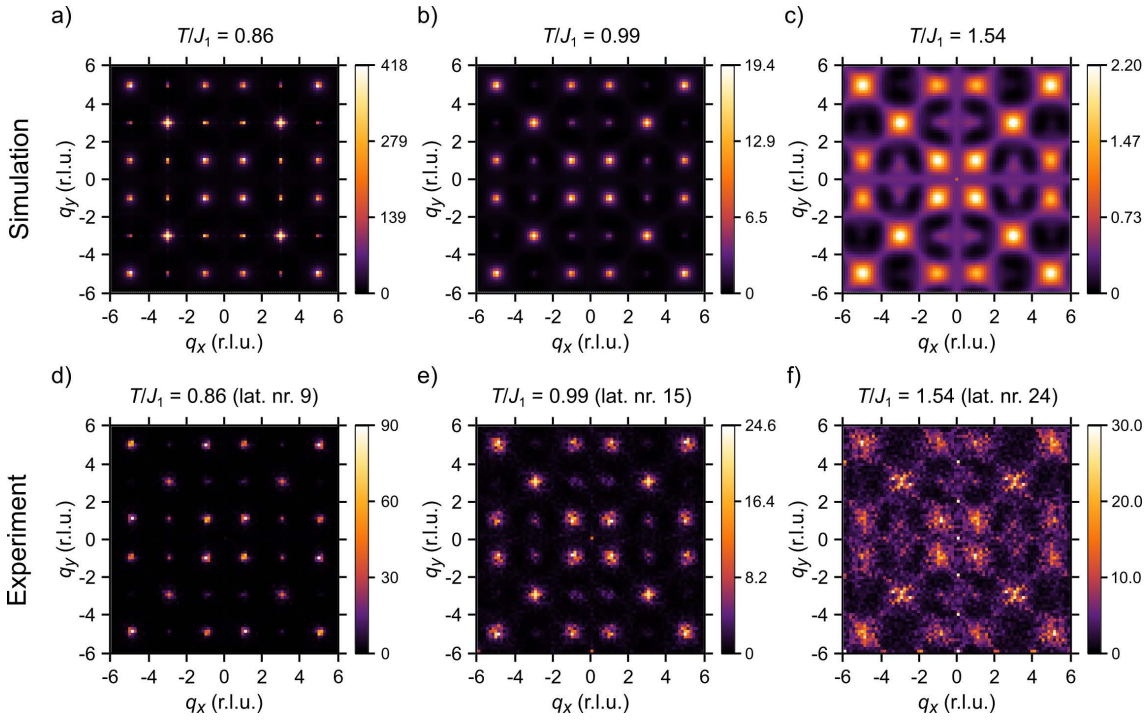

Fig. 5.16: (a-c) Magnetic structure factors calculated by numerical simulations for $J_2/J1 = 0.75$. Monte Carlo temperature for each intensity plot is provided above. (d-f) Experimental magnetic structure factors (averaged over four series, $w = 100$ nm, $D_7 = 1200$ µC/cm^2). The label above each intensity plot indicates the lattice number and the effective temperature, for which the best fit against the vertex populations simulated by Monte Carlo (with $J_2/J_1 = 0.75$) is obtained. All plots are computed for 81×81 points covering the area of $\pm 6 \times \pm 6$ $(\pi/a)^2$ in reciprocal space. The intensity scale bar is provided right next to each plot.

Looking at the first row of Fig. 5.16, we observe that for the lowest presented Monte Carlo temperature (first image on the left, Fig. 5.16a), the magnetic structure factor exhibits strong Bragg peaks characteristic of type I tiling, which approaches the ground-state configuration. As the Monte Carlo temperature is increased, we observe that the intensity of the peaks is lowered significantly and their width is increased (see Fig. 5.16b and 5.16c). This shows how the correlations of the system are weakening as the temperature is increased.

If we compare the experimental MSF against the respective numerical one above, a qualitative agreement is observed for the first two of them (see Fig. 5.16d and Fig. 5.16e). For the third one, obtained for the lattice with the largest gap in the

studied range, we observe that additional sharp peaks are present, which are not observed in the simulations (see Fig. 5.16f and Fig. 5.16c). This is not specific to the lattices with the largest gap, and we observe the formation of those peaks (same position, different intensity) for roughly the upper half of the considered gap range (lat. nr. 17–24, see Fig. A.5 and A.6). Comparison with computed MSF for different type II backgrounds shows that these peaks originate from clusters of type II vertices organised in a saturated-like manner (vertex net moment has a preferred direction). Therefore, for reason not currently identified, the field demagnetisation seems to be less efficient for the $w = 100$ nm lattices with larger gaps.

We now focus on the lattices with magnet width $w = 150$ nm. One might wonder whether we observe the same deviation between the numerical and experimental MSF for the sparser lattices as for the narrower magnets. Interestingly, looking at Fig. 5.17, we see that it is not the case for the wider magnets and qualitative agreement is recovered across the series.

Looking at Fig. 5.17d, which belongs to the lattice with the smallest gap for which the agreement with the Monte Carlo prediction is still observed (see Fig. 5.15a), we again observe strong Bragg peaks, indicating that the type I ground-state configuration is being approached. For the middle point of the considered gap series (shown in Fig. 5.17e), we observe a significant broadening of the peaks accompanied by their intensity decrease. The magnetic structure factor computed for the lattice with the largest gap in the series (see Fig. 5.17f) not only shows a further broadening of the peaks (again accompanied by their intensity reduction) but we also observe that a diffused pattern in the background starts to appear.

By comparing the three above-discussed experimental magnetic structure factors with their respective numerically simulated counterparts (see Fig. 5.17a-5.17c), we observe robust agreement across the full range of gaps. This qualitative agreement is not exclusive to the three examples provided in Fig. 5.17, as evidenced by the complete series comparison provided in the Appendix (see Fig. A.7 and A.8). Therefore, we might conclude that for the $w = 150$ nm lattices, our approach indeed yields a series of spin configurations representative of at-equilibrium physics of a single spin model probed at different effective temperatures. This conclusion finds support through an agreement observed in both the vertex population curves and the magnetic structure factors when compared to a single spin model. Our study thus complements the previous works, which assessed the agreement between the experiment and the numerical model solely based on the vertex populations [40, 124], which might not be a conclusive approach, as we have observed for the $w = 100$ nm lattices (see Fig. 5.16f and 5.16c).

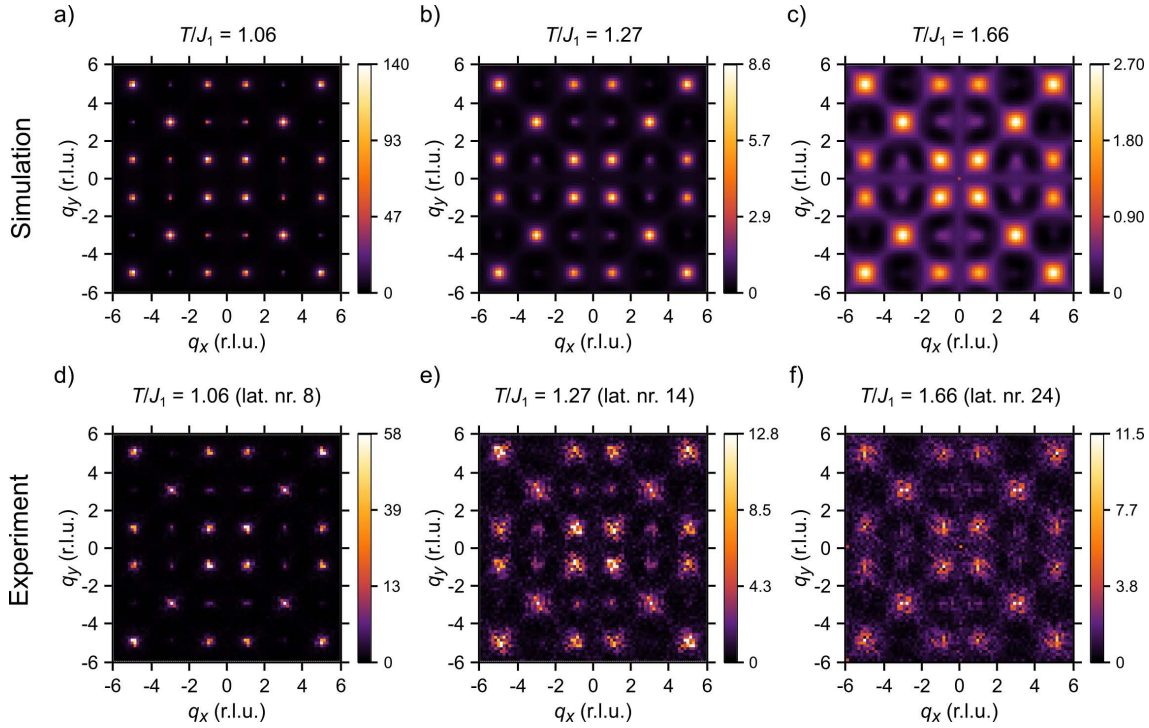

Fig. 5.17: (a-c) Magnetic structure factors calculated by numerical simulations for $J_2/J_1 = 0.675$, Monte Carlo temperature for each intensity plot is provided above. (d-f) Experimental magnetic structure factors (averaged over four series, $w = 150$ nm, $D_5 = 1000$ µC/cm^2. The label above each intensity plot indicates the lattice number and the effective temperature, for which the best fit against the vertex populations simulated by Monte Carlo (with $J_2/J1 = 0.65$) is obtained. All plots are computed for 81×81 points covering the area of $\pm 6 \times \pm 6$ $(\pi/a)^2$ in reciprocal space. The intensity scale bar is provided right next to each plot.

5.5 Discussion: trend deviation for small gaps

The remaining point to address is the trend deviation for small gaps, which is observed both for the $w = 100$ nm series (saturation of type I) and for the $w = 150$ nm series (reversal of the trend). We note that both effects are unexpected, as the general hypothesis is that denser lattice spacing should yield more strongly interacting nanoislands, subsequently leading to more strongly correlated (i.e., ordered) configurations. While the type I plateau could be attributed, for example, to the presence of quenched disorder, which prevents further reduction of the system energy, the trend reversal seems to appear without obvious reason. Is there a possible explanation that would account for both effects?

First, we focus on lattices with magnet width $w = 100$ nm, for which we observe type I population saturation for small gaps. We aggregated the relevant plots discussed here to Fig. 5.18 for convenience. Fig. 5.18a presents a detail of the exper-

imentally observed vertex populations as a function of the gap, with a specific focus on smaller gaps. This plot shows that for lat. nr. 8–6, the type I vertex population plateaus, while the type II vertex population slightly increases and the type III vertex population proportionally decreases. This evolution of the vertex populations continues also for lat. nr. 5–4, but for those lattices, minute connections between perpendicular neighbouring magnets start to appear, which might introduce other effects, so we exclude those lattices from the following analysis.

Fig. 5.18c then shows a detail of the experimental vertex populations plot against the Monte Carlo simulation for the ratio $J_2/J_1 = 0.75$ that provides the best fit for the whole series (complete chart is provided in Fig. 5.14a). In the plot, we observe that for lat. nr. 9 and 10, the agreement between the experiment and the simulation is obtained (as is for the rest of the series, lat. nr. 11–24), but the experimental data points for lat. nr. 8 starts to deviate from the simulation (essentially, there is an excess of type II and a lack of type III vertices). As we observe that for even smaller gaps (lat. nr. 7 and 6), the type II (type III) population increases (decreases), the agreement between the considered model and the experiment can only worsen.

At this point, it is worth reiterating that, we have tried to represent the experimental data with a single spin model (one J_2/J_1 ratio). However, the results of micromagnetic simulations indicate that the J_2/J_1 ratio depends on the gap and increases as the gap is reduced. Additionally, the rate of increase of the J_2/J_1 ratio increases for small gaps (see Fig. 5.18b for detail focusing on the small gaps and Fig. 5.11 for the entire gap range). This observation prompts the question of whether it is necessary to change the model for small gaps in order to recover the agreement with the experimental results.

This is indeed the case as we observe improved agreement for the lat. nr. 8 if the ratio is increased to $J_2/J_1 = 0.80$ (shown in Fig. 5.18d). To obtain a good fit for the lat. nr. 6 and 7, further increase of the ratio to $J_2/J_1 = 0.85$ is required (see Fig. 5.18e).

Therefore, we might conclude that while our single model approximation shows remarkable agreement for the majority of the studied series, it fails to capture the observed physics in the case of the small gap lattices and models with different J_2/J_1 ratios are needed to capture the experimental results accurately (see Fig. 5.18b). In all cases, the J_2/J_1 ratio that provides the best fit for the considered lattice(s) is greater than the magnetostatic estimation obtained via micromagnetic simulations. We attribute this effect to the fact that the J_2 coupling strength is kinetically amplified during the field demagnetisation process by the previously described mechanism.

We now focus on the lattices with magnet width $w = 150$ nm and repeat the analysis for the trend deviation observed for the lattices with small gaps. We again aggregated the relevant charts that will be discussed here into one figure for con-

venience (see Fig. 5.19). Fig. 5.19a shows a detail of the experimentally observed vertex populations as a function of the gap, explicitly focusing on the smallest gaps. This plot shows that the general trend, rising population of type I vertices and proportionally declining populations of type II and III vertices as the gap is reduced, which is observed for the majority of the series (see Fig. 5.10), culminates for lat. nr. 5. For smaller gaps, the trend abruptly reverses, and the type II population increases at the expense of type I, while the type III population continues to decrease. We note that for the lattices with the reversed trend (lat. nr. 3 and 4), the magnets are not melted (see Fig. 5.4, dose D_5).

Fig. 5.19c then shows a detail of the experimental vertex populations plot against the Monte Carlo prediction for the ratio $J_2/J_1 = 0.675$, which provides the best fit for the majority of the considered series (complete chart is provided in Fig. 5.15a). In the plot, we observe that for lat. nr. 8 and lower, the experimental results start to deviate from the simulation, as there is an excess of type II and a lack of type III vertices. Could this be accounted for if we consider different J_2/J_1 ratios for the Monte Carlo simulations, similarly to what we showed for the $w = 100$ nm arrays? We note that similar to the narrower magnets, the micromagnetic simulations for wider magnets also show an increase of the J_2/J_1 ratio as the gap is reduced (see Fig. 5.19b for detail focusing on the small gaps and Fig. 5.12 for the entire gap range).

We find that this is indeed the case, as a good fit for all considered "small gap" lattices is found by a subsequent increase of the J_2/J_1 ratio (see Fig. 5.19d to 5.19h). We note that this approach works also for the lattices with reversed trend, for which the J_2/J_1 ratio must be increased considerably to represent the experimental data accurately (see Fig. 5.19g for lat. nr. 4 and Fig. 5.19h for lat. nr. 3). Interestingly, for the lat. nr. 3 (lowest gap for which no melting of magnets is observed), the ratio that provides the best fit is $J_2/J_1 = 0.95$, which approaches the ice condition $J_2/J_1 = 1$. This means that if slightly more dense lattice spacing were fabricated, one could hope to recover the spin-liquid phase using the conventional square lattice. This could be an interesting approach, particularly as we observe that the type III population is only 0.5 % for the lat. nr. 3, which is significantly lower compared to experimental realisations of the square ice model [22, 31, 37].

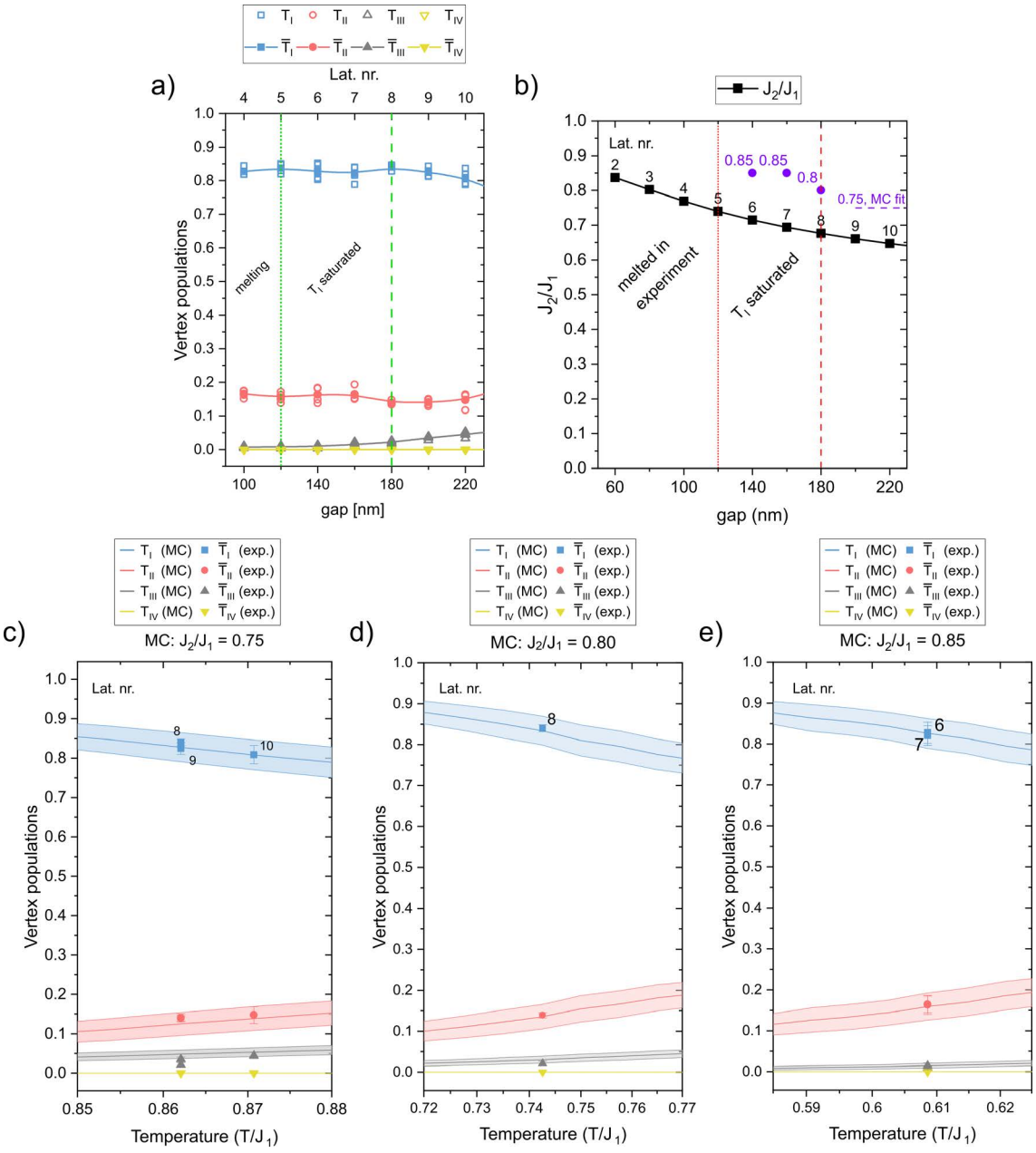

Fig. 5.18: Analysis of the trend deviation for the small gaps ($w = 100$ nm series). a) Vertex populations as a function of the gap (subset from the Fig. 5.7). b) J_2/J_1 ratio as a function of the gap (MuMax3 simulations, subset from Fig. 5.11). c-e) Fit of experimental vertex populations against Monte Carlo simulations for three different J_2/J_1 ratios (indicated above each plot). c) The ratio that was selected as the best fit for the majority of the experimental series (see Fig. 5.14) fails to represent the populations observed for lat. nr. 8. and below. d) Higher J_2/J_1 ratio accurately fits the lat. nr. 8 data points. e) To accurately fit the data points for lat. nr. 7 and 6, the J_2/J_1 ratio must be increased again. Therefore, the single model approximation of the experimental results fails for the smallest gaps, and different models must be used to represent the experimental results accurately.

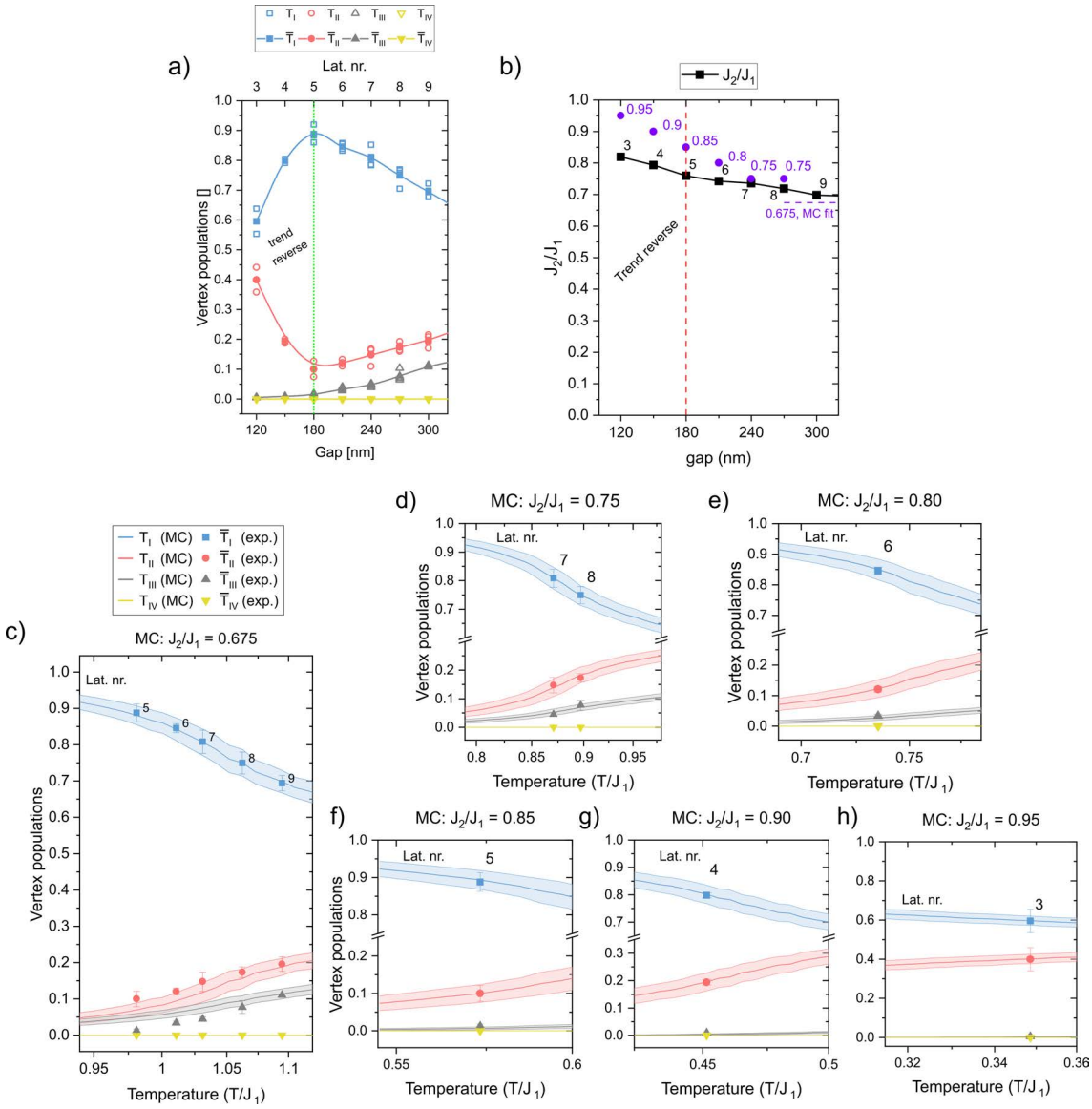

Fig. 5.19: Analysis of the trend deviation for the small gaps (w = 150 nm series). a) Vertex populations as a function of the gap (subset from the Fig. 5.10). b) J_2/J_1 ratio as a function of the gap (MuMax3 simulations, subset from Fig. 5.12). c-h) Fit of experimental vertex populations against Monte Carlo simulations for different J_2/J_1 ratios (indicated above each plot). c) The ratio that was selected as the best fit for the majority of the experimental series (see Fig. 5.15) fails to represent the populations observed for lat. nr. 8. and below. d-h) Higher J_2/J_1 ratios must be selected to fit the data points accurately for lat. nr. 7 and lower. Therefore, our single-model approximation fails for the smallest gaps, and different models must be used to represent the experimental data accurately. The legend for the charts (d-h) is the same as in (c).

We thus conclude that for the $w = 150$ nm arrays, the single model approximation also fails at reproducing the physics observed experimentally for the small gaps. Similarly as for the narrower magnets, different models (i.e. with different J_2/J_1 ratios) must be used to represent the experimental results for the densely spaced lattices accurately.

5.6 Summary

In this study, we have applied a field demagnetisation protocol to a series of athermal square lattices, in which the lattice parameter is gradually varied to tune the interaction strengths. Such a strategy was reported in several previous works, in which different field profiles were used for the demagnetisation [12, 54–57]. The same strategy was also employed for at-growth thermalised artificial square networks [39, 40], where a closer approach to ground-state ordering was reported compared to field demagnetisation protocols.

The first outcome of our work is that field demagnetisation of conventional square arrays can lead to a significantly closer approach to ground-state ordering compared to the above-mentioned studies by different groups. The enhanced efficiency of the field demagnetisation protocol is most likely attributed to the significantly extended duration of the protocol we employed, providing more time for the correlations to develop. Other contributing factors might include stronger coupling strengths resulting from the larger volume of the magnets or superior fabrication quality, although the latter is somewhat challenging to compare directly. However, based on the maximum type I vertex fraction achieved, our results still somewhat underperform (approx. by 10 %) what was reported for thermally active systems, be they thermalised at-growth [40] or post-growth [33, 41, 71].

The second outcome of this work is that a series of field-demagnetised conventional square lattices with gradually varied lattice parameter yields microstates that correspond to a single short-range spin model probed at distinct effective temperatures. In other words, the lattice parameter can be viewed as an experimental knob, which allows for probing the thermodynamics of a given spin model. Our findings are supported by the strong agreement observed for the experimental vertex populations and spin-spin correlations (investigated through magnetic structure factor) when compared to Monte Carlo simulations.

We find that the single-model approximation has its limitations, as it fails to capture the physics observed for very densely spaced lattices, while it provides an accurate description for the remainder (majority) of the series. In order to accurately represent the experimental results obtained for the densely spaced networks,

models with different balance of J_1 and J_2 coupling strengths must be utilised.

Interestingly, deviations in trends are observed for those lattices with relatively small lattice spacings compared to the rest of the series. Particularly for the lattices with wider magnets, we observe complete and unexpected trend reversal. These results can also be accounted for if the J_2/J_1 ratio of the model is considerably increased. Notably, for the most densely spaced lattice featuring the wider magnets, the ratio that provides the best fit for the experimental results $J_2/J_1 = 0.95$ approaches the ice condition $J_2/J_1 = 1$. This intriguing result indicates that if lattice with slightly smaller lattice spacing would be fabricated (which is still geometrically possible before the magnets are in contact), it might be possible to obtain the spin liquid regime utilising conventional square lattice formed by individual nanomagnets, which was thought impossible.

6 SUMMARY

Since their introduction almost twenty years ago [12–15], artificial arrays of magnetic nanostructures have proven themselves as a powerful experimental platform in which to investigate emergent exotic properties associated with low-energy manifolds of frustrated magnetic systems. To some extent, artificial arrays of elongated nanomagnets can be considered experimental simulators of frustrated (Ising) spin models. Lithographic techniques define the geometry and the interaction landscape, and energy minimisation is done by applying field-driven protocol or thermal annealing. The readout (on the scale of spin degree of freedom) is provided by magnetic imaging techniques directly in real space. This approach provides a valuable opportunity to test, revisit and extend various theoretical predictions from frustrated spin models [44].

The presented thesis has focused on experimental investigations of field demagnetised artificial square arrays of elongated nanomagnets (namely conventional square lattices and vertically offset square lattices) while considering the implications of mimicking Ising spin models by arrays of nanomagnets coupled by magnetostatic interactions.

In the first presented study, we have focused on the experimental investigation of farther neighbour coupling signatures in spin liquid configurations retained in vertically offset square lattices. Following a previously reported work [31], we implemented a height offset that effectively restores the balance among the six nearest-neighbour interactions, enabling us to experimentally access the disordered square ice manifold in our two-dimensional artificial system. While the previous works on artificial square ice [31, 37] reported results well approximated by a short-range description, we were able to identify subtle differences (additional features) in the experimental magnetic structure factor that cannot be accounted for by the short-range square ice model.

We have identified the origins of those features and showed that they correspond to the ground-state properties of the dipolar (i.e., long-range) square ice model. Utilising Monte Carlo simulations, we have shown how these additional features can be recovered numerically if interactions extending beyond nearest neighbours are included in the spin model. Additionally, we have shown that our findings are valid even if the ice condition is detuned. Such a scenario would correspond to if the height offset were slightly below or above the optimal value. In this case, interactions extending beyond nearest neighbours must also be considered to account for all of the features observed experimentally.

The main outcome of this study is that interactions from farther neighbour cou-

plings influence the magnetic correlations within or near the ice manifold. While this outcome may be anticipated given the dipolar nature of the magnetostatically coupled arrays of nanomagnets used in our study, the fact that we were able to detect their signatures experimentally is a significant result. Consequently, artificial square ice arrays like ours are expected to undergo an ordering transition at (very) low temperature, as predicted by the dipolar square ice model [65]. Reaching the ground state configuration is, however, experimentally challenging, if possible, as the further minimisation of the system energy employing experimental protocols is limited by dynamical freezing or intrinsic disorder effects. This is a typical experimental challenge that has been encountered in other dipolar artificial arrays [44].

Our findings also have implications for the properties of local excitations (magnetic monopoles) that violate the ice rule constraint. In a pure ice manifold (i.e., square ice with only nearest neighbour interaction), magnetic monopoles are deconfined quasiparticles that are free to move (without energy penalty; the energy cost is associated only with their nucleation) and interact via effective Coulomb interaction that has entropic origin [67]. On the other hand, in a square ice manifold perturbed by long-range interactions, the magnetic monopoles additionally interact via genuine magnetic Coulomb interaction [67, 69]. Additionally, if the long-range interactions are considered, the energy landscape is no longer entirely flat (as for the short-range description), leading to additional binding of the monopole pairs [69]. In other words, the magnetic monopoles we observe in our experiments are not fully deconfined and should behave as weakly bound, as the string tension bounding the pairs of oppositely charged monopoles do not entirely vanish (even within the ice manifold) [70].

In the second presented study, we have investigated a response of the very same artificial athermal square ice magnet (i.e., vertically offset square lattice) to successive applications of a field demagnetisation protocol. We have applied the field demagnetisation protocol four times, and we found that the obtained magnetic configurations share similar global properties, but the local configurations differ substantially. To evaluate the level of stochasticity/determinism present in our results, we have computed vertex density maps, which helped to reveal how the different possible local configurations were spatially distributed over the lattice after successive demagnetisations.

Analysing these density maps (resp. vertex overlap probabilities), we showed that our field protocol is a stochastic process, although some level of magnetic determinism is present. By analysing spin states present at the lattice sites at which the deterministic behaviour was observed, we found a tendency to host the same spin state across the applied demagnetisations, indicating a presence of intrinsic

disorder (i.e., imperfections that locally bias the energetic landscape or the reversal dynamics). The tendency to repeatedly host the same spin state was particularly evident for lattice sites recurrently occupied by magnetic monopoles.

The most significant outcome of this study is that the field demagnetisation protocol is not a purely deterministic process, as substantially different arrested configurations were obtained after applying the field protocol four times, and consistent results were obtained for two nominally identical vertically offset square lattices. We showed that room-temperature thermal fluctuations might impact the magnetisation reversal processes during the field-driven demagnetisation protocol using micromagnetic simulations. Although it is acknowledged that extrinsic sources of randomness (minor differences between the applied field protocols) cannot be entirely discounted, it is proposed that an intrinsic source of randomness is at play, which is linked to thermal fluctuations.

Our findings have implications for handling artificial spin systems consisting of athermal nanomagnets in the experiment. We showed that it is a reasonable approach to apply field demagnetisation several times to the same artificial array to improve the statistical relevance of the results, as a given array is not predetermined to provide the same configurations persistently. We note that the vertex density maps have proven to be a valuable analysis tool that helped identify regions that remained unaffected (or almost unaffected) across consecutive demagnetisations. This approach might be used for future experimental studies in which cycling the field demagnetisation or thermal annealing might be utilised. The use of density maps might then help to identify "frozen"regions, aiding in the analysis of deviations from equilibrium states. For instance, repeated demagnetisations could differentiate between "true" monopoles and those arising from quenched disorder, as the former change locations while the latter remain fixed.

In the third presented study, we studied results obtained for a field demagnetised series of conventional square lattices, in which the lattice parameter was gradually varied to tune the interaction strengths. By carefully comparing vertex populations and magnetic structure factors obtained by the experiment and Monte Carlo simulations, we showed that the results obtained for such a series mostly correspond to a single short-range spin model (one J_2/J_1 ratio) probed at distinct effective temperatures. In other words, the lattice parameter can be viewed as an experimental knob, which allows for probing the effective thermodynamics of a given spin model in a series of field-demagnetised athermal lattices. This is quite an intriguing result, considering that micromagnetic simulations showed that the value of J_2/J_1 ratio depends on the gap (resp. lattice spacing) and increases as the gap is reduced (once the magnets are brought closely together, the ratio rises faster).

However, we also found that in some parts of the series (i.e., for certain parts of the range of lattice parameters studied), the agreement between the experiment and Monte Carlo simulations for a single spin model was lost. One peculiar case was identified for coarsely spaced lattices with narrower magnets ($w = 100$ nm), for which the agreement was only partial. While the experimental results agreed with the simulated vertex populations, analysis of magnetic correlations via magnetic structure factor revealed additional peaks indicating the presence of saturated-like ordering, suggesting inefficient demagnetisation for those lattices. Conversely, for a series of lattices with wider magnets ($w = 150$ nm), the agreement was observed for the vertex populations and the magnetic correlations. It would be interesting to find out whether the demagnetisation for lattices with narrower magnets could be improved (longer protocol or higher initial field strength) or whether narrower magnets are, for some reason, less suitable building blocks for artificial spin systems. A comparable observation regarding the efficacy of wider magnets for achieving low-energy configurations in similarly sized magnets was recently reported in a study on kagome chains originating from our group [125].

The other case where our single-model approximation failed to represent the experimental results was for the densely spaced lattices. In that case, adjusting the model (increasing the J_2/J_1 ratio) was necessary to recover the agreement with the experiment. Interestingly, we found unexpected and abrupt trend reversal for the very densely spaced lattices with the magnet width $w = 150$ nm. These results could also be accounted for by further adjustment of the spin model (a further increase of J_2/J_1 ratio). Notably, the increase of the J_2/J_1 ratio needed to accurately represent the results obtained for the very densely spaced lattices was observed to be greater than what was estimated by the micromagnetic simulations, indicating a possible kinetic effect originating from the field-driven demagnetisation protocol. In fact, for the most dense lattice spacing in the case of the $w = 150$ nm magnets, the ratio that approximated the experimental results was $J_2/J_1 = 0.95$ which considerably approaches the ice condition $J_2/J_1 = 1$, indicating that obtaining the ice manifold might be possible in a conventional square lattice after all.

REFERENCES

[1]K. Kanô and S. Naya, "Antiferromagnetism. the kagomé ising net", Progress of Theoretical Physics **10**, 158–172 (1953).

[2]A. Y. Klimenko, "Teaching the third law of thermodynamics", The Open Thermodynamics Journal **6**, 1–14 (2012).

[3]J. D. Bernal and R. H. Fowler, "A theory of water and ionic solution, with particular reference to hydrogen and hydroxyl ions", The Journal of Chemical Physics **1**, 515–548 (1933).

[4]S. T. Bramwell, M. J. P. Gingras, and P. C. W. Holdsworth, "Spin ice", in *Frustrated spin systems* (WORLD SCIENTIFIC, Nov. 15, 2012), pp. 383–474.

[5]W. F. Giauque and M. F. Ashley, "Molecular rotation in ice at 10\ifmmodeˆ\circ\else\textdegree free energy of formation and entropy of water", Physical Review **43**, Publisher: American Physical Society, 81–82 (1933).

[6]W. F. Giauque and J. W. Stout, "The entropy of water and the third law of thermodynamics. the heat capacity of ice from 15 to 273°k.", Journal of the American Chemical Society **58**, Publisher: American Chemical Society, 1144–1150 (1936).

[7]L. Pauling, "The structure and entropy of ice and of other crystals with some randomness of atomic arrangement", Journal of the American Chemical Society **57**, Publisher: American Chemical Society, 2680–2684 (1935).

[8]M. J. Harris, S. T. Bramwell, D. F. McMorrow, T. Zeiske, and K. W. Godfrey, "Geometrical frustration in the ferromagnetic pyrochlore ho 2 ti 2 o 7", Physical Review Letters **79**, 2554–2557 (1997).

[9]A. P. Ramirez, A. Hayashi, R. J. Cava, R. Siddharthan, and B. S. Shastry, "Zero-point entropy in 'spin ice'", Nature **399**, 333–335 (1999).

[10]J. Snyder, J. S. Slusky, R. J. Cava, and P. Schiffer, "How 'spin ice' freezes", Nature **413**, Publisher: Nature Publishing Group, 48–51 (2001).

[11]Y. Tabata, H. Kadowaki, K. Matsuhira, Z. Hiroi, N. Aso, E. Ressouche, and B. Fåk, "Kagomé ice state in the dipolar spin ice dy 2 ti 2 o 7", Physical Review Letters **97**, 257205 (2006).

[12]R. F. Wang, C. Nisoli, R. S. Freitas, J. Li, W. McConville, B. J. Cooley, M. S. Lund, N. Samarth, C. Leighton, V. H. Crespi, and P. Schiffer, "Artificial 'spin ice' in a geometrically frustrated lattice of nanoscale ferromagnetic islands", Nature **439**, Number: 7074 Publisher: Nature Publishing Group, 303–306 (2006).

[13]M. Tanaka, E. Saitoh, H. Miyajima, and T. Yamaoka, "Magnetization process and magnetic structure in a NiFe honeycomb nano-network", Journal of Magnetism and Magnetic Materials, International Symposium on Advanced Magnetic Technologies **282**, 22–24 (2004).

[14]M. Tanaka, E. Saitoh, H. Miyajima, T. Yamaoka, and Y. Iye, "Domain structures and magnetic ice-order in NiFe nano-network with honeycomb structure", Journal of Applied Physics **97**, Publisher: American Institute of Physics, 10J710 (2005).

[15]M. Tanaka, E. Saitoh, H. Miyajima, T. Yamaoka, and Y. Iye, "Magnetic interactions in a ferromagnetic honeycomb nanoscale network", Physical Review B **73**, 052411 (2006).

[16]S. Zhang, J. Li, I. Gilbert, J. Bartell, M. J. Erickson, Y. Pan, P. E. Lammert, C. Nisoli, K. K. Kohli, R. Misra, V. H. Crespi, N. Samarth, C. Leighton, and P. Schiffer, "Perpendicular magnetization and generic realization of the ising model in artificial spin ice", Physical Review Letters **109**, Publisher: American Physical Society, 087201 (2012).

[17]I. A. Chioar, N. Rougemaille, A. Grimm, O. Fruchart, E. Wagner, M. Hehn, D. Lacour, F. Montaigne, and B. Canals, "Nonuniversality of artificial frustrated spin systems", Physical Review B **90**, Publisher: American Physical Society, 064411 (2014).

[18]S. Kempinger, R. D. Fraleigh, P. E. Lammert, S. Zhang, V. H. Crespi, P. Schiffer, and N. Samarth, "Imaging the stochastic microstructure and dynamic development of correlations in perpendicular artificial spin ice", Physical Review Research **2**, Publisher: American Physical Society, 012001 (2020).

[19]U. B. Arnalds, M. Ahlberg, M. S. Brewer, V. Kapaklis, E. T. Papaioannou, M. Karimipour, P. Korelis, A. Stein, S. Ólafsson, T. P. A. Hase, and B. Hjörvarsson, "Thermal transitions in nano-patterned XY-magnets", Applied Physics Letters **105**, 042409 (2014).

[20]D. Louis, D. Lacour, M. Hehn, V. Lomakin, T. Hauet, and F. Montaigne, "A tunable magnetic metamaterial based on the dipolar four-state potts model", Nature Materials **17**, Publisher: Nature Publishing Group, 1076–1080 (2018).

[21]M. Massouras, D. Lacour, M. Hehn, and F. Montaigne, "Probing the antiferromagnetic-paramagnetic transition in artificial spin ice by tuning interactions", Physical Review B **101**, Publisher: American Physical Society, 174421 (2020).

[22]E. Östman, H. Stopfel, I.-A. Chioar, U. B. Arnalds, A. Stein, V. Kapaklis, and B. Hjörvarsson, "Interaction modifiers in artificial spin ices", Nature Physics **14**, Number: 4 Publisher: Nature Publishing Group, 375–379 (2018).

[23] J. C. Gartside, A. Vanstone, T. Dion, K. D. Stenning, D. M. Arroo, H. Kurebayashi, and W. R. Branford, "Reconfigurable magnonic mode-hybridisation and spectral control in a bicomponent artificial spin ice", Nature Communications **12**, Publisher: Nature Publishing Group, 2488 (2021).

[24] W.-C. Yue, Z. Yuan, Y.-Y. Lyu, S. Dong, J. Zhou, Z.-L. Xiao, L. He, X. Tu, Y. Dong, H. Wang, W. Xu, L. Kang, P. Wu, C. Nisoli, W.-K. Kwok, and Y.-L. Wang, "Crystallizing kagome artificial spin ice", Physical Review Letters **129**, 057202 (2022).

[25] J. Drisko, T. Marsh, and J. Cumings, "Topological frustration of artificial spin ice", Nature Communications **8**, Publisher: Nature Publishing Group, 14009 (2017).

[26] V. Schánilec, O. Brunn, M. Horáček, S. Krátký, P. Meluzín, T. Šikola, B. Canals, and N. Rougemaille, "Approaching the topological low-energy physics of the f model in a two-dimensional magnetic lattice", Physical Review Letters **129**, 027202 (2022).

[27] V. Schánilec, B. Canals, V. Uhlíř, L. Flajšman, J. Sadílek, T. Šikola, and N. Rougemaille, "Bypassing dynamical freezing in artificial kagome ice", Physical Review Letters **125**, 057203 (2020).

[28] K. Hofhuis, S. H. Skjærvø, S. Parchenko, H. Arava, Z. Luo, A. Kleibert, P. M. Derlet, and L. J. Heyderman, "Real-space imaging of phase transitions in bridged artificial kagome spin ice", Nature Physics **18**, Number: 6 Publisher: Nature Publishing Group, 699–705 (2022).

[29] S. H. Skjærvø, C. H. Marrows, R. L. Stamps, and L. J. Heyderman, "Advances in artificial spin ice", Nature Reviews Physics **2**, Number: 1 Publisher: Nature Publishing Group, 13–28 (2020).

[30] O. Brunn, Y. Perrin, B. Canals, and N. Rougemaille, "Signatures of farther neighbor couplings in artificial square ice", Physical Review B **103**, Publisher: American Physical Society, 094405 (2021).

[31] Y. Perrin, B. Canals, and N. Rougemaille, "Extensive degeneracy, coulomb phase and magnetic monopoles in artificial square ice", Nature **540**, Number: 7633 Publisher: Nature Publishing Group, 410–413 (2016).

[32] I. A. Chioar, B. Canals, D. Lacour, M. Hehn, B. Santos Burgos, T. O. Menteş, A. Locatelli, F. Montaigne, and N. Rougemaille, "Kinetic pathways to the magnetic charge crystal in artificial dipolar spin ice", Physical Review B **90**, Publisher: American Physical Society, 220407 (2014).

[33]A. Farhan, P. M. Derlet, A. Kleibert, A. Balan, R. V. Chopdekar, M. Wyss, J. Perron, A. Scholl, F. Nolting, and L. J. Heyderman, "Direct observation of thermal relaxation in artificial spin ice", Physical Review Letters **111**, Publisher: American Physical Society, 057204 (2013).

[34]G. M. Macauley, G. W. Paterson, Y. Li, R. Macêdo, S. McVitie, and R. L. Stamps, "Tuning magnetic order with geometry: thermalization and defects in two-dimensional artificial spin ices", Physical Review B **101**, Publisher: American Physical Society, 144403 (2020).

[35]J. Drisko, S. Daunheimer, and J. Cumings, "${\mathrm{FePd}}_{3}$ as a material for studying thermally active artificial spin ice systems", Physical Review B **91**, Publisher: American Physical Society, 224406 (2015).

[36]D. J. P. Morris, D. A. Tennant, S. A. Grigera, B. Klemke, C. Castelnovo, R. Moessner, C. Czternasty, M. Meissner, K. C. Rule, J.-U. Hoffmann, K. Kiefer, S. Gerischer, D. Slobinsky, and R. S. Perry, "Dirac strings and magnetic monopoles in the spin ice dy2ti2o7", Science **326**, Publisher: American Association for the Advancement of Science, 411–414 (2009).

[37]A. Farhan, M. Saccone, C. F. Petersen, S. Dhuey, R. V. Chopdekar, Y.-L. Huang, N. Kent, Z. Chen, M. J. Alava, T. Lippert, A. Scholl, and S. van Dijken, "Emergent magnetic monopole dynamics in macroscopically degenerate artificial spin ice", Science Advances **5**, Publisher: American Association for the Advancement of Science, eaav6380 (2019).

[38]R. Dusad, F. K. K. Kirschner, J. C. Hoke, B. R. Roberts, A. Eyal, F. Flicker, G. M. Luke, S. J. Blundell, and J. C. S. Davis, "Magnetic monopole noise", Nature **571**, 234–239 (2019).

[39]J. P. Morgan, A. Stein, S. Langridge, and C. H. Marrows, "Thermal ground-state ordering and elementary excitations in artificial magnetic square ice", Nature Physics **7**, Number: 1 Publisher: Nature Publishing Group, 75–79 (2011).

[40]J. P. Morgan, J. Akerman, A. Stein, C. Phatak, R. M. L. Evans, S. Langridge, and C. H. Marrows, "Real and effective thermal equilibrium in artificial square spin ices", Physical Review B **87**, 024405 (2013).

[41]I. Gilbert, G.-W. Chern, S. Zhang, L. O'Brien, B. Fore, C. Nisoli, and P. Schiffer, "Emergent ice rule and magnetic charge screening from vertex frustration in artificial spin ice", Nature Physics **10**, Number: 9 Publisher: Nature Publishing Group, 670–675 (2014).

[42]C. Nisoli, R. Moessner, and P. Schiffer, "*Colloquium* : artificial spin ice: designing and imaging magnetic frustration", Reviews of Modern Physics **85**, 1473–1490 (2013).

[43]L. J. Heyderman and R. L. Stamps, "Artificial ferroic systems: novel functionality from structure, interactions and dynamics", Journal of Physics: Condensed Matter **25**, Publisher: IOP Publishing, 363201 (2013).

[44]N. Rougemaille and B. Canals, "Cooperative magnetic phenomena in artificial spin systems: spin liquids, coulomb phase and fragmentation of magnetism – a colloquium", The European Physical Journal B **92**, 62 (2019).

[45]Z. Budrikis, "Chapter two - disorder, edge, and field protocol effects in athermal dynamics of artificial spin ice", in *Solid state physics*, Vol. 65, edited by R. E. Camley and R. L. Stamps (Academic Press, Jan. 1, 2014), pp. 109–236.

[46]C. H. Marrows, "Experimental studies of artificial spin ice", in *Spin ice*, edited by M. Udagawa and L. Jaubert (Springer International Publishing, Cham, 2021), pp. 455–478.

[47]S. Lendinez and M. B. Jungfleisch, "Magnetization dynamics in artificial spin ice", Journal of Physics: Condensed Matter **32**, Publisher: IOP Publishing, 013001 (2019).

[48]A. Libál, C. Reichhardt, and C. J. O. Reichhardt, "Realizing colloidal artificial ice on arrays of optical traps", Physical Review Letters **97**, Publisher: American Physical Society, 228302 (2006).

[49]Y. Han, Y. Shokef, A. M. Alsayed, P. Yunker, T. C. Lubensky, and A. G. Yodh, "Geometric frustration in buckled colloidal monolayers", Nature **456**, Number: 7224 Publisher: Nature Publishing Group, 898–903 (2008).

[50]A. Ortiz-Ambriz and P. Tierno, "Engineering of frustration in colloidal artificial ices realized on microfeatured grooved lattices", Nature Communications **7**, Number: 1 Publisher: Nature Publishing Group, 10575 (2016).

[51]P. Mellado, A. Concha, and L. Mahadevan, "Macroscopic magnetic frustration", Physical Review Letters **109**, Publisher: American Physical Society, 257203 (2012).

[52]C. Sirote-Katz, D. Shohat, C. Merrigan, Y. Lahini, C. Nisoli, and Y. Shokef, *Emergent disorder and mechanical memory in periodic metamaterials*, version: 5, June 27, 2023.

[53]M. Alfonso-Moro, V. Guisset, P. David, B. Canals, J. Coraux, and N. Rougemaille, "Geometrical frustration, correlated disorder, and emerging order in a corrugated c 60 monolayer", Physical Review Letters **131**, 186201 (2023).

[54]R. F. Wang, J. Li, and W. McConville, "Demagnetization protocols for frustrated interacting nanomagnet arrays", J. Appl. Phys., 4 (2007).

[55]X. Ke, J. Li, C. Nisoli, P. E. Lammert, W. McConville, R. F. Wang, V. H. Crespi, and P. Schiffer, "Energy minimization and ac demagnetization in a nanomagnet array", Physical Review Letters **101**, 037205 (2008).

[56]Z. Budrikis, J. P. Morgan, J. Akerman, A. Stein, P. Politi, S. Langridge, C. H. Marrows, and R. L. Stamps, "Disorder strength and field-driven ground state domain formation in artificial spin ice: experiment, simulation, and theory", Physical Review Letters **109**, 037203 (2012).

[57]J. Morgan, A. Bellew, A. Stein, S. Langridge, and C. Marrows, "Linear field demagnetization of artificial magnetic square ice", Frontiers in Physics **1** (2013).

[58]Z. Budrikis, K. L. Livesey, J. P. Morgan, J. Akerman, A. Stein, S. Langridge, C. H. Marrows, and R. L. Stamps, "Domain dynamics and fluctuations in artificial square ice at finite temperatures", New Journal of Physics **14**, Publisher: IOP Publishing, 035014 (2012).

[59]J. M. Porro, A. Bedoya-Pinto, A. Berger, and P. Vavassori, "Exploring thermally induced states in square artificial spin-ice arrays", New Journal of Physics **15**, 055012 (2013).

[60]V. Kapaklis, U. B. Arnalds, A. Farhan, R. V. Chopdekar, A. Balan, A. Scholl, L. J. Heyderman, and B. Hjörvarsson, "Thermal fluctuations in artificial spin ice", Nature Nanotechnology **9**, Publisher: Nature Publishing Group, 514–519 (2014).

[61]J. P. Morgan, A. Stein, S. Langridge, and C. H. Marrows, "Magnetic reversal of an artificial square ice: dipolar correlation and charge ordering", New Journal of Physics **13**, 105002 (2011).

[62]C. Phatak, A. K. Petford-Long, O. Heinonen, M. Tanase, and M. De Graef, "Nanoscale structure of the magnetic induction at monopole defects in artificial spin-ice lattices", Physical Review B **83**, 174431 (2011).

[63]I. Gilbert, G.-W. Chern, B. Fore, Y. Lao, S. Zhang, C. Nisoli, and P. Schiffer, "Direct visualization of memory effects in artificial spin ice", Physical Review B **92**, Publisher: American Physical Society, 104417 (2015).

[64]S. D. Pollard, V. Volkov, and Y. Zhu, "Propagation of magnetic charge monopoles and dirac flux strings in an artificial spin-ice lattice", Physical Review B **85**, Publisher: American Physical Society, 180402 (2012).

[65]G. Möller and R. Moessner, "Artificial square ice and related dipolar nanoarrays", Physical Review Letters **96**, Publisher: American Physical Society, 237202 (2006).

[66]N. Rougemaille and B. Canals, "The magnetic structure factor of the square ice: a phenomenological description", Applied Physics Letters **118**, 112403 (2021).

[67]C. L. Henley, "The "coulomb phase" in frustrated systems", Annual Review of Condensed Matter Physics **1**, Publisher: Annual Reviews, 179–210 (2010).

[68]C. Castelnovo, R. Moessner, and S. L. Sondhi, "Magnetic monopoles in spin ice", Nature **451**, Number: 7174 Publisher: Nature Publishing Group, 42–45 (2008).

[69]L. A. Mól, R. L. Silva, R. C. Silva, A. R. Pereira, W. A. Moura-Melo, and B. V. Costa, "Magnetic monopole and string excitations in two-dimensional spin ice", Journal of Applied Physics **106**, Publisher: American Institute of Physics, 063913 (2009).

[70]L. A. S. Mól, W. A. Moura-Melo, and A. R. Pereira, "Conditions for free magnetic monopoles in nanoscale square arrays of dipolar spin ice", Physical Review B **82**, Publisher: American Physical Society, 054434 (2010).

[71]S. Zhang, I. Gilbert, C. Nisoli, G.-W. Chern, M. J. Erickson, L. O'Brien, C. Leighton, P. E. Lammert, V. H. Crespi, and P. Schiffer, "Crystallites of magnetic charges in artificial spin ice", Nature **500**, Number: 7464 Publisher: Nature Publishing Group, 553–557 (2013).

[72]N. S. Bingham, S. Rooke, J. Park, A. Simon, W. Zhu, X. Zhang, J. Batley, J. D. Watts, C. Leighton, K. A. Dahmen, and P. Schiffer, "Experimental realization of the 1d random field ising model", Physical Review Letters **127**, Publisher: American Physical Society, 207203 (2021).

[73]V. Schánilec, "Artificial arrays of magnetic nanostructures", PhD thesis (2022).

[74]M. J. Donahue and D. G. Porter, "OOMMF user's guide, version 1.0", NIST IR 6376 (1999).

[75]A. Vansteenkiste, J. Leliaert, M. Dvornik, M. Helsen, F. Garcia-Sanchez, and B. Van Waeyenberge, "The design and verification of MuMax3", AIP Advances **4**, 107133 (2014).

[76]J. Leliaert, M. Dvornik, J. Mulkers, J. De Clercq, M. V. Milošević, and B. Van Waeyenberge, "Fast micromagnetic simulations on GPU—recent advances made with $\mathsf{mumax}ˆ3$", Journal of Physics D: Applied Physics **51**, 123002 (2018).

[77]J. Leliaert, J. Mulkers, J. De Clercq, A. Coene, M. Dvornik, and B. Van Waeyenberge, "Adaptively time stepping the stochastic landau-lifshitz-gilbert equation at nonzero temperature: implementation and validation in MuMax ^{3}", AIP Advances **7**, 125010 (2017).

[78]J. J. Joos, P. Bassirian, P. Gypens, J. Mulkers, K. Litzius, B. Van Waeyenberge, and J. Leliaert, "Tutorial: simulating modern magnetic material systems in mumax3", Journal of Applied Physics **134**, 171101 (2023).

[79]L. Exl, S. Bance, F. Reichel, T. Schrefl, H. Peter Stimming, and N. J. Mauser, "LaBonte's method revisited: an effective steepest descent method for micromagnetic energy minimization", Journal of Applied Physics **115**, 17D118 (2014).

[80]E. Mengotti, L. J. Heyderman, A. Fraile Rodríguez, A. Bisig, L. Le Guyader, F. Nolting, and H. B. Braun, "Building blocks of an artificial kagome spin ice: photoemission electron microscopy of arrays of ferromagnetic islands", Physical Review B **78**, 144402 (2008).

[81]A. Remhof, A. Schumann, A. Westphalen, H. Zabel, N. Mikuszeit, E. Y. Vedmedenko, T. Last, and U. Kunze, "Magnetostatic interactions on a square lattice", Physical Review B **77**, 134409 (2008).

[82]N. Rougemaille, F. Montaigne, B. Canals, A. Duluard, D. Lacour, M. Hehn, R. Belkhou, O. Fruchart, S. El Moussaoui, A. Bendounan, and F. Maccherozzi, "Artificial kagome arrays of nanomagnets: a frozen dipolar spin ice", Physical Review Letters **106**, Publisher: American Physical Society, 057209 (2011).

[83]V. Brajuskovic, F. Barrows, C. Phatak, and A. K. Petford-Long, "Real-space observation of magnetic excitations and avalanche behavior in artificial quasicrystal lattices", Scientific Reports **6**, Publisher: Nature Publishing Group, 34384 (2016).

[84]Y. Chen, K. Bi, Q. Wang, M. Zheng, Q. Liu, Y. Han, J. Yang, S. Chang, G. Zhang, and H. Duan, "Rapid focused ion beam milling based fabrication of plasmonic nanoparticles and assemblies via "sketch and peel" strategy", ACS Nano **10**, Publisher: American Chemical Society, 11228–11236 (2016).

[85]Y. Chen, Q. Xiang, Z. Li, Y. Wang, Y. Meng, and H. Duan, ""sketch and peel" lithography for high-resolution multiscale patterning", Nano Letters **16**, Publisher: American Chemical Society, 3253–3259 (2016).

[86]V.-D. Nguyen, Y. Perrin, S. Le Denmat, B. Canals, and N. Rougemaille, "Competing interactions in artificial spin chains", Physical Review B **96**, Publisher: American Physical Society, 014402 (2017).

[87]Y. Perrin, "Résaux artificiels á frustration géometrique", PhD thesis (2016).

[88]M. Zálešák, "Artificial shakti ice magnets: ground state degeneracy, coulomb phase and monopole excitations", MA thesis (2023).

[89]*KLayout layout viewer and editor*, `https://www.klayout.de/doc.html` (visited on 03/14/2024).

[90] J. Singh and D. E. Wolfe, "Review nano and macro-structured component fabrication by electron beam-physical vapor deposition (EB-PVD)", Journal of Materials Science **40**, 1–26 (2005).

[91] A. Wajid, "On the accuracy of the quartz-crystal microbalance (QCM) in thin-film depositions", Sensors and Actuators A: Physical **63**, 41–46 (1997).

[92] A. Farhan, P. M. Derlet, A. Kleibert, A. Balan, R. V. Chopdekar, M. Wyss, L. Anghinolfi, F. Nolting, and L. J. Heyderman, "Exploring hyper-cubic energy landscapes in thermally active finite artificial spin-ice systems", Nature Physics **9**, Number: 6 Publisher: Nature Publishing Group, 375–382 (2013).

[93] V. Schánilec, "Magnetic spin ice states in artificial magnetic frustrated systems", MA thesis (2018).

[94] Y. Martin and H. K. Wickramasinghe, "Magnetic imaging by "force microscopy" with 1000 å resolution", Applied Physics Letters **50**, Publisher: American Institute of Physics, 1455–1457 (1987).

[95] O. Kazakova, R. Puttock, C. Barton, H. Corte-León, M. Jaafar, V. Neu, and A. Asenjo, "Frontiers of magnetic force microscopy", Journal of Applied Physics **125**, Publisher: American Institute of Physics, 060901 (2019).

[96] D. Nečas and P. Klapetek, "Gwyddion: an open-source software for SPM data analysis", Open Physics **10**, Publisher: De Gruyter Open Access, 181–188 (2012).

[97] O. Brunn, "Magnetic phases in an artificial realization of the square ice model", MA thesis (2019).

[98] I.-A. Chioar, "Artificial kagome spin networks - from short-range degeneracy towards long-range dipolar order", PhD thesis (2016).

[99] I. A. Chioar, N. Rougemaille, and B. Canals, "Ground-state candidate for the classical dipolar kagome ising antiferromagnet", Physical Review B **93**, 214410 (2016).

[100] G.-W. Chern, P. Mellado, and O. Tchernyshyov, "Two-stage ordering of spins in dipolar spin ice on the kagome lattice", Physical Review Letters **106**, 207202 (2011).

[101] A. S. Wills, R. Ballou, and C. Lacroix, "Model of localized highly frustrated ferromagnetism: the *kagomé* spin ice", Physical Review B **66**, 144407 (2002).

[102] G. Möller and R. Moessner, "Magnetic multipole analysis of kagome and artificial spin-ice dipolar arrays", Physical Review B **80**, Publisher: American Physical Society, 140409 (2009).

[103]B. Canals, I.-A. Chioar, V.-D. Nguyen, M. Hehn, D. Lacour, F. Montaigne, A. Locatelli, T. O. Menteş, B. S. Burgos, and N. Rougemaille, "Fragmentation of magnetism in artificial kagome dipolar spin ice", Nature Communications **7**, Number: 1 Publisher: Nature Publishing Group, 11446 (2016).

[104]M. E. Brooks-Bartlett, S. T. Banks, L. D. C. Jaubert, A. Harman-Clarke, and P. C. W. Holdsworth, "Magnetic-moment fragmentation and monopole crystallization", Physical Review X **4**, Publisher: American Physical Society, 011007 (2014).

[105]D. Thonig, S. Reißaus, I. Mertig, and J. Henk, "Thermal string excitations in artificial spin-ice square dipolar arrays", Journal of Physics: Condensed Matter **26**, 266006 (2014).

[106]F. Rys, "Über ein zweidimensionales klassisches Konfigurationsmodell", Medium: text/html,application/pdf,text/html Publisher: Birkhäuser, 10.5169/SEALS-113387 (1963).

[107]E. H. Lieb, "Exact solution of the f model of an antiferroelectric", Physical Review Letters **18**, 1046–1048 (1967).

[108]E. H. Lieb, "Exact solution of the two-dimensional slater KDP model of a ferroelectric", Physical Review Letters **19**, 108–110 (1967).

[109]N. Rougemaille, F. Montaigne, B. Canals, M. Hehn, H. Riahi, D. Lacour, and J.-C. Toussaint, "Chiral nature of magnetic monopoles in artificial spin ice", New Journal of Physics **15**, Publisher: IOP Publishing, 035026 (2013).

[110]S. Gliga, A. Kákay, L. J. Heyderman, R. Hertel, and O. G. Heinonen, "Broken vertex symmetry and finite zero-point entropy in the artificial square ice ground state", Physical Review B **92**, 060413 (2015).

[111]G. W. Paterson, G. M. Macauley, Y. Li, R. Macêdo, C. Ferguson, S. A. Morley, M. C. Rosamond, E. H. Linfield, C. H. Marrows, R. L. Stamps, and S. McVitie, "Heisenberg pseudo-exchange and emergent anisotropies in field-driven pinwheel artificial spin ice", Physical Review B **100**, 174410 (2019).

[112]S. D. Slöetjes, B. Hjörvarsson, and V. Kapaklis, "The effect of confinement on thermal fluctuations in nanomagnets", Applied Physics Letters **118**, 142407 (2021).

[113]B. E. Skovdal, S. D. Slöetjes, M. Pohlit, H. Stopfel, V. Kapaklis, and B. Hjörvarsson, "Thermal excitations within and among mesospins in artificial spin ice", Physical Review B **107**, L060406 (2023).

[114]R. G. Melko and M. J. P. Gingras, "Monte carlo studies of the dipolar spin ice model", Journal of Physics: Condensed Matter **16**, R1277 (2004).

[115]C. Nisoli, R. Wang, J. Li, W. F. McConville, P. E. Lammert, P. Schiffer, and V. H. Crespi, "Ground state lost but degeneracy found: the effective thermodynamics of artificial spin ice", Physical Review Letters **98**, 217203 (2007).

[116]V. Kapaklis, U. B. Arnalds, A. Harman-Clarke, E. T. Papaioannou, M. Karimipour, P. Korelis, A. Taroni, P. C. W. Holdsworth, S. T. Bramwell, and B. Hjörvarsson, "Melting artificial spin ice", New Journal of Physics **14**, 035009 (2012).

[117]F. Montaigne, D. Lacour, I. A. Chioar, N. Rougemaille, D. Louis, S. M. Murtry, H. Riahi, B. S. Burgos, T. O. Menteş, A. Locatelli, B. Canals, and M. Hehn, "Size distribution of magnetic charge domains in thermally activated but out-of-equilibrium artificial spin ice", Scientific Reports **4**, Number: 1 Publisher: Nature Publishing Group, 5702 (2014).

[118]K. Hofhuis, A. Hrabec, H. Arava, N. Leo, Y.-L. Huang, R. V. Chopdekar, S. Parchenko, A. Kleibert, S. Koraltan, C. Abert, C. Vogler, D. Suess, P. M. Derlet, and L. J. Heyderman, "Thermally superactive artificial kagome spin ice structures obtained with the interfacial dzyaloshinskii-moriya interaction", Physical Review B **102**, Publisher: American Physical Society, 180405 (2020).

[119]G.-W. Chern, M. J. Morrison, and C. Nisoli, "Degeneracy and criticality from emergent frustration in artificial spin ice", Physical Review Letters **111**, 177201 (2013).

[120]Z. Budrikis, P. Politi, and R. L. Stamps, "Disorder regimes and equivalence of disorder types in artificial spin ice", Journal of Applied Physics **111**, 07E109 (2012).

[121]R. D. Fraleigh, S. Kempinger, P. E. Lammert, S. Zhang, V. H. Crespi, P. Schiffer, and N. Samarth, "Characterization of switching field distributions in ising-like magnetic arrays", Physical Review B **95**, 144416 (2017).

[122]K. J. Kirk, M. R. Scheinfein, J. N. Chapman, S. McVitie, M. F. Gillies, B. R. Ward, and J. G. Tennant, "Role of vortices in magnetization reversal of rectangular NiFe elements", Journal of Physics D: Applied Physics **34**, 160–166 (2001).

[123]T. J. Hayward, "Intrinsic nature of stochastic domain wall pinning phenomena in magnetic nanowire devices", Scientific Reports **5**, Number: 1 Publisher: Nature Publishing Group, 13279 (2015).

[124]C. Nisoli, J. Li, X. Ke, D. Garand, P. Schiffer, and V. H. Crespi, "Effective temperature in an interacting vertex system: theory and experiment on artificial spin ice", Physical Review Letters **105**, 047205 (2010).

[125]L. Salmon, V. Schánilec, J. Coraux, B. Canals, and N. Rougemaille, "Effective interaction quenching in artificial kagomé spin chains", Physical Review B **109**, 054425 (2024).

LIST OF APPENDICES

A SUPPLEMENTARY DATA FOR CHAPTER 5

A.1 Spin and vertex maps, example of full series for $w = 100$ nm

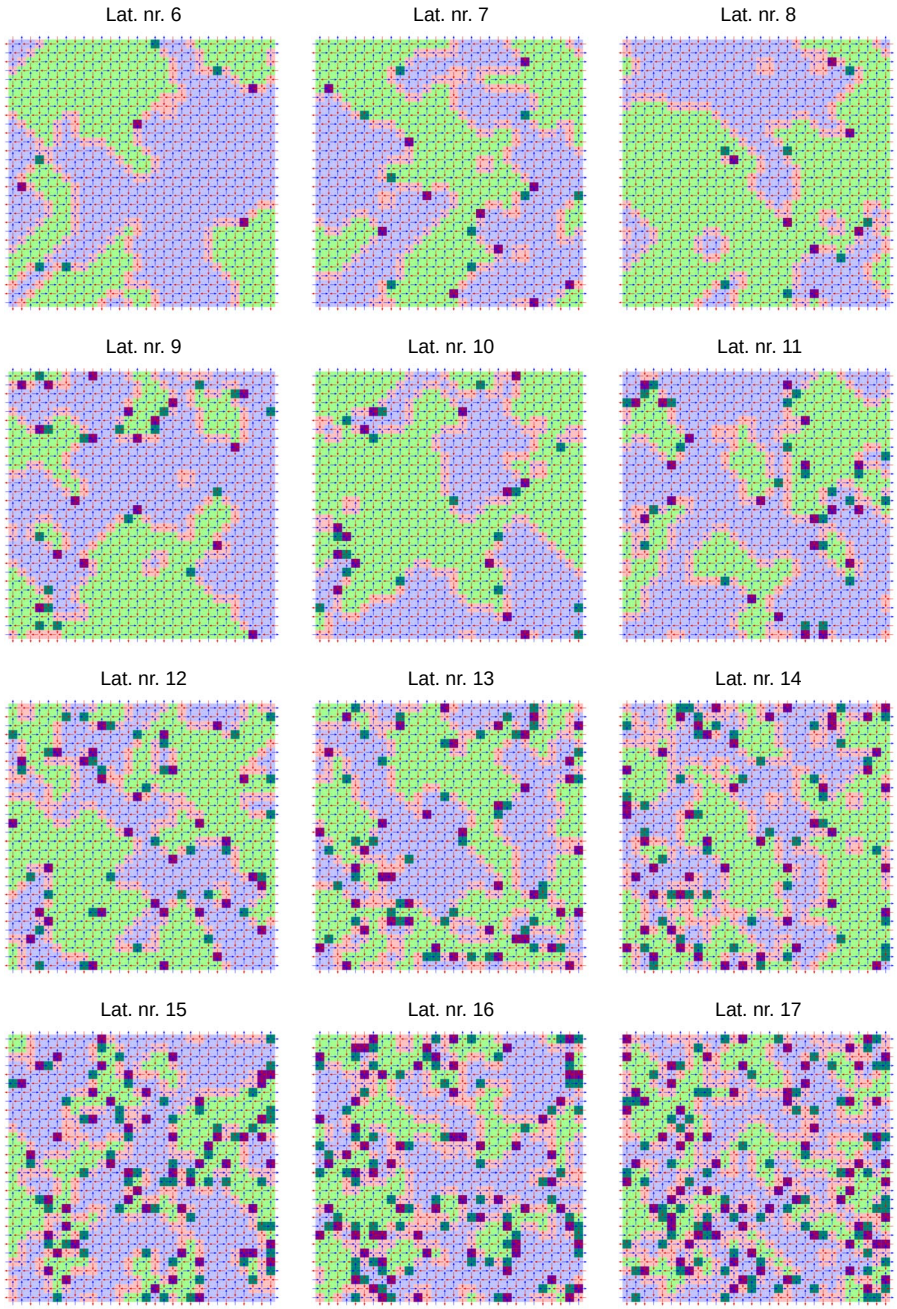

Fig. A.1: Spin and vertex maps for one of four series of lattices with magnet width $w = 100$ nm, part A. Three examples from this series are provided directly in the text of the thesis.

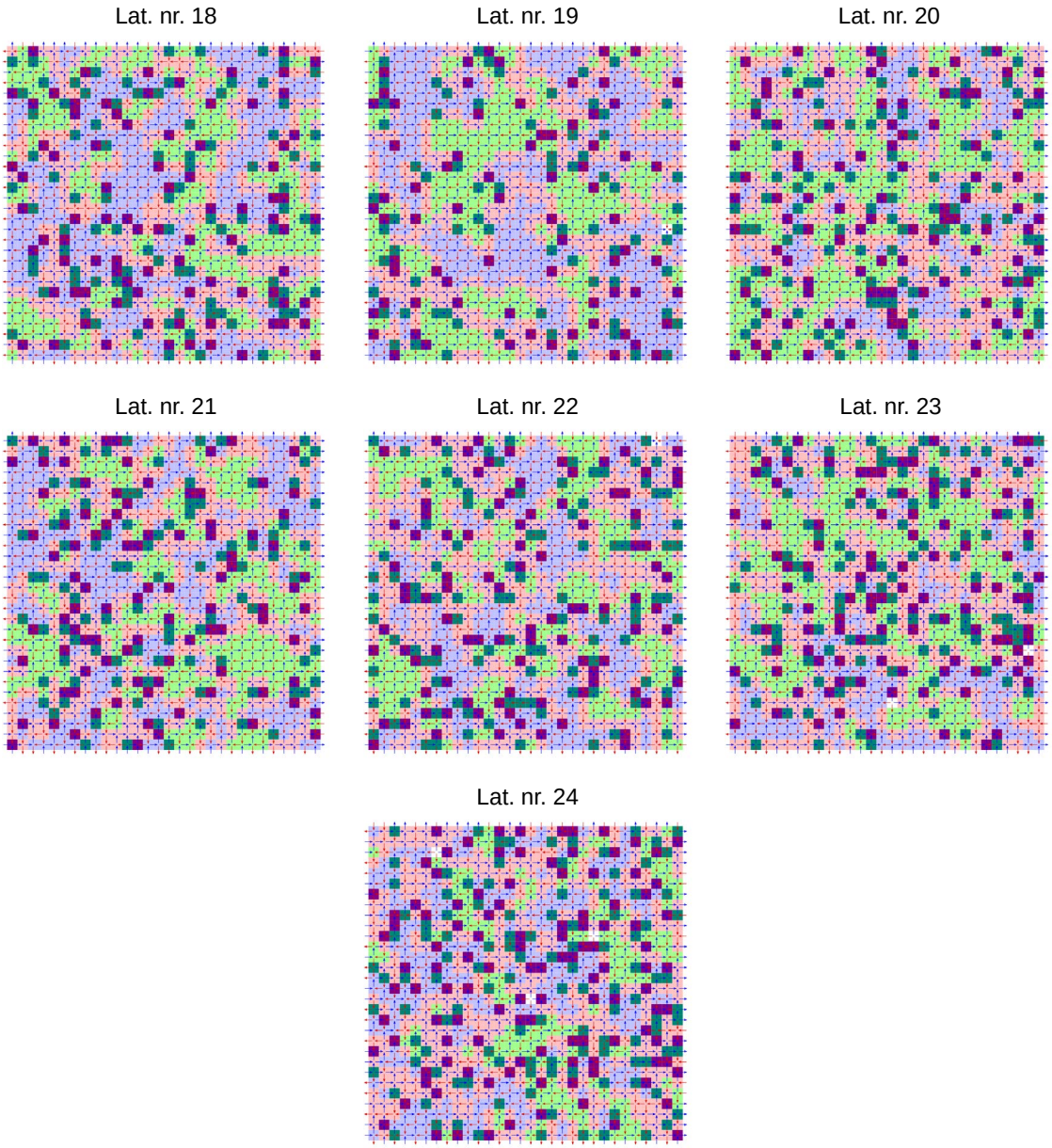

Fig. A.2: Spin and vertex maps for one of four series of lattices with magnet width $w = 100$ nm, part B. Three examples from this series are provided directly in the text of the thesis.

A.2 Spin and vertex maps, example of full series for $w = 150$ nm

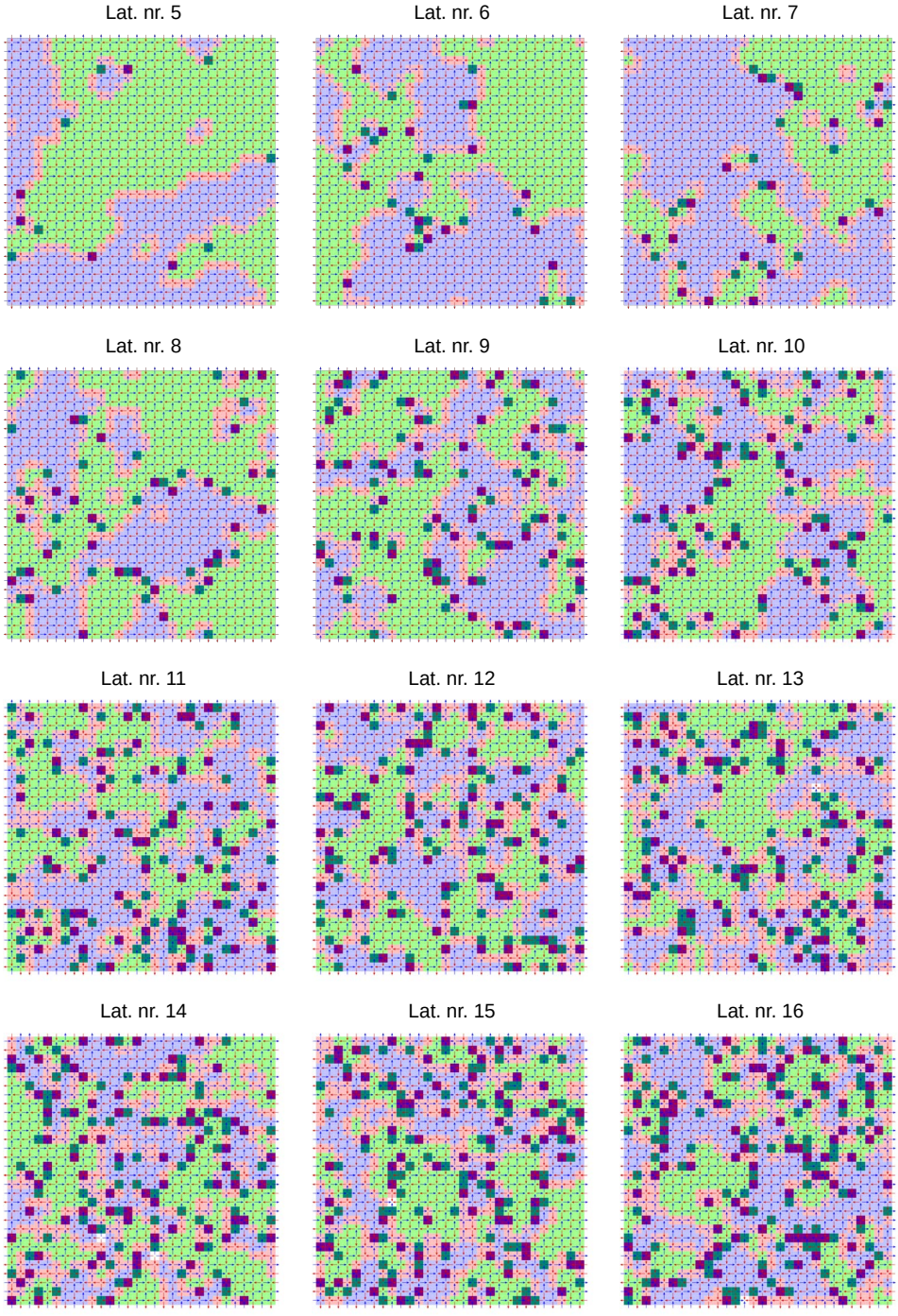

Fig. A.3: Spin and vertex maps for one of four series of lattices with magnet width $w = 150$ nm, part A. Three examples from this series are provided directly in the text of the thesis.

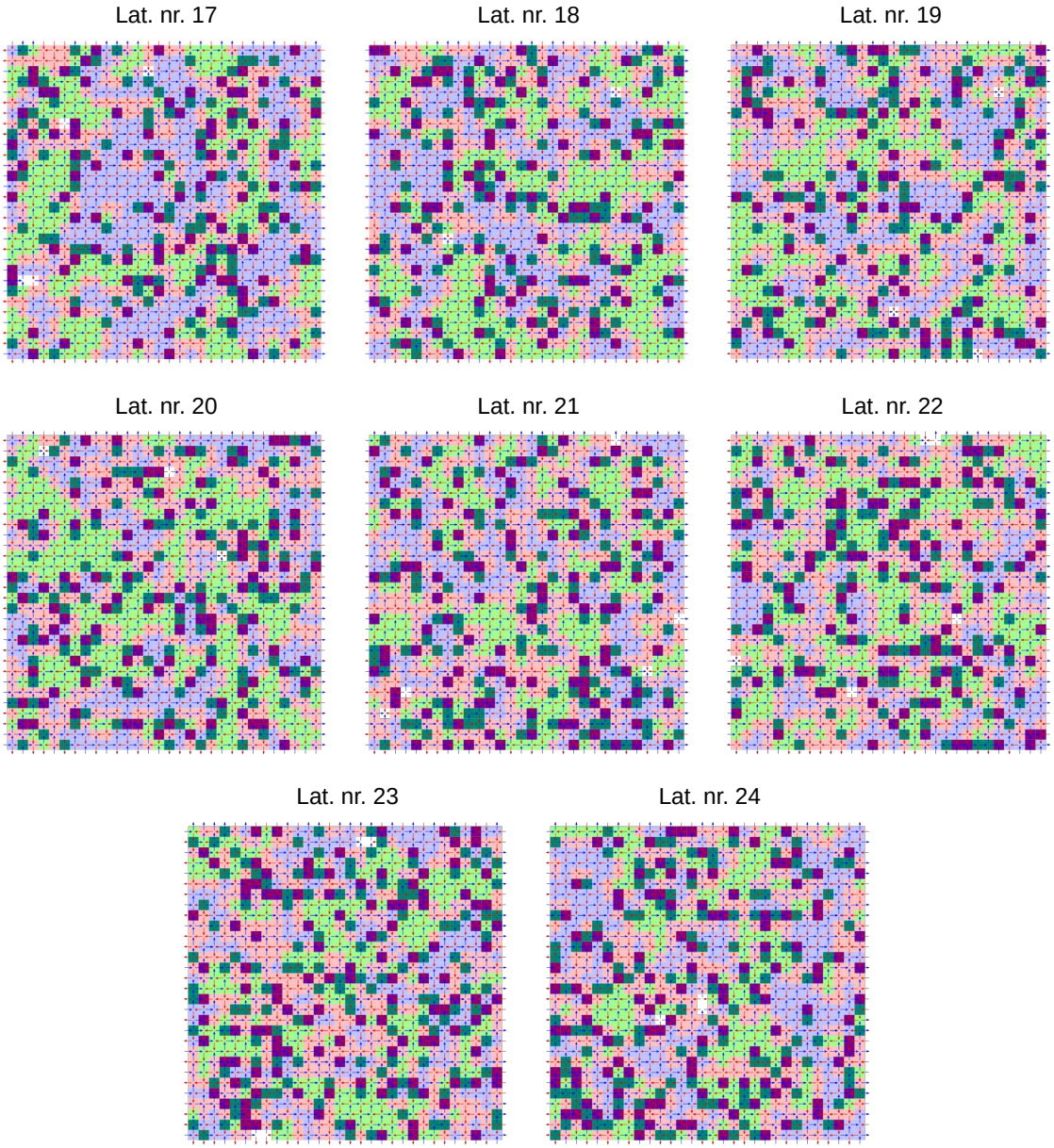

Fig. A.4: Spin and vertex maps for one of four series of lattices with magnet width $w = 150$ nm, part B. Three examples from this series are provided directly in the text of the thesis.

A.3 Average experimental MSF, $w = 100$ nm series

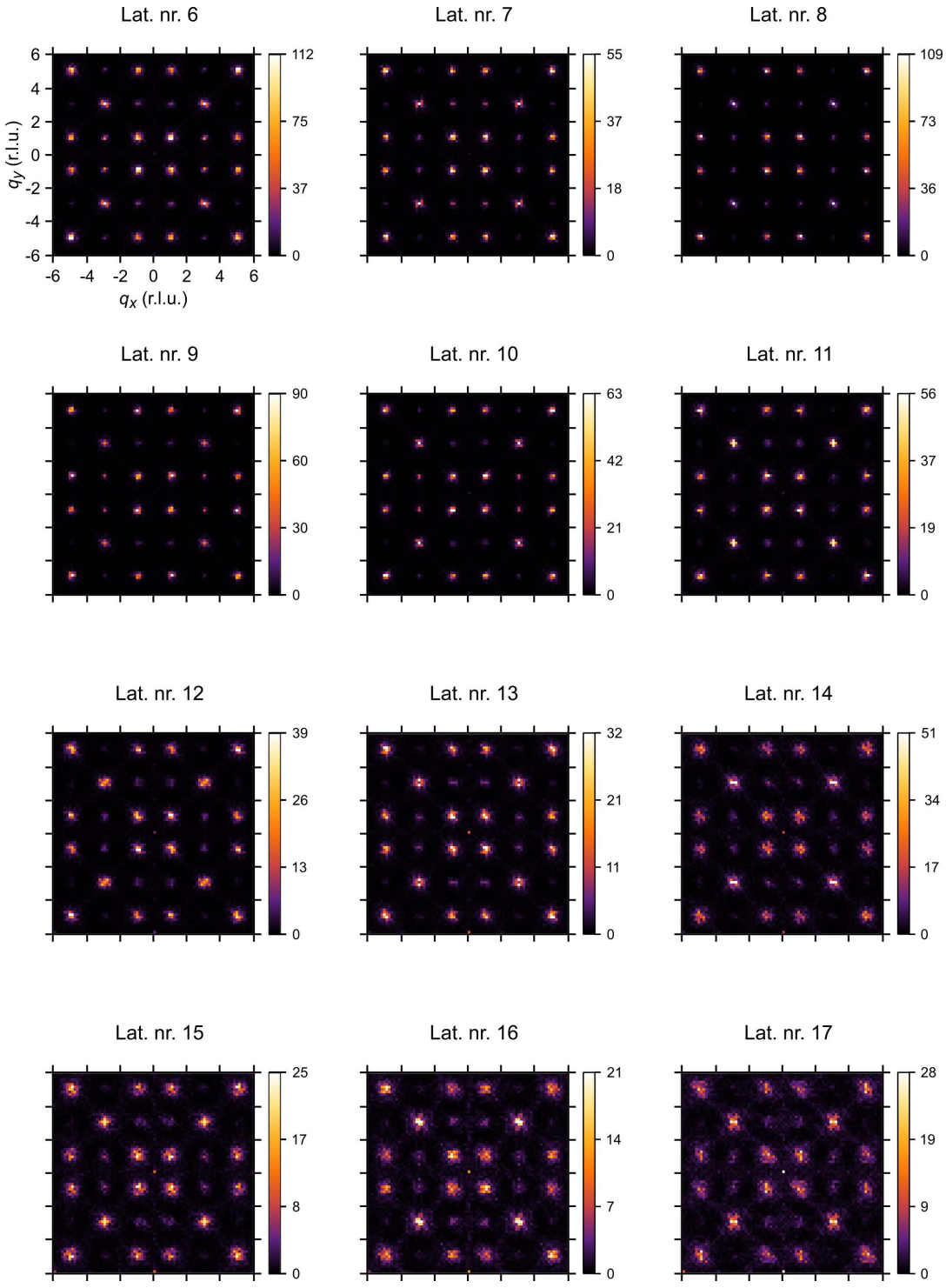

Fig. A.5: Full series of average experimental MSF for lattices with magnet width $w = 100$ nm, part A. Three examples from this series are provided directly in the text of the thesis and compared against numerical MSFs.

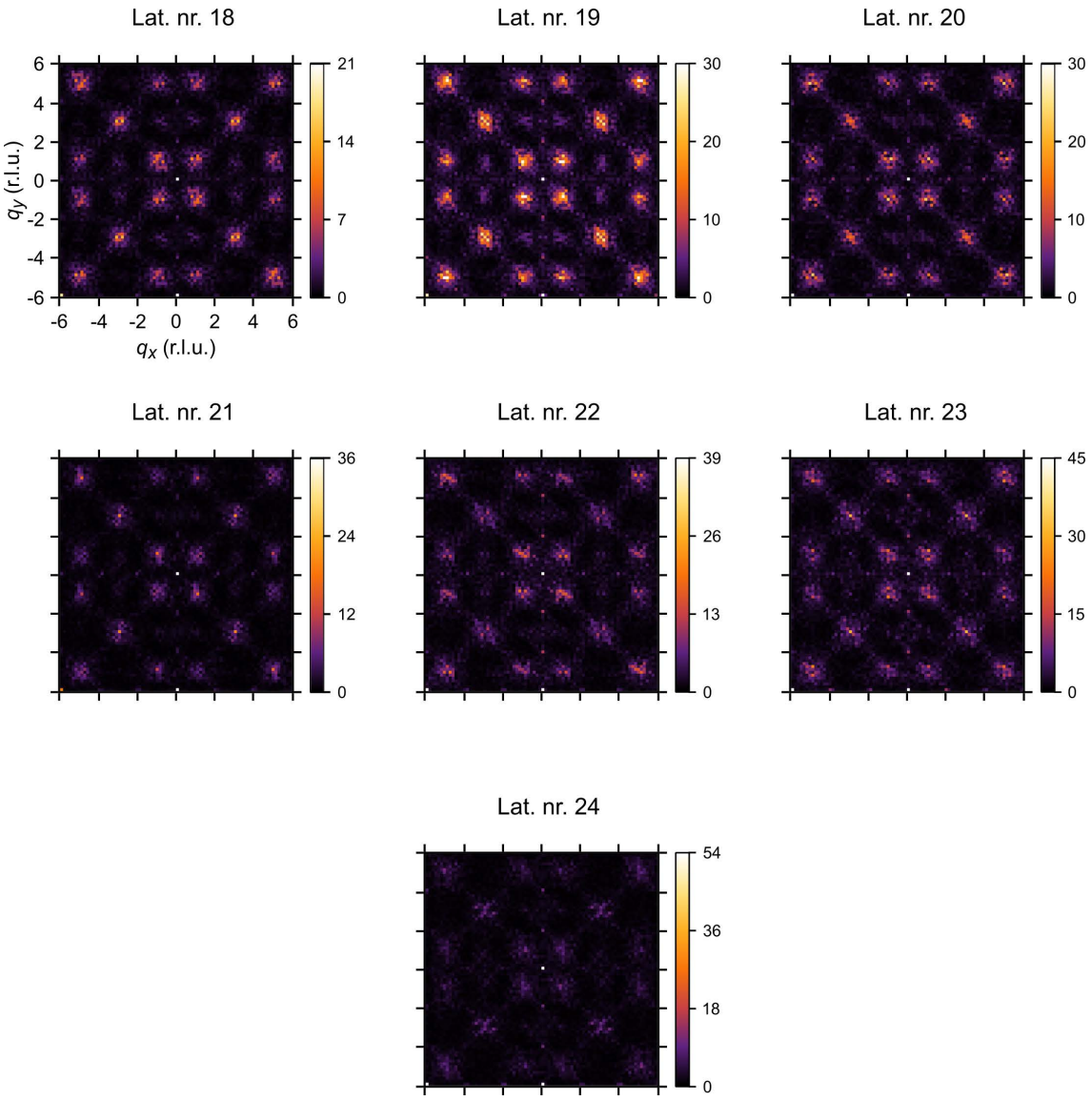

Fig. A.6: Full series of average experimental MSF for lattices with magnet width $w = 100$ nm, part B. Three examples from this series are provided directly in the text of the thesis and compared against numerical MSFs. Note the formation of Bragg peaks at y axis, these are indicative of residual saturated-like ordering, indicating inefficient demagnetisation. These features are not present in the numerical MSFs.

A.4 Average experimental MSF, $w = 150$ nm series

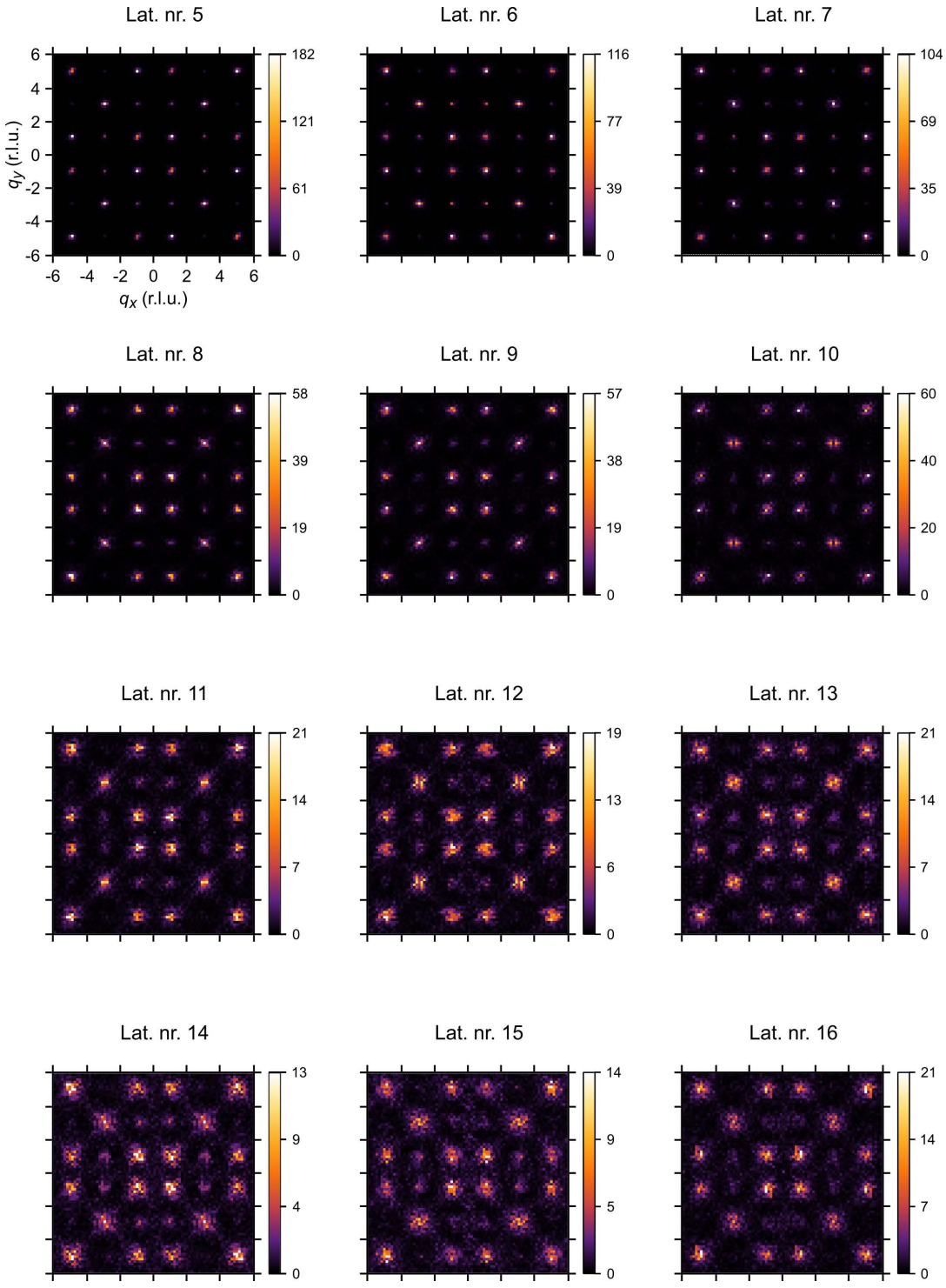

Fig. A.7: Full series of average experimental MSF for lattices with magnet width $w = 150$ nm, part A. Three examples from this series are provided directly in the text of the thesis and compared against numerical MSFs.

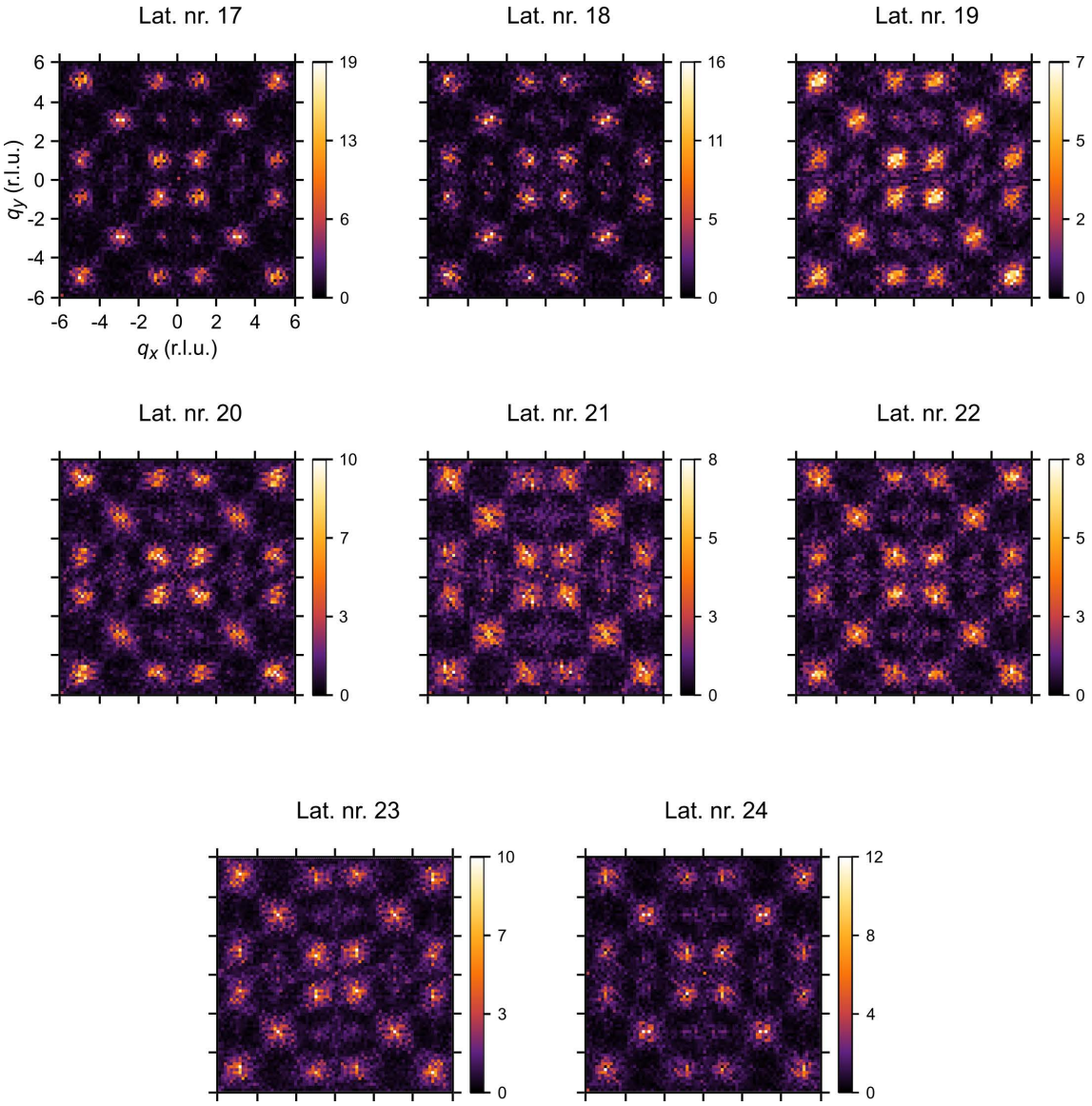

Fig. A.8: Full series of average experimental MSF for lattices with magnet width $w = 150$ nm, part B. Three examples from this series are provided directly in the text of the thesis and compared against numerical MSFs.